MECHANICAL RESPONSE OF SPRING FILMS UNDER COMPRESSION AND SHEAR LOADING

BY

RYAN NICHOLAS MOTT

THESIS

Submitted in partial fulfillment of the requirements
for the degree of Master of Science in Aerospace Engineering
in the Graduate College of the
University of Illinois at Urbana-Champaign, 2015

Urbana, Illinois

Adviser:

Professor Ioannis Chasiotis

ABSTRACT

Thin films of discrete micro and nanostructures fabricated by the method of Glancing Angle Deposition (GLAD) provide a means to build compliant interfaces that maintain important properties of the constituent materials, such as thermal and electrical conductivity while enabling interfacial resilience. In this dissertation research, the normal compressive and transverse stiffnesses of a variety of Si and Cu spring films were determined experimentally in order to assess the effect of geometric parameters on the mechanical response. Si springs of either 4 or 10 coil turns were deposited on unseeded and seeded Si wafers with seed spacing of 900 nm or 1500 nm. The Cu springs had 10 coil turns and were deposited on silicon wafers with 2000 nm, 2400 nm, 2800 nm, or 3200 nm seed spacing or unseeded Si substrates. Larger seed spacing resulted in Cu springs with larger coil diameters and larger wire thickness compared to seeded Si springs.

Compression tests were conducted at stress amplitudes between 0.5 MPa and 50 MPa on Si films and between 5 MPa and 50 MPa on Cu films. The test samples were circular areas of ~90 μm diameter, subjected to compression with a flat punch. The force vs. displacement curves were used to compute the film stiffness while scanning electron microscope (SEM) images were collected to measure the residual compression. The stiffness of the Si films at the lowest applied stress of 500 kPa varied between 24 ± 0.2 and 66 ± 3.4 MPa for different spring configurations. At the common test condition of 5 MPa applied stress, the stiffness of Si films was between 44 ± 0.2 and 165 ± 1 MPa, while Cu spring films had stiffnesses between 184 ± 2 and 353 ± 15 MPa. At the other extreme of an applied stress of 50 MPa, the stiffness of Si films ranged between 291 ± 0.5 and 810 ± 6 MPa and of Cu films between 611 ± 5 and 1308 ± 28 MPa. Notably, the Si films experienced more permanent deformation at lower stresses compared to Cu, reaching 6.5% at 5 MPa, while Cu films showed no permanent strain until 20 MPa, at which point they experienced only 2% permanent strain. The maximum permanent strains occurring at 50 MPa were 38% for Si and only 12% for Cu.

Shear tests were performed with both types of films using a custom apparatus. The shear stiffness was between 7 ± 0.6 and 27 ± 7 MPa for Si, and between 218 ± 37

and 322 ± 85 MPa for Cu. The higher stiffness of Cu films originated in their significantly larger coil and wire diameter compared to Si. However, the shear strength of seeded Cu springs, between 2 ± 0.4 and 4 ± 1.2 MPa, was approximately the same as that of Si, which had a range of 1 ± 0.05 to 4 ± 0.7 MPa. Cu springs failed at the seeding post which was the most slender point in the structure. Unseeded Cu springs failed within the spring layer with shear strength of 16 ± 0.9 MPa. In shear, the Si films experienced failure at different locations between the capping layer and just above the seed post, whereas the seeded Cu springs experienced failure directly at the seed post, which prevented the determination of the true shear strength of seeded Cu spring films.

ACKNOWLEDGMENTS

The completion of any project as large as a dissertation requires the help and guidance of many people, whether they be teachers, mentors, or friends. I would like to acknowledge all of the people that have in any way contributed to the research contained within this document, as well as the development of me as a student, engineer, and person.

First, I would like to thank my research advisor, Dr. Ioannis Chasiotis. I cannot express the gratitude I have for him for reaching out to me after I applied to the master's program at the University of Illinois and giving me an opportunity to conduct research in such a unique field. Nanomechanics carries a specific set of challenges, and his expertise has been invaluable in developing sound methods for conducting my research. I would also like to thank him for guiding and mentoring me in school and beyond. I will always be grateful of everything he has done for me.

I want to thank my colleagues in the NanoMechanics Research Lab, who led by example and pushed me to always do my best. Dr. Tanil Ozkan trained me on nearly every aspect of my research, and he was my primary mentor for my first year in the program. I will always be thankful of his helpfulness and friendship. Mr. Dimitrios Antartis has also been a terrific mentor and friend. I am grateful to have been able to work side-by-side with him on this project, and his support and friendship have been instrumental towards my development as a researcher. I would like to thank Dr. Pavan Kolluru, Mr. Debashish Das, Mr. Korhan Sahin, Ms. Julia Liu, and Mr. Fan Yang for all of their friendship and assistance. I am grateful to have worked with all of you, and I thank you for sharing your time with me.

I would like to express my gratitude to Air Force Office of Scientific Research Grant # FA9550-13-1-0149 and program manager Dr. B.L. Lee for providing the funding for this project. I hope that my results are as beneficial to them as this Grant has been to me.

None of my research could have been completed without the great work by the staff of the Frederick Seitz Materials Research Laboratory Central Facilities at UIUC. I would like to thank Dr. James Mabon and Mr. Matt Bresin for their training and ongoing support on the Helios 600i FIB, with which I performed all ion-milling and the majority of SEM imaging. I also want to express my gratitude to Dr. Kathy Walsh for training me on the Hysitron TriboIndenter and for helping me out any time I had issues with it. I would like to thank Ms. Honghui Zhou for training me on the SEM 4700 and SEM 4800 and ensuring that those machines were always operational, despite their high volume of use. I would like to thank the rest of the staff at the MRL for being quick to help when I had a question or issue.

I also owe thanks to Mr. Greg Milner and everyone else at the Aerospace Department's machine shop. I brought countless drawings to them over my two years on this project, and they were always quick to provide me with a flawless part. I also owe Staci McDannel and the rest of the Aerospace Department a large thanks. They made sure that I was able to focus on learning and working without worrying about administrative issues. Finally, I would like to thank my family and friends for always being there for me. Their support and encouragement has meant everything to me, and I know I will always be able to draw on that for the rest of my life.

TABLE OF CONTENTS

CHAPTER 1

INTRODUCTION

Interfaces between different materials must be able to endure strains induced by differences in the mechanical properties of the materials, such as the coefficient of thermal expansion, or by mismatches in the elastic moduli during flexure. Such interfaces, however, must provide additional benefits such as good thermal or electrical conductivity. For instance, porous copper (Cu) films have been found to withstand thermomechanical loads due to thermal mismatch, but at the expense of thermal conductivity when compared to bulk Cu [1]. Multifunctional interfaces, made of micro or nanosprings or nanowires, may provide the benefit of concurrently favorable mechanical, thermal, and electrical properties [2]. Thin films comprised of nanosprings have been shown to allow for large deformation while eliminating stress singularities near the edge of an interface and at an interface crack tip [3]. Such films fabricated by Glancing Angle Deposition (GLAD) have been produced in various materials and geometries [4] whose details, such as size and shape, are dependent on the GLAD parameters. However, there is limited information whether the material constitutive properties of GLAD fabricated springs correspond to those of bulk, which further hinders our ability to design GLAD interfaces with desirable mechanical properties.

1.1 Description of Glancing Angle Deposition (GLAD) Method

In the recent years, the GLAD method has emerged as the means to produce "sculptured films" comprised of a variety of micro and nanoscale structures [4,5,6,7,8]. The GLAD process is an extension of the Oblique Angle Deposition (OAD) of ceramic, metal and polymeric materials, which can be deposited via thermal evaporation,

sputtering, or pulsed laser deposition [5]. Under the OAD process, vapor approaches a substrate at an incident angle, α, with respect to the substrate normal and upon reaching the surface creates a random distribution of nuclei. Over time, more material is deposited on these nuclei that begin to form slanted columns with inclination angle, β. While growing, these columns shadow the deposition of vapor on smaller adjacent columns. The mechanism of growth of slanted posts by OAD is shown in Figure 1.1(a,b). It is important to note that the inclination angle of the posts, β, is dependent on, but not equal to, the incident angle of the vapor, α, as indicated in Figure 1.2.

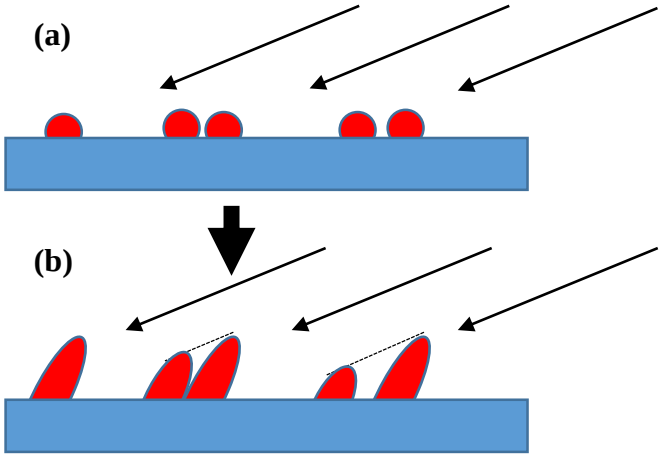

Figure 1.1 (a) Vapor arrives at an incident angle causing a random distribution of nuclei on the substrate. **(b)** As nuclei grow into columns, the shadowing effect of large columns prevents smaller columns from growing [4]. Reproduced with permission by Springer.

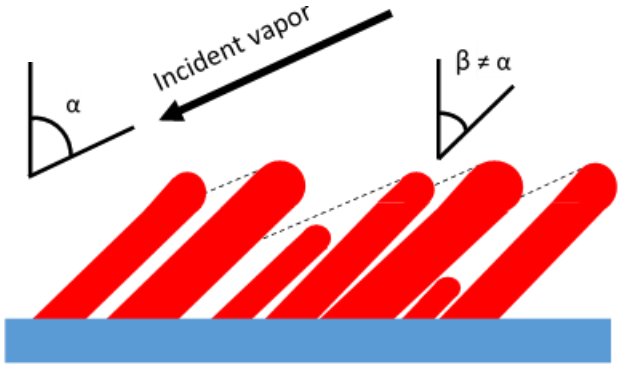

Figure 1.2 Example of OAD growth showing that incident angle, α, is not equal to the column inclination angle, β [5]. Reproduced with permission by Elsevier Books.

GLAD differs from OAD because it allows to dynamically alter the columnar structures by rotating the substrate during deposition [5], as shown in Figure 1.3. Two motors vary the incident angle, α, and the substrate rotation angle, φ, to form several basic GLAD structures [6], as shown in Figure 1.4(a-d). Each structure is created by holding α constant throughout deposition and varying φ. If φ is held constant, slanted posts are formed, Figure 1.4(a), while by rotating the substrate by 180^o during successive steps of growth, chevrons are formed, Figure 1.4(b). If φ changes continuously at slow rate, helical columns or springs, form, Figure 1.4(c). It has been shown [6] that the pitch of the helices, namely the vertical distance between successive turns in a helix, approaches the diameter of the column as the angular velocity of the substrate rotation is increased, thus resulting in loss of helical geometry, and the formation of vertical columns, Figure 1.4(d). Any of these structures can be combined without removing the substrate from the deposition chamber by simply altering α and φ [5]. An example of such a complex shape is shown in Figure 1.5. Furthermore, a dense capping layer can be grown on any GLAD film to provide a non-porous sheet of material for further processing and additional growth steps [7]. Capping layers are formed by decreasing the incident angle to 0^o during deposition, thus eliminating the shadowing effect and forming a dense layer of material on top of GLAD structures.

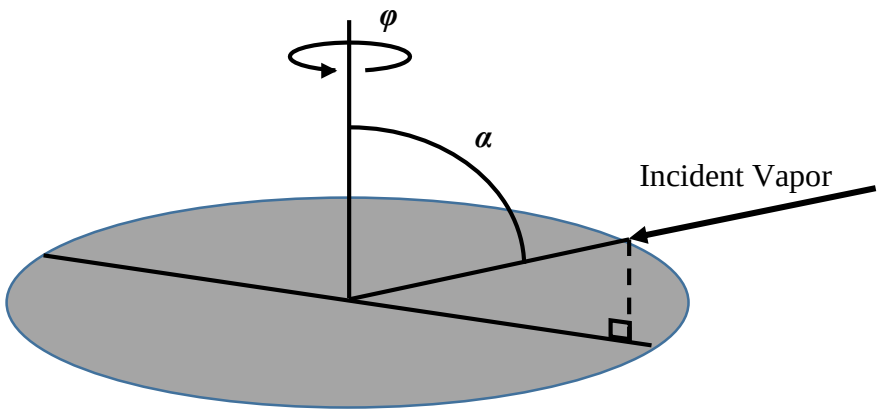

Figure 1.3 Substrate coordinate system, showing the vapor incident angle, α, the substrate rotation angle, φ [5]. Reproduced with permission by Elsevier Books.

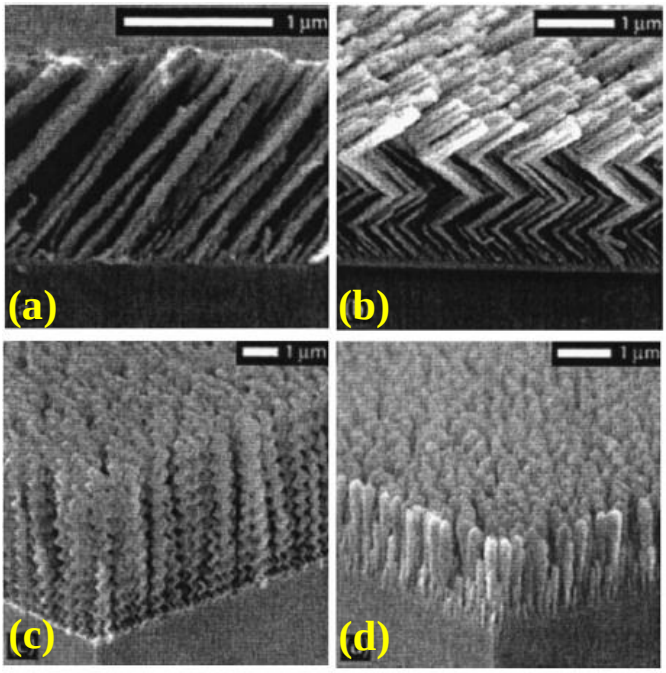

Figure 1.4 Basic GLAD structures forming as a result of constant α, and constant, discrete, or continuous change of φ: (a) slanted posts, (b) chevrons, (c) helical columns, and (d) vertical columns [6]. Used with permission by Journal of Vacuum Science & Technology.

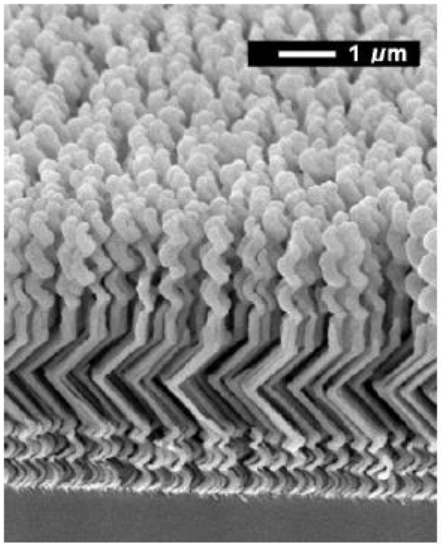

Figure 1.5 GLAD deposited structure combining (from bottom to top) helical columns, chevrons, short vertical post, and additional helical columns [5]. Used with permission by Elsevier Books.

1.2 Properties of Thin Films Grown via GLAD

The GLAD method allows for modification of the physical properties of a surface by customization of the geometrical features of a thin film. For example, Akkari et al. [8] examined columnar structured copper indium disulfide ($CuInS_2$) thin films fabricated at various incident angles with and without substrate rotation and showed that, in the absence of rotation, the inclination angle of the columns increased with the incident angle, while the absorption coefficients were enhanced when deposited without rotation, just by varying the incident angle. Xiao et al [9] examined the dependency of inclination angle on the structural and optical properties of niobium oxide (Nb_2O_5) thin films. As α increased, the packing density of the material decreased, causing an increase in porosity and a decrease in the film's refractive index. Gospodyn et al. [10] examined the photoluminescence PL of yttrium oxide (Y_2O_3) films fabricated with GLAD and showed the ability to design films with specific angular emission profiles. Bezuidenhout and Brett [11] investigated the effect of α and film layer height on the porosity of GLAD films composed of six-sided spiral shaped silicon dioxide (SiO_2) structures formed using the same method as chevrons, except the substrate was rotated by 60^o in each time interval, as opposed to 180^o. Their results showed that the top of the film became more porous when either the incident angle increased or the film height increased. In both cases, the length of the shadows cast by a column increased, either due to an increase in the incident angle or the height, thus restricting the growth of smaller columns that a shadow was cast upon. This relationship between porosity and incident angle was also confirmed in the aforementioned study of Nb_2O_5 thin films by Xiao et al. [9].

1.3 Mechanical Behavior of Nanospring Films Fabricated by GLAD

The mechanical behavior of films fabricated by GLAD is expected to depart significantly from that of solid films fabricated by the same materials. In the past, several studies approached this question with experiments at the level of a few springs. Hirakata et al. [3,12] used an atomic force microscope (AFM) to apply vertical and lateral forces on capped tantalum oxide (Ta_2O_5) helical nanospring films, Figure 1.6(a,b). The authors

found that the film's shear and Young's moduli were 2-3 orders smaller than those of solid Ta_2O_5, with Young's moduli of 0.38 ± 0.03 GPa for the spring film vs. 117 ± 10 GPa for solid Ta_2O_5. However, these experiments were performed using a pointed diamond tip, resulting in non-uniform stresses across the nanospring film.

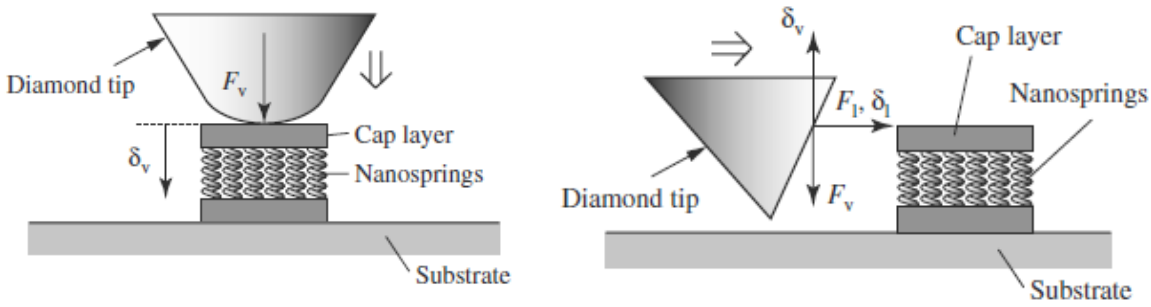

(a) **(b)**

Figure 1.6 AFM experiments performed on spring films: **(a)** Compression test with a rounded diamond tip, and **(b)** shear test via a side force to the cap layer [12]. Used with permission by International Journal of Solids and Structures.

Liu et al. [13] performed multiple compression tests on individual Si nanosprings within a bulk forest using an AFM with a tip height of 5-7 μm and a radius of curvature of approximately 10 nm. These tests were performed on Si nanosprings with seed spacing of 1000 nm (spring A) and 600 nm (spring B), both grown on a templated Si substrate using OAD at an incident angle of 85°. The springs were grown on 150 nm diameter tungsten posts, with a square seed pattern for spring A and a triangular seed pattern for spring B. The two types of springs had the same pitch angle of 28° and pitch of 950 nm, but differed greatly in the wire thickness: 350 ± 20 nm for spring A and 225 ± 10 nm for spring B and slightly in the coil diameter: 570 ± 30 nm for spring A and 590 ± 10 nm for spring B. Spring A with wire thickness of approximately 1.6 times that of spring B, showed 4 times larger average stiffness. However, these experiments were performed on single springs inside a film where the adjacent nanosprings could play a significant role, especially at large displacements. For this reason, the precise stiffness values reported in [13] may not be the same as those of isolated Si springs.

Seto et al. [14,15] examined the effective Young's modulus of 2 μm thick silicon monoxide (SiO) microspring films of 1, 2, and 3 turns, as well as dense SiO films, by using a spherical indenter with a tip of 100 μm radius. Microspring films were approximately 1000 times more compliant than dense SiO films. The film areal stiffness, defined as the stiffness per unit area that was tested, in this case approximated to a circular flat contact area, was calculated by dividing the slope of the load vs. displacement curve by the total area that was compressed. The authors found that the areal stiffness increased with the number of turns from 10.0 $(Nm^{-1})/\mu m^2$ to 17.8 $(Nm^{-1})/\mu m^2$, while the dense SiO film had a stiffness of 18,500 $(Nm^{-1})/\mu m^2$. Notably, the load vs. displacement plots were hysteretic, Figure 1.7, according to the authors due to a difference between the loading strain rate and the strain rate during recovery under unloading. A shortcoming of this study stems from the use of a spherical tip which results in non-uniform stress. The springs directly under the tip experience a higher displacement than those outside of the tip contact.

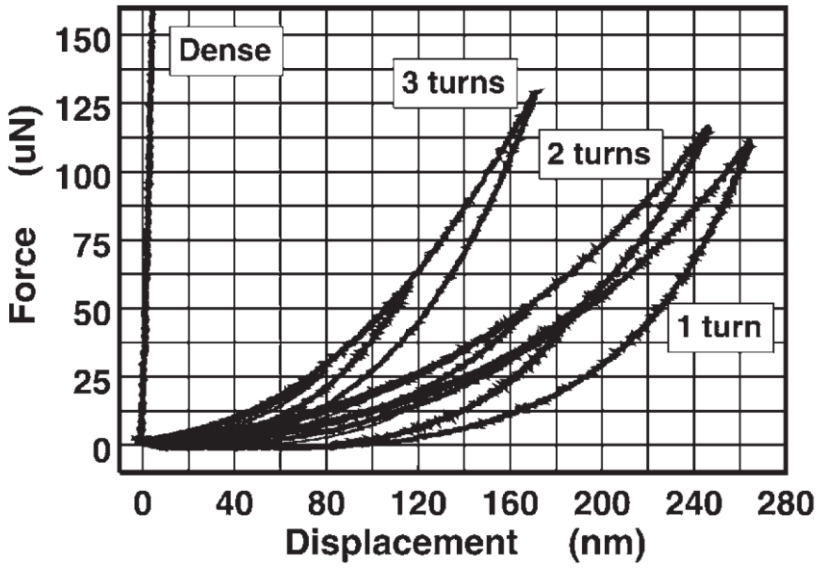

Figure 1.7 Nanoindentation plots of various SiO spring films and a dense SiO film. The stiffness increases with the number of turns but hysteresis persists in all SiO nanospring films [15]. Used with permission from Journal of Micromechanics and Microengineering.

Zhang and Zhao [16] used Finite Element Modeling (FEM) to obtain predictions for the mechanical behavior of the same spring geometries as in Seto's study [15]. Their model demonstrated a large dependency on the precise boundary conditions, as springs restricted from rotation were 2-3 times stiffer than those that were free to rotate.

Each of the studies described above involved the displacement of nanosprings by 15 nm [12], 100 nm [13], and 300 nm [15], producing small strains in most cases. It is of interest to extend such experiments to large strains and measure the associated changes in normal and shear compliance as well as the residual compressive strain and shear strength. Such experiments can further involve comparisons of the mechanical behavior between isolated springs and films of springs to deduce the role of spring interactions within a film.

1.4 Objectives of Dissertation Research

The focal points of this thesis are the effects of compressive and shear loading on the elastic and plastic deformation of Cu and Si spring films. For a given spring height, the coil angle, coil diameter, coil wire diameter, and the overlap between coils represent important parameters to assess in the design of experiments. In the present study, experiments were conducted with spring films of Cu which is a ductile material and very important thermal and electrical conductor, and of Si which is brittle material with multifunctional applications in energy harvesting and storage. Within the control provided by the GLAD process, the combined effect of spring intertwining and coil parameters on the elastic and inelastic mechanical behavior of Cu and Si films is investigated to identify parameters that would facilitate high normal shear compliance while maintaining large elastic compression and shear strength.

The test specimens are Cu films with different spacing between adjacent seeds, and Si films with two different coil angles and two seed spacings which control the wire diameter and the overlap between springs. Compression tests are performed on patterned sections of films to determine the compressive stiffness and permanent deformation as a

function of load. Likewise, shear tests are performed on isolated rectangular areas to obtain the shear stiffness and shear strength. The methods employed in the experiments carried out in this dissertation are:

- Compression experiments with large areas of seeded and unseeded Cu and Si spring films using an instrumented nanoindenter that is equipped with a flat punch to apply uniform normal loading and displacements. The residual deformation is measured *post mortem* using a Scanning Electron Microscope (SEM).
- In-plane shear tests with large areas of seeded and unseeded Cu and Si spring films using an in-house developed apparatus to obtain the shear stiffness and strength.

A major challenge in the aforementioned experiments is the ability to measure very small normal and shear displacements with resolution of the order of a few tens of nanometers.

CHAPTER 2

MATERIALS AND EXPERIMENTAL METHODS

The experiments in this dissertation research were developed to measure the mechanical response of isolated areas of Si and Cu spring films under uniform compressive and shear stress. Cu and Si selected for the experiments to assess the behavior of spring films comprised of a ductile and a brittle material. Spring films with different structural parameters, such as the number of coil turns for a fixed height, the wire diameter, and the spring spacing were tested to determine the effects of each parameter on the elastic and plastic film properties. Compression tests were performed at several stress ranges to examine the relationship between the applied stress and the resulting compressive film stiffness, and the influence of cyclic loading on film stiffness and residual compression. The shear stiffness and ultimate shear strength of the same types of capped films were determined. In the aforementioned experiments, the selection of the best experimental approach was made based on availability of appropriate experimental tools. The compression experiments were conducted using a commercial apparatus for instrumented nanoindentation, while the shear experiments were conducted using a custom built apparatus. Although the force measurements were in the range of mN which is reasonably easy to measure with most available methods, the associate film deformation was in the range of 10-1000 nm requiring high displacement resolution and experimental fidelity.

2.1 Materials

2.1.1 Silicon Spring Films

The Si spring films tested in this work were fabricated by GLAD at Micralyne, a MEMS and small structures manufacturer in Edmonton, Canada. The choice of deposition parameters provided a variation in wire diameter, coil diameter, and coil angle. The films were deposited on seeded and unseeded substrates. Although unseeded films are easier to prepare, they demonstrate a large distribution of spring sizes [17] and they are intertwined which prevents the use of analytical calculations to obtain property estimates based on known mechanical models for springs. In the case of seeded springs, increased seed spacing and small coil height also reduces the degree of intertwining between adjacent springs.

Seeds for spring growth were patterned on 0.8 μm thick photoresist, Ultra-i 123. The pattern was transferred to the Si wafer using deep reactive-ion etching (DRIE) with a depth of 500 nm, leaving a regular pattern of 500 nm tall Si posts. A layer of photoresist was deposited onto the wafer to protect the posts during the next step. The back side of the wafer was scribed to create a 1×1 cm^2 grid to facilitate post-fabrication dicing into dies that could be individually tested. Finally, the photoresist was removed, and the substrate was ready for GLAD. Three types of Si spring films were fabricated that were either unseeded or had seed spacings of 900 nm or 1500 nm. For each seed spacing, Si springs with 1000 nm and 2500 nm pitch were fabricated, thus resulting in six different types of films. All Si springs were approximately 10 μm tall consisting of 4 or 10 turns. Si springs were deposited at a rate of 10 Å/s, as reported by Micralyne, and an incident angle of 85^o with respect to the substrate normal and were grown in four deposition steps of 2500 nm each. The 4-turn springs were deposited with a substrate rotation rate of 4.2^o/min, whereas the 10-turn springs were deposited with a substrate rotation rate of 10.6^o/min, as computed using the deposition times reported by Micralyne. Images of uncapped Si springs are shown in Figure 2.1(a-f). The 4-turn structures approximated open-coiled springs, whereas the 10-turn, 1500-nm spaced structures were screw-like with filled center. Top views of the seeded springs are shown in Figure 2.2(a-d).

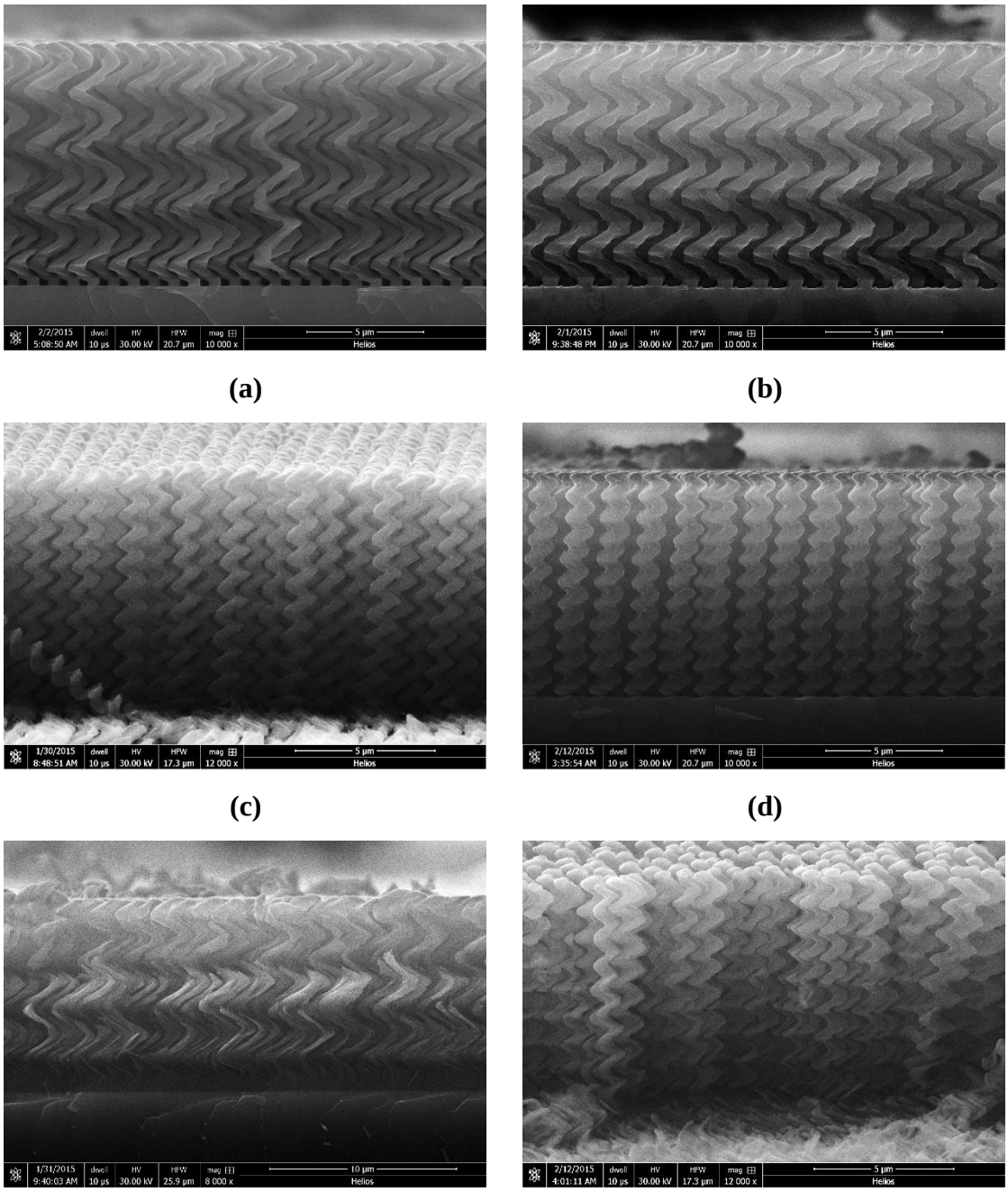

(a) **(b)**

(c) **(d)**

(e) **(f)**

Figure 2.1 Si spring films with **(a)** 4 coil turns and 900 nm seed spacing, **(b)** 4 coil turns and 1500 nm seed spacing, **(c)** 10 coil turns and 900 nm seed spacing, **(d)** 10 coil turns and 1500 nm seed spacing, **(e)** 4 coil turns and unseeded substrate, and **(f)** 10 coil turns and unseeded substrate.

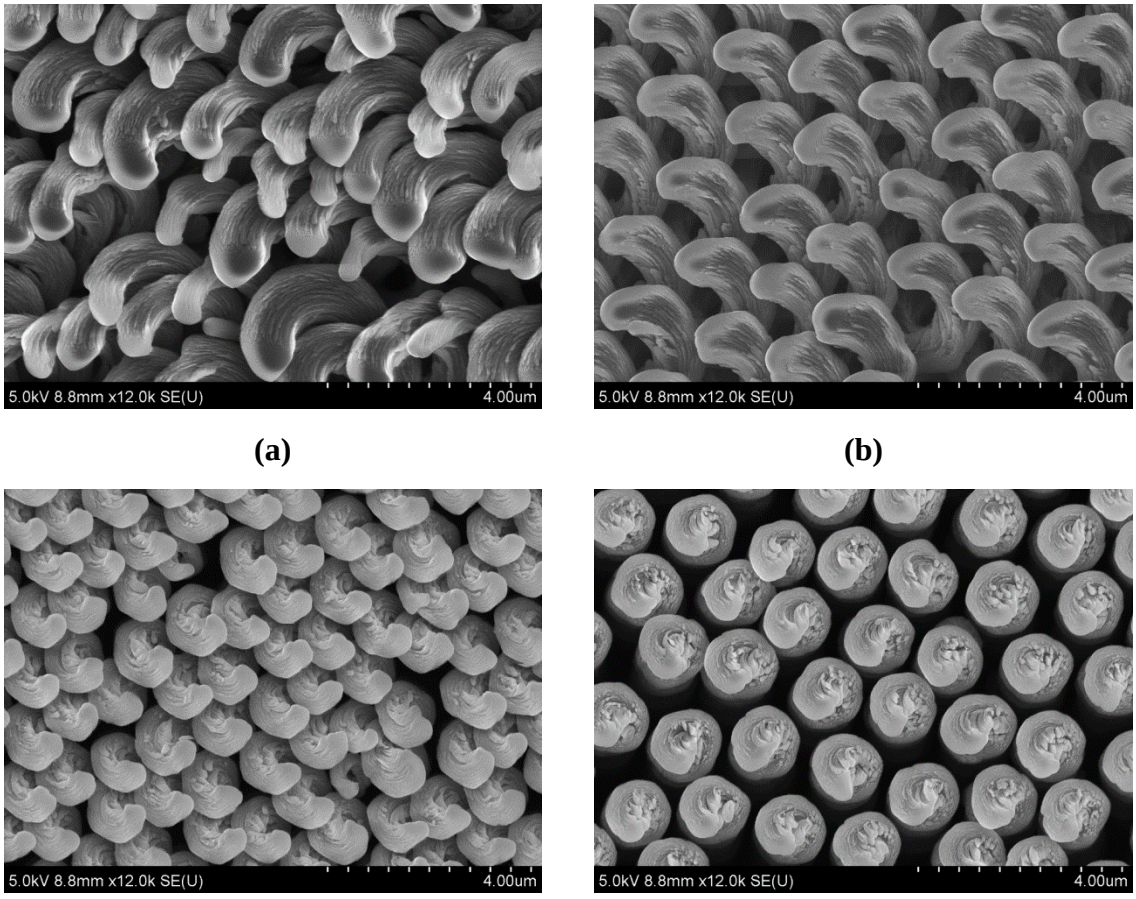

Figure 2.2 Top views of Si spring films with **(a)** 4 coil turns and 900 nm seed spacing, **(b)** 4 coil turns and 1500 nm seed spacing, **(c)** 10 coil turns and 900 nm seed spacing, and **(d)** 10 coil turns and 1500 nm seed spacing.

Half of the films were capped with an additional 1000 nm layer of solid Si. The capped films were utilized for the shear tests but were also characterized by different boundary conditions in comparison to the uncapped films. This capping layer was also deposited at a rate of 10 Å/s, and substrate rotation rate of 2400^{o}/min, with an incident angle of 20^{o} with respect to the substrate normal. Seeded Si springs with a capping layer are shown in Figure 2.3(a-d). The capping layer was continuous in the case of 4-turn springs that demonstrated significant overlap, while the capping layer was not cohesive in the case of 10-turn springs, especially for 1500 nm seed spacing.

The exact geometry of 4-turn Si springs was determined from SEM images, such as those in Figure 2.4(a-c) and Figures 2.5(a-c), which were used to determine the major and minor axes, 2*a*, *2b* of the elliptical wire cross-section and the coil diameter, *D*, which is defined as the diameter of the midline of the spring wire. The geometrical properties of the 4-turn, seeded Si springs are given in Table 2.1. The geometry of 10-turn structures departed significantly from that of a spring, therefore the details of their geometry were not possible to determine accurately.

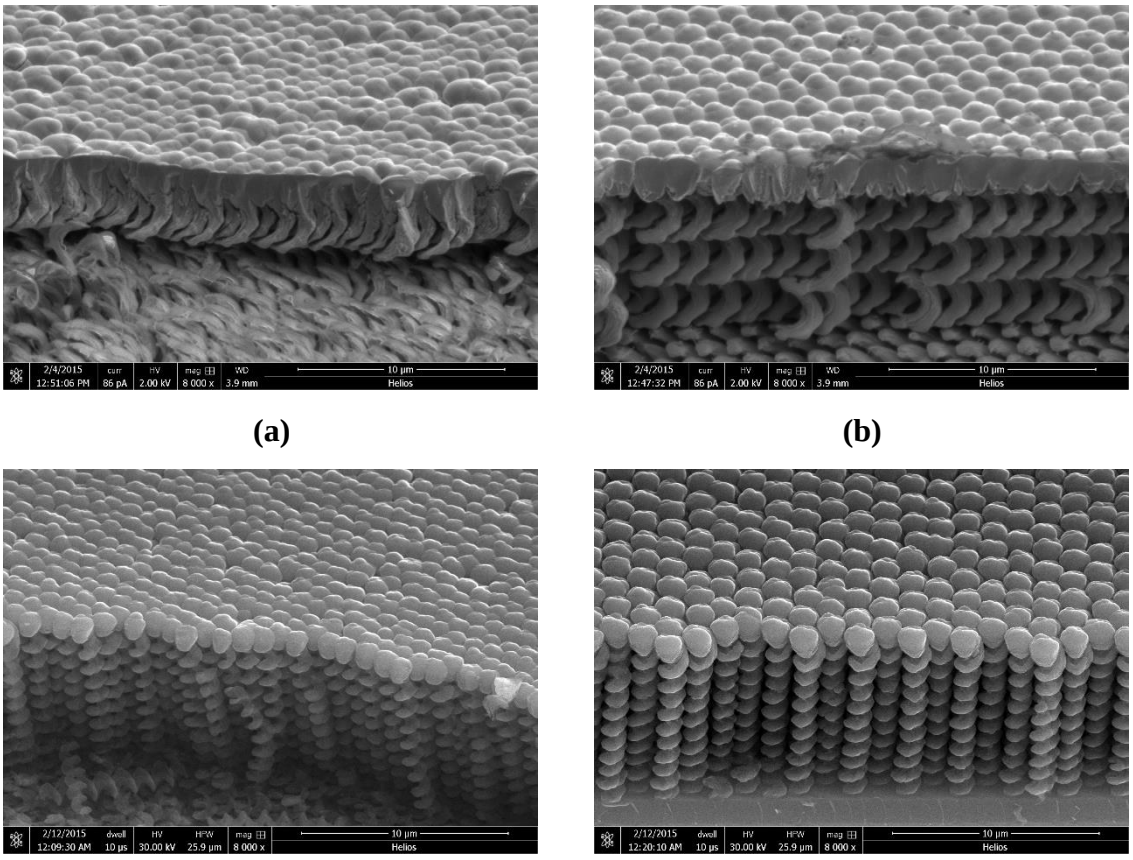

(a) **(b)**

(c) **(d)**

Figure 2.3 Si spring films with 1000 nm capping layer and **(a)** 4 coil turns and 900 nm seed spacing, **(b)** 4 coil turns and 1500 nm seed spacing, **(c)** 10 coil turns and 900 nm seed spacing, and **(d)** 10 turns and 1500 nm seed spacing.

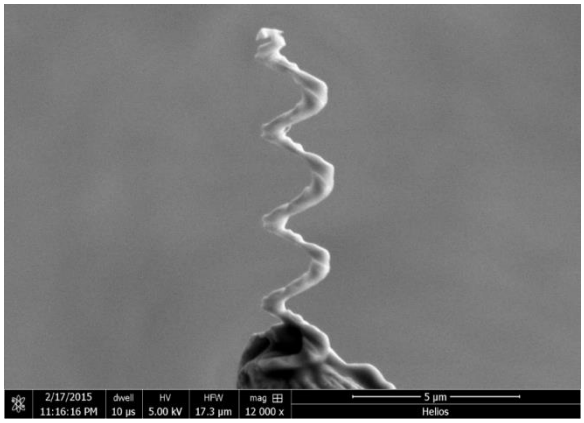

(a)

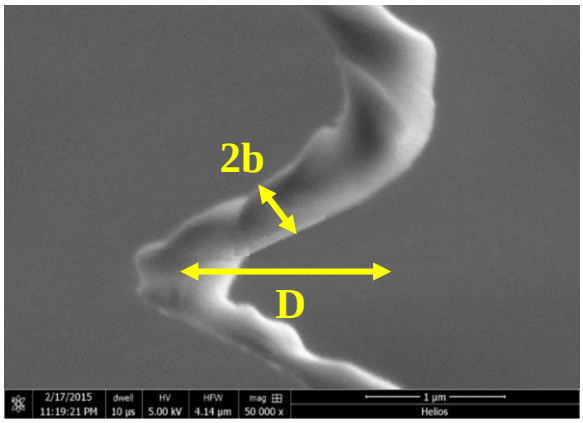

(b)

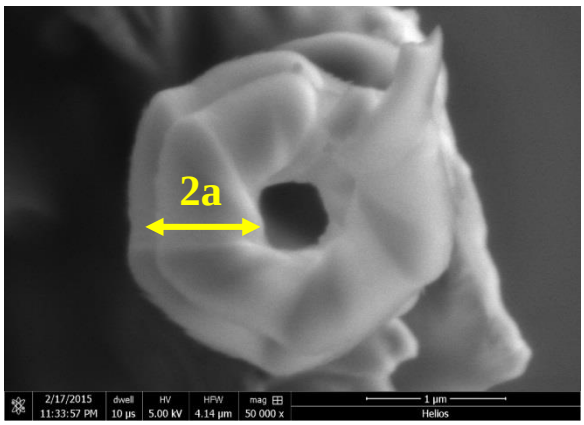

(c)

Figure 2.4 SEM images of a 4-turn Si spring from a film with 900 nm seed spacing. **(a)** side view, **(b)** magnified side view, and **(c)** top view. The coil diameter and minor axis were measured from the side view images, while the major axis was measured from the top view image.

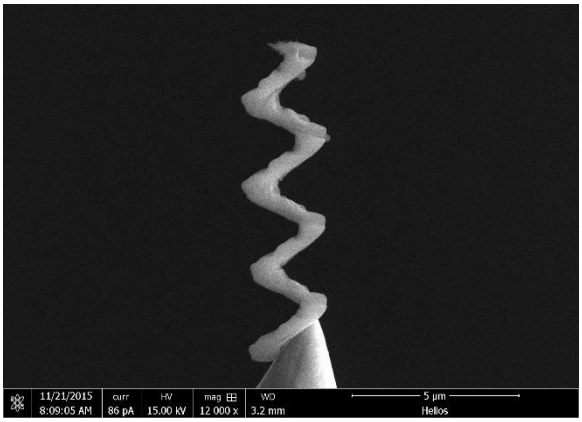

(a)

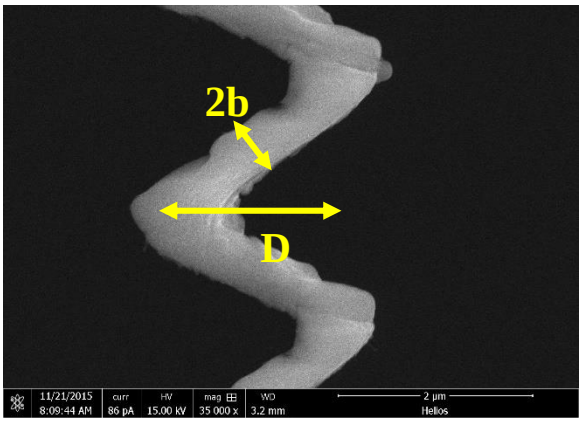

(b)

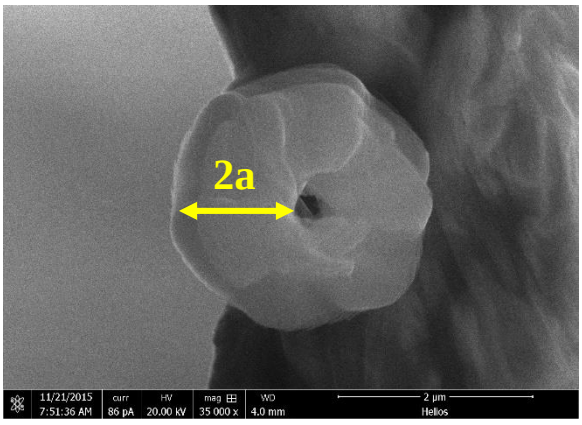

(c)

Figure 2.5 SEM images of a 4-turn Si spring from a film with 1500 nm seed spacing. **(a)** Side view, **(b)** magnified side view, and **(c)** top view. The coil diameter and minor axis were measured from the side view images, while the major axis was measured from the top view image.

Table 2.1 Geometrical parameters of seeded, 4-turn, Si springs.

Spring type	Height (μm)	Major Axis (μm)	Minor Axis (μm)	Coil Diameter (μm)
4-turn, 900 nm	10.23	0.76	0.44	1.53
4-turn, 1500 nm	10.14	0.94	0.52	1.57

2.1.2 Copper Spring Films

The Cu spring films were fabricated at Micralyne using GLAD on seeded silicon wafers. Seeds were patterned with 0.6-μm thick photoresist, MicroChem SPR 660. 10-μm high, 10-turn Cu spring films, Figure 2.6(a-e), were deposited with seed spacings of 2000 nm, 2400 nm, 2800 nm and 3200 nm. Portions of the wafers also contained unseeded Cu springs films. Larger seed spacing resulted in larger coil diameter and less overlap between adjacent springs. Thus, the interaction between adjacent springs could decrease as the seed spacing increases. The Cu films were deposited at a rate of 20 Å/s and an incident angle of 86^o with respect to the substrate normal and were grown in 4 stages, each stage producing 2.5 turns and an approximate film thickness of 2,500 nm. The substrate rotation speed was 7.1^o/min.

Notably, the geometry of 10-turn Cu springs was quite different from that of 10-turn Si springs. This difference was due to the deposition rate and substrate rotation speed. For 10-turn Si, the deposition rate was 10 Å/s and the rotation rate was 10.6^o/min, while the 10-turn Cu films had deposition rate of 20 Å/s and rotation rate of 7.1^o/min. This corresponds to a deposition rate of 56.6 Å per degree of rotation for Si and 169.0 Å per degree of rotation for Cu. Therefore, the Cu springs had nearly 3 times more material deposited for each degree of rotation. Because of the large incident angle of the vapor during the GLAD process, the additional Cu material caused the springs to grow outward, away from their axis. This explains why Si springs were more columnar and screw-like, while Cu springs were wide and more spring-like.

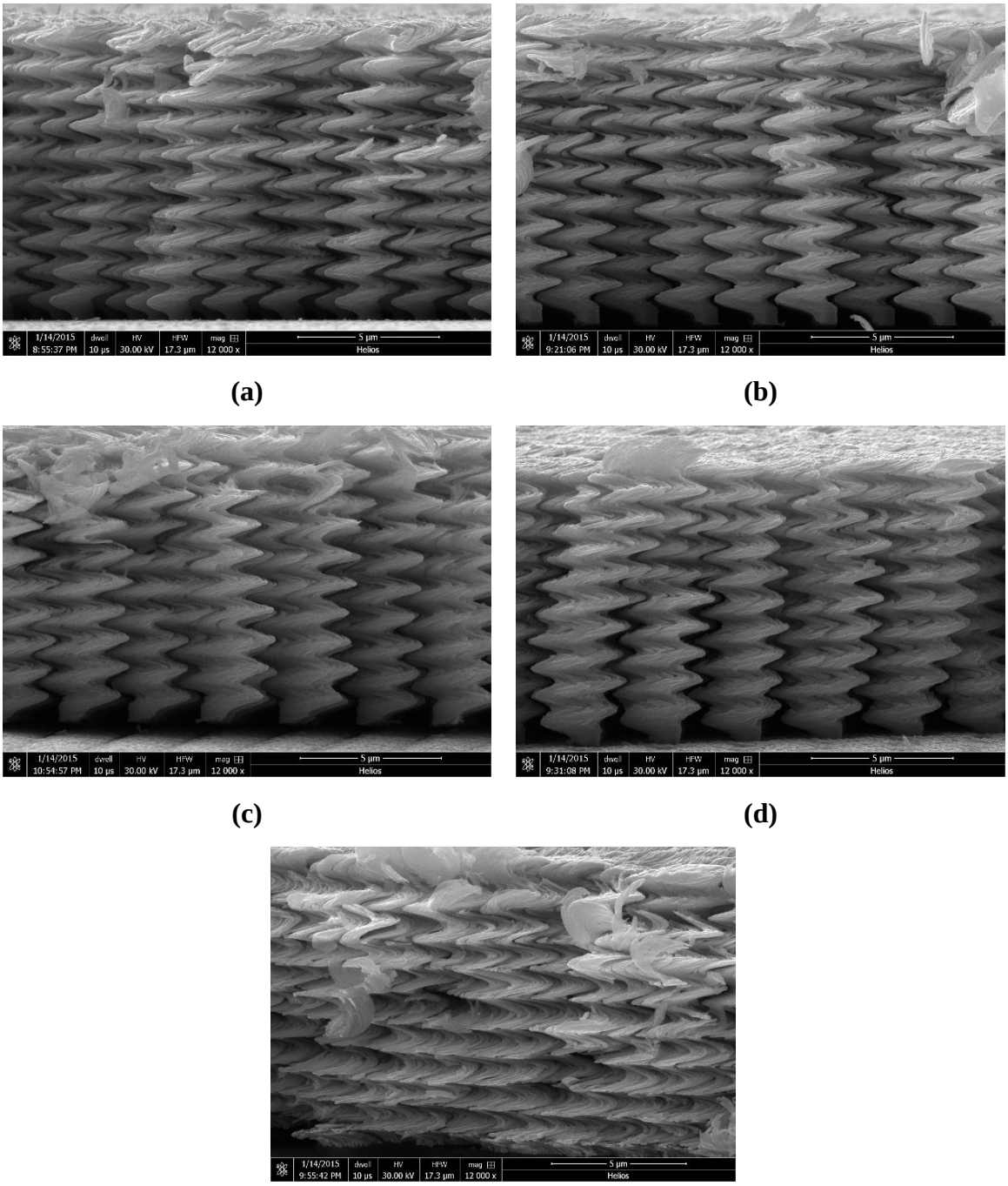

Figure 2.6 Cu springs with 10 coil turns and **(a)** 2000 nm, **(b)** 2400 nm, (c) 2800 nm, **(d)** 3200 nm seed spacing, and **(e)** on unseeded substrate.

2.2 Compression Experiments with GLAD Films

Compression tests were performed on uncapped seeded and unseeded Si and Cu spring films deposited on Si wafers. Precise tests areas were prepared using a Focused Ion Beam (FIB). First, a ring with outer diameter of 130 μm and inner diameter of 100 μm was milled at 30 kV and 21-47 nA through the thickness of each film, as shown in Figure 2.7(a). The adjacent springs outside of each resulting cylindrical area were then removed using a fine blade leaving behind a test sample as shown in Figure 2.7(b). As a result of the initial milling, a fused layer of Si or Cu formed at the outermost edges of the test areas, Figure 2.8(a,b), which was then removed by FIB ion-milling at the low power level of 30 kV and 9 nA. This process created circular test areas with no fused springs at the edges, similar to those shown in Figure 2.7(c). Compression tests were performed with a Hysitron TI 950 TriboIndenter and a 188-μm diameter circular flat punch made of sapphire. The dies carrying the spring film samples were attached to a steel sample disc with cyanoacrylate adhesive, which was clamped on a two-axis tilt stage to allow for tilt adjustments of the sample die. Each test area was subjected to a 10-cycle loading and unloading between 0 MPa and 0.5, 5, 10, 15, 20, 25, 30, 40, or 50 MPa. Only the Si films were exposed to 0.5 MPa. Each sample was subjected to an additional 10-cycle loading and unloading in a ±10% range about each chosen stress value. The compressive stiffness, E_{comp}, was then calculated from the slope of the load vs. displacement plot by:

$$E_{comp} = k_{comp}\frac{h}{A} \tag{2.1}$$

where k_{comp} is the slope of the curve constructed with data taken at the ±10% range of each stress value, h is the mean height of the spring film where the slope was computed, and A is the test area. The loading and unloading compressive stiffnesses were calculated for each cycle of the test. A plot of the load vs. displacement data for 4-turn, 900 nm seeded Si springs at 5 MPa mean stress is shown in Figure 2.9(a). The same data with each cycle separated for clarity are plotted in Figure 2.9(b). h was calculated by subtracting the total unloading displacement of the indenter tip, as computed from the mean value in each cycle, from the final height of the film. The final height of the film, as

determined from SEM images, did not include the permanent deformation induced to the test area during the initial loading to the mean stress value.

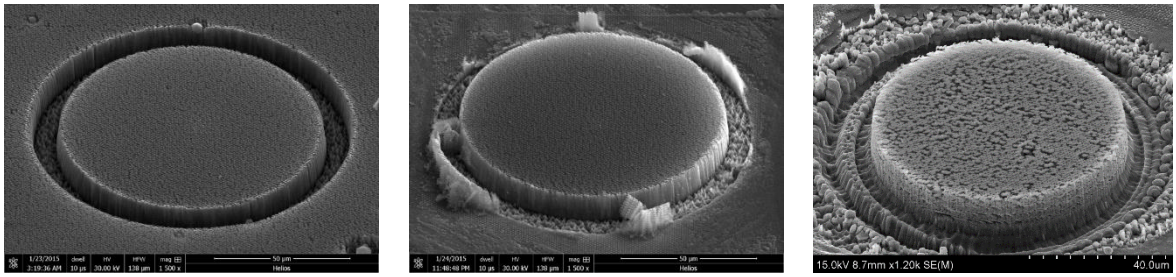

(a) **(b)** **(c)**

Figure 2.7 Test area definition for a 4-turn Si spring film with 900 nm seed spacing: **(a)** Initial FIB milling of a cylinder with fused edges, **(b)** springs were removed outside of the cylinder using a sharp blade, **(c)** fine FIB ion-milling removed fused springs at the edges.

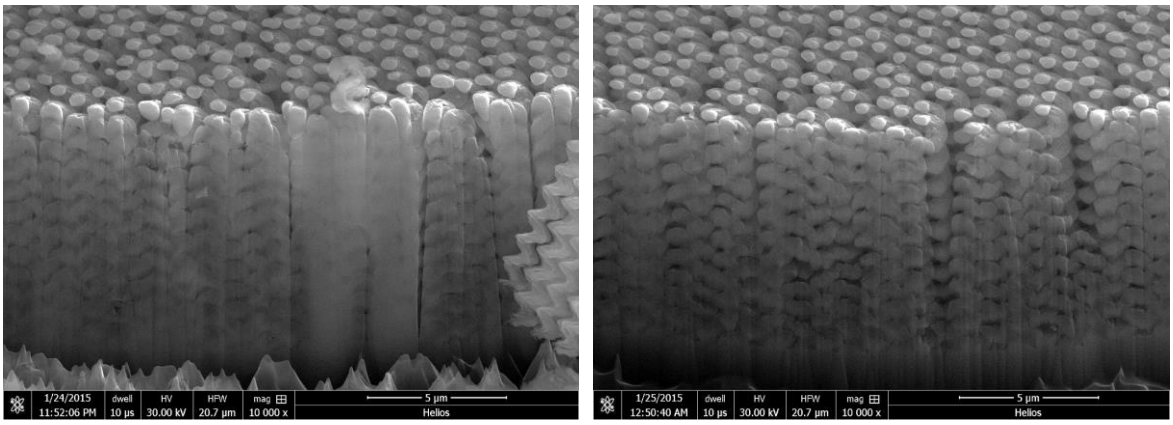

(a) **(b)**

Figure 2.8 Edge of a test area of 10-turn Si springs with 900 nm seed spacing. **(a)** Several springs on the edge are fused. **(b)** Edge after fine ion-milling showing that all edge springs are clearly separated.

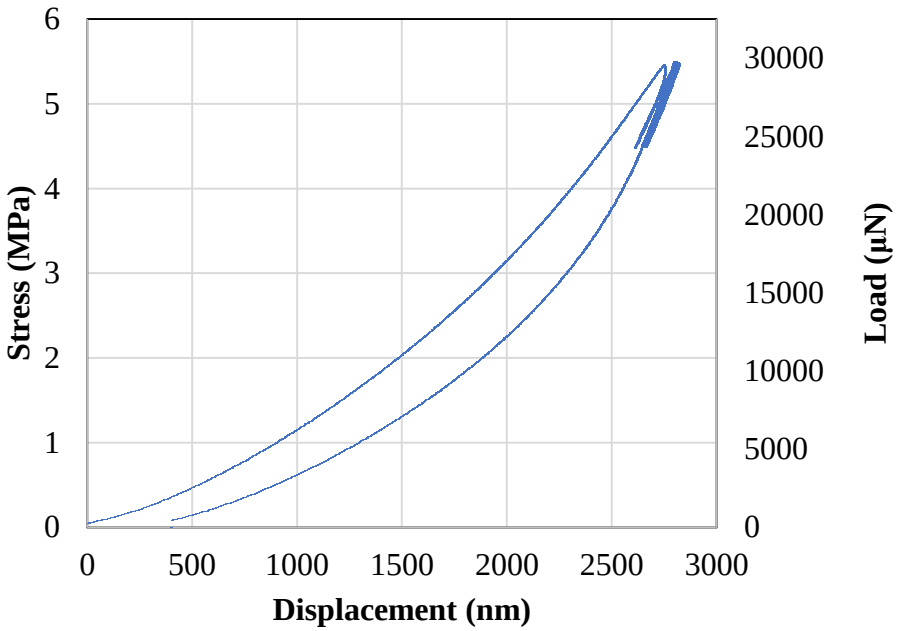

(a)

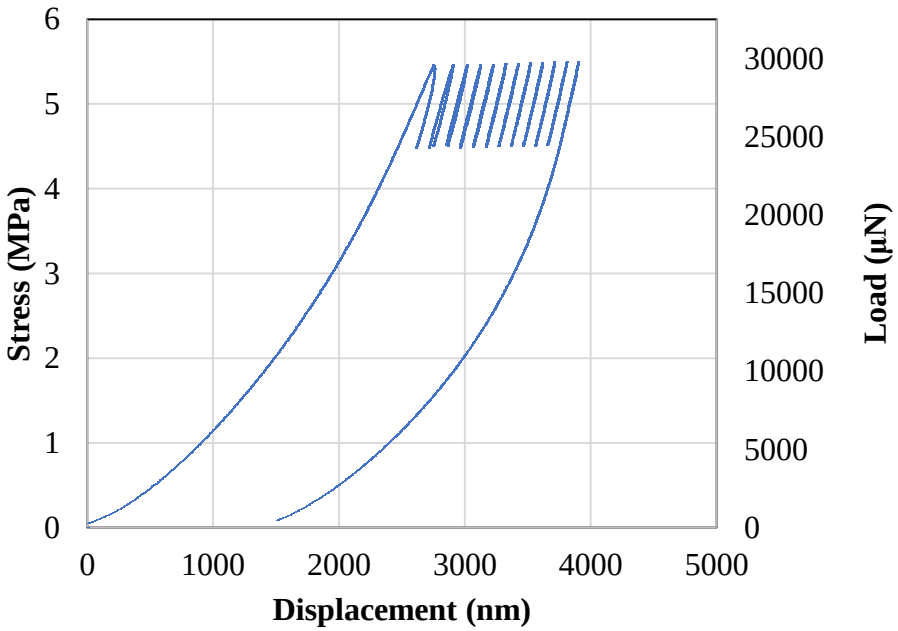

(b)

Figure 2.9 (a) Load vs. displacement plot of a 4-turn and 900 nm seeded Si spring film subjected to 0-5 MPa. In **(b)** each loading-unloading cycle with amplitude of 10% of the mean is separated in this plot for clarity. Detailed plots of the cyclic component of loading are shown in Appendix A.

2.3 Shear Experiments with GLAD Films

Shear tests were performed using the apparatus shown in Figure 2.10 [18]. The force was measured with a 50 g load cell and shear displacements were imposed with a horizontal probe that was displaced parallel to the sample surface and driven by a linear PZT picomotor™. The apparatus was placed under an optical microscope with a CCD camera to record images of the sample surface during testing at a rate of 5 Hz. Shear displacements were imposed with a 130-170 μm thick glass probe that was attached with UV-curable adhesive to the surface of the spring film. Because of the use of an adhesive, the film specimens prepared for shear testing required a capping layer to prevent the flow of adhesive in the spring layer. While Si springs films were deposited with a 1000 nm thick capping layer, the as-received Cu spring films had no capping layer. Therefore, a 1000 nm capping layer of gold-palladium (Au-Pd) was deposited using an Emitech K575 sputter coater. The films were placed in the sputter coater on a tilt stage such that the incident angle of the Au-Pd was 20 degrees. The original films were coated with 100 nm Au-Pd, and then were rotated by 90 degrees with respect to the tilt stage. This process was repeated until the film of Au-Pd was ~800 nm thick. The die was then oriented such that the incident angle was normal to the substrate surface to deposit a final 200 nm layer, resulting in a capping layer, Figure 2.11. While not a completely coherent cap, this additional layer provided a 1000 nm thick barrier to adhesive. Rectangular test areas of 100×200 μm^2 were FIB-milled at 30 kV and 65 nA and the surrounding springs were removed using a fine blade. The fused springs were then removed by subsequent FIB ion-milling at 30 kV and 9 nA, creating perfectly rectangular test areas, as shown in Figure 2.12. Using UV-curable adhesive (Norland Optical Adhesive 68), a glass probe with a width of ~200 μm was attached to the surface of each test area. Due to the glass probe, the focal plane of the test area was higher than the focal plane of the adjacent springs whose surface served as reference for displacement calculations. Therefore, an identical glass probe was bonded to the adjacent springs. The optical images collected during testing were analyzed using Digital Image Correlation (DIC), the sample surfaces had a natural pattern that facilitated the use of DIC, to determine the net displacement, u_{net}, via the relationship:

$$u_{net} = u_{test} - u_{ref} \tag{2.2}$$

where u_{test} and u_{ref} are the displacements of the test and the reference area, respectively. An example of a DIC calculation in an unseeded, 4-turn, Si spring film is shown in Figure 2.13. The slope of the plot of the applied force vs. displacement, k_{shear} was used to calculate the shear modulus of the film, G_{shear} using the equation:

$$G_{shear} = k_{shear} \frac{H}{A} \tag{2.3}$$

where H is the height of the nanospring film not including the cap and A is the test area. A sample plot of the load vs. displacement curve is shown in Figure 2.14.

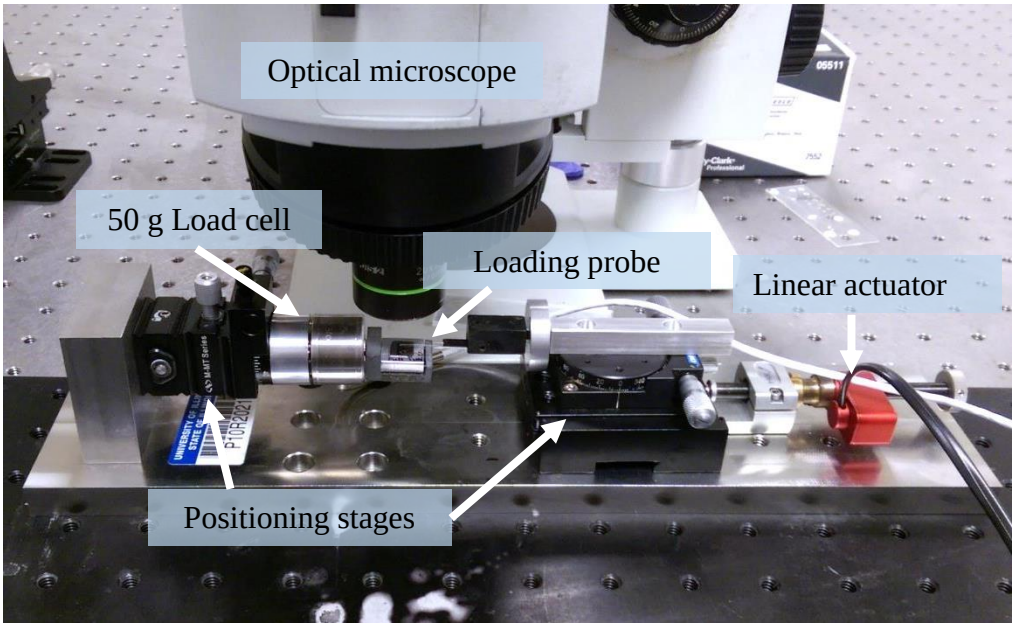

Figure 2.10 Apparatus for testing spring films in shear [18].

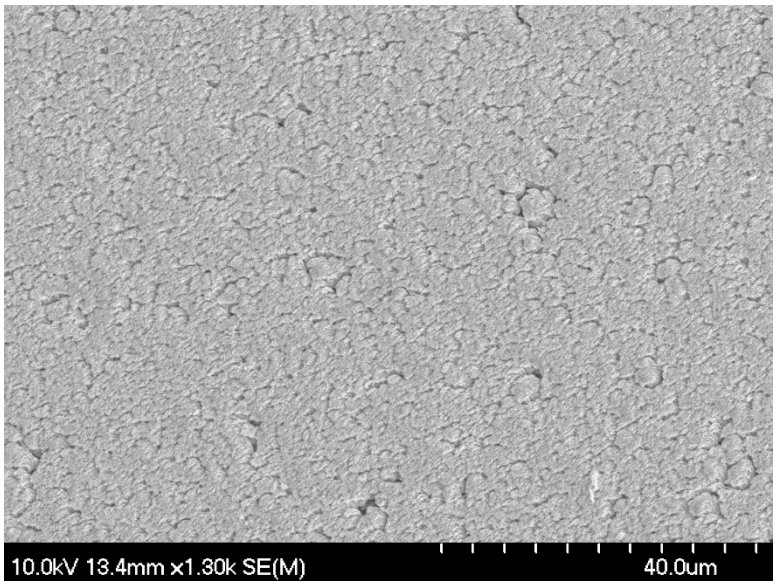

(a)

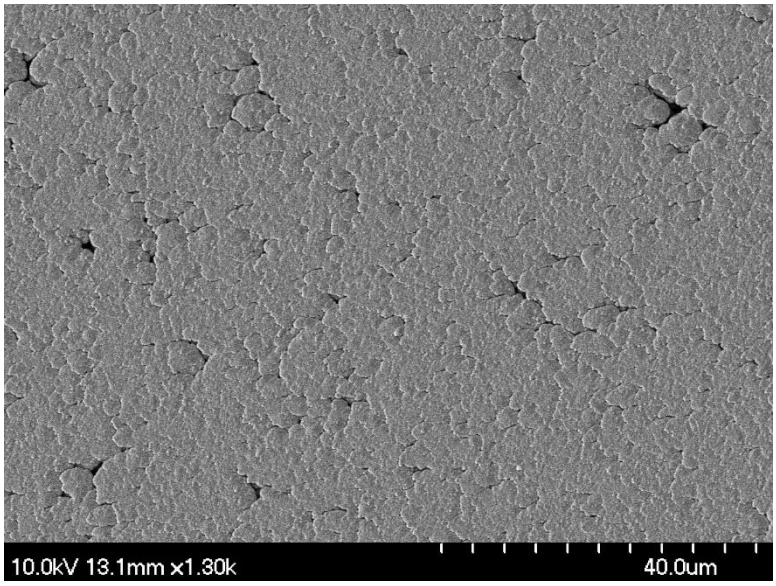

(b)

Figure 2.11 Cu spring film with 2,000 nm seed spacing **(a)** before and **(b)** after sputter coating.

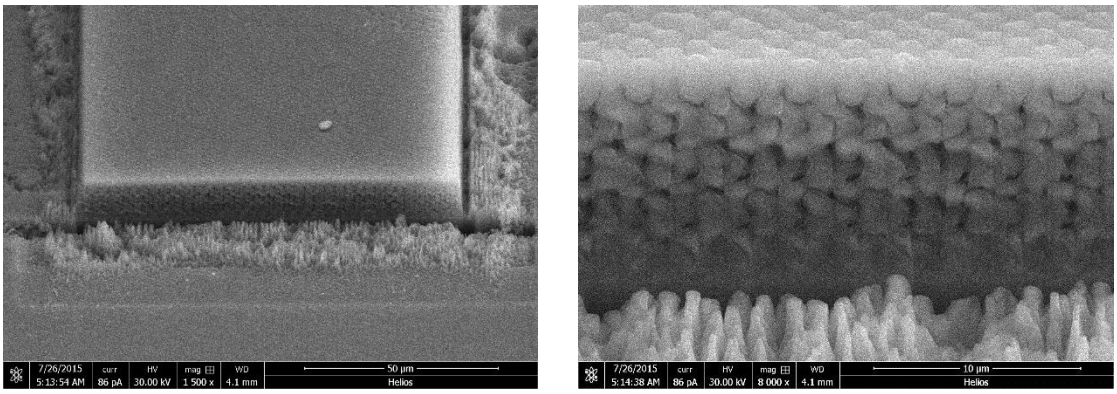

(a) **(b)**

Figure 2.12 Shear test area of 4-turn, 1500 nm seeded Si springs after ion-milling at **(a)** 1,500×, and **(b)** 8,000× magnification.

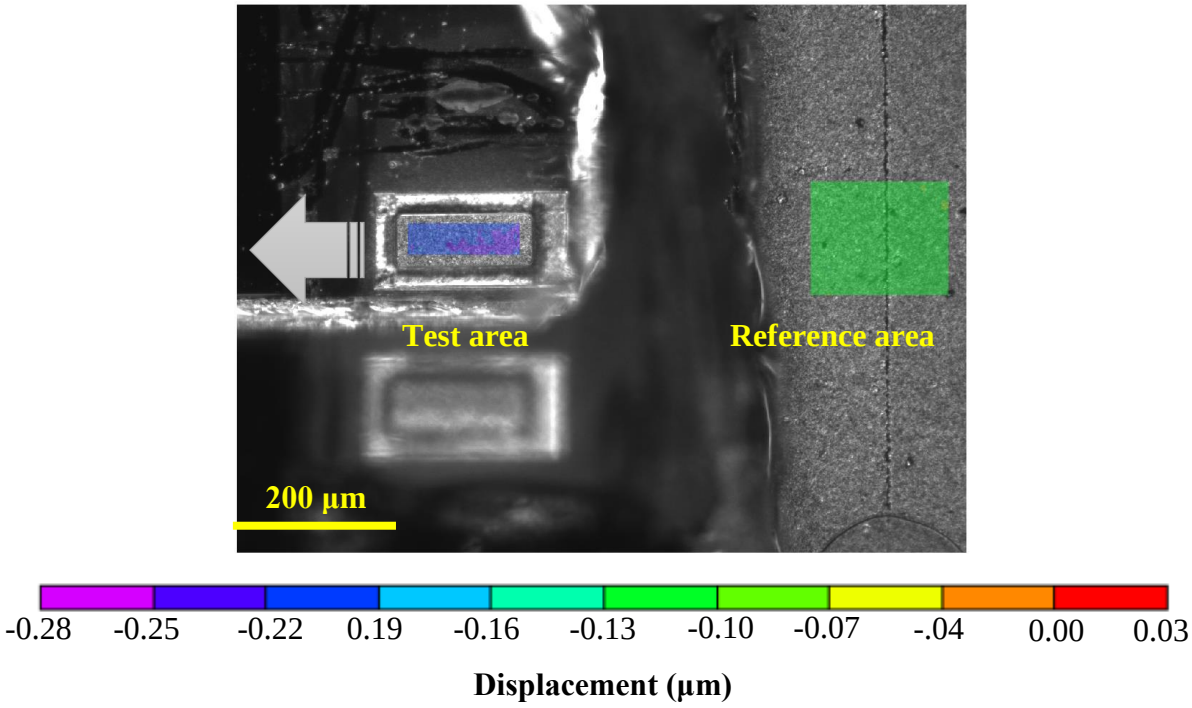

Figure 2.13 DIC contours from the shear test of a 10-turn, Cu spring film with 2400 nm seed spacing. During testing, the glass probe pulls the test area to the left, away from the reference area.

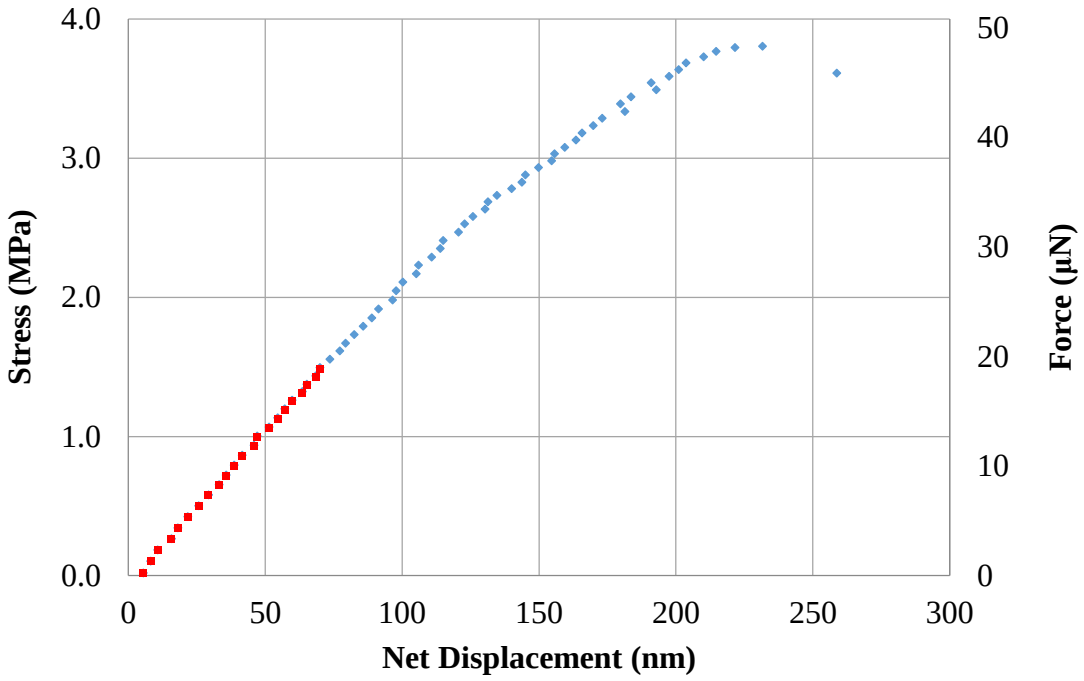

Figure 2.14 Load vs. displacement plot for a 10-turn, 2000 nm seeded Si spring film subjected to shear loading. The red data were used to compute the shear stiffness.

CHAPTER 3

COMPRESSIVE AND SHEAR RESPONSE OF Si SPRING FILMS

3.1 Compression of Si GLAD Films

The compressive moduli of films with different seed spacing during loading and unloading of Si spring films, as determined using Equation (2.1) are shown in Figure 3.1(a-f). In the majority of test samples, the effective compressive modulus increased with the applied stress, potentially due to contact between adjacent springs, thus restricting further displacement. In most cases, the loading and unloading moduli were approximately equal. Some films, such as 4-turn, 900 nm; 10-turn, 900 nm; 10-turn, 1500 nm, demonstrated loading moduli that were greater by 44%, 7%, and 19%, respectively, than the unloading moduli at the highest applied stress of 50 MPa. Spring buckling at higher stress ranges could produce a similar behavior, as the restoring spring force would be higher during loading than unloading.

A comparison between the average unloading moduli of all samples is shown in Figure 3.2 and Figure 3.3. At the lowest stress of 500 kPa, the stiffnesses of 4-turn spring films were 23.7 ± 0.2 MPa for 900 nm seed spacing, 37.1 ± 0.7 MPa for 1500 nm seed spacing, and 29.9 ± 0.6 MPa for springs grown with no seeding. In the 10-turn coil case, the stiffnesses were 37.7 ± 0.8 MPa for 900 nm seed spacing, 66.2 ± 3.4 MPa for 1500 nm seed spacing, and 29.8 ± 0.8 MPa for unseeded springs. For a tenfold increase in stress to 5 MPa, the 4-turn spring film stiffnesses were approximately equal for the seeded springs, 45.4 ± 0.9 MPa for 900 nm seed spacing and 44.0 ± 0.2 MPa for 1500 nm seed spacing, while unseeded spring films had the highest stiffness of 54.4 ± 0.4 MPa.

The 10-turn spring films demonstrated a different trend, with increasing stiffness from 78.3 ± 1.0 MPa for unseeded spring films, to 119 ± 1.0 MPa for films with 900 nm seed spacing, and finally 164 ± 1.3 MPa for films with 1500 nm seed spacing. At the highest applied stress of 50 MPa, the 4-turn spring films experienced a large variation in stiffness due to seed spacing, with stiffnesses of 291 ± 1 MPa for unseeded springs, 528 ± 3 MPa for the 900 nm seed spacing, and 810 ± 6 MPa for the 1500 nm seed spacing. The 10-turn springs, however, had similar stiffnesses at 50 MPa, with 728 ± 6 MPa for the 900 nm seed spacing, 720 ± 7 MPa for the 1500 nm seed spacing, and 779 ± 5 MPa for the springs with no seeding.

In general, the 4-turn coil film stiffness increased with seed spacing: as a result of the mechanics of the GLAD process, all other deposition parameters being equal, larger seed spacings resulted in springs with larger wire diameters and therefore springs with 1500 nm seed spacing had larger wire diameters than those with 900 nm seed spacing. In the case of coils with 10 turns and for most stress levels, the unseeded films had higher stiffness that those seeded with 900 nm spacing. For the same number of turns and at lower stress levels, the stiffness of films with 1500 nm seed spacing was considerably greater than the unseeded films. However, as the stress increased, unseeded stiffness approached that of the 1500 nm seeded films, eventually surpassing it at 40-50 MPa. As shown in Figure 2.1(c,d,f), the 10-turn springs were quite columnar, and therefore more prone to buckling when the degree of intertwining between springs decreased significantly for 1500 nm seed spacing, Figure 2.2(d).

The effect of cyclic loading on film stiffness was also examined: the unloading stiffness in each of the 10 cycles was found to remain fairly constant, contrary to a clear trend of increasing loading stiffness. In Figure 3.4(a-f) and Figure 3.5(a-f) the unloading stiffness during the 1^{st} cycle of each test is compared with the 10^{th} cycle and the average unloading stiffness. In each case, the final loading stiffness was higher than the initial loading, while in many tests, the loading stiffness was initially less than the average unloading stiffness, but surpassed it by the final loading.

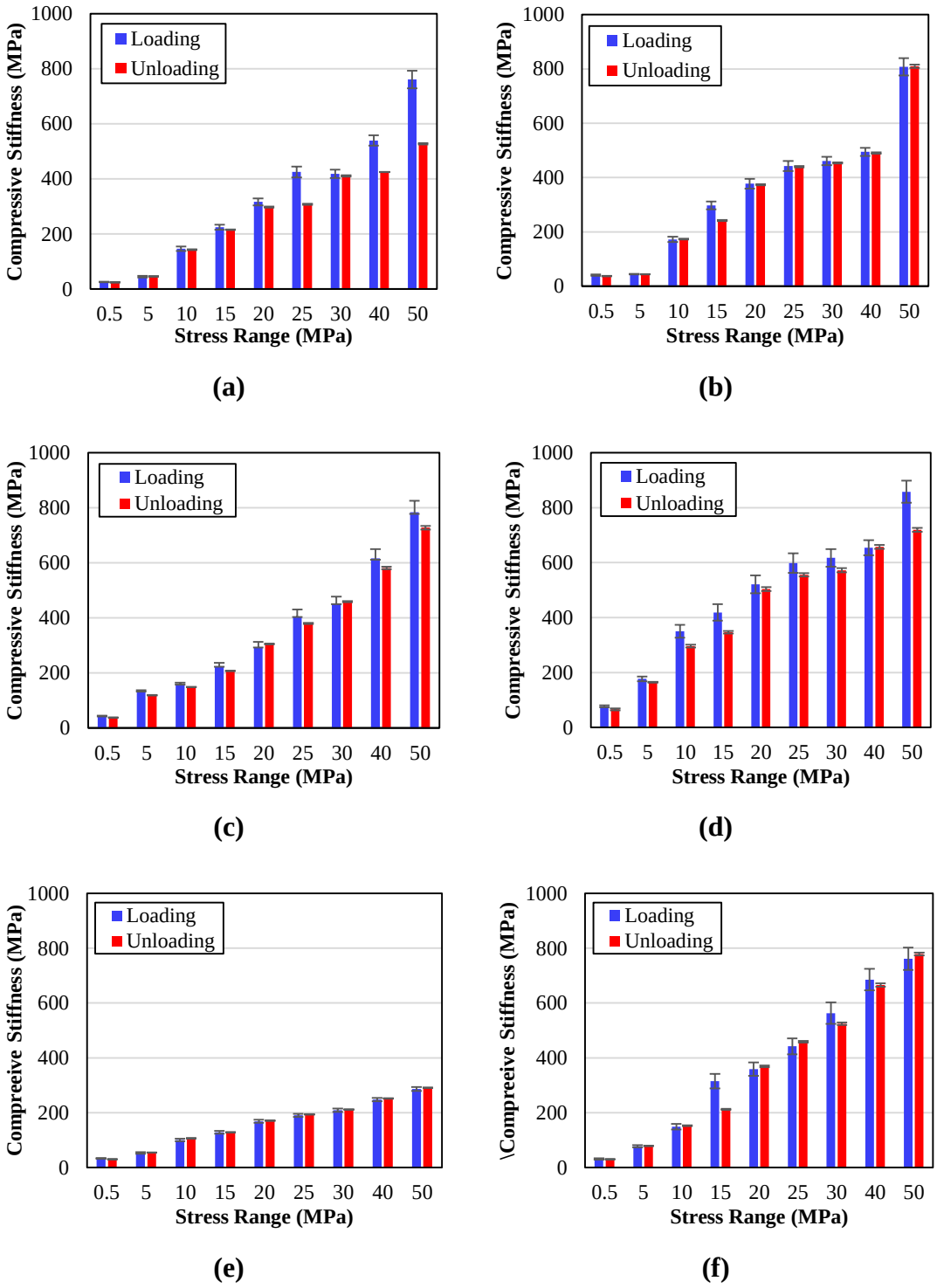

Figure 3.1 Compressive response of Si springs with: **(a)** 4 turns and 900 nm seed spacing, **(b)** 4 turns and 1500 nm seed spacing, **(c)** 10 turns and 900 nm seed spacing, **(d)** 10 turns and 1500 nm seed spacing, **(e)** 4 turns and unseeded substrate, and **(f)** 10 turns and unseeded substrate.

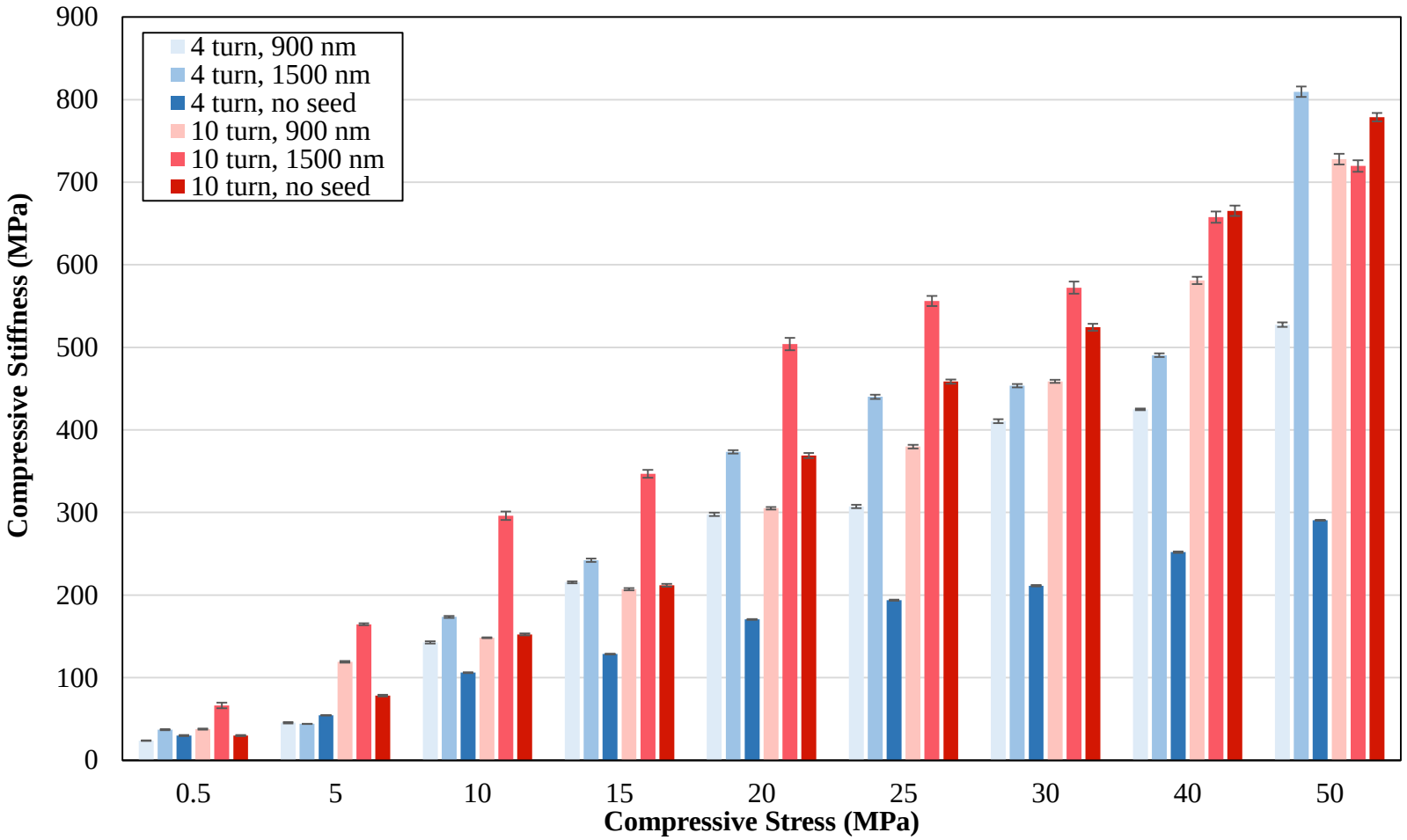

Figure 3.2 Comparison of stiffness values in unloading for all Si spring types.

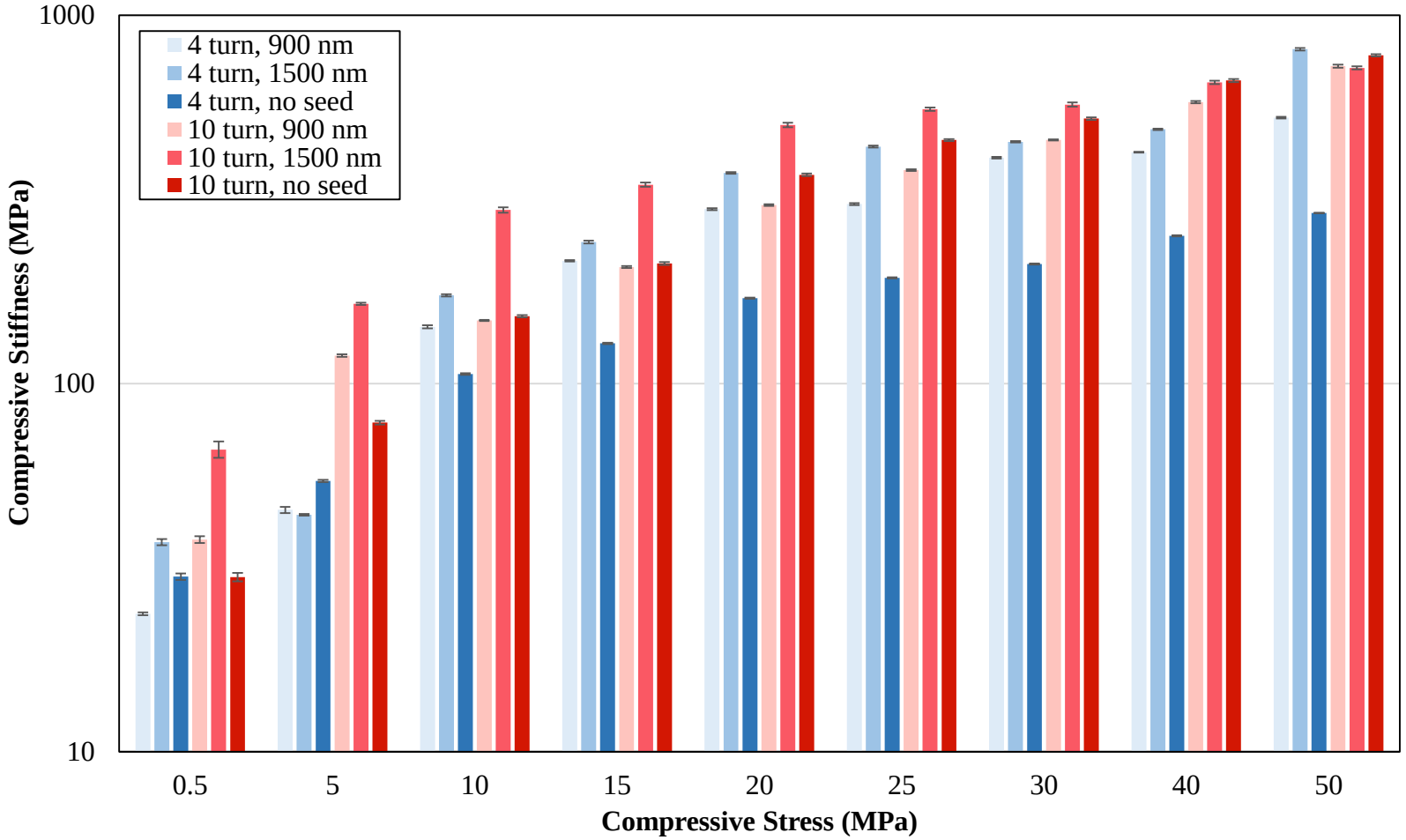

Figure 3.3 Comparison of stiffness values in unloading for all Si spring types. Logarithmic scale has been used to distinguish small stiffness values.

Finally, the permanent film compression at each stress was quantified using SEM images. For a brittle material such as silicon, permanent changes in height would be attributed to buckling or spring shifting and tilting: Figure 3.6 shows a comparison of 10-turn, 1500 nm seed spaced Si test areas after compression at (a) 5 MPa and (b) 50 MPa where at high stresses the springs along the edge of the test area tilted outwards. Due to this spring shifting, the film height after unloading was measured from cut-outs made with a FIB at low power (30 kV, 2.5 nA) which also provided a view of the internal springs, as shown for example in Figure 3.7(a-c). The final film thickness was divided by the initial height to determine the permanent strain, which is given in Figure 3.8(a-b). In the case of Si films with 4 turn coils and 900 nm seed spacing, and 10 turns and 1500 nm seed spacing a permanent strain of 6.5% strain and 2.0%, respectively, occurred at the lowest stress of 5 MPa. In all other cases, permanent strain between 0.6% and 5.1% occurred for the first time at 10 MPa. Beginning at 15 MPa, all 4-turn Si films experienced similar permanent strain regardless of seed spacing, varying between 12.4% - 18.9% for stresses between 15 MPa and 30 MPa. Notably, while films with 4 turn coils and 900 nm seed spacing demonstrated the most residual compression until 30 MPa stress, at stresses equal or higher than 40 MPa were surpassed by unseeded films but only by a small margin. Furthermore, the residual compression of films with 900 nm seed spacing remained rather unchanged at 18-20% for stresses $\geq$ 25 MPa. At intermediate stresses of 15-30 MPa unseeded films demonstrated the most resilience to compression with 12-16% permanent strain, which increased rather abruptly to 21.5% and 22.5% at 40 MPa and 50 MPa, respectively.

On the other hand, 10-turn structures showed steady increase in permanent strain with applied stress. Films of springs with 10 turns and 1500 nm seed spacing were the earliest to experience 2.0% permanent strain for as low as 5 MPa, Figure 3.8(b), which drastically increased to 19% at 10 MPa, only to increase thereafter by 2-3% for each 5 MPa of stress increment, finally reaching 38% at 50 MPa. On the contrary, films with springs of 900 nm seed spacing and unseeded incurred permanent strains of 0.6% and 2.3%, respectively. For stresses lower than 15 MPa, films of springs with 900 nm spacing were proven to be the most resilient of all films tested. A similar drastic increase in residual compression occurred for films with 10-turn coils and 900 nm seed spacing from

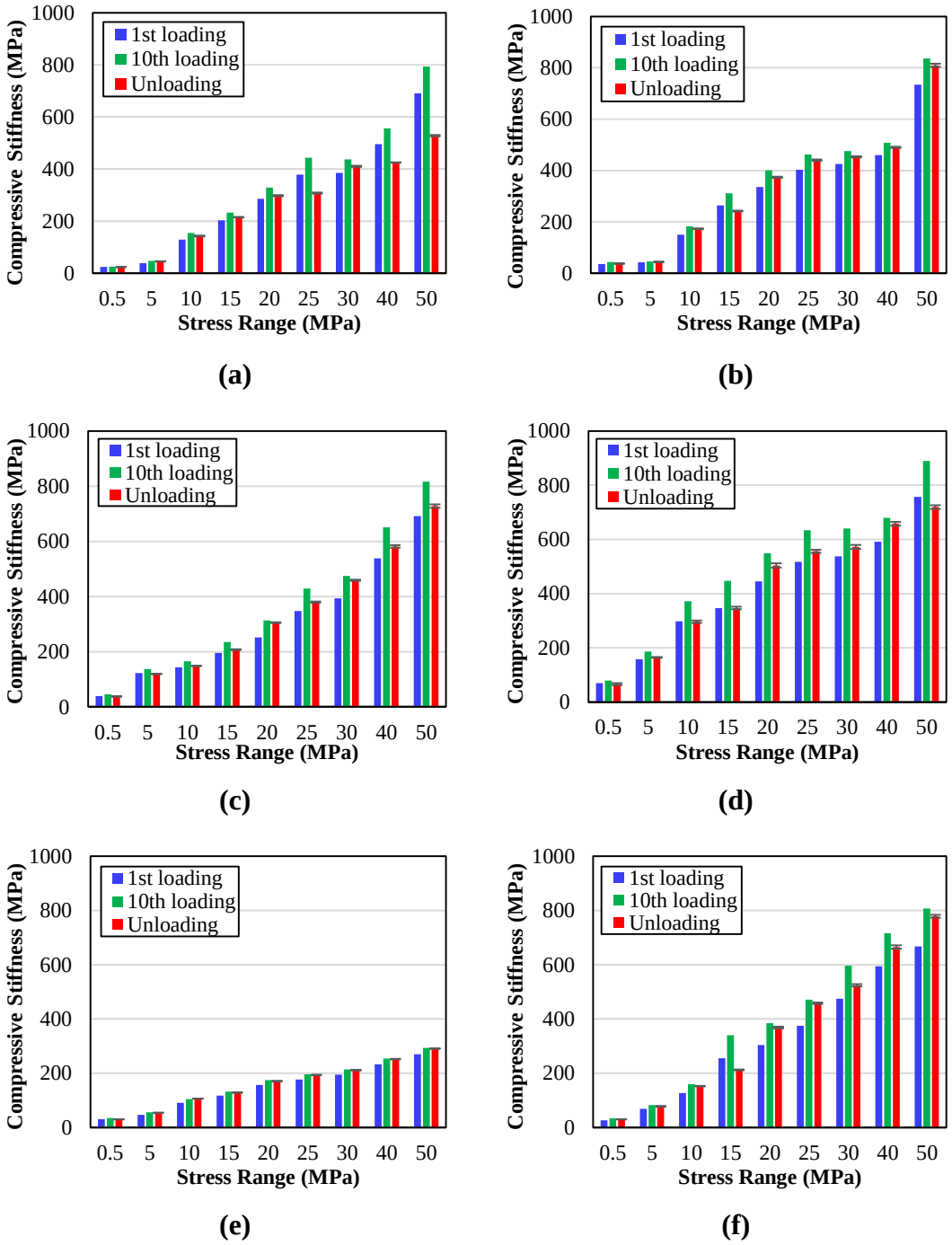

Figure 3.4 Stiffness of Si spring films with **(a)** 4 turns, 900 nm seed spacing, **(b)** 4 turns, 1500 nm seed spacing, **(c)** 10 turns, 900 nm seed spacing, **(d)** 10 turns, 1500 nm seed spacing, **(e)** 4 turns, unseeded substrate, and **(f)** 10 turns, unseeded substrate. The error bars in the unloading data signify one standard deviation.

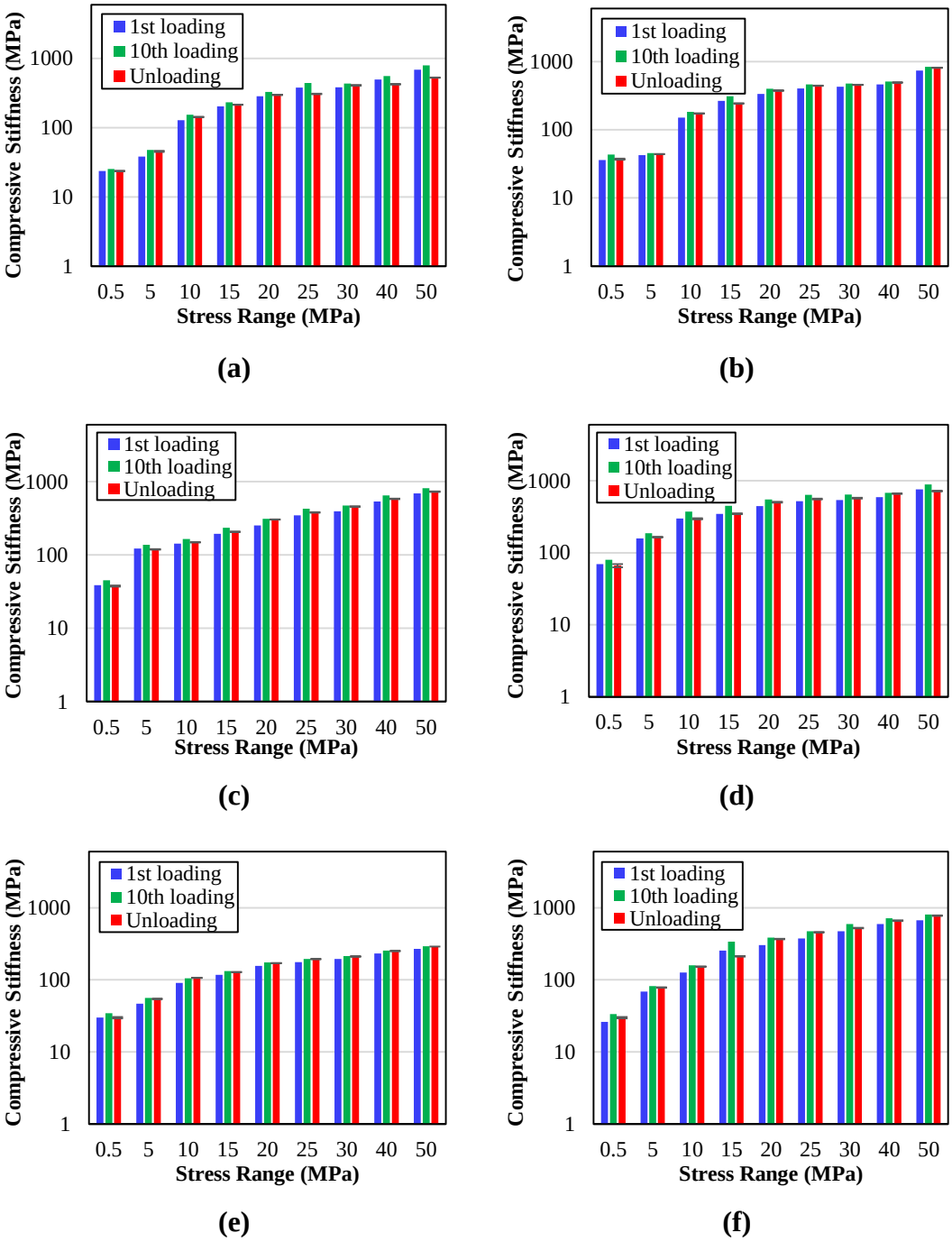

Figure 3.5 Stiffness of Si spring films with **(a)** 4 turns, 900 nm seed spacing, **(b)** 4 turns, 1500 nm seed spacing, **(c)** 10 turns, 900 nm seed spacing, **(d)** 10 turns, 1500 nm seed spacing, **(e)** 4 turns, unseeded substrate, and **(f)** 10 turns, unseeded substrate. The error bars in the unloading data signify one standard deviation. Logarithmic axes were used to enhance viewing of small values.

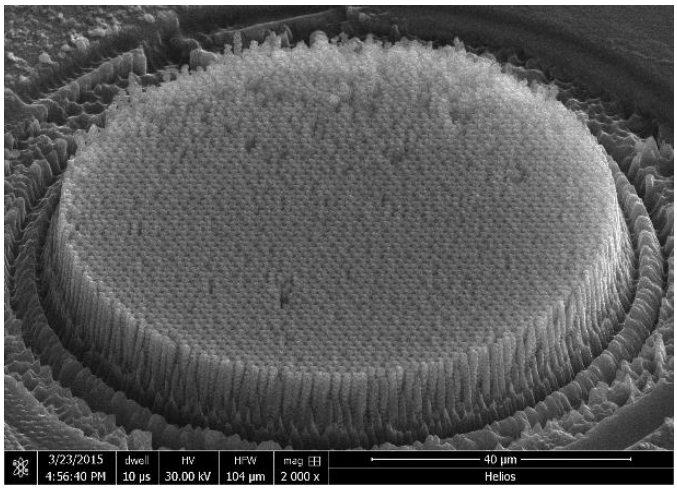

(a)

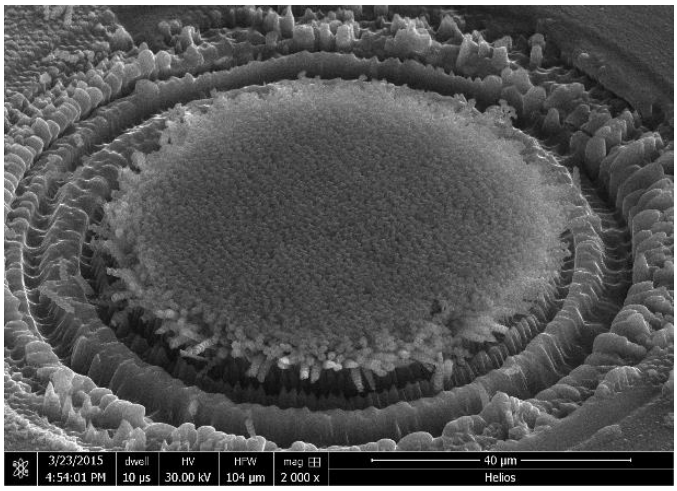

(b)

Figure 3.6 Si films with 10-turn springs at 1500 nm seed spacing after testing at: **(a)** 5 MPa and **(b)** 50 MPa. The edge springs buckled outward as a result of high loading.

2% at 15 MPa to ~13% at 20 MPa. Films with 10-turn unseeded springs demonstrated the most consistent increase in residual strain of 2-3% for each 5 MPa of stress increment, reaching 19% residual strain at 50 MPa. The permanent strain in 10-turn spring films varied greatly depending on the seed spacing: films with 10 turns and 1500 nm seed spacing demonstrated the highest permanent strain, followed by those with 900 nm seed spacing, and finally the unseeded springs. Therefore, unseeded films provided a clear advantage in 10-turn spring films, but provided limited advantage in 4-turn spring films.

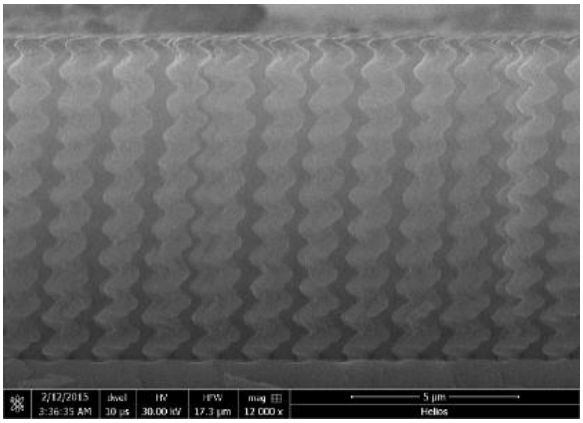

(a)

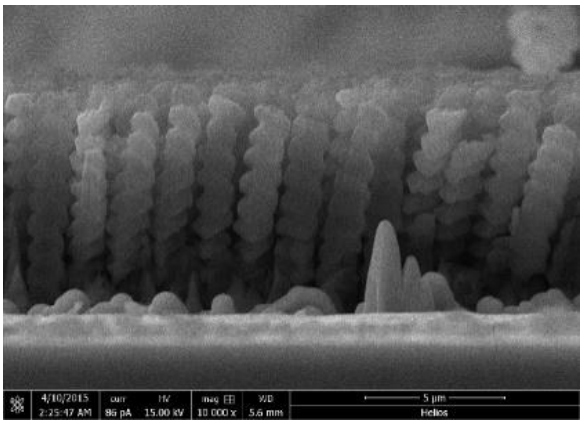

(b)

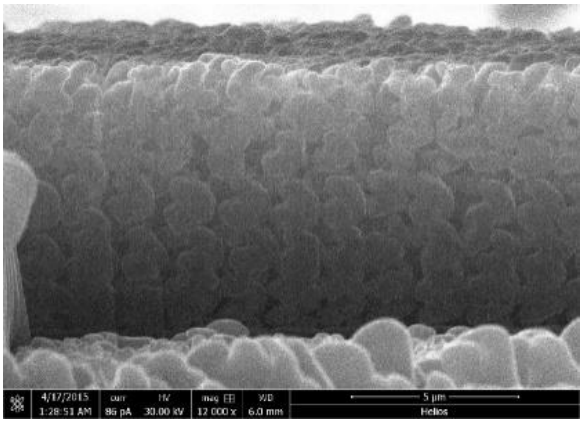

(c)

Figure 3.7 Si films with 10-turn springs at 1500 nm seed spacing that were loaded to 10 MPa stress: **(a)** before testing, **(b)** after testing, and **(c)** after testing and with the outer springs removed by FIB ion-milling. Images of each test area are shown in Appendix B.

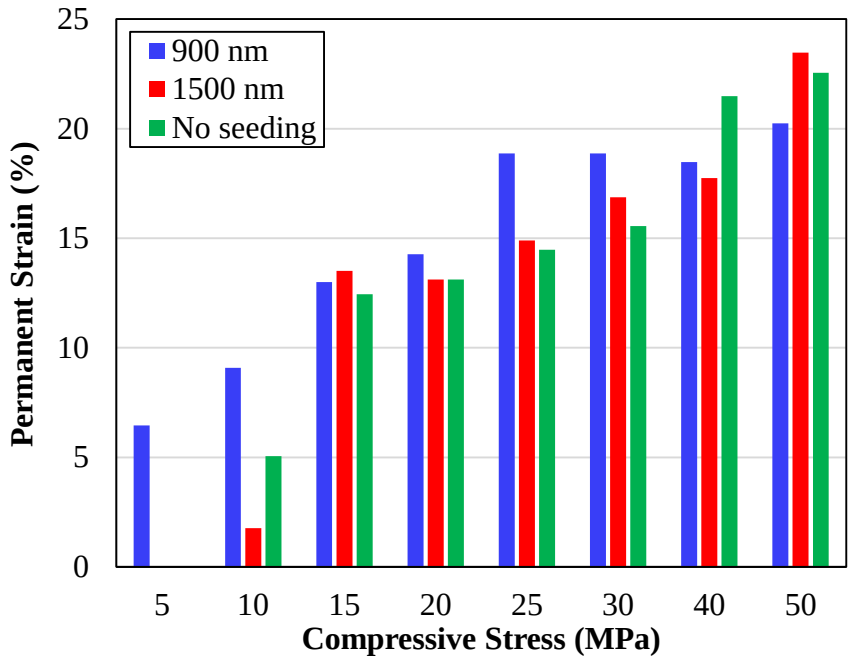

(a)

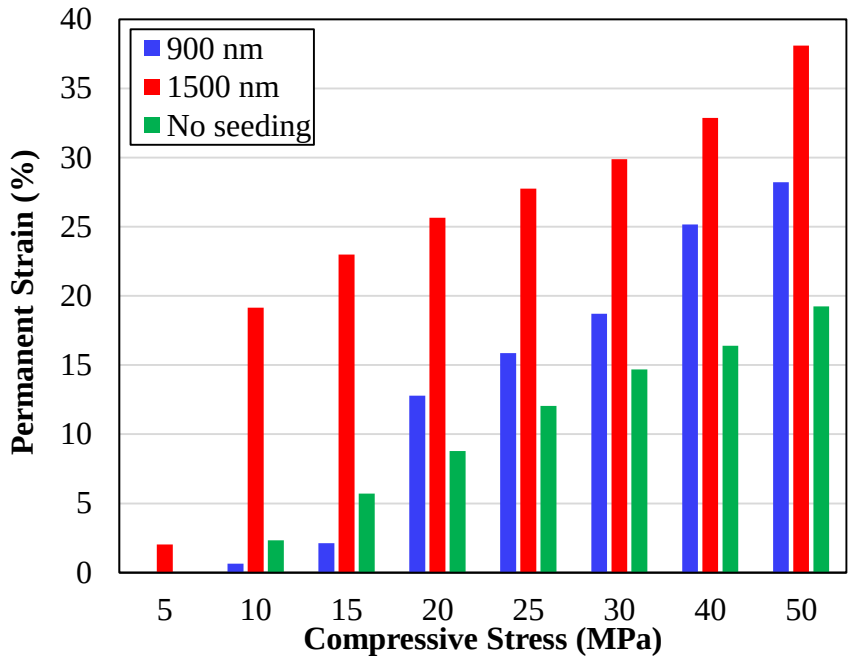

(b)

Figure 3.8 Permanent strain of films with **(a)** 4-turn, and **(b)** 10-turn Si springs, after compression.

3.2 Shear Behavior of Si Spring Films

The shear moduli of the different Si films, as determined using Equation (2.3), are shown in Figure 3.9. The loading plots that the moduli were extracted from are shown in Appendix C. The shear modulus of films with 4-turn springs spaced at 1500 nm (3 tests) was 25.7 ± 2.0 MPa, which is considerably greater than that of films of springs with 900 nm spacing (3 tests), 16.8 ± 1.8 MPa. This difference is an immediate result of the dimensions of the two types of 4-turn springs, which are given in Table 2.1: Springs with 1500 nm seed spacing had larger wire diameter than those with 900 nm seed spacing and as a result larger stiffness. Films with 4-turn unseeded springs (3 tests) had shear stiffness that was comparable to the 4-turn springs with 1500 nm, with a value of 26.8 ± 7.1 MPa. As shown in Figure 2.1, unseeded springs formed much denser films compared to those that were seeded, hence promoting significantly more intertwining and lateral interaction through contact between adjacent springs. The standard deviation for each case represents the deviation observed in the stiffness values for three different experiments, except for the unseeded case, in which stiffness is extracted from two tests.

Films with 10-turn springs did not follow the same trends as those with 4-turn springs. 10-turn structures with 900 nm and 1500 nm seed spacings differed in shear stiffness, with values of 26.1 ± 4.7 MPa and 6.6 ± 0.6 MPa, respectively. Although the latter had larger effective wire diameter, there were fewer springs per unit area than in the case of films with 900-nm seed spacing. Therefore, the smaller spring density of films with 1500-nm seed spacing spring, combined with the smaller lateral overlap between adjacent springs, resulted in smaller shear stiffness than in films with the 900-nm seed spacing. Finally, similarly to films with 4-turn springs, films with unseeded 10-turn springs had shear stiffness that was near that of the stiffer seeded spring film (23.5 ± 3.2 MPa) than those with seeded springs due to the close proximity of adjacent springs.

Compared to seeded films of springs, unseeded films reduce the compressive stiffness but increase the shear stiffness by a factor of two or more. In all experiments, the spring films failed before debonding of the adhesive between the grip and the cap. Thus, the highest recorded shear stress represented the ultimate shear strength of spring films. The results are shown in Figure 3.10. All 4-turn spring films demonstrated a similar shear

strength regardless of seed spacing, amounting to 2.4 ± 0.2 MPa, 2.4 ± 0.1 MPa, and 2.3 ± 0.1 MPa, for 900 nm seed spacing, 1500 nm seed spacing, and unseeded films, respectively. Due to the mechanics of GLAD, films with larger seed spacing had larger coil and wire diameters, but fewer springs than those with smaller seed spacing. Therefore, although the individual spring geometries varied greatly, the film shear strengths were quite consistent because each film contained the same amount of Si per unit area. Films with 10-turn coils behaved differently: Films with 900-nm seed spacing and unseeded films had similar shear strength, of 3.2 ± 0.5 MPa and 3.9 ± 0.7 MPa, respectively. However films with 1500 nm seed spacing resulted in much lower shear strength of only 0.9 ± 0.05 MPa. The low strength of the spring film with 10-turn, 1500 nm seed spacing had two causes: (1) the spring posts were smaller in diameter than the spring wire and (2) when compared to the 900 nm seed spacing and the no seed spacing cases, there were fewer springs in the test area resulting in a smaller area of contact between the springs and the substrate. Therefore for a given stress, each spring in the 1500 nm seed spacing spring film experienced a higher load than the other 10-turn spring films.

To further understand the shear strength results, it is important to examine the location of failure for each spring type. SEM images of the springs after shear testing are shown in Appendix D. The 4-turn seeded springs failed randomly through the thickness, with each area experiencing spring failure anywhere between 1 turn and 4 turns, where the capping layer began. The 4-turn springs with no seeding experienced failure consistently between the 3rd and 4th turn. The 10-turn seeded springs experienced failure exclusively at the post, whereas the 10-turn unseeded springs failed similarly to the 4-turn, seeded springs, with a random assortment of springs breaking near the base and the cap.

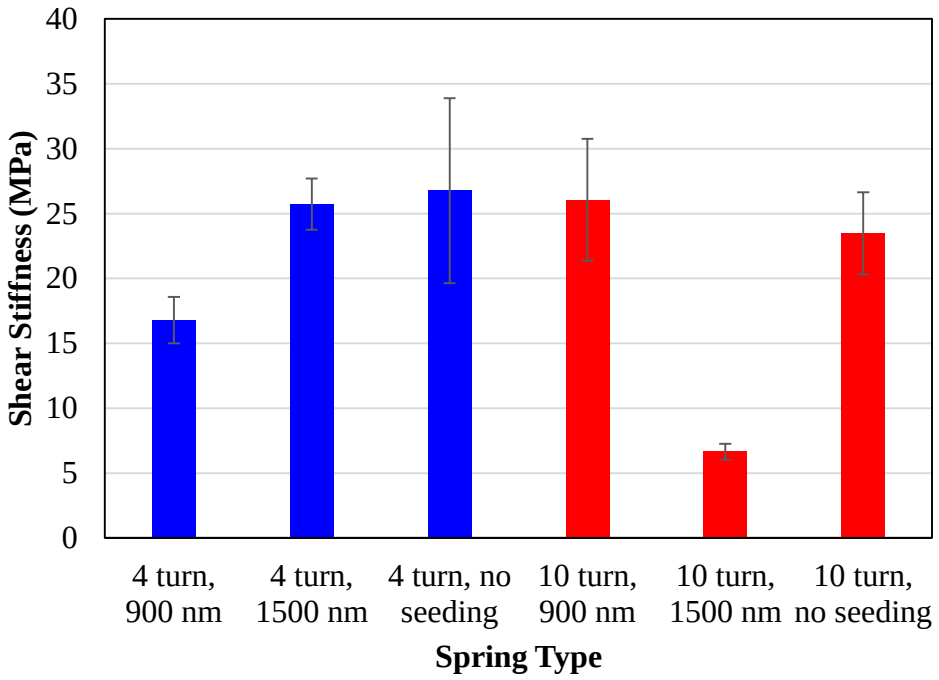

Figure 3.9 Shear stiffness of Si spring films.

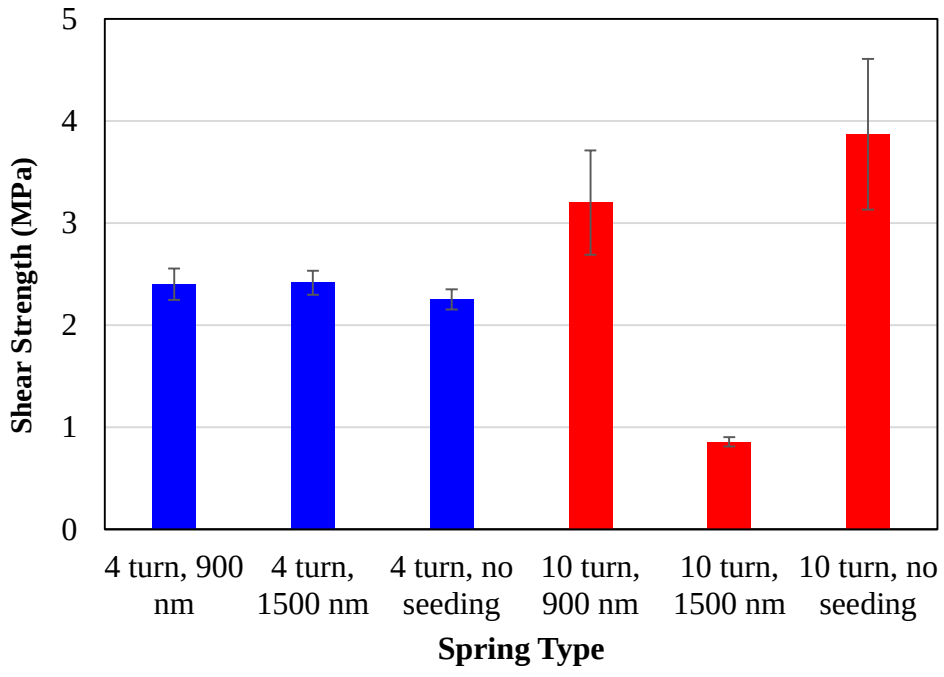

Figure 3.10 Ultimate shear strength of Si spring films.

3.3 Conclusions

The compressive stiffness of all Si spring films increased with applied stress. This is due to adjacent springs coming in contact during compression. At most applied stress values, the loading and unloading stiffnesses were approximately the same. However, at high loads, the loading stiffness substantially exceeded the unloading stiffness, indicating that permanent damage in the form of individual spring buckling might have occurred during loading. In all experiments, the unloading stiffness remained constant contrary to the loading stiffness that increased with cycling. Qualitatively speaking, the initiation and evolution of permanent set were different for 4-turn vs. 10-turn spring films. In the former, permanent set occurred suddenly at 5 MPa, and increased steadily with stress; for all films with 900 nm seed spacing, the permanent set was in the range of 20-23% strain, namely 2.1-2.4 μm. The 10-turn spring films, on the other hand, experienced a steady increase in permanent set, until the maximum stress of 50 MPa, suggesting that the overlap between adjacent springs was not enough to restrict deformation throughout loading, as was the case for 4-turn spring films at high stress.

The shear stiffness of 4-turn springs followed an increasing trend with seed spacing. While of similar coil diameter and larger wire diameter compared to 900 nm seeded films, springs with 1500 nm seed spacing still overlapped with adjacent ones. Under shear deformation, the springs came in contact resulting in film stiffening. Seeded 10-turn springs were not as intertwined as their 4-turn counterparts, thus resulting in less lateral overlap and lower shear stiffness. Due to their columnar shape, the 10-turn, 1500 nm spaced springs provided the lowest ultimate shear strength of 0.9 ± 0.05 MPa, while the 10-turn unseeded films had the highest shear strength of 3.9 ± 0.7 MPa due to its large contact area with the substrate. On the other hand, all seeded and unseeded 4-turn Si films had similar shear strengths of 2.3 - 2.4 MPa, due to similar degree of intertwining.

CHAPTER 4

COMPRESSIVE AND SHEAR RESPONSE OF Cu SPRING FILMS

4.1 Compression Results of Cu Spring Films

A summary of the loading and unloading compressive stiffnesses of Cu spring films is given in Figure 4.1(a-e). At low stresses, the loading stiffness was slightly greater than or equal to the unloading stiffness. As the applied stress is increased, the unloading stiffness became considerably greater than the loading stiffness, up to 13% higher than the loading stiffness for Cu springs with 2800 nm seed spacing loaded at 40 MPa. Seto et al. [15] argued that the hysteresis in the load vs. displacement plots is caused by a difference between the loading strain rate and the strain rate during recovery. The material might gradually recover from some or all of the strain after the load is completely removed. Therefore, as the load is removed from the sample, the spring experiences smaller displacement than during loading. Therefore, the unloading stiffness is greater. A comparison of the unloading stiffness of the different types of Cu spring films is shown in Figure 4.2. The stiffness of Cu films with 2400 nm or the 2800 nm seed spacing gradually increased with stress ranging from 300 ± 8.5 MPa and 320 ± 6.7 MPa, respectively, at 5 MPa stress, to 1310 ± 28.2 MPa and 1170 ± 18.2 MPa, respectively, at 50 MPa stress. However, the compressive stiffness of films with 2000 nm and 3200 nm seed spacing monotonically increased up to 30 MPa stress, reaching 975 ± 19.6 MPa and 930 ± 18.2 MPa, respectively. Notably, the stiffness of both types of films decreased when the stress increased from 30 to 40 MPa, slightly for the springs with 2000 nm seed spacing to 974 ± 15.2 MPa, but drastically for films with 3200 nm seed spacing to 790 ±

15.2 MPa. In the stress increment between 40 to 50 MPa, the film stiffness increased again for both spring types, to 1015 ± 16.7 MPa for films with 2000 nm seed spacing, and to 860 ± 13.0 MPa for films with 3200 nm seed spacing. The stiffness of unseeded films was 184 ± 2.2 MPa at 5 MPa, and increased steadily to between 402 ± 3.3 MPa and 410 ± 4.3 MPa for stresses between 20 and 30 MPa. A further increase in stress from 30 to 40 MPa produced a stiffness increase to 610 ± 5.6 MPa, but no further increase occurred when the stress increased to 50 MPa, suggesting that between 30 and 40 MPa, the degree of contact between adjacent springs was substantially greater than it was between 20 and 30 MPa, which did not change in the next stress increment to 50 MPa.

The unseeded films demonstrated the smallest stiffness at all stress levels, only reaching 600 MPa at 40 and 50 MPa. For stresses ≤30 MPa, the compressive stiffness of all film types was less than 1000 MPa. At stresses ≤25 MPa, films with 3200 nm seed spacing had the largest stiffness among all samples, due to their largest coil and wire diameter. At stresses ≥30 MPa, the stiffness of films with 2000 nm seed spacing remained rather unchanged, while the stiffness of films with 3200-nm seeding and reached a plateau of ~800 MPa at 40 MPa.

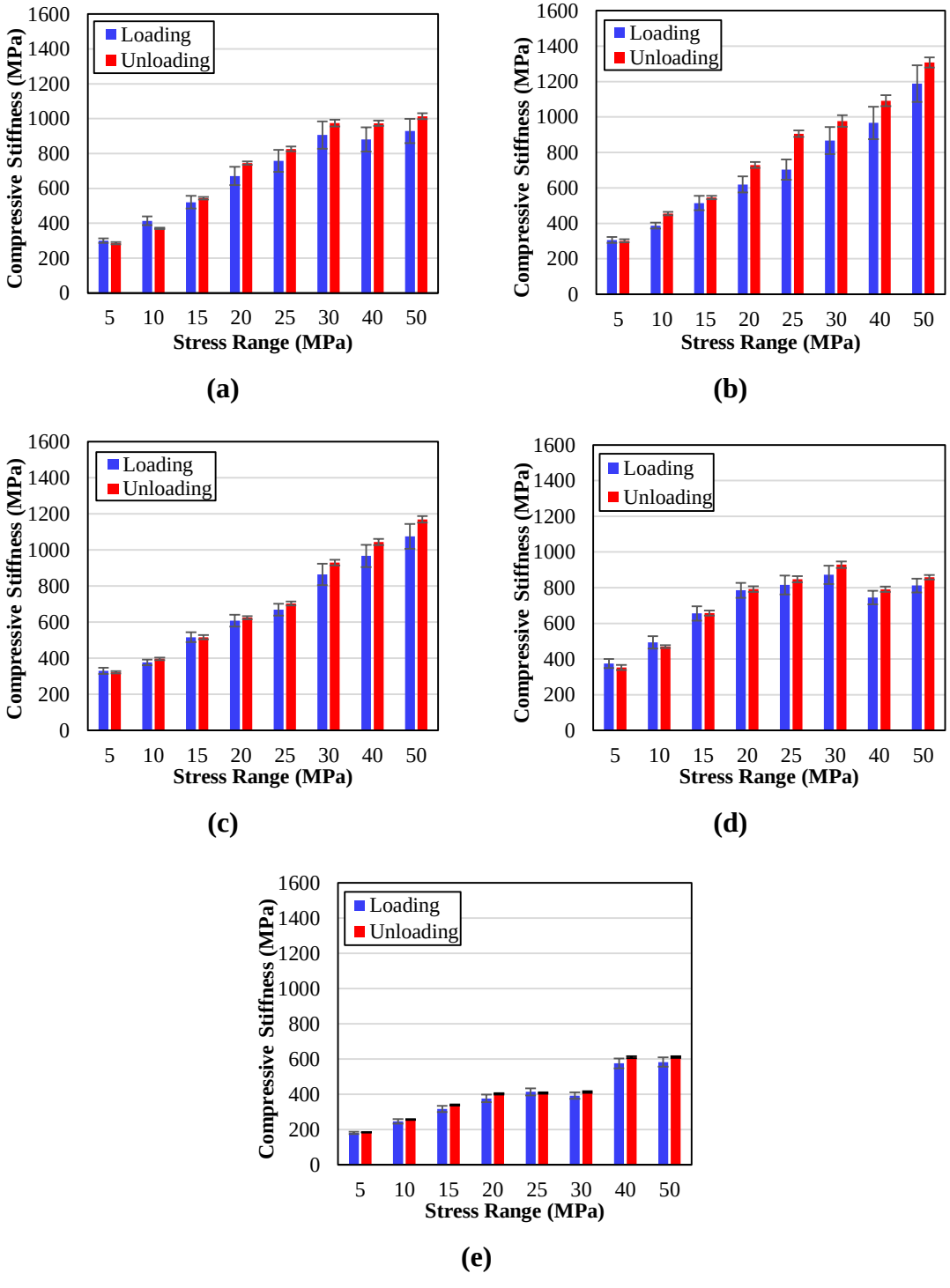

Figure 4.1 Compressive response of Cu spring films with: **(a)** 2000 nm, **(b)** 2400 nm, **(c)** 2800 nm and **(d)** 3200 nm seed spacing, as well as **(e)** no seeding.

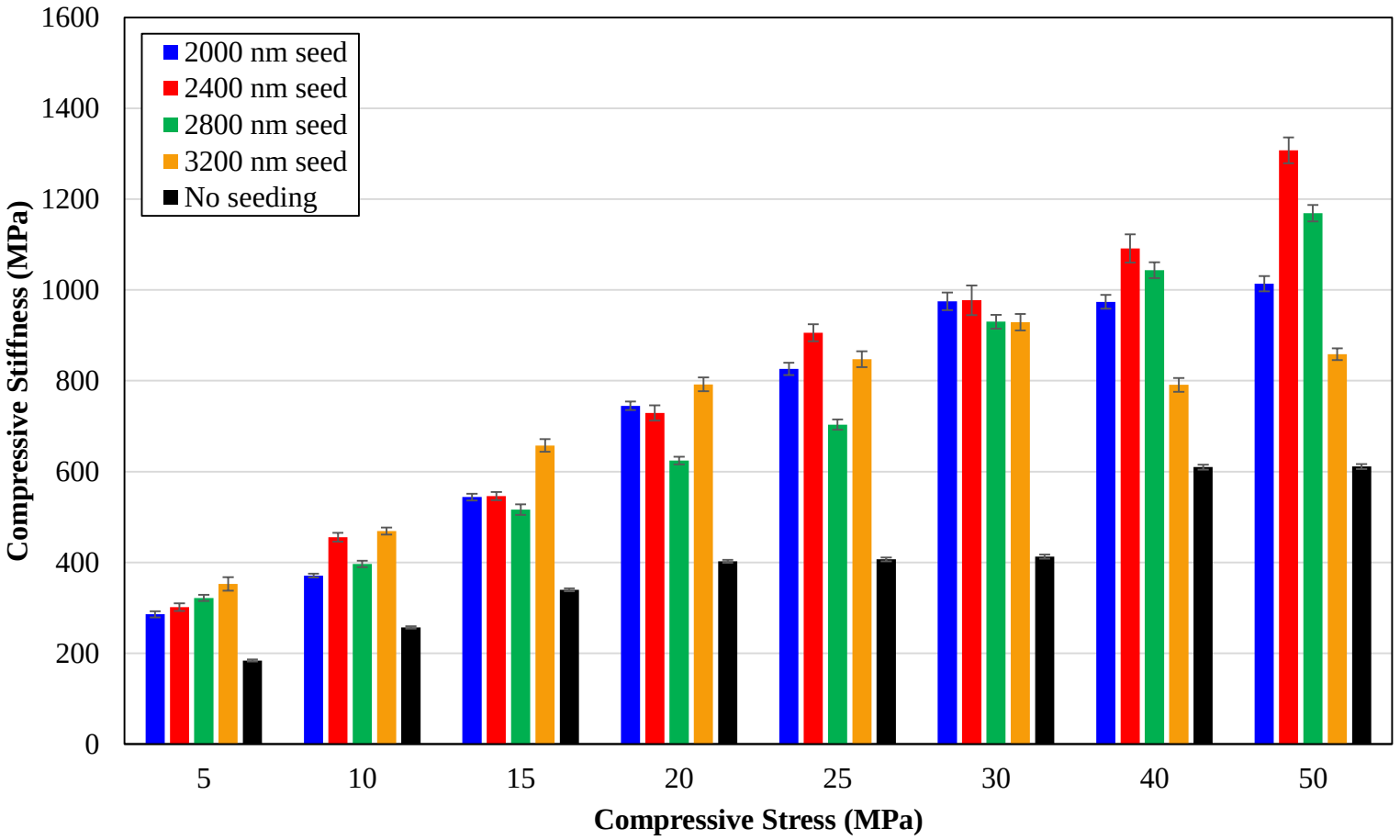

Figure 4.2 Compressive unloading stiffness of different types of Cu spring films.

The unloading stiffness of Cu films was fairly constant during cycling (10 cycles), but the loading stiffness increased gradually, similarly to Si films. Figure 4.3(a-e) and Figure 4.4(a-e) provide a comparison of the stiffness obtained in the first loading, the tenth loading, and the average unloading for all cycles. The difference between the stiffness values of the first and tenth loadings increased with applied stress. At low stress values, the first loading stiffness was less than the average unloading stiffness, by as much as 10% at 5 MPa for films with 2800 nm seed spacing, while the loading stiffness in the tenth cycle was often greater, by as much as 17% at 10 MPa stress for springs with 2000 nm seed spacing. At higher stress, the first loading stiffness was much less than the unloading stiffness, reaching 37% at 25 MPa for films with 2400 nm seed spacing, whereas the loading stiffness in the tenth cycle was generally only slightly less than the unloading stiffness, with as little as 2% difference at 50 MPa for films with 2400 nm seed spacing.

Cu films resisted permanent deformation more than Si films. In Cu, each test area deformed uniformly, and the edge springs did not tilt outward as in Si films. The permanent set was calculated from SEM images captured before and after testing. An example of an unseeded test area subjected to 50 MPa is shown in Figure 4.5(a,b), while images of all test areas are shown in the Appendix B. The permanent set for each specimen type is provided in Figure 4.6. For Cu films with 2000 nm and 2800 nm seed spacing, ~2% permanent strain occurred first at 20 MPa, while in all other films, the first instance of permanent strain was recorded at 25 MPa and varied between 1% for unseeded films to 2% for films with 2400 nm and 3200 nm seed spacing. Unseeded films of springs experienced large permanent set 10.4% strain at 30 MPa, but at higher stresses, the rate of change in permanent set decreased significantly, reaching 12% at 50 MPa. Seeded films experienced consistently increasing permanent set with applied stress. At 50 MPa, the permanent set of films with 2000 nm and 3200 nm seed spacing was 8%, and 6%, respectively.

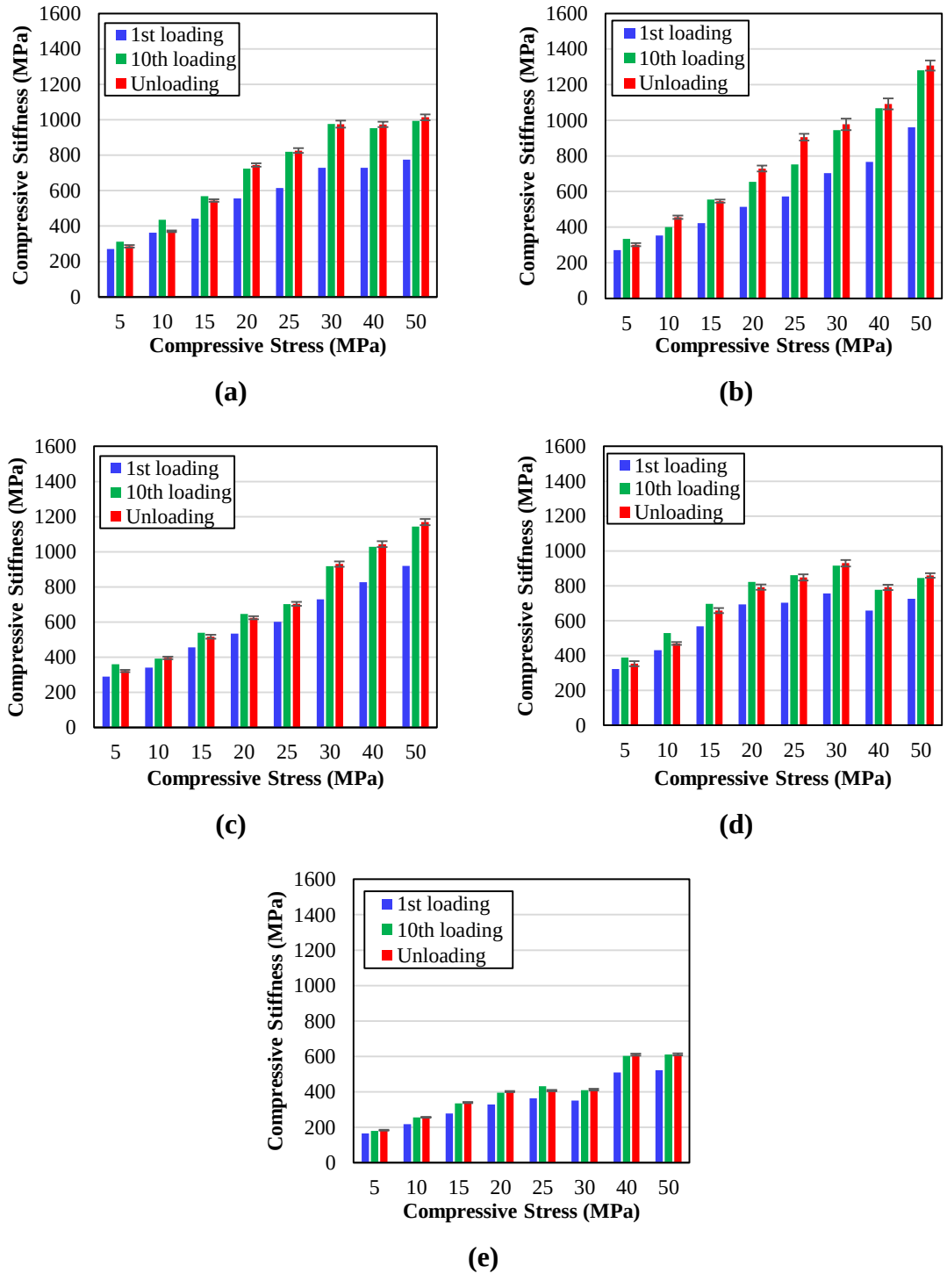

Figure 4.3 Loading stiffness of Cu spring films with: **(a)** 2000 nm, **(b)** 2400 nm, **(c)** 2800 nm and **(d)** 3200 nm seed spacing, as well as **(e)** no seeding.

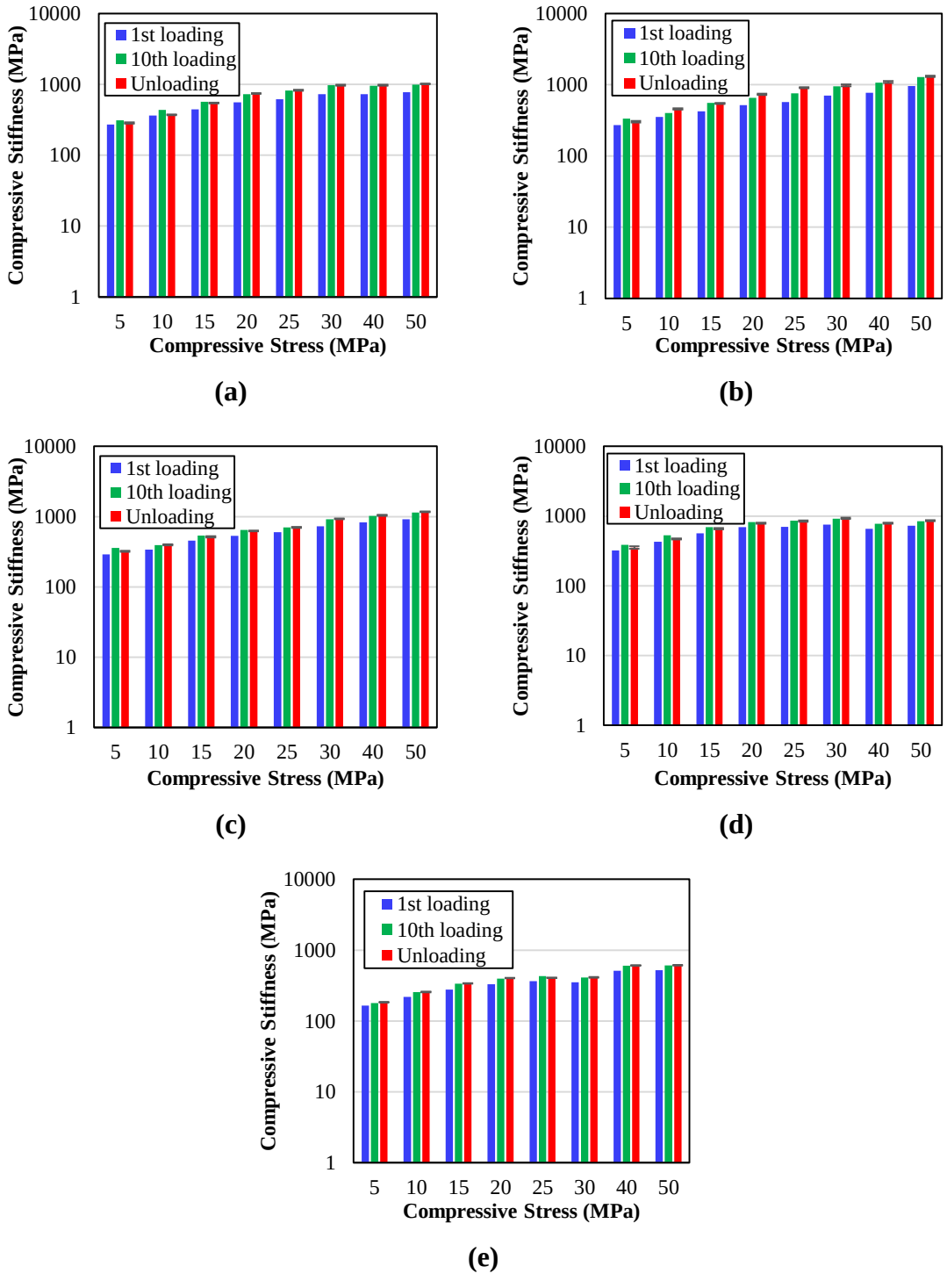

Figure 4.4 Loading stiffness of Cu spring films with: **(a)** 2000 nm, **(b)** 2400 nm, **(c)** 2800 nm and **(d)** 3200 nm seed spacing, as well as **(e)** no seeding. Logarithmic axes were used to enhance viewing of the plots.

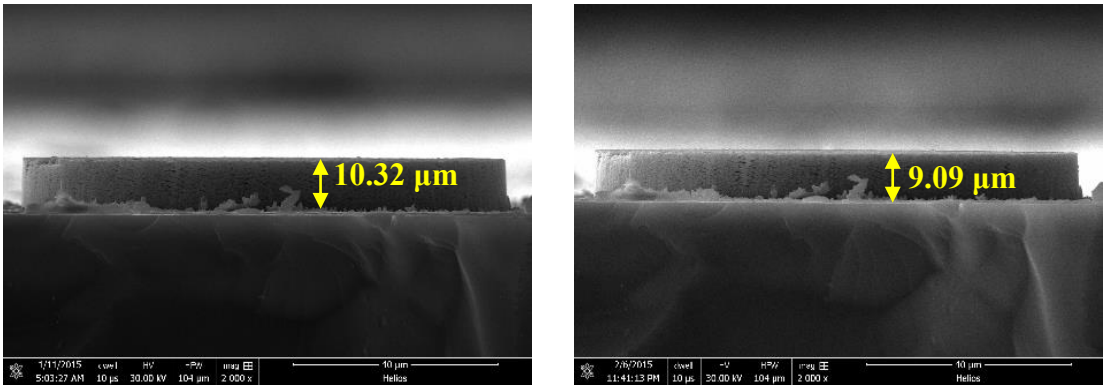

(a) **(b)**

Figure 4.5 Height measurements of unseeded Cu spring film subjected to 50 MPa compression **(a)** before test, and **(b)** after test. A collection of all images used in height measurements are included in Appendix B.

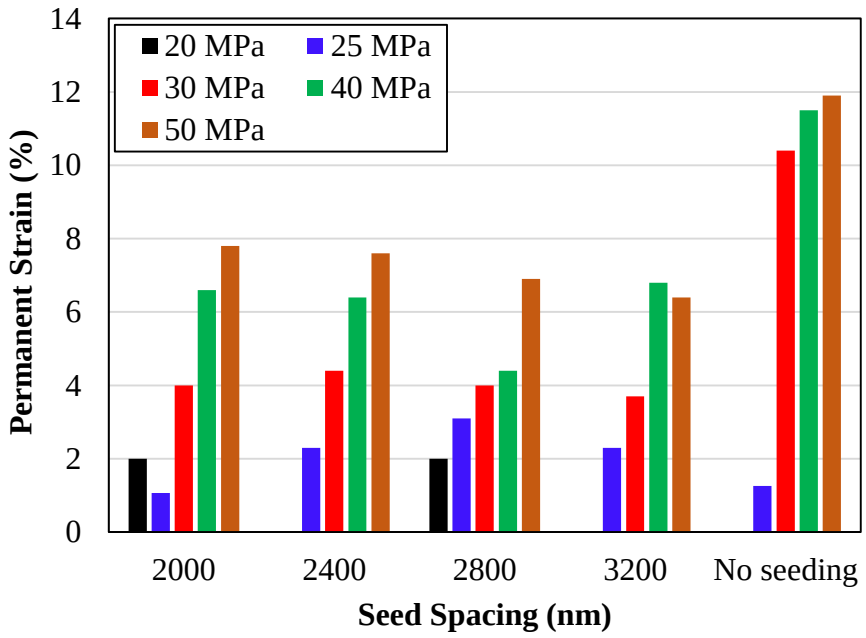

Figure 4.6 Permanent compressive strain of Cu spring films.

4.2 Results of Shear Tests on Cu Films

Cu spring films were tested in shear to determine the shear stiffness and ultimate shear strength. As shown in Figure 4.7, all Cu spring films had shear stiffnesses that varied regardless of seed spacing, ranging between 218 and 322 MPa with no discernable trend. The stiffnesses of films with 2000 nm (3 tests), 2400 nm (3 tests), 2800 nm (2 tests), and 3200 nm (4 tests) seed spacing were 244 ± 21 MPa, 218 ± 37 MPa, 322 ± 85 MPa, and 253 ± 10, MPa respectively, while unseeded Cu films had a stiffness (3 tests) of 288 ± 49 MPa. The similar stiffness values were due to the inverse relationship between seed spacing and the resulting spring density. Larger seed spacings resulted in larger spring features, such as wire and coil diameter, but smaller number of springs per film unit area compered to films with smaller seed spacing. Also, the effect of spring intertwining is important in shear tests. Films with smaller seed spacings had more spring overlap, and thus, came into contact at smaller shear displacements compared to springs with larger seed spacing.

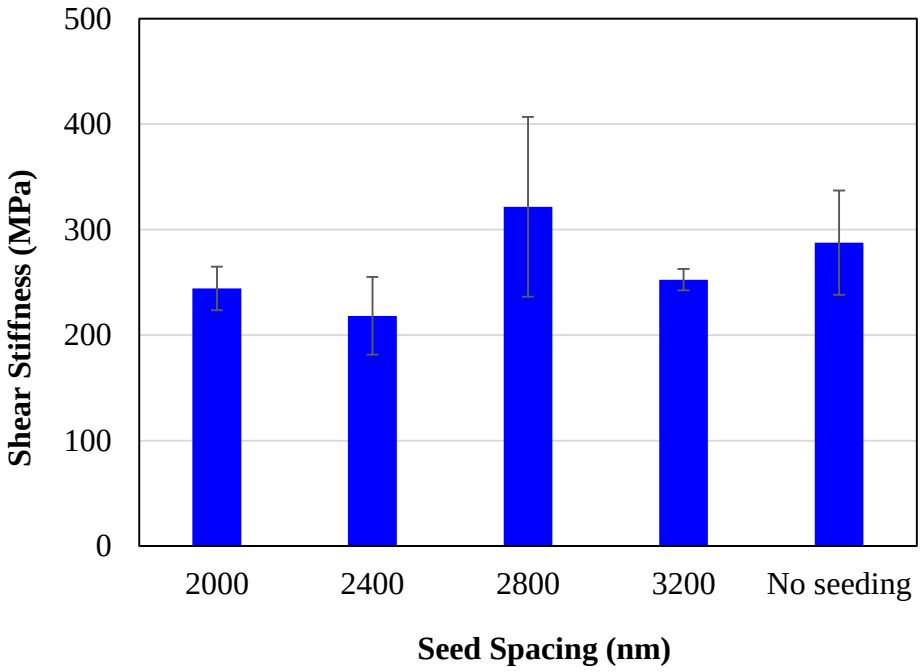

Figure 4.7 Shear stiffness of Cu spring films.

The ultimate shear strength values, shown in Figure 4.8, of seeded Cu films were quite similar. Films with 2000 nm (3 tests) seed spacing had the largest strength of 4.1 ± 1.2 MPa, while films with 2400 nm (3 tests) seed spacing had the lowest strength of 1.8 ± 0.4 MPa. The shear strengths of films with 2800 nm (2 tests) and 3200 nm (4 tests) seed spacing were 2.6 ± 0.4 MPa and 3.9 ± 0.4 MPa, respectively. However, unseeded films (2 tests) had much greater strength, reaching 16.1 ± 0.9 MPa. Seeded springs were deposited on narrow posts that provided a weak location for failure under shear loading. Unseeded spring films on the other hand, had a much larger base at the substrate and resulted in relatively larger shear strengths. SEM images of the failure surfaces are shown in Appendix D.

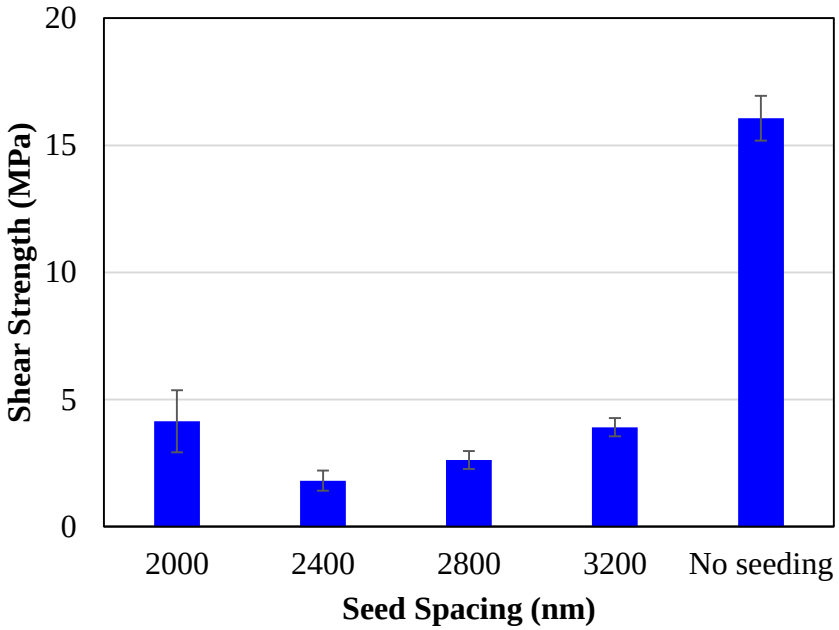

Figure 4.8 Ultimate shear strength of Cu spring films.

4.3 Comparison of Mechanical Properties of Si and Cu Spring Films

Although the Si and Cu spring films were both deposited using the GLAD method, the individual spring geometries, and thus, the spring film mechanical properties were vastly different. The larger Cu springs resulted in greater compressive and shear film stiffness than their Si counterparts. Under 5 MPa compression, the Cu films had unloading stiffness values of 286 - 353 MPa for seeded springs and 184 ± 2.2 MPa for unseeded springs, while at the same stress the unloading stiffness values of Si films were 44 - 45.5 MPa for 4-turn, seeded films, 54 ± 0.4 MPa for 4-turn, unseeded films, 119 - 165 MPa for 10-turn, seeded and 78 ± 1.0 MPa for 10-turn, unseeded films. At 50 MPa, the unloading stiffness of Cu films was 860 - 1310 MPa for seeded films and 610 ± 5.5 MPa for unseeded films. Si spring films had unloading stiffness values of 528 - 810 MPa for 4-turn, seeded films, 291 ± 2.7 MPa for 4-turn, unseeded films, 720 - 728 MPa for 10-turn, seeded films, and 780 ± 5.2 MPa for 10-turn, unseeded films. At all stress levels, the Cu seeded and unseeded films were stiffer in compression than Si. This trend continued for the amount of permanent strain experienced by Cu and Si springs. Cu films began to experience a permanent strain of 2.0% at 20 MPa, whereas Si films experienced permanent strains of up to 6.5% as early as 5 MPa. The maximum permanent strain recorded for Cu was 7.8% for films with 2000 nm seed spacing and 12% for unseeded samples, both at an applied stress of 50 MPa. For Si, the maximum permanent strain also occurred at 50 MPa, with values of 38.1% for 10-turn, 1500 nm seed spacing and 22.5% for 4-turn, unseeded films. Thus, the amount of permanent strain experienced by seeded Si films was up to 3 times that at 5 MPa, and up to 4.9 times that at 50 MPa for seeded Cu springs, and 1.9 times that of unseeded Cu films for unseeded Si films.

The shear stiffness for Cu springs ranged from 218 ± 37 to 322 ± 85 MPa for seeded and 288 ± 49 MPa for unseeded films. For Si, however, the shear stiffness of 4-turn, seeded films was between 16.8 ± 1.8 and 25.7 ± 2.0 MPa, with a stiffness value of 26.8 ± 7.1 MPa for 4-turn, unseeded films. For 10-turn springs, the shear stiffness of seeded films was between 6.6 ± 0.6 and 26.1 ± 4.7 MPa, and 23.5 ± 3.2 MPa for unseeded films. The trends in shear strength differed, however. The shear strength of all seeded Cu films was between 1.8 ± 0.4 and 4.1 ± 1.2 MPa, and was 16.1 ± 0.9 MPa for

unseeded Cu. For seeded Si, the shear strength ranged between 0.9 ± 0.05 and 3.2 ± 0.5 MPa, while the unseeded Si shear strength was 2.3 ± 0.1 to 3.9 ± 0.7 MPa. While the shear strength of Si is less than that of Cu, the difference in strength is not as great as that in stiffness. This is because the seeded Cu films broke at the attachment point to the substrate, which is quite narrower than the cross-sectional area of any of the seeded Cu spring wires; any transverse stress applied to a Cu spring will first reach a critical value at the post. In Si springs the wire diameter was approximately the same as the Si posts that they were grown on, thus allowing for failure to occur within the spring.

4.4 Conclusions

The compressive stiffness of Cu spring films demonstrated an increasing trend with applied load. For some of the films, the stiffness reached a plateau value, suggesting contact between springs. The loading stiffness gradually increased during a ten cycle loading/unloading while the unloading stiffness remained constant. No permanent set occurred until 20 MPa for films with 2000 nm and 2800 nm seed spacing, and until 25 MPa for all other film types. In the case of seeded films, the permanent strain increased steadily with stress from 2% at 20 MPa to 6.4 - 7.8% at 50 MPa, while for unseeded Cu films there was a sudden increase in permanent strain from 1.3% at 25 MPa to 10.4% at 30 MPa, before reaching a plateau of 12% strain at 50 MPa. This is likely the point at which adjacent springs came in complete contact.

The shear stiffness of all Cu spring film types was roughly equal, regardless of seed spacing, at 218 ± 37 to 322 ± 85 MPa. However, there was a drastic difference between the shear strength of seeded and unseeded films, with strength values of 1.8 ± 0.4 to 4.1 ± 1.2 MPa for all types of seeded spring films and 16.1 ± 0.9 MPa for unseeded springs. The narrow seed posts in seeded Cu spring films resulted in failure at small shear stresses, compared to unseeded Cu springs which were grown directly on the substrate.

CHAPTER 5

CONCLUSIONS

5.1 Summary of Results

The role of geometry on the mechanical properties of Si and Cu spring films was evaluated by uniform compression and shear experiments. For all types of Si and Cu spring films, the compressive stiffness increased with compressive stress. At 5 MPa stress, 4-turn Si spring films had compressive stiffnesses of 44 ± 0.2 to 54 ± 0.4 MPa, while 10-turn Si spring films had stiffnesses of 78 ± 1.0 to 165 ± 1.3 MPa, which is less than 0.03% and 0.10% of the stiffness of bulk Si (169 GPa), respectively [19]. For the same applied stress, the 10-turn Cu spring films had stiffnesses between 184 ± 2.2 and 353 ± 14.8 MPa, which is less than 0.3% of the stiffness of bulk Cu, 117 GPa [20]. The stiffness of 4-turn Si spring films showed large dependency on seed spacing at large loads, while the 10-turn Si spring films had similar stiffness values at large loads. The Cu spring films had stiffness values between 611 ± 5.5 and 1308 ± 13 MPa for 50 MPa stress. The deposition process of Cu, which was characterized by larger seed spacing and higher vapor flux than Si, thus producing wider and stiffer springs.

The Cu spring films provided more resistance to permanent compression than the Si spring films. Permanent set began at 20 MPa for Cu with a residual strain of 2 %, finally reaching a maximum permanent strain of 12 % for unseeded Cu at a stress level of 50 MPa. In general, all seeded Cu spring films experienced similar permanent strain for each level of stress, reaching 8 % strain at 50 MPa. These values are more desirable than those of Si, which displayed permanent strains of up to 7 % for 4-turn, 900 nm seed spacing at 5 MPa and up to 38% for 10-turn, 1500 nm seed spacing at 50 MPa. Beyond 15 MPa applied stress, the 4-turn Si spring films experienced similar permanent strain at each level of stress, while the 10-turn Si spring films displayed a clear trend, with the

1500 nm seed spacing experiencing the highest amount of permanent set, followed by films with 900 nm seed spacing and then the unseeded spring films. This trend can be explained by the geometry of the Si springs. The 4-turn springs have much larger overlap than the 10-turn springs which are more columnar shaped and isolated. At larger stresses, the 4-turn springs came into contact and resisted movement thereby withstanding more stress with minimal deformation. Therefore, the amount of permanent deformation at high loads was less in 4-turn spring films than in the 10-turn spring films. Unseeded spring films had the most overlap, followed by spring films with 900 nm and finally 1500 nm seed spacing. This order corresponds to the inverse order of permanent deformation experienced by each spring layer.

The shear stiffness of 4-turn Si films increased with seed spacing, with values of 16.8 ± 1.8 MPa for spring films with 900 nm seed spacing and 25.7 ± 2.0 MPa for spring films with 1500 nm seed spacing. The opposite trend was true for films with 10-turn springs: spring films with 900 nm seed spacing had a stiffness of 26.1 ± 4.7 MPa, while spring films with 1500 nm seed spacing had a stiffness of 6.6 ± 0.6 MPa. The unseeded spring films had stiffness values that were comparable to the stiffer seeded springs in each coil turn case, with a stiffness of 26.8 ± 7.1 MPa for 4-turn springs and 23.5 ± 3.2 MPa for 10-turn springs. The large difference in stiffness between film types was due to the intertwining of springs in the films. The springs in unseeded films were much more densely packed than in seeded films. In the case of 4-turn coils both seeded spring types were highly intertwined. Therefore, the higher stiffness in spring films with 1500 nm seed spacing was due to the springs' thicker wires than their counterparts with 900 nm seed spacing. In the case of 10-turn springs, the films with 1500 nm seed spacing showed a smaller degree of spring intertwining than films with 900 nm seed spacing, which explains in part the drastic difference in shear stiffness values. Cu spring films had shear stiffness values that displayed no trend with respect to seed spacing, varying between 218 ± 37 and 322 ± 85 MPa. Similarly to the compression results, the difference in stiffness between Si and Cu springs was due to the larger coil diameter and wider spring geometry of Cu springs. The shear strength values of 4-turn Si springs were very similar, between 2.3 ± 0.1 MPa and 2.4 ± 0.2 MPa, while the stiffness of 10-turn Si spring films varied depending on seed spacing. 10-turn Si springs had shear strengths of 3.2 ± 0.5 MPa, 0.9 ±

0.05 MPa, and 3.9 ± 0.7 MPa for 900 nm seed spacing, 1500 nm seed spacing, and no seed spacing, respectively. SEM images of the failure surfaces showed that seeded 10-turn spring films failed at the base of the springs where nucleation during the GLAD took place. Films with 10-turn springs and 900 nm seed spacing had higher strength than films with 10-turn springs and 1500 nm seed spacing because the former resulted in ~2.8 times the number of springs compared to the latter.

The seeded Cu spring films had shear strength values between 1.8 ± 0.4 and 4.1 ± 1.2 MPa, which were much less than the unseeded Cu films, with strength of 16.1 ± 0.9 MPa. This large discrepancy was due to the seed posts that the Cu springs were deposited on, which had a much smaller diameter than the wire diameter of the Cu springs; when transverse stress was applied, failure occurred at the narrowest point at the posts. Films with unseeded Cu springs had at least 4 times the shear strength of any of the Si films.

REFERENCES

[1] Z. V. Goryacheva, Y. A. Kuzma-Kichta, V. A. Len'kov, D. N. Sorokin, R. A.Khaikin, B. F. Shibryaev, and B. A. Stutman. "Determination of the Thermal Resistance of Porous Sintered Films Made of Metal Powders." Khimicheskoe I Neftyanoe Machinostroenie 15 (5) , pp. 10-12, (1979).

[2] D. Shaddock, S. Weaver, I. Chasiotis, B. Shah and D. Zhong, "Development of a compliant nanothermal interface material," Proc ASME 2011, pp. 1-5, (2011).

[3] T. Sumiwaga, H. Hirakata, M. Takemura, S. Matsumoto, M. Suzuki, and T. Kitamura. "Disappearance of Stress Singularity at Interface Edge Due to Nanostructured Thin Film," Engineering Fracture Mechanics, 75 (10), pp. 3073-3083, (2008).

[4] Y. Zhao. "Growth and Synthesis of Nanostructured Thin Films," Functional Thin Films and Nanostructures for Sensors, pp. 31-64, (2009).

[5] M. T. Taschuk, M. M. Hawkeye, and M. J. Brett. "Glancing Angle Deposition." Handbook of Deposition Technologies for Films and Coatings, third ed. Elsevier, Amsterdam, pp. 621-678.

[6] M. Hawkeye and M. J. Brett. "Glancing Angle Deposition: Fabrication, Properties, and Applications of Micro-and Nanostructured Thin Films," Journal of Vacuum Science and Technology A 25 (5), pp. 1317-1335, (2007).

[7] K. Robbie and M. J. Brett. "Sculptured Thin Films and Glancing Angle Deposition: Growth Mechanics and Applications," Journal of Vacuum Science and Technology A 15 (3), pp. 1460-1465 (1997).

[8] F. C. Akkari, M. Kanzari, and B. Rezig. "Growth and Properties of the $CuInS_2$ Thin Films Produced by Glancing Angle Deposition," Materials Science and Engineering C 28, pp. 692-696, (2008).

[9] X. Xiao, G. Dong, C. Xu, H. He, H. Qi, Z. Fan, and J. Shao. "Structure and Optical Properties of Nb2O5 Sculptured Thin Films by Glancing Angle Deposition," Applied Surface Science 255, pp. 2192-2195, (2008).

[10] J. Gospodyn, M. T. Taschuk, P. C. P. Hrudey, S. Y. Tsui, R. Fedosejevs, M. J. Brett, and J. C. Sit. “Photoluminescence Emission Profiles of Y2O3: Eu Films 49 Composed of High-Low Density Stacks Produced by Glancing Angle Deposition,” Applied Optics 47 (15), pp. 2798-2805, (2008).

[11] L. W. Bezuidenhout and M. J. Brett. “Ultrathin Layer Chromatography on Nanostructured Thin Films,” Journal of Chromatography A 1183, pp. 175-179, (2008).

[12] H. Hirakata, S. Matsumoto, M. Takemura, M. Suzuki, and T. Kitamura. “Anisotropic Deformation of Thin Films Comprised of Helical Nanosprings,” International Journal of Solids and Structures 44, pp. 4030-4038, (2007).

[13] D. Liu, D. X. Ye, F. Khan, F. Tang, B. K. Lim, R. C. Picu, G. C. Wang, and T. M. Lu. "Mechanics of Patterned Helical Si Springs on Si Substrate," Journal of Nanoscience and Nanotechnology 3 (6), pp. 492-495, (2003).

[14] M. W. Seto, K. Robbie, D. Vick, M. J . Brett and L. Kuhn, “Mechanical response of thin films with helical microstructures”, Journal of Vacuum Science and Technology, B 17, pp. 2172-2177, (1999).

[15] M. W. Seto, B. Dick, M. J. Brett, “Microsprings and Microcantilevers: Studies of Mechanical Response,” Journal of Micromechanics and Microengineering, 11, pp. 582-588, (2001).

[16] G. Zhang and Y. Zhao. “Mechanical Characteristics of Nanoscale Springs.” Journal of Applied Physics 95 (1), pp. 267-271, (2004).

[17] M. Malac, R. F. Egerton, M. J. Brett and B. Dick, “Fabrication of submicrometer regular arrays of pillars and helices”, Journal of Vacuum Science & Technology B, 17, pp. 2671-2674, (1999).

[18] M. Naraghi, I. Chasiotis, H. Kahn, Y. Wen and Y. Dzenis, “Mechanical deformation and failure of electrospun polyacrylonitrile nanofibers as a function of strain rate,” Applied Physics Letters, 91, pp. 151901, (2007).

[19] M. A. Hopcroft, W. D. Nix, and T. W. Kenny, "What is the Young's Modulus of Silicon?", IEEE Journal of Microelectromechanical Systems, vol. 19, Issue 2, pp. 229-238, 2010.

[20] C.L. Cheng. Mechanical and Microstructural Characterization of Copper Microsamples After Cold Drawing. Master of Science Thesis in Mechanical Engineering, University of Maryland, Baltimore County, 2008, pp. 19.

Appendix A

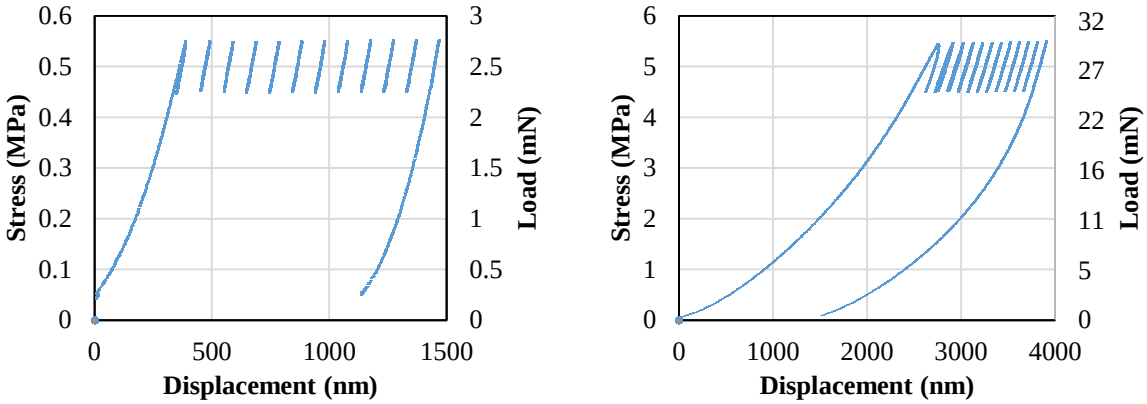

(a)

(b)

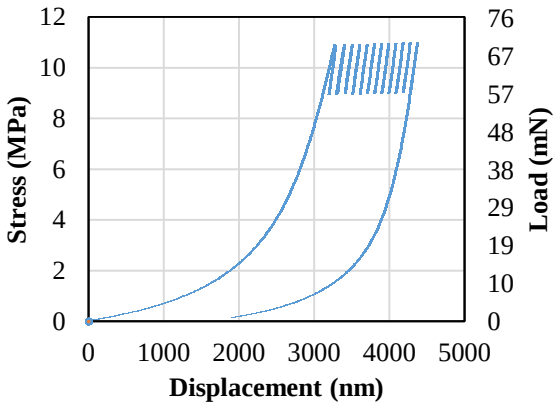

(c)

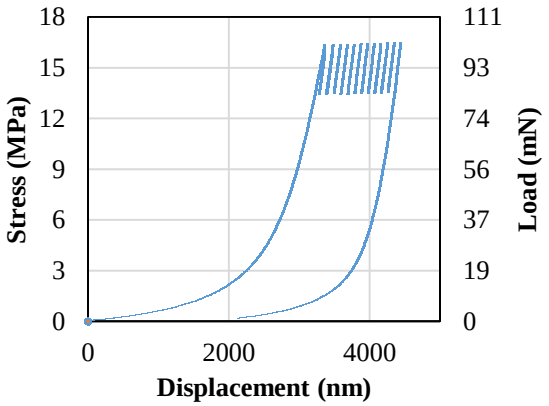

(d)

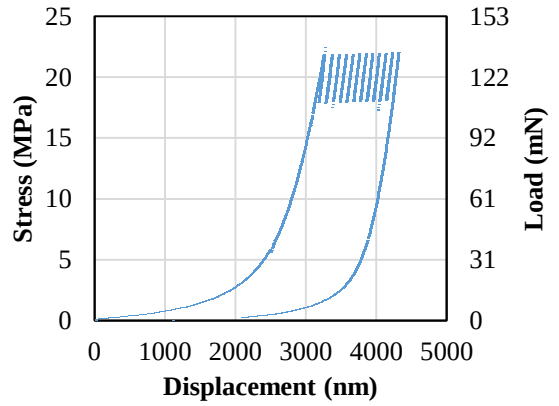

(e)

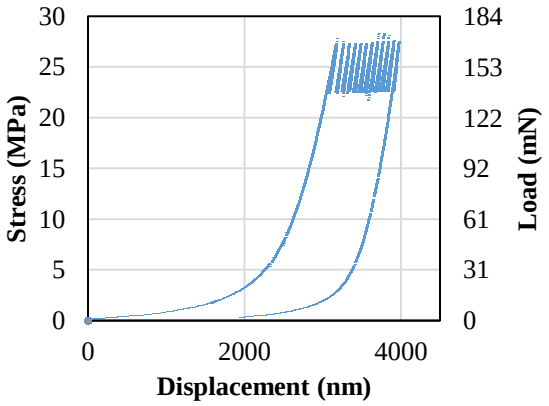

(f)

Figure A.1 (cont.)

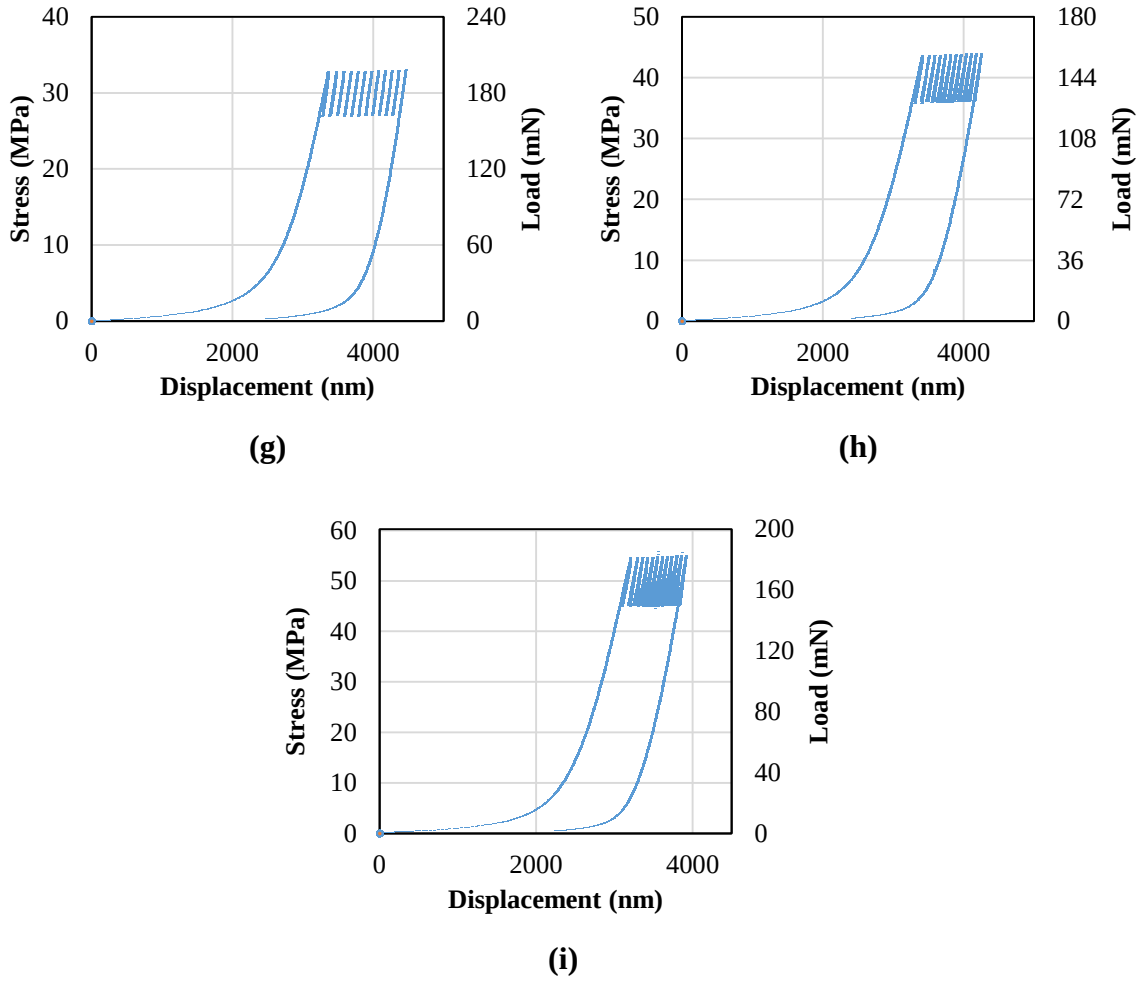

Figure A.1 Cyclic compression of 4-turn Si spring films with 900 nm seed spacing subjected to **(a)** 0.5 MPa, **(b)** 5 MPa, **(c)** 10 MPa, **(d)** 15 MPa, **(e)** 20 MPa, **(f)** 25 MPa, **(g)** 30 MPa, **(h)** 40 MPa, **(i)** 50 MPa mean stress.

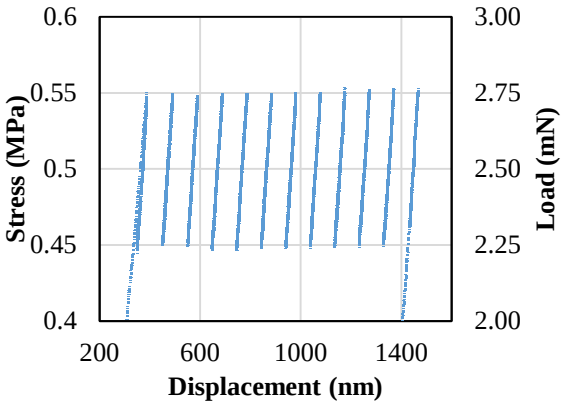

(a)

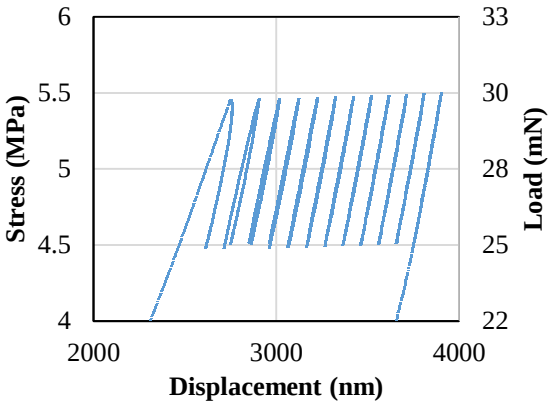

(b)

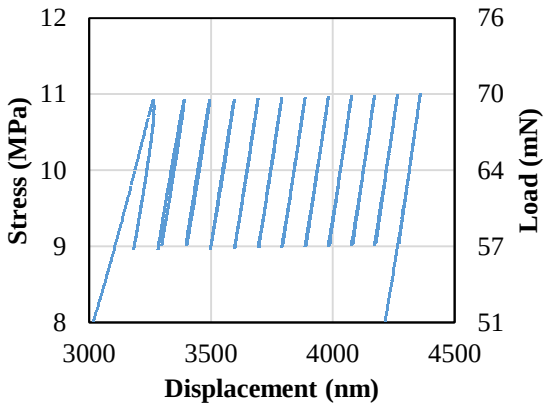

(c)

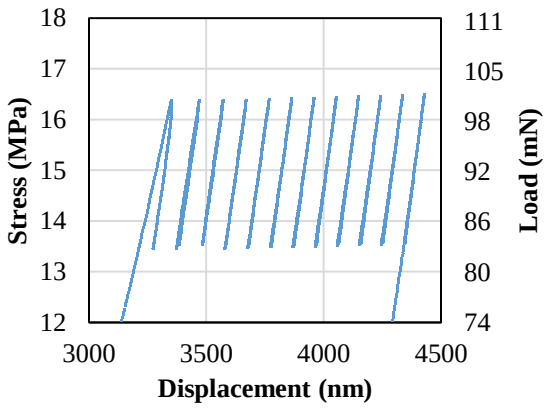

(d)

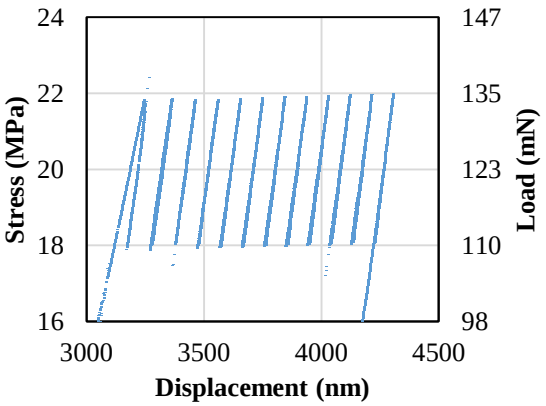

(e)

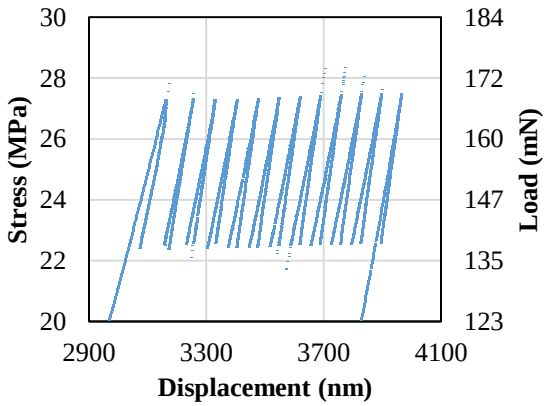

(f)

Figure A.2 (cont.)

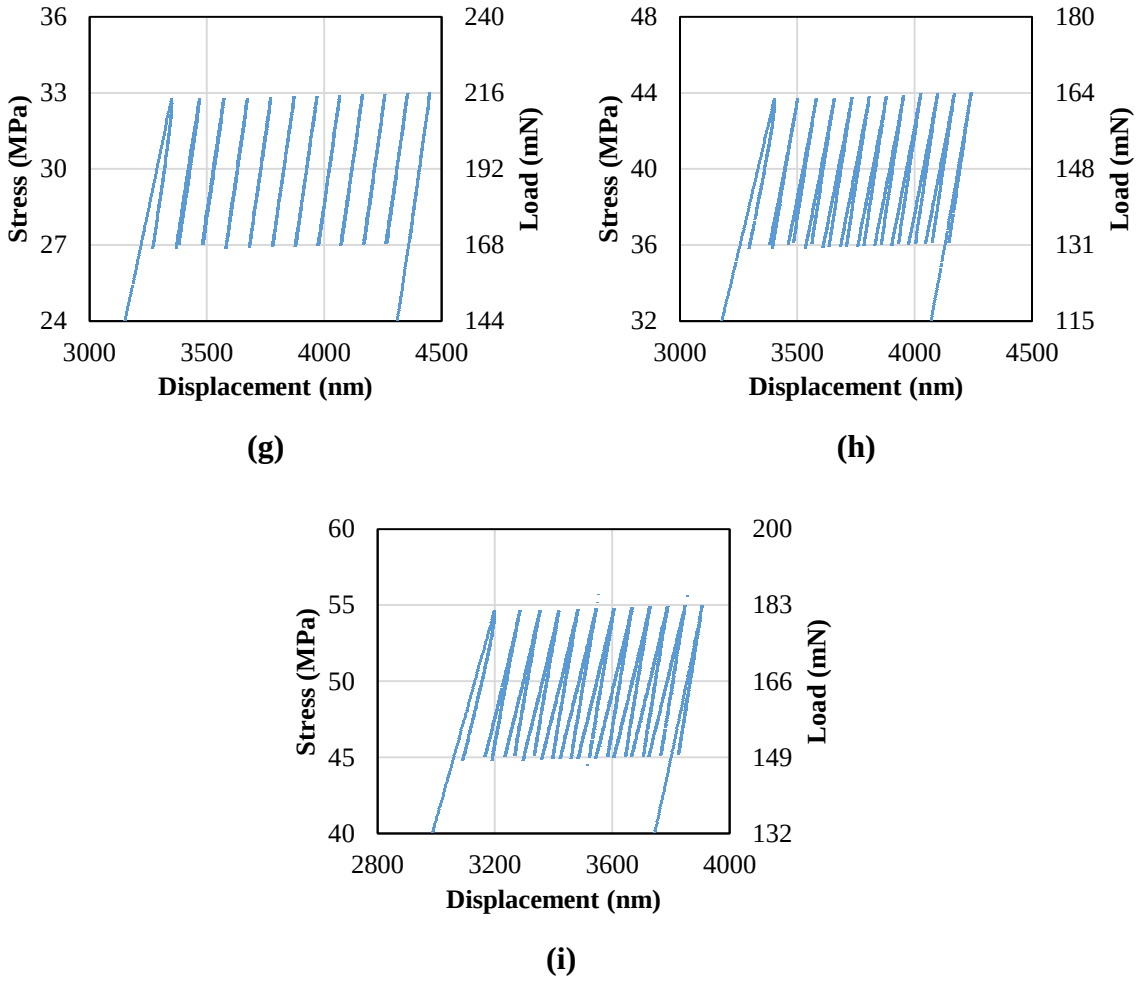

Figure A.2 Detail of cyclic compression of 4-turn Si spring films with 900 nm seed spacing subjected to **(a)** 0.5 MPa, **(b)** 5 MPa, **(c)** 10 MPa, **(d)** 15 MPa, **(e)** 20 MPa, **(f)** 25 MPa, **(g)** 30 MPa, **(h)** 40 MPa, **(i)** 50 MPa mean stress with an amplitude of 10% of the mean.

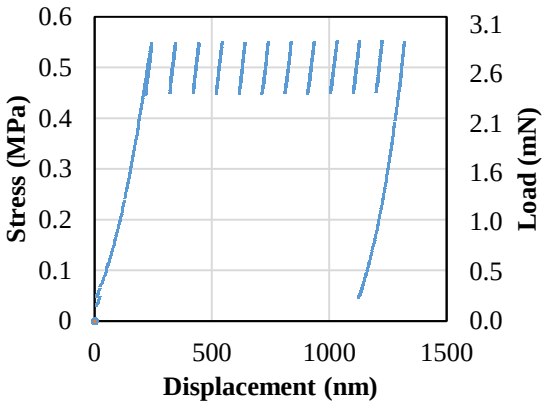

(a)

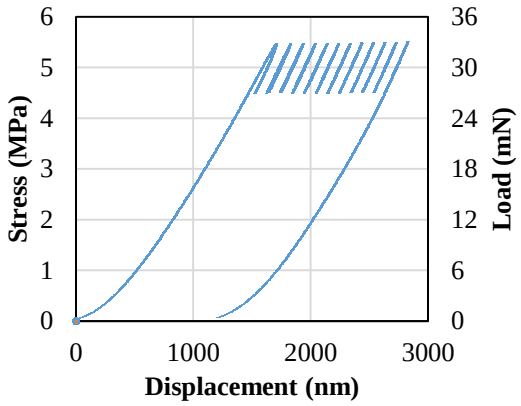

(b)

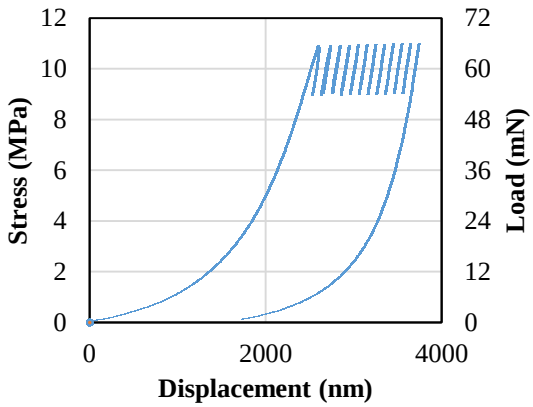

(c)

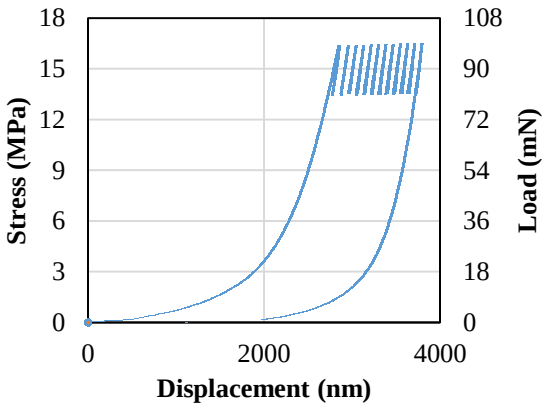

(d)

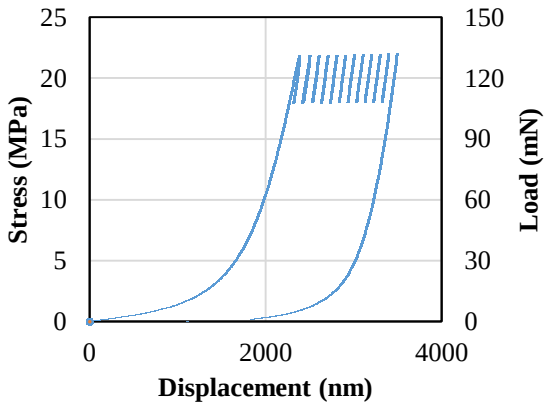

(e)

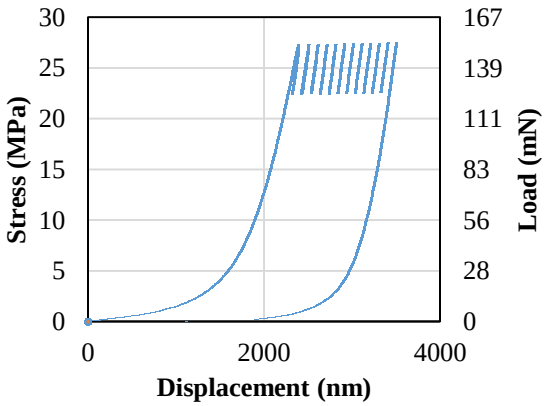

(f)

Figure A.3 (cont.)

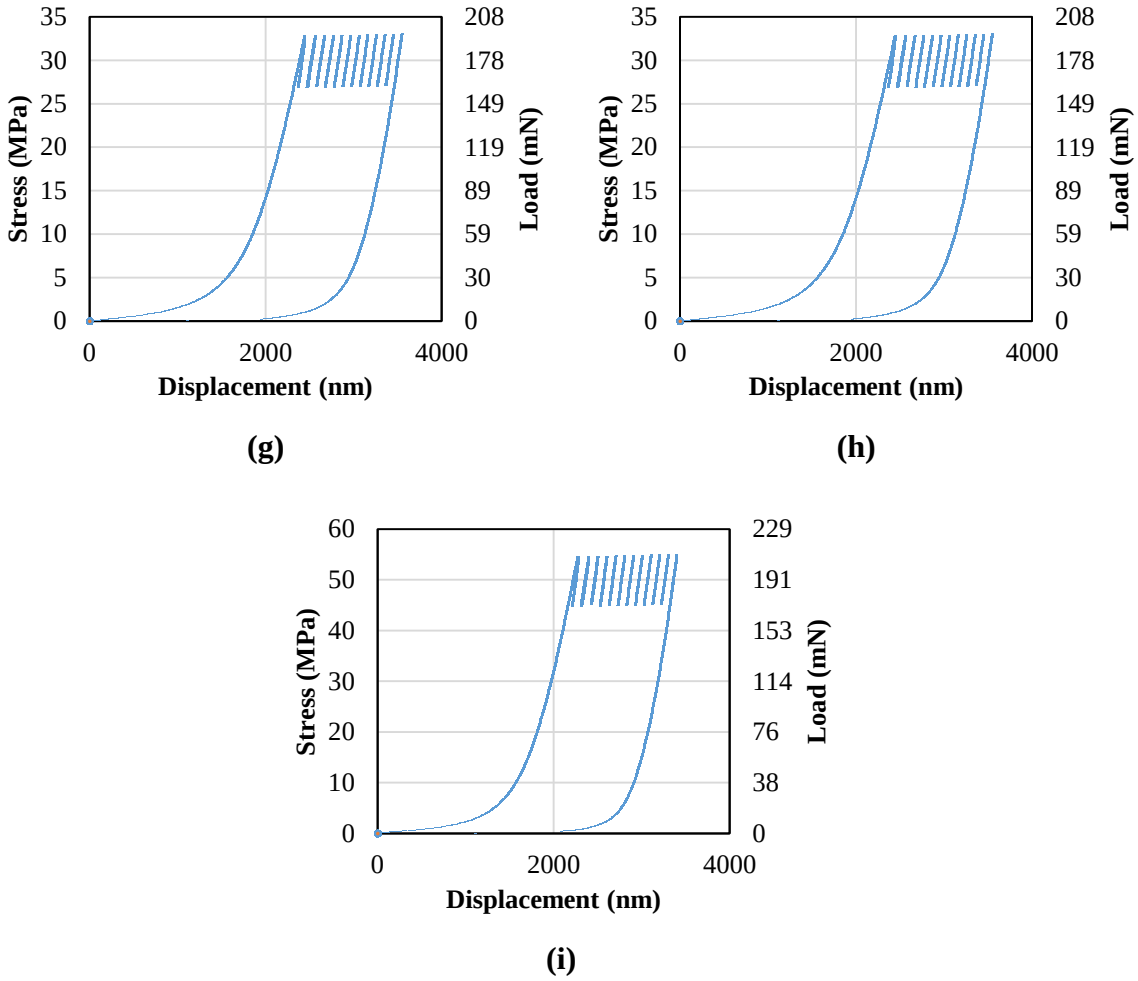

Figure A.3 Cyclic compression of 4-turn Si spring films with 1500 nm seed spacing subjected to **(a)** 0.5 MPa, **(b)** 5 MPa, **(c)** 10 MPa, **(d)** 15 MPa, **(e)** 20 MPa, **(f)** 25 MPa, **(g)** 30 MPa, **(h)** 40 MPa, **(i)** 50 MPa mean stress.

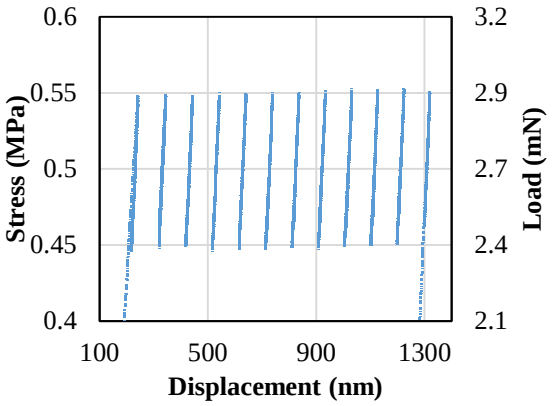

(a)

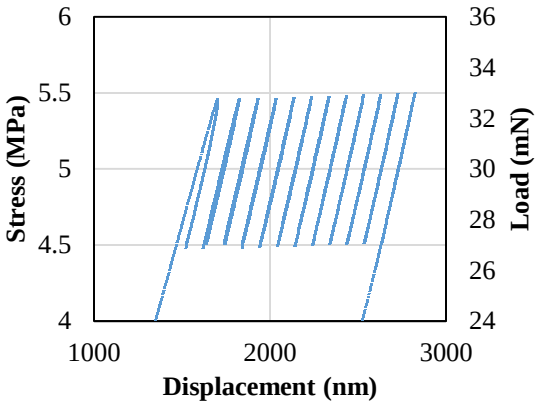

(b)

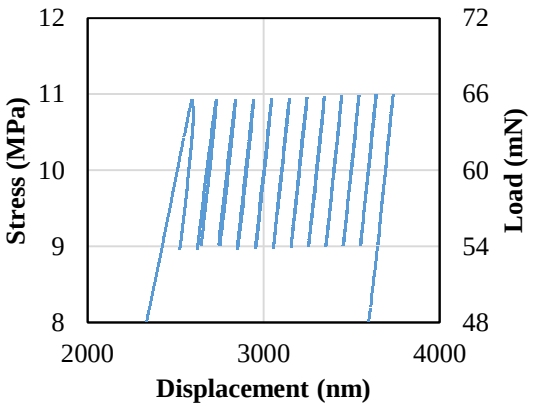

(c)

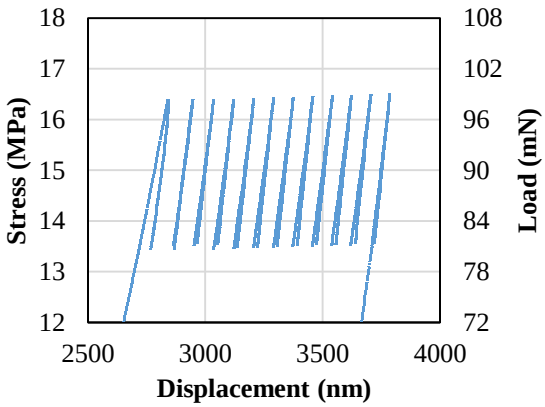

(d)

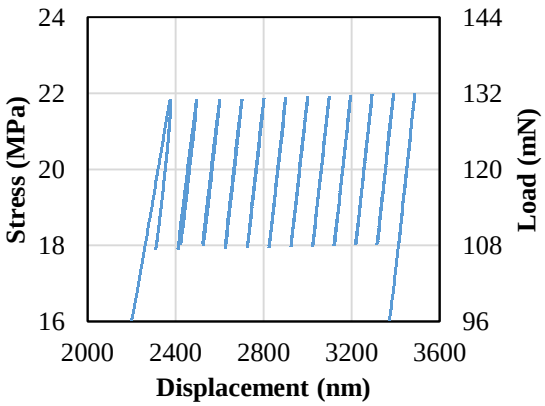

(e)

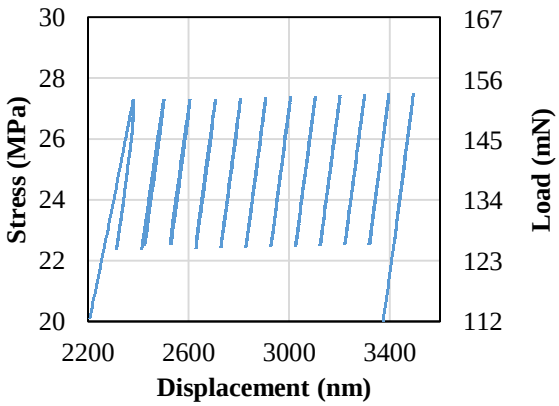

(f)

Figure A.4 (cont.)

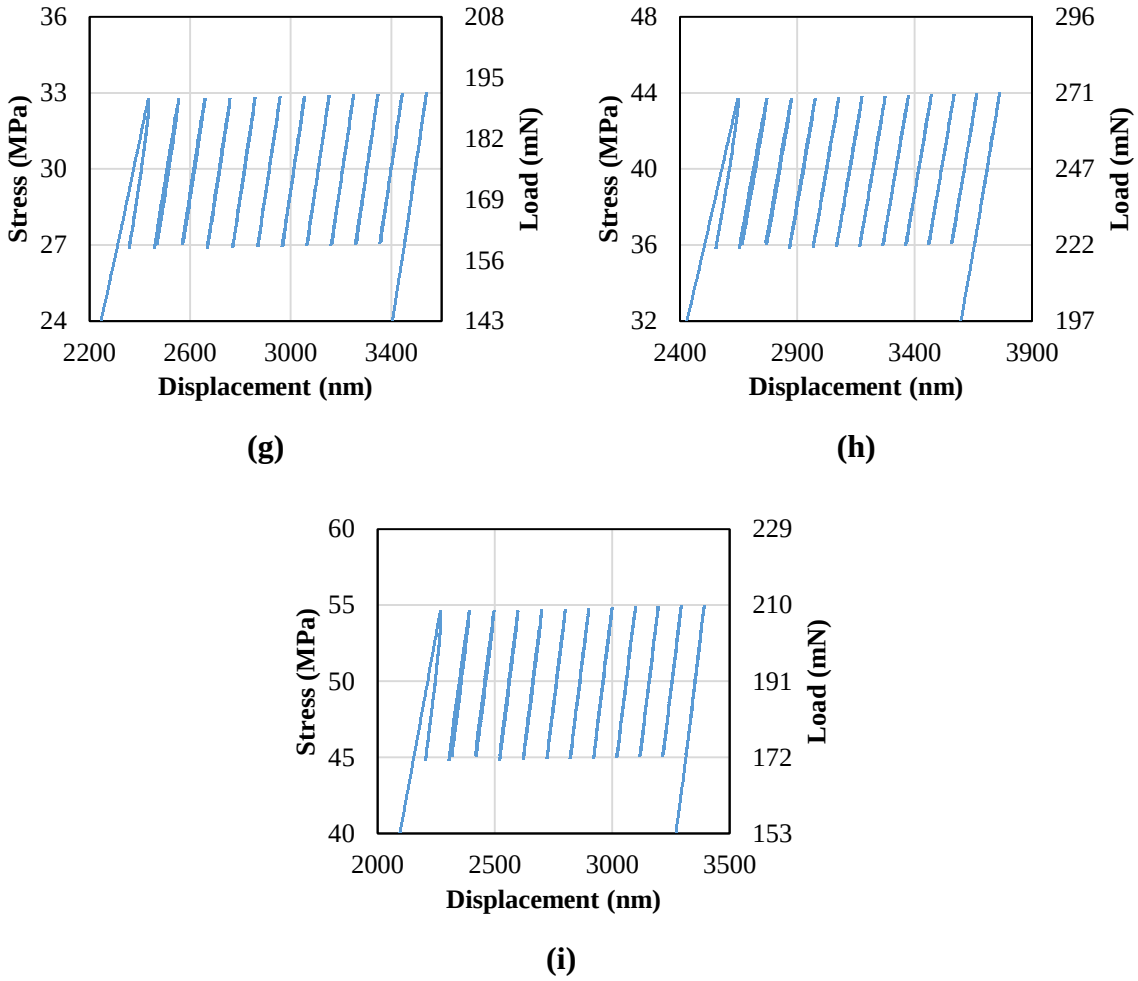

Figure A.4 Detail of cyclic compression of 4-turn Si spring films with 1500 nm seed spacing subjected to **(a)** 0.5 MPa, **(b)** 5 MPa, **(c)** 10 MPa, **(d)** 15 MPa, **(e)** 20 MPa, **(f)** 25 MPa, **(g)** 30 MPa, **(h)** 40 MPa, **(i)** 50 MPa mean stress with an amplitude of 10% of the mean.

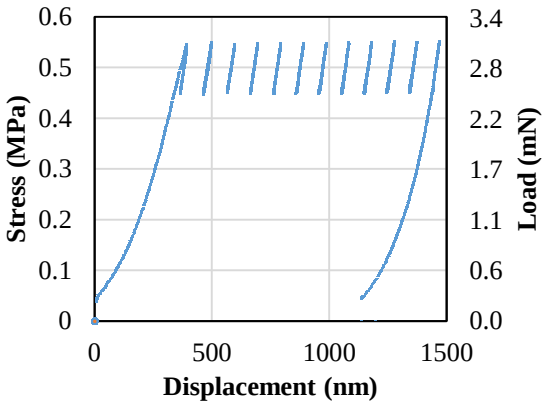

(a)

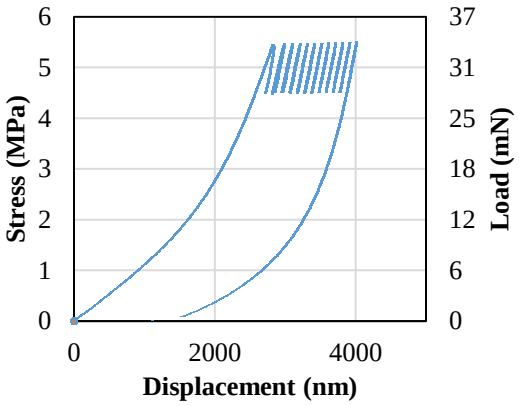

(b)

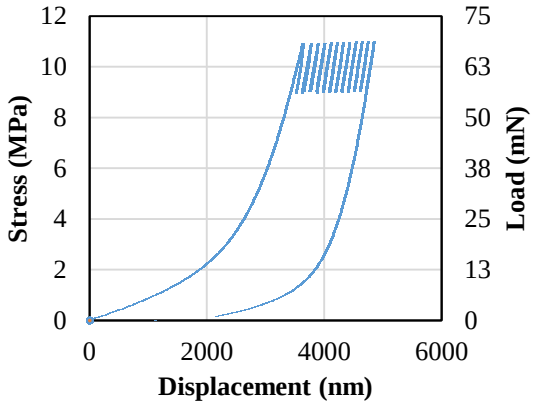

(c)

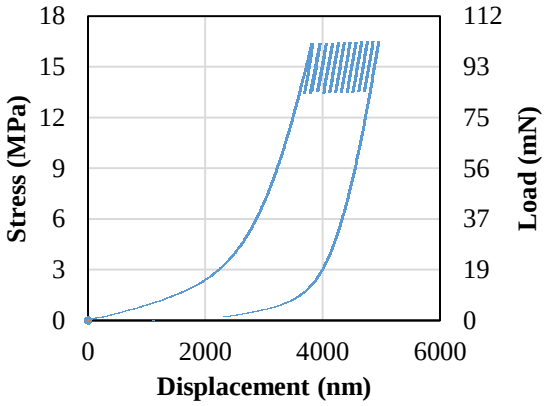

(d)

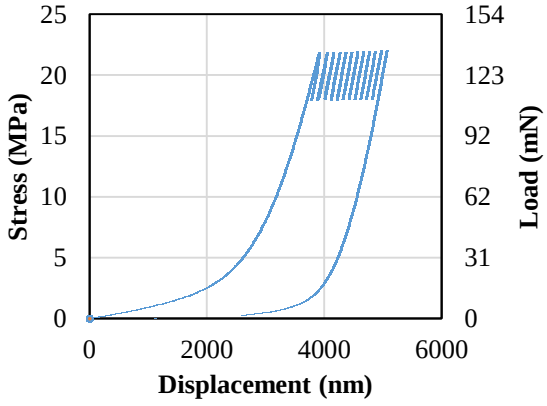

(e)

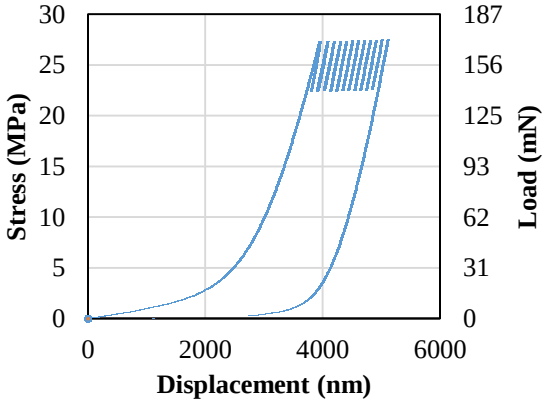

(f)

Figure A.5 (cont.)

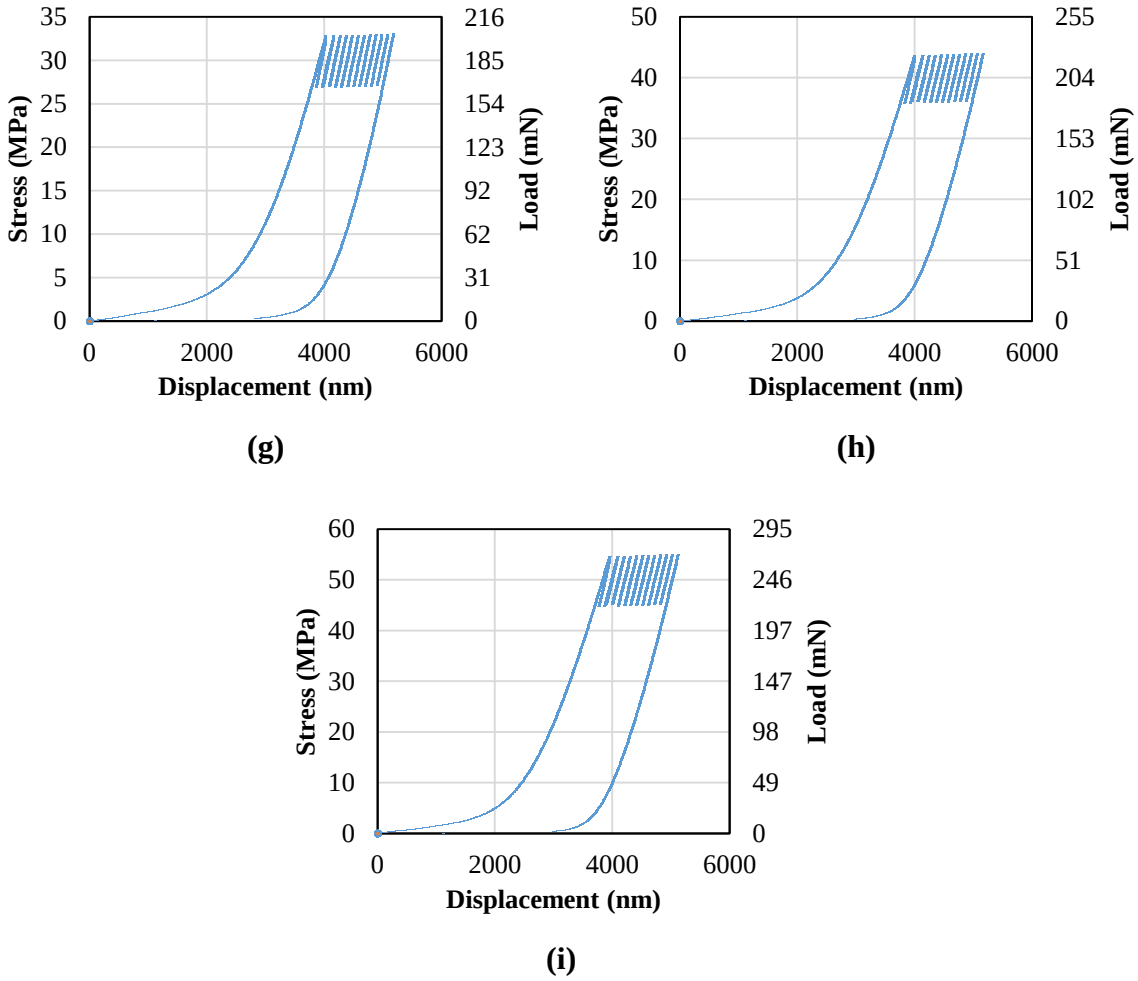

Figure A.5 Cyclic compression of 4-turn Si spring films on unseeded substrate subjected to **(a)** 0.5 MPa, **(b)** 5 MPa, **(c)** 10 MPa, **(d)** 15 MPa, **(e)** 20 MPa, **(f)** 25 MPa, **(g)** 30 MPa, **(h)** 40 MPa, **(i)** 50 MPa mean stress.

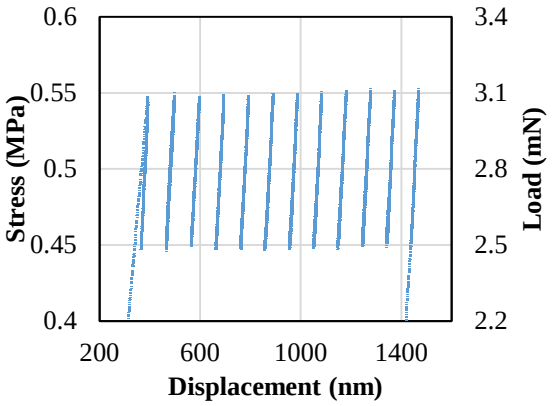

(a)

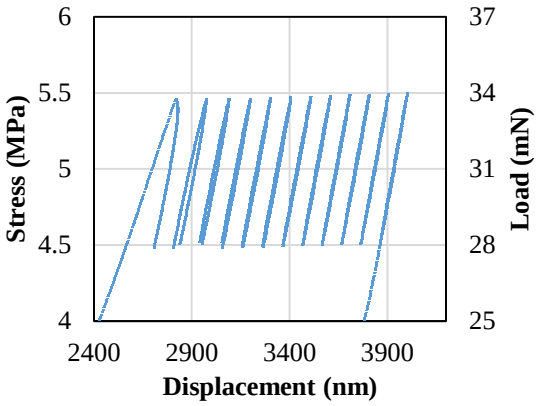

(b)

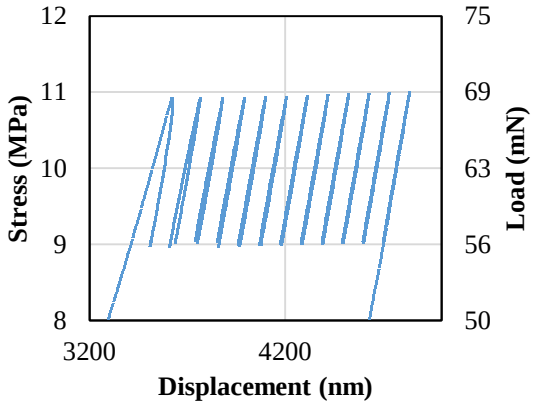

(c)

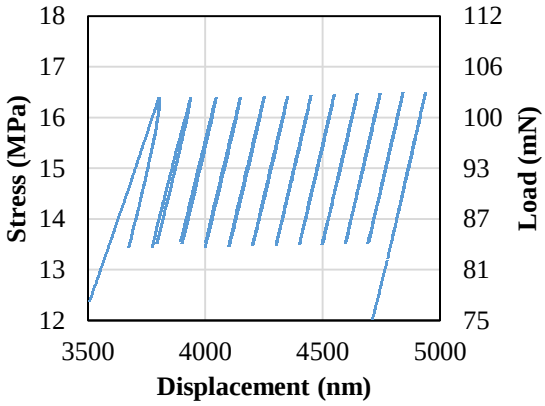

(d)

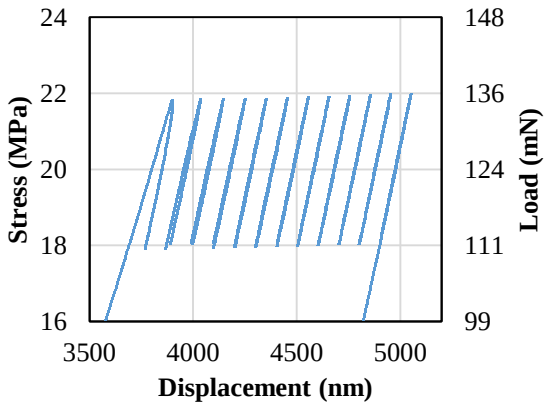

(e)

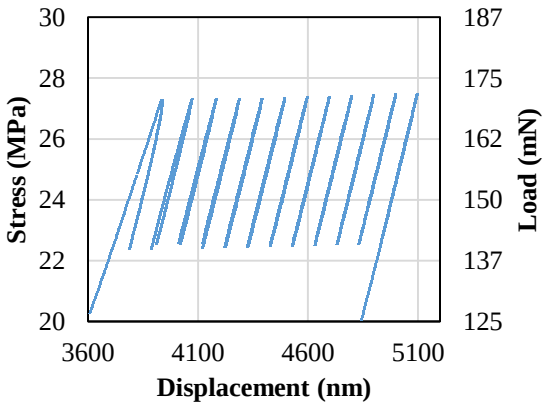

(f)

Figure A.6 (cont.)

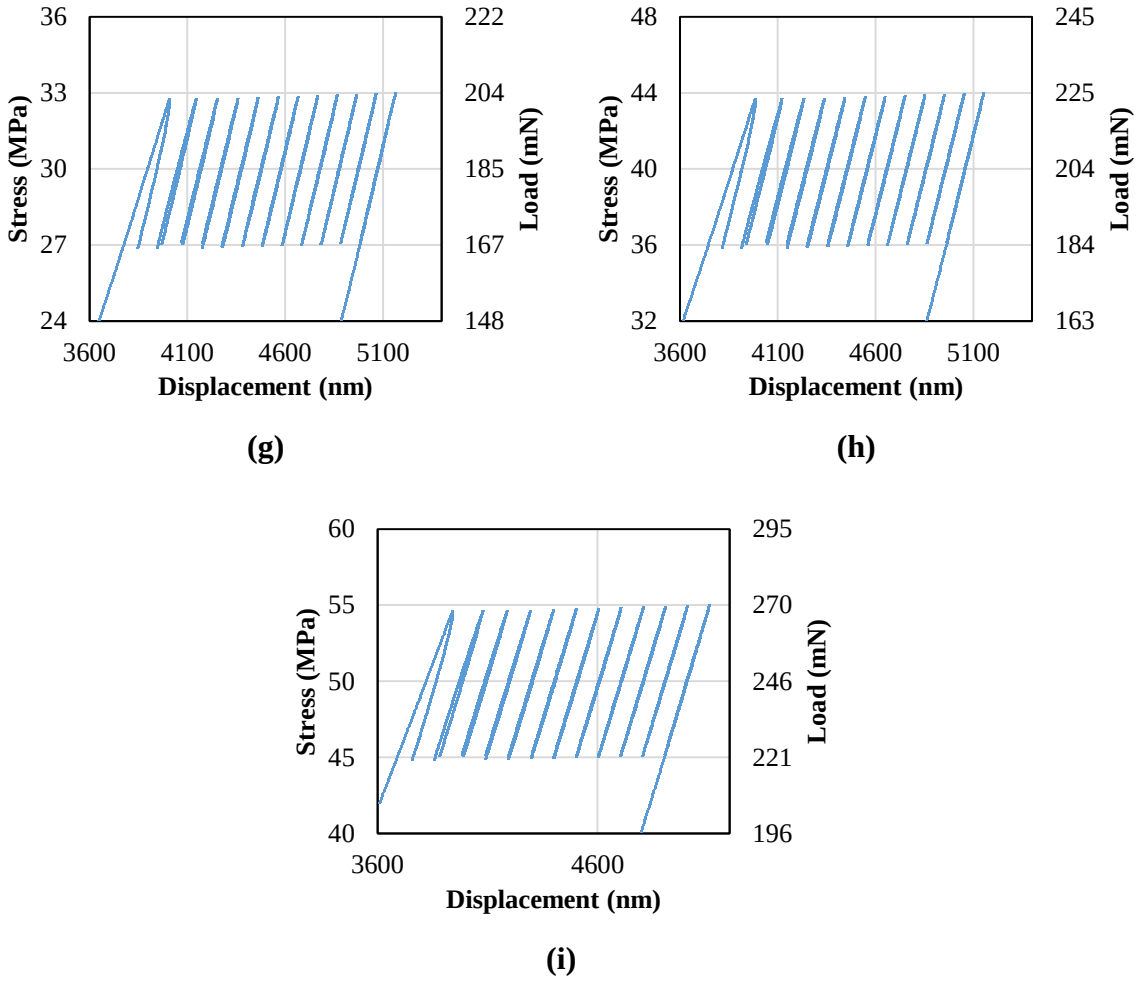

Figure A.6 Detail of cyclic compression of 4-turn Si spring films on unseeded substrate subjected to **(a)** 0.5 MPa, **(b)** 5 MPa, **(c)** 10 MPa, **(d)** 15 MPa, **(e)** 20 MPa, **(f)** 25 MPa, **(g)** 30 MPa, **(h)** 40 MPa, and **(i)** 50 MPa mean stress with an amplitude of 10% of the mean.

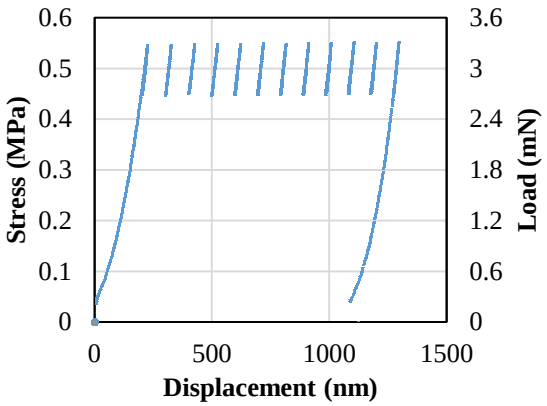

(a)

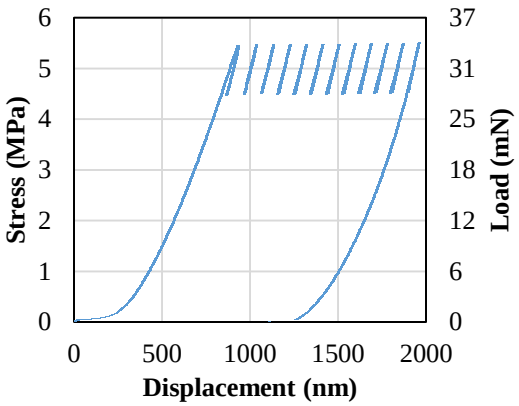

(b)

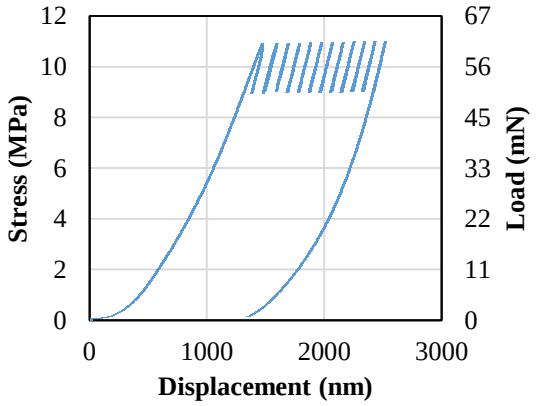

(c)

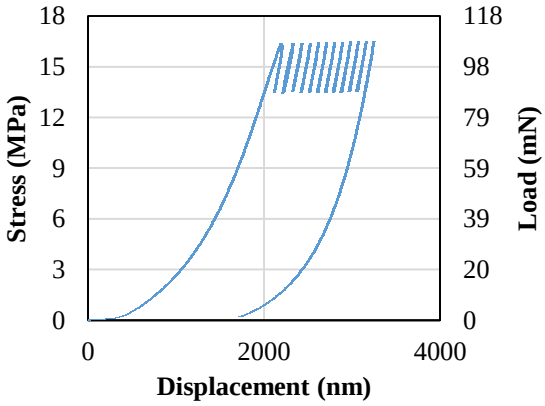

(d)

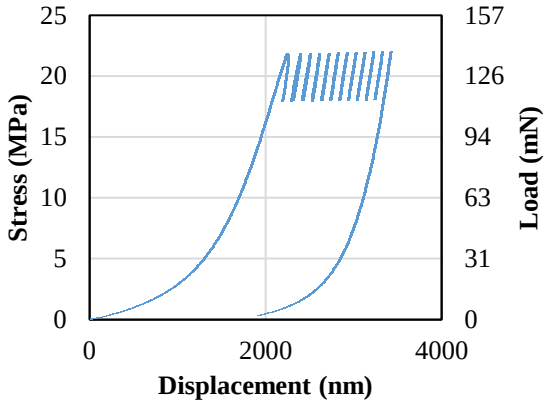

(e)

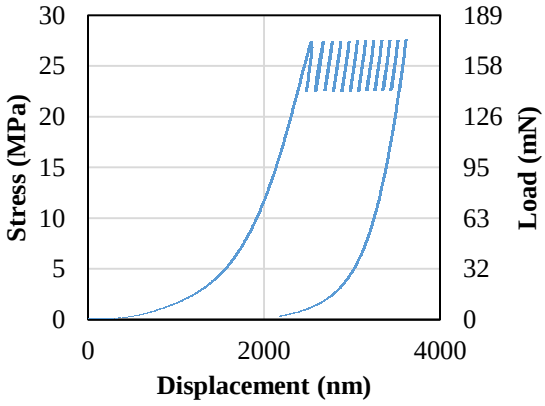

(f)

Figure A.7 (cont.)

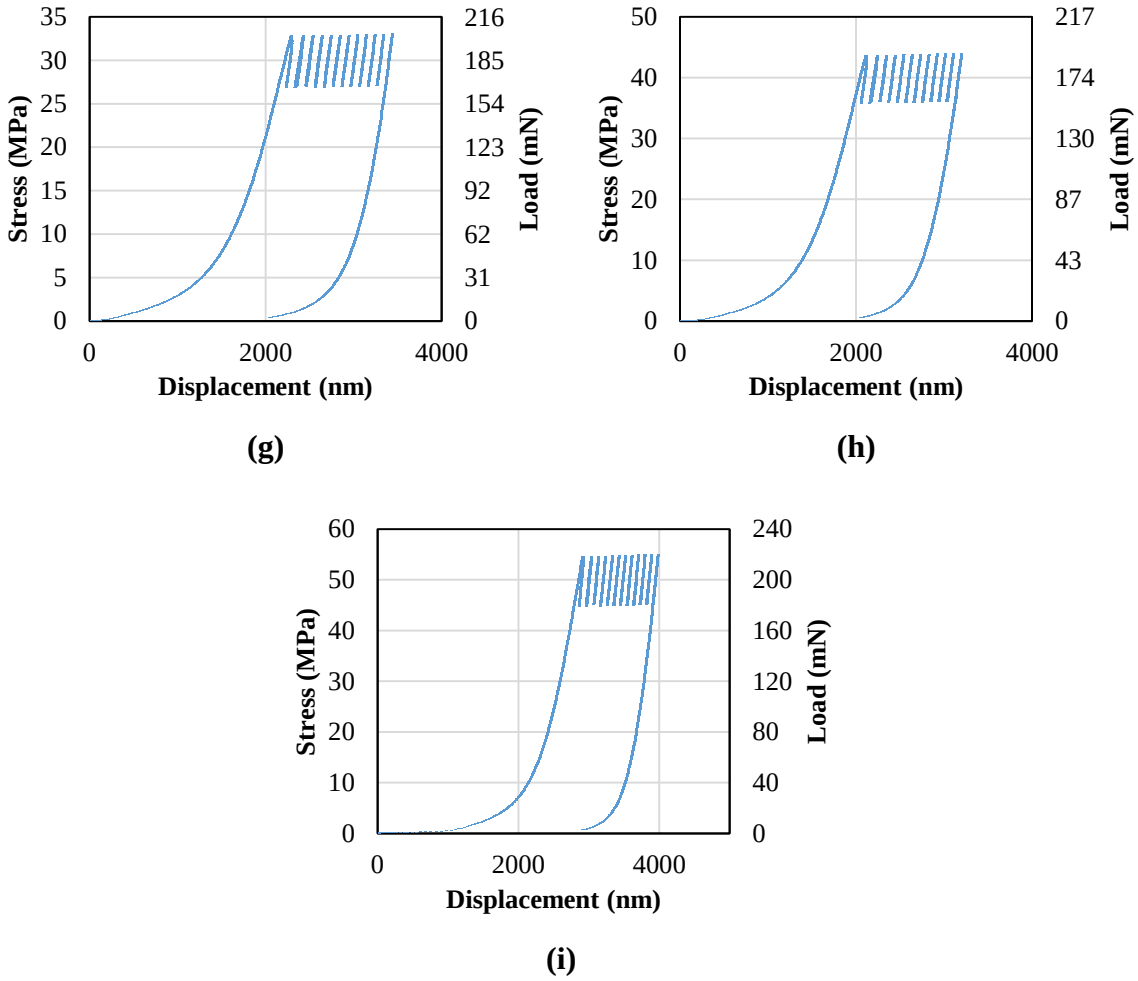

Figure A.7 Cyclic compression of 10-turn Si spring films with 900 nm seed spacing subjected to **(a)** 0.5 MPa, **(b)** 5 MPa, **(c)** 10 MPa, **(d)** 15 MPa, **(e)** 20 MPa, **(f)** 25 MPa, **(g)** 30 MPa, **(h)** 40 MPa, **(i)** 50 MPa mean stress.

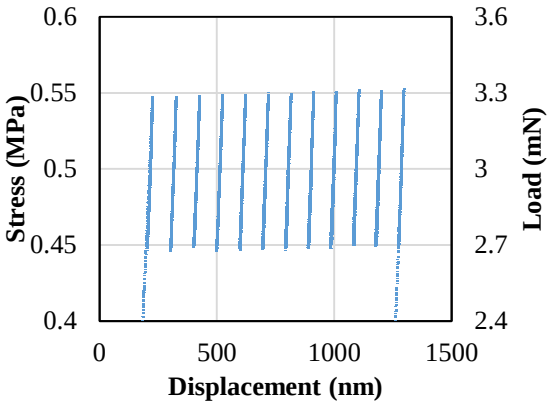

(a)

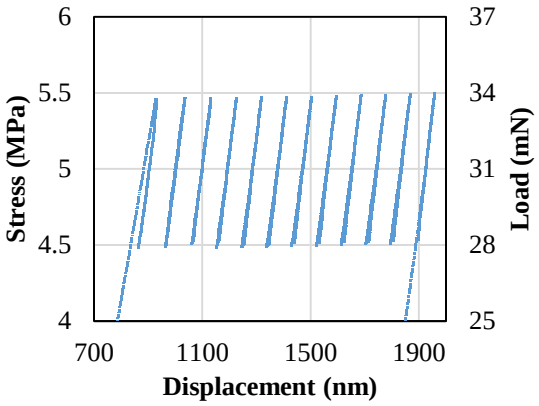

(b)

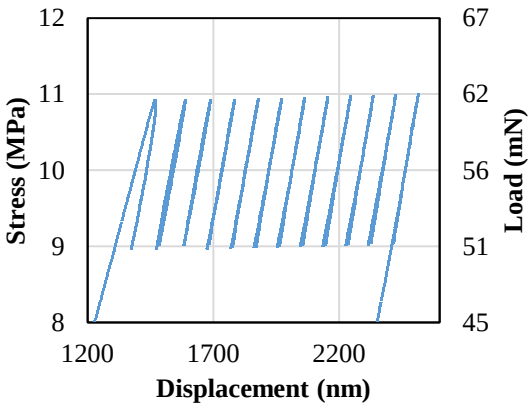

(c)

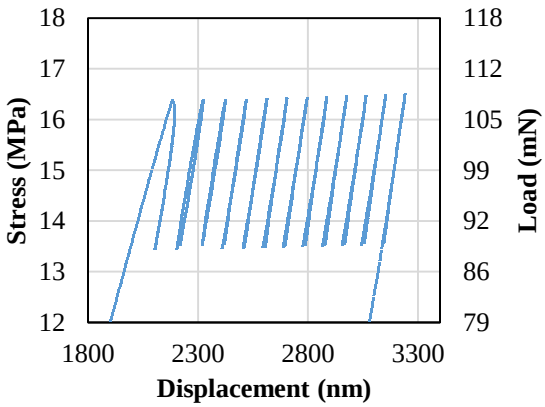

(d)

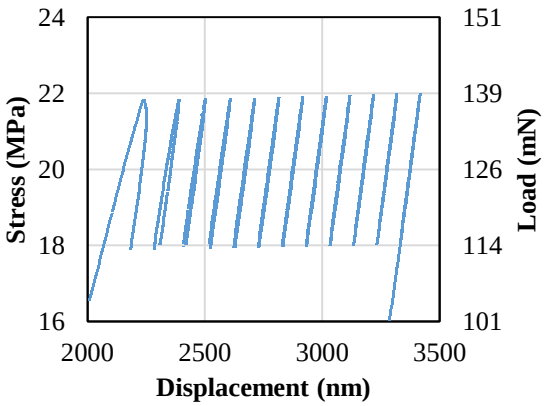

(e)

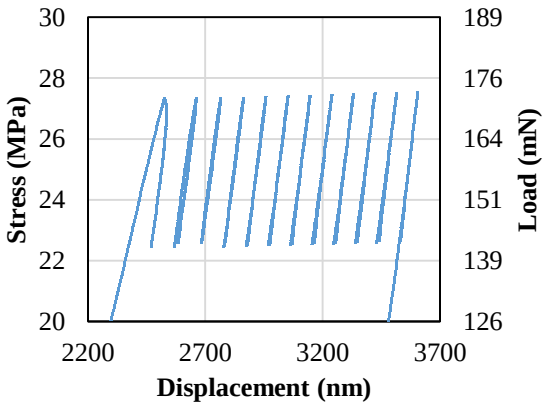

(f)

Figure A.8 (cont.)

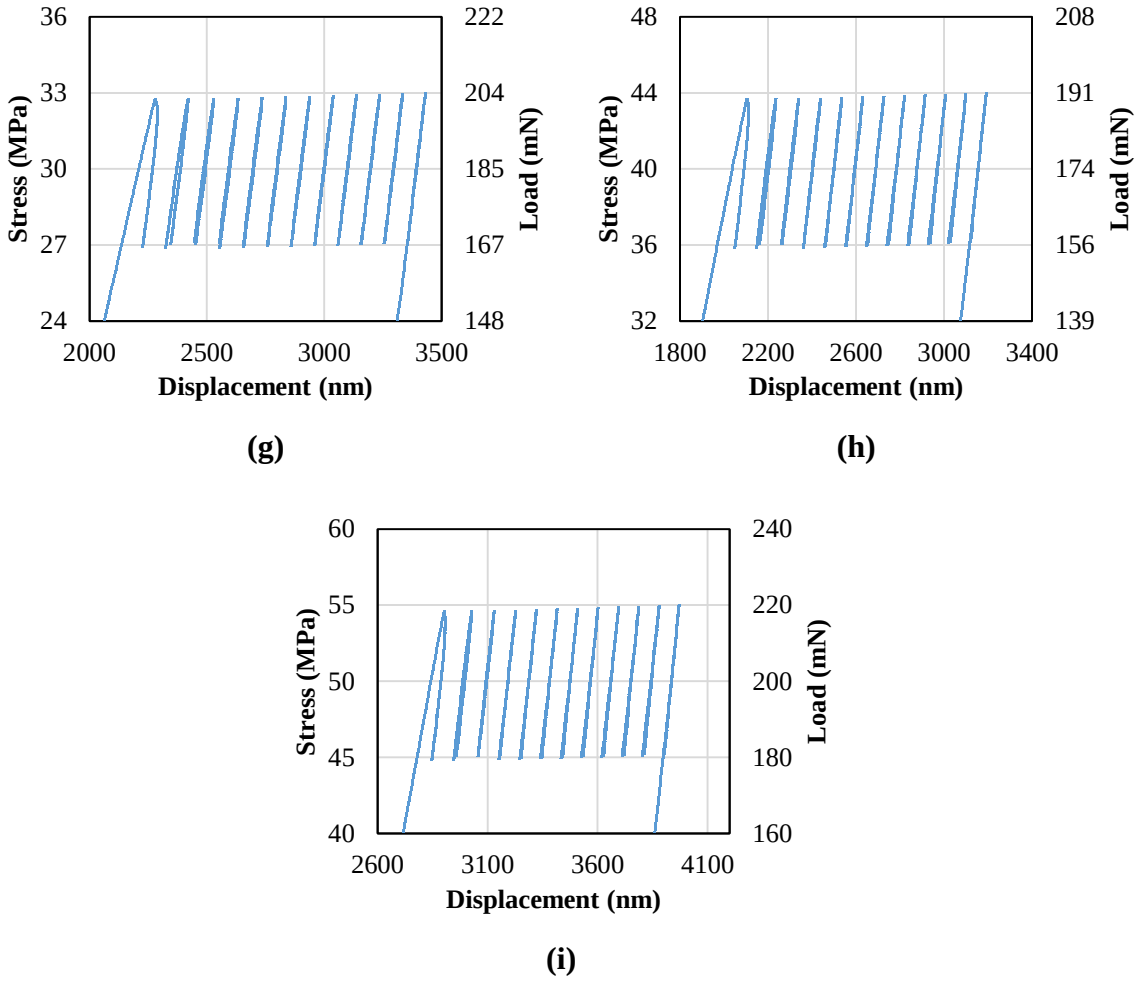

Figure A.8 Detail of cyclic compression of 10-turn Si spring films with 900 seed spacing subjected to **(a)** 0.5 MPa, **(b)** 5 MPa, **(c)** 10 MPa, **(d)** 15 MPa, **(e)** 20 MPa, **(f)** 25 MPa, **(g)** 30 MPa, **(h)** 40 MPa, **(i)** 50 MPa mean stress with an amplitude of 10% of the mean.

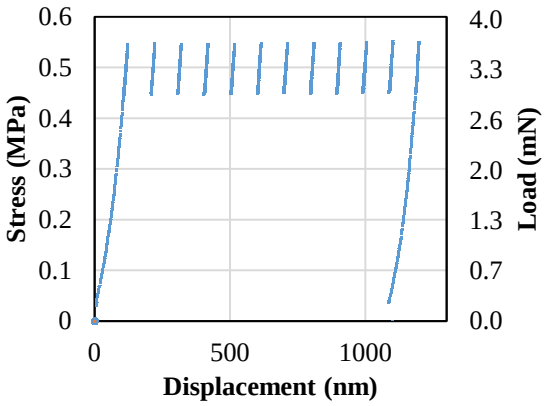

(a)

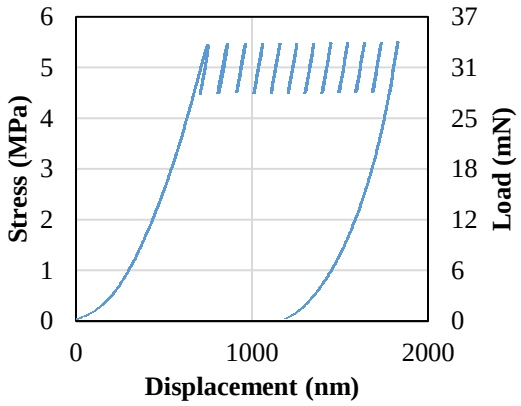

(b)

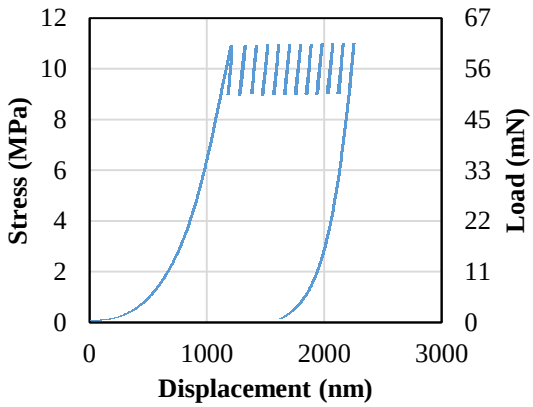

(c)

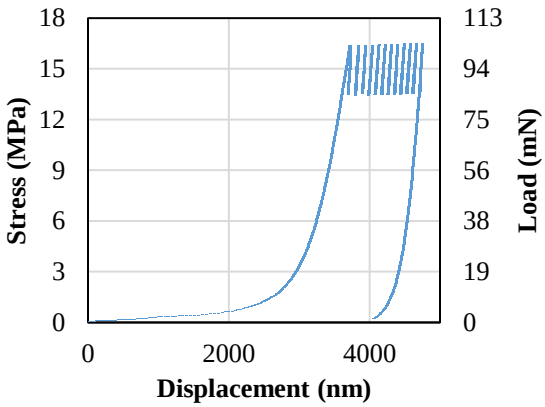

(d)

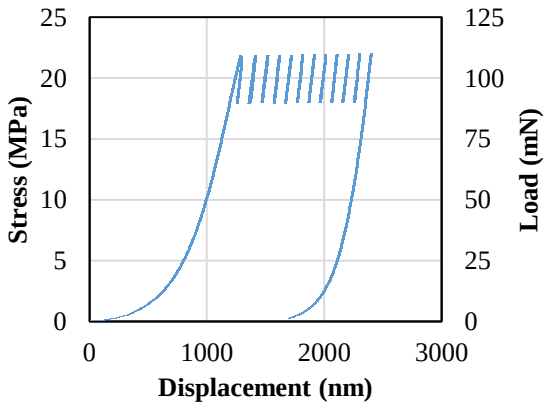

(e)

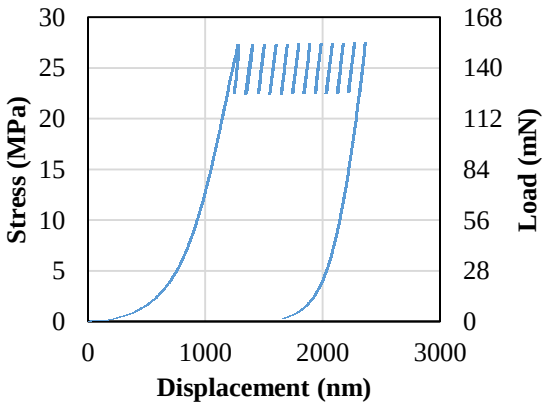

(f)

Figure A.9 (cont.)

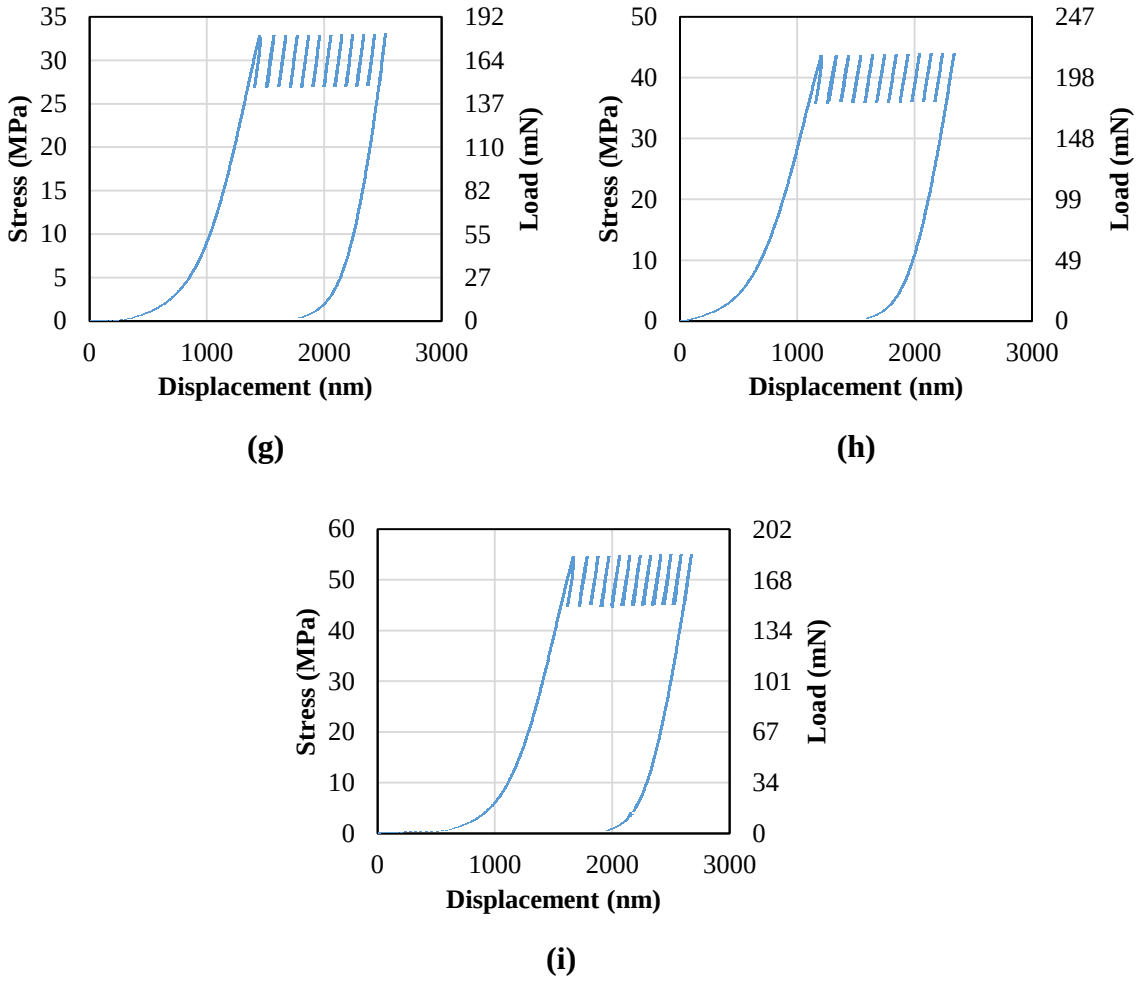

Figure A.9 Cyclic compression of 10-turn Si spring films with 1500 nm seed spacing subjected to **(a)** 0.5 MPa, **(b)** 5 MPa, **(c)** 10 MPa, **(d)** 15 MPa, **(e)** 20 MPa, **(f)** 25 MPa, **(g)** 30 MPa, **(h)** 40 MPa, **(i)** 50 MPa mean stress.

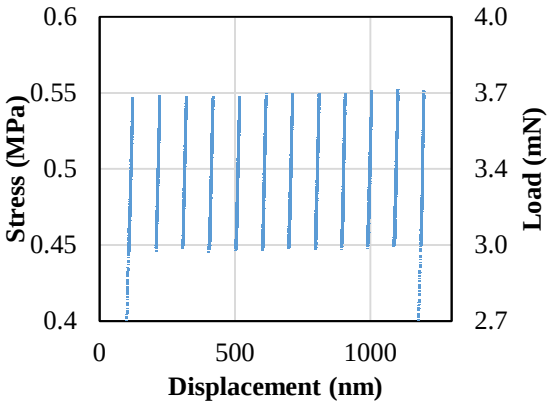

(a)

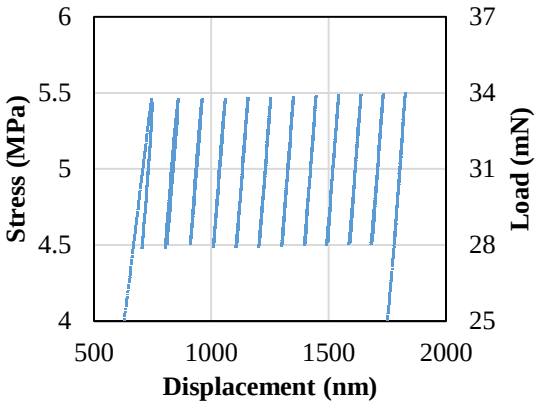

(b)

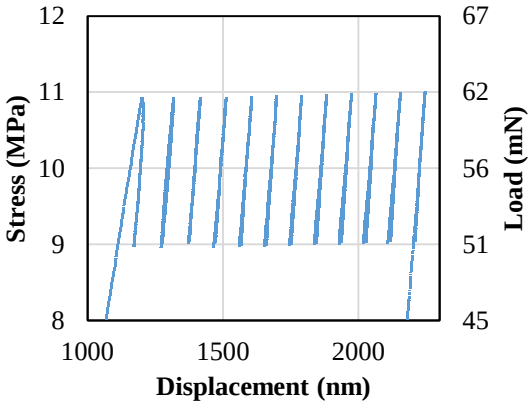

(c)

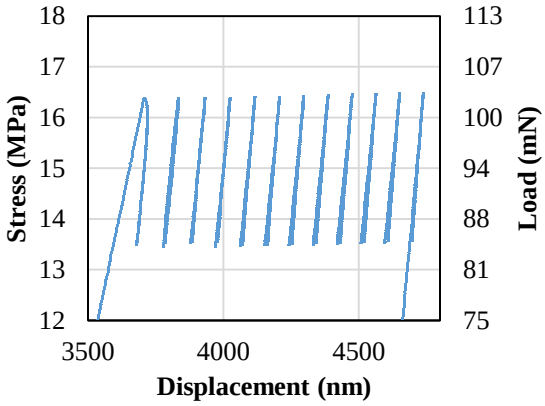

(d)

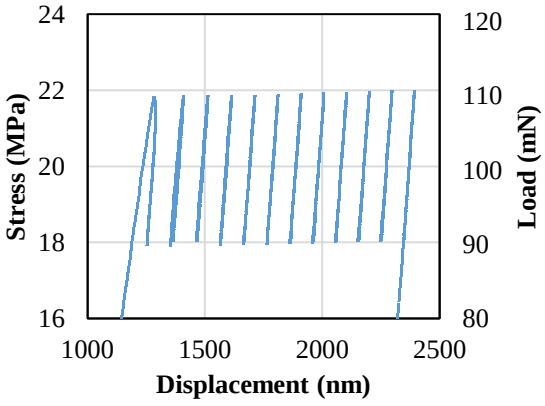

(e)

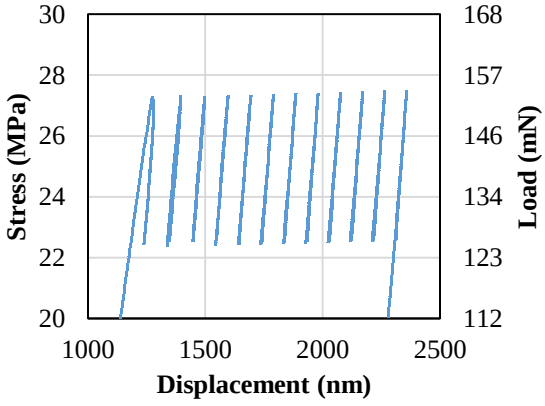

(f)

Figure A.10 (cont.)

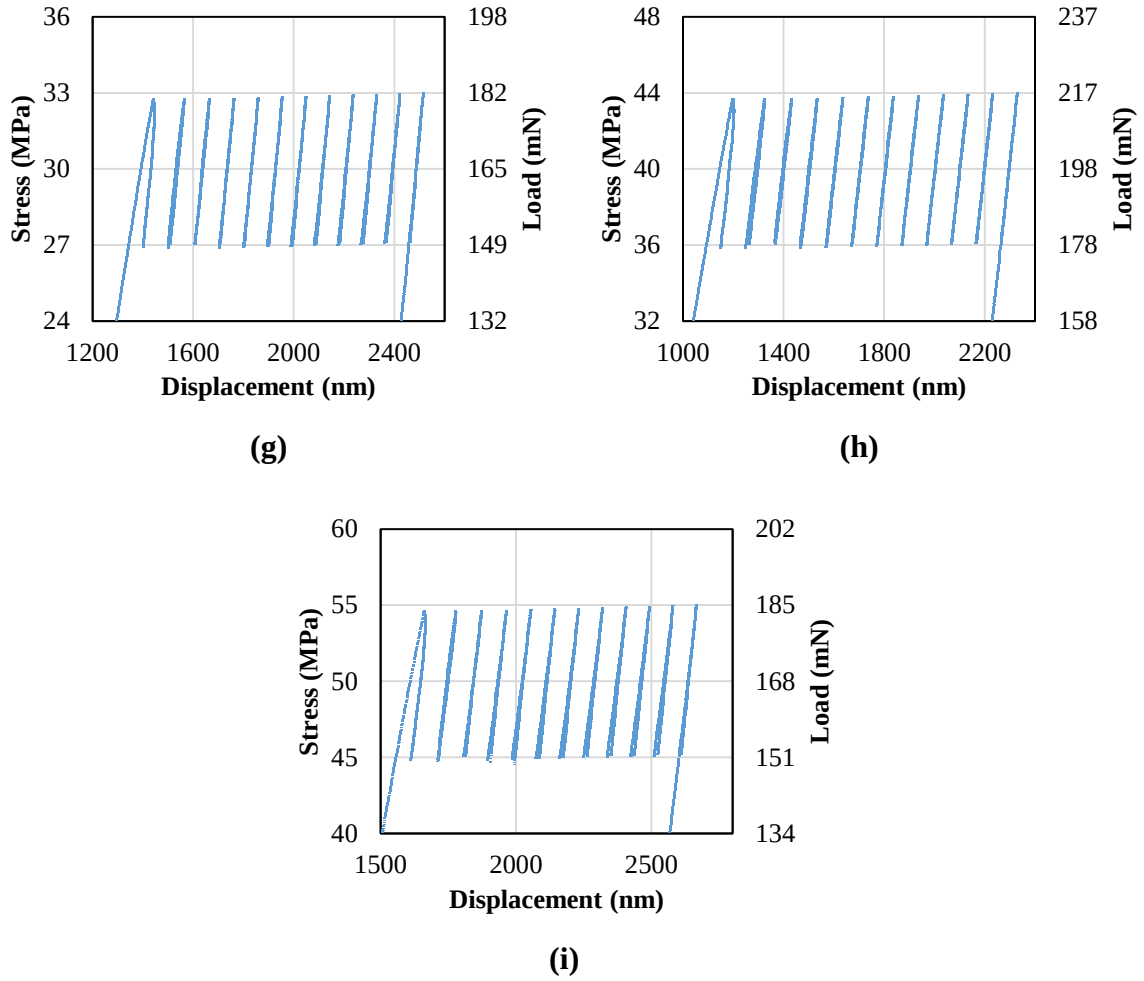

Figure A.10 Detail of cyclic compression of 10-turn Si spring films with 1500 seed spacing subjected to **(a)** 0.5 MPa, **(b)** 5 MPa, **(c)** 10 MPa, **(d)** 15 MPa, **(e)** 20 MPa, **(f)** 25 MPa, **(g)** 30 MPa, **(h)** 40 MPa, **(i)** 50 MPa mean stress with an amplitude of 10% of the mean.

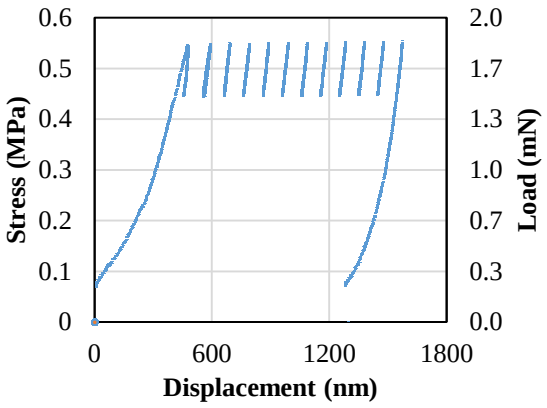

(a)

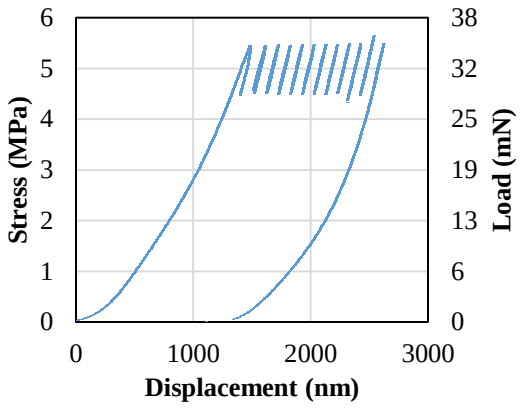

(b)

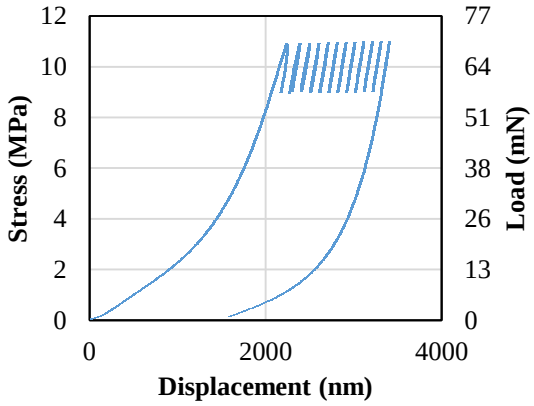

(c)

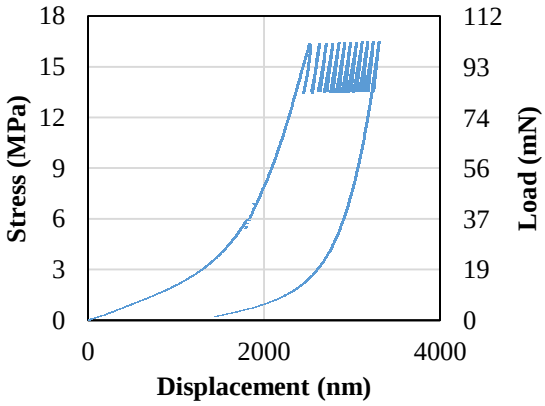

(d)

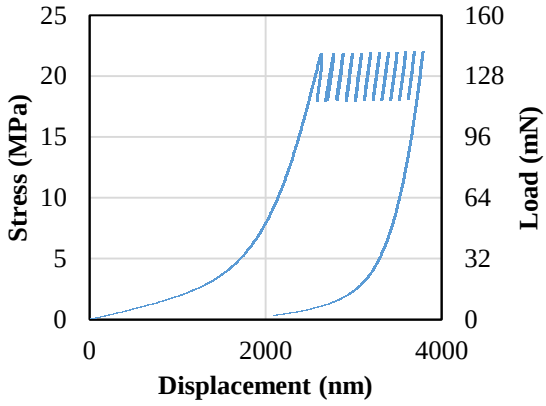

(e)

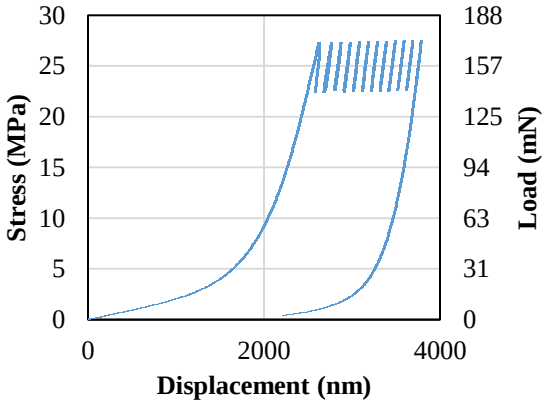

(f)

Figure A.11 (cont.)

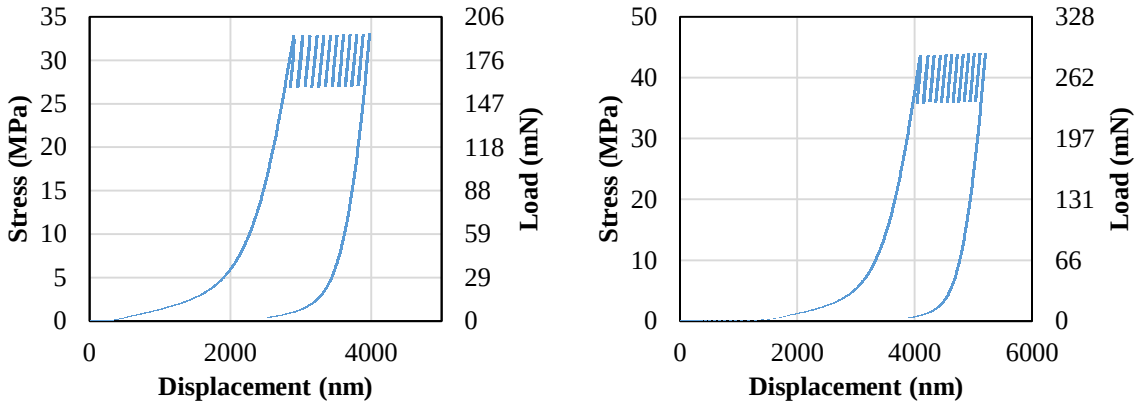

(g)

(h)

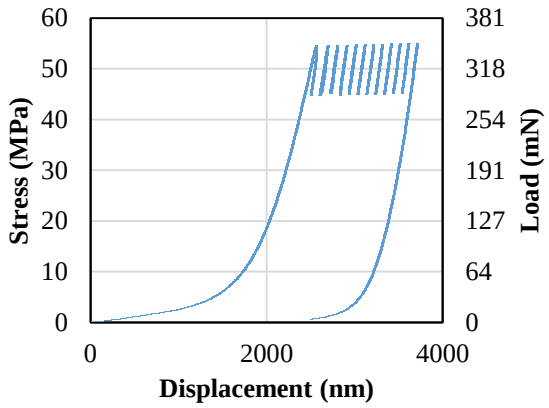

(i)

Figure A.11 Cyclic compression of 10-turn Si spring films on unseeded substrate subjected to **(a)** 0.5 MPa, **(b)** 5 MPa, **(c)** 10 MPa, **(d)** 15 MPa, **(e)** 20 MPa, **(f)** 25 MPa, **(g)** 30 MPa, **(h)** 40 MPa, **(i)** 50 MPa mean stress.

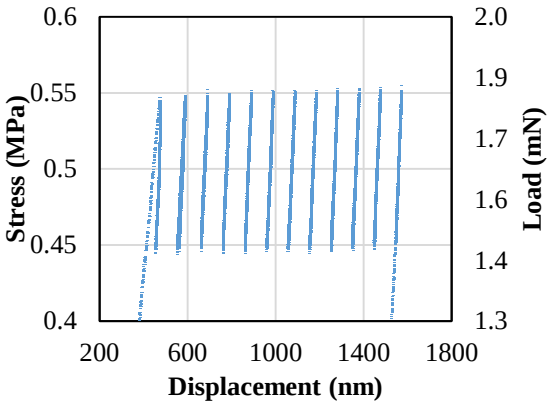

(a)

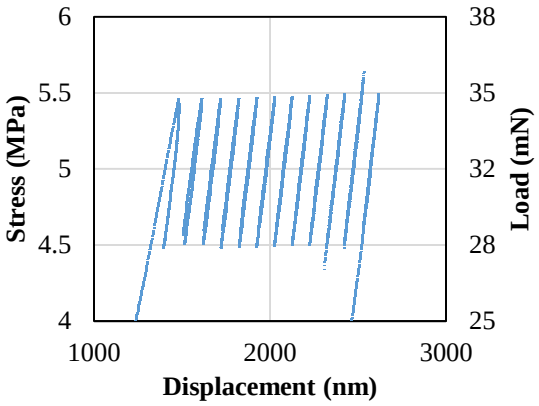

(b)

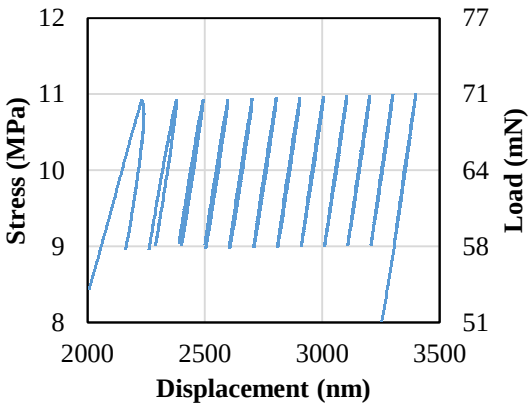

(c)

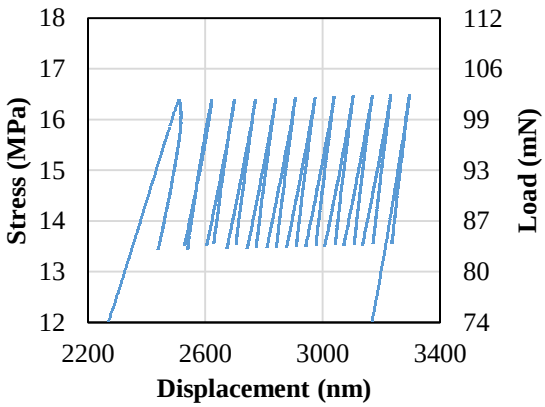

(d)

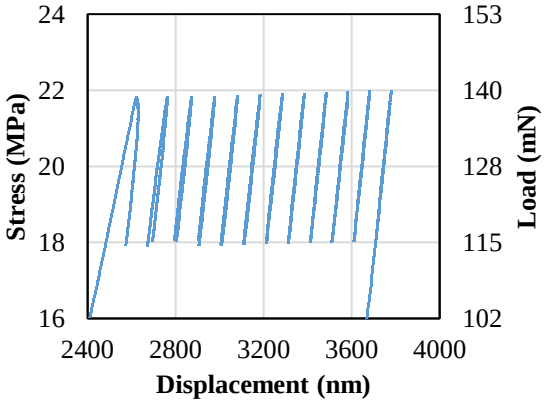

(e)

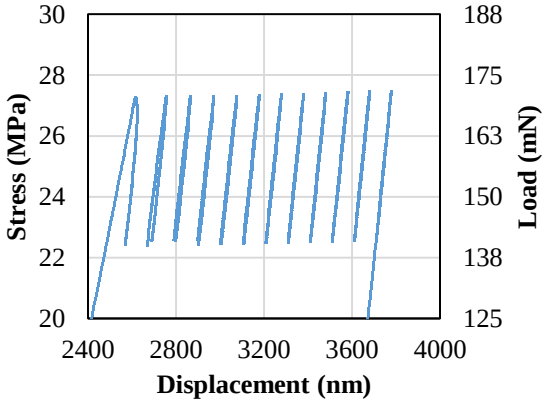

(f)

Figure A.12 (cont.)

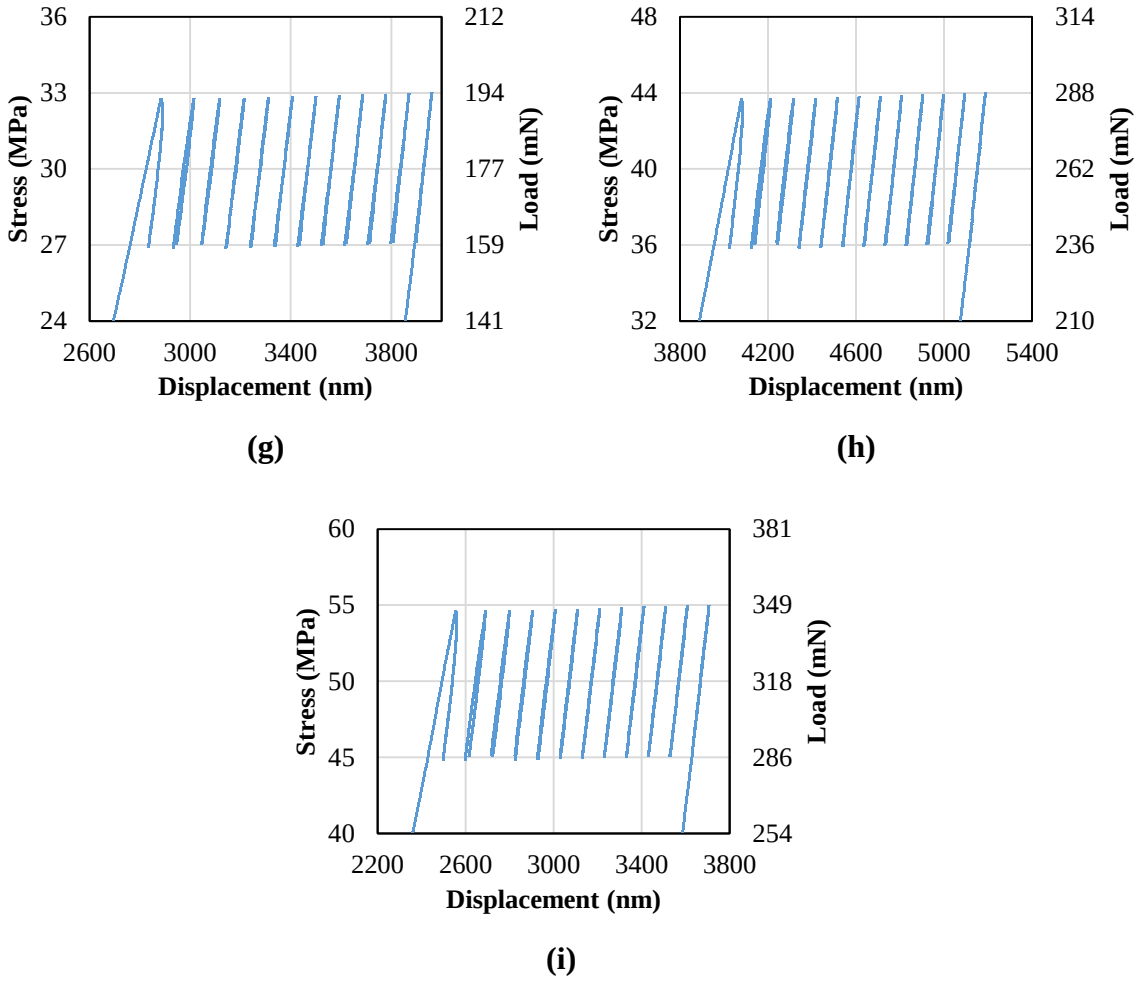

Figure A.12 Detail of cyclic compression of 10-turn Si spring films on unseeded substrate subjected to **(a)** 0.5 MPa, **(b)** 5 MPa, **(c)** 10 MPa, **(d)** 15 MPa, **(e)** 20 MPa, **(f)** 25 MPa, **(g)** 30 MPa, **(h)** 40 MPa, **(i)** 50 MPa mean stress with an amplitude of 10% of the mean.

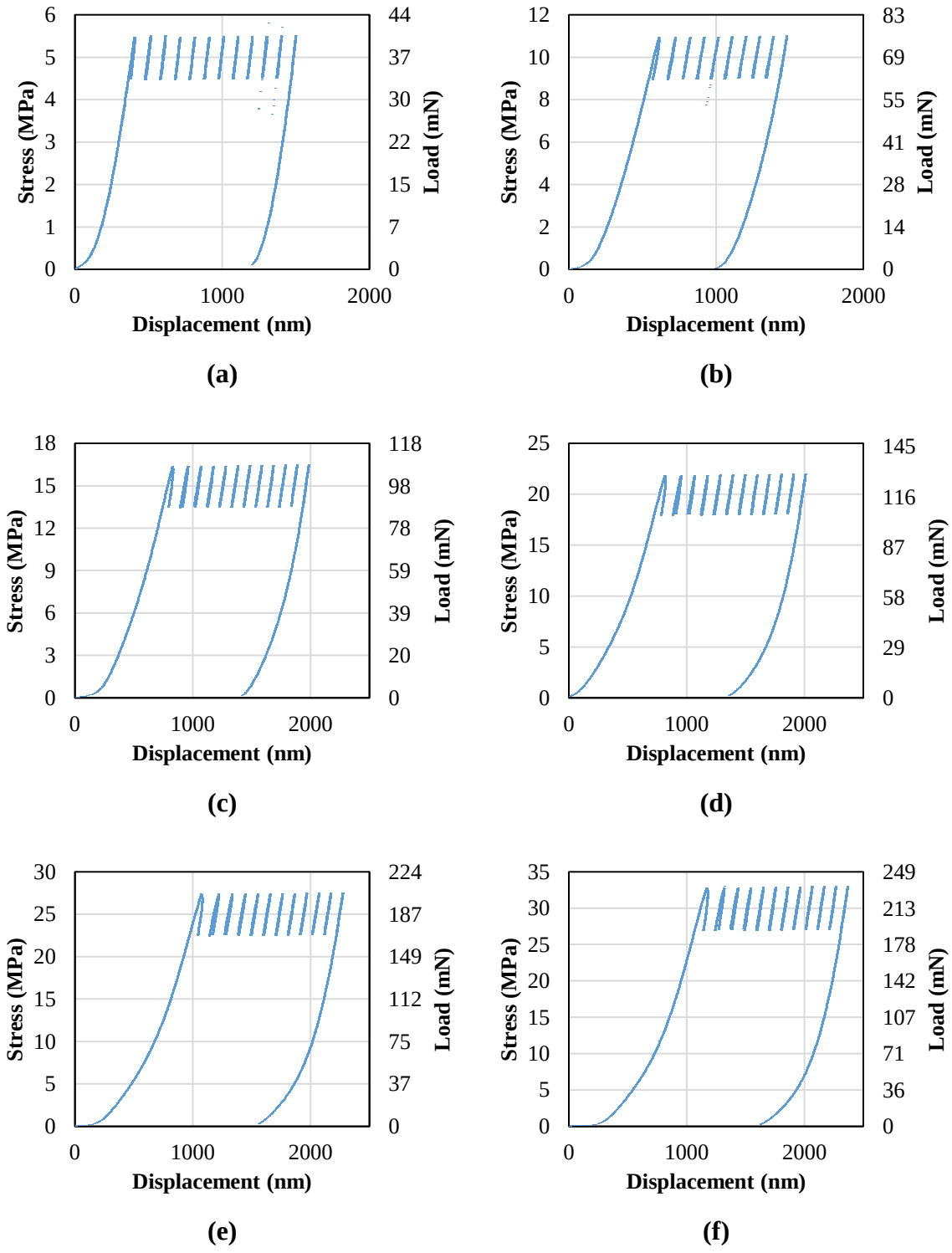

Figure A.13 (cont.)

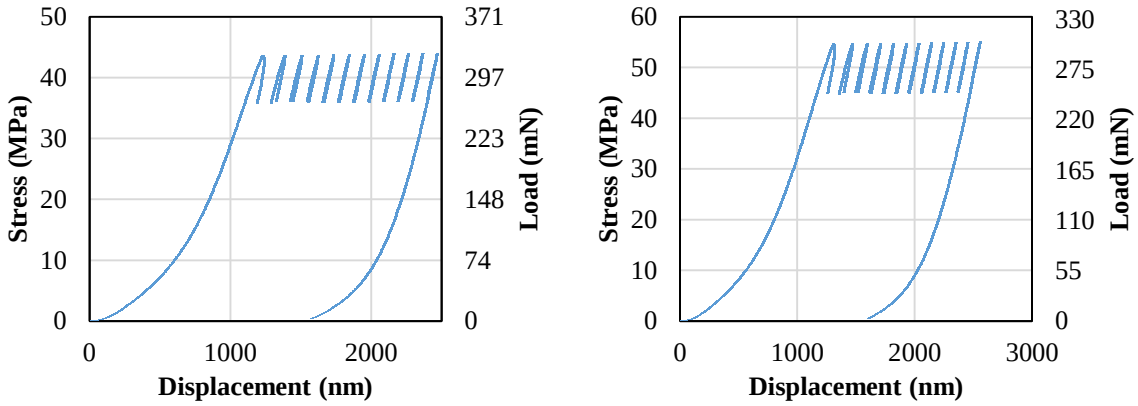

(g) **(h)**

Figure A.13 Cyclic compression of Cu spring films with 2000 nm seed spacing subjected to **(a)** 5 MPa, **(b)** 10 MPa, **(c)** 15 MPa, **(d)** 20 MPa, **(e)** 25 MPa, **(f)** 30 MPa, **(g)** 40 MPa, **(h)** 50 MPa mean stress.

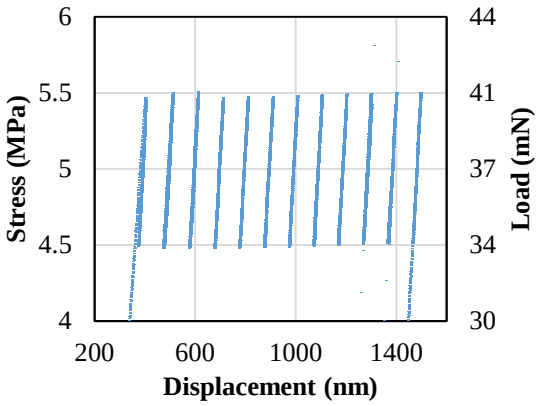

(a)

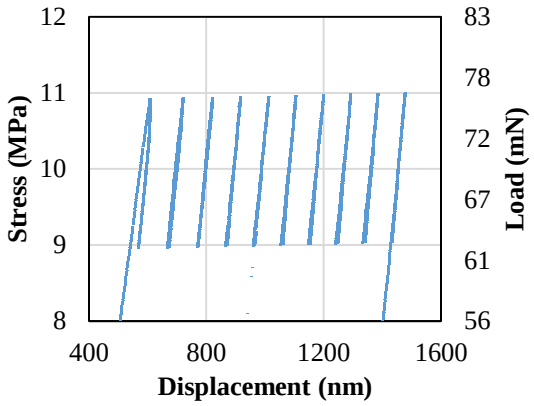

(b)

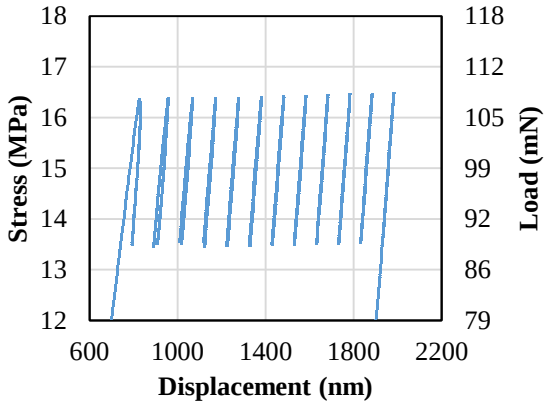

(c)

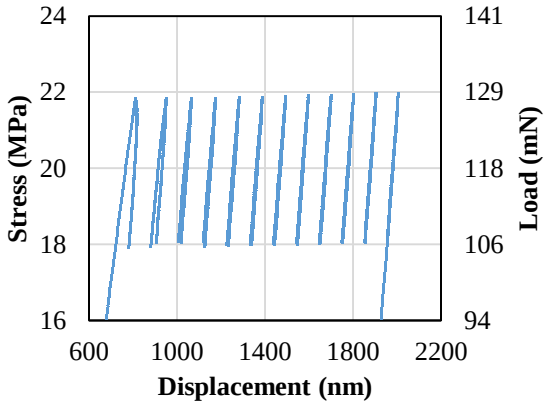

(d)

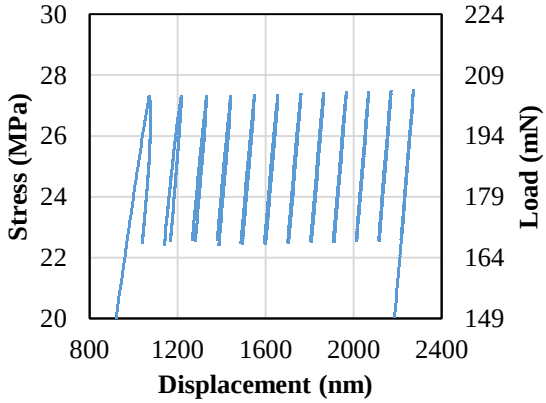

(e)

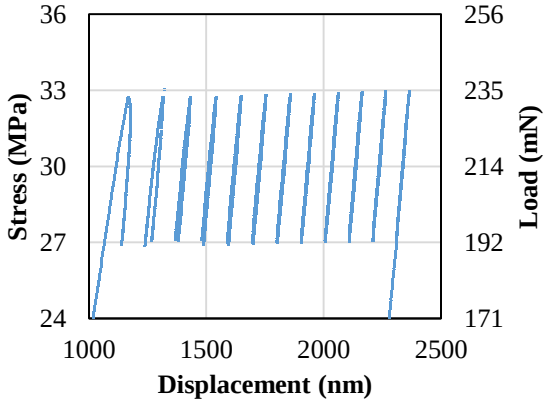

(f)

Figure A.14 (cont.)

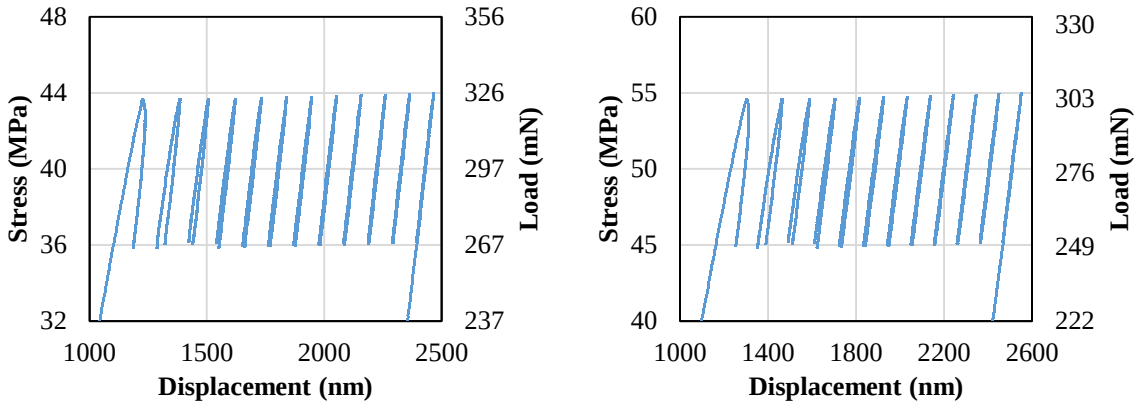

(g) **(h)**

Figure A.14 Detail of cyclic compression of Cu spring films with 2000 nm seed spacing subjected to **(a)** 5 MPa, **(b)** 10 MPa, **(c)** 15 MPa, **(d)** 20 MPa, **(e)** 25 MPa, **(f)** 30 MPa, **(g)** 40 MPa, **(h)** 50 MPa mean stress with an amplitude of 10% of the mean.

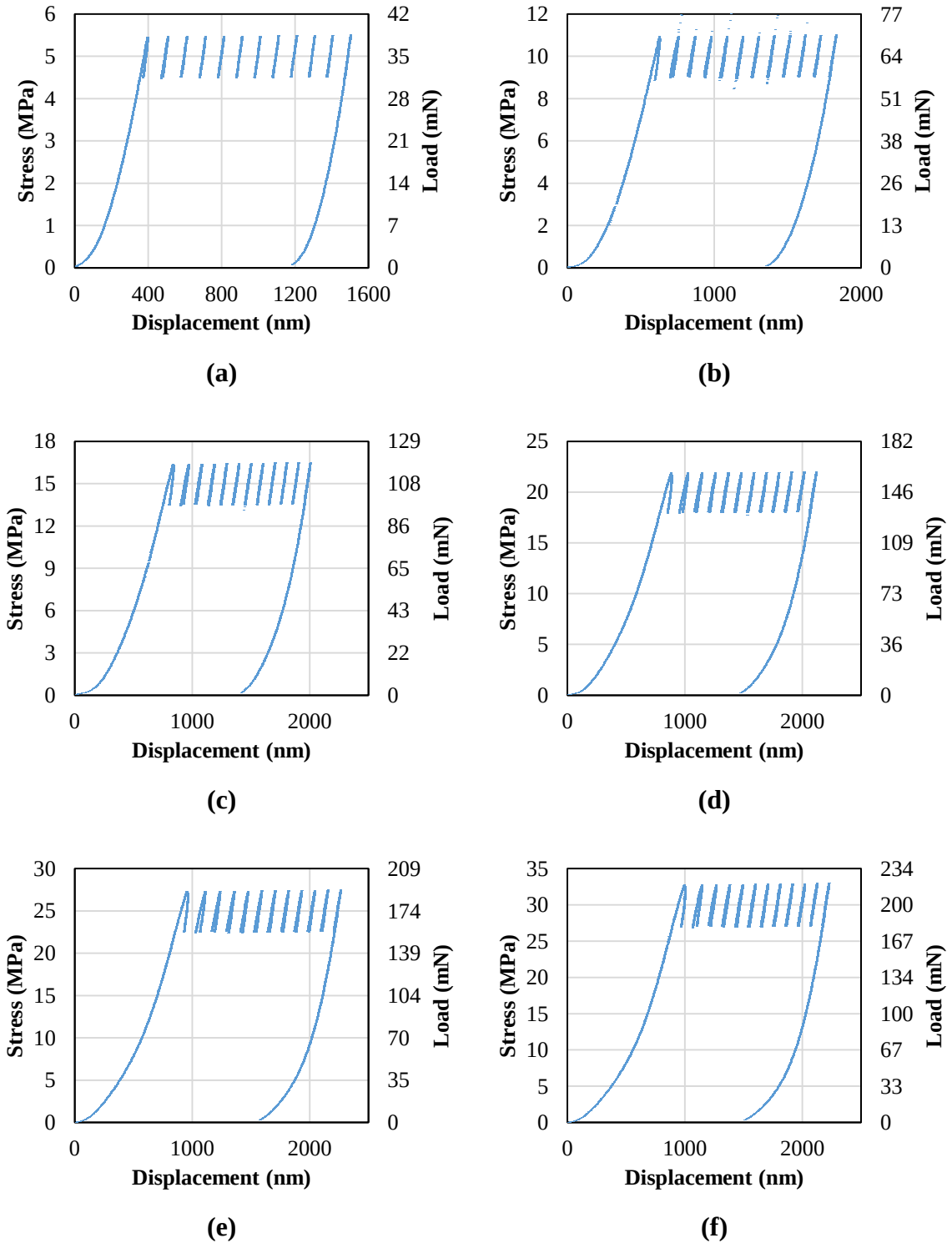

Figure A.15 (cont.)

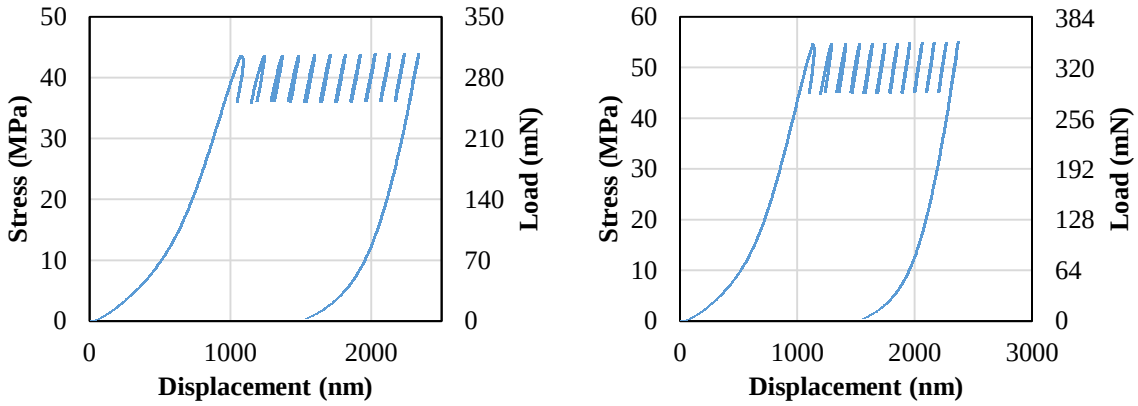

(g) **(h)**

Figure A.15 Cyclic compression of Cu spring films with 2400 nm seed spacing subjected to **(a)** 5 MPa, **(b)** 10 MPa, **(c)** 15 MPa, **(d)** 20 MPa, **(e)** 25 MPa, **(f)** 30 MPa, **(g)** 40 MPa, and **(h)** 50 MPa mean stress.

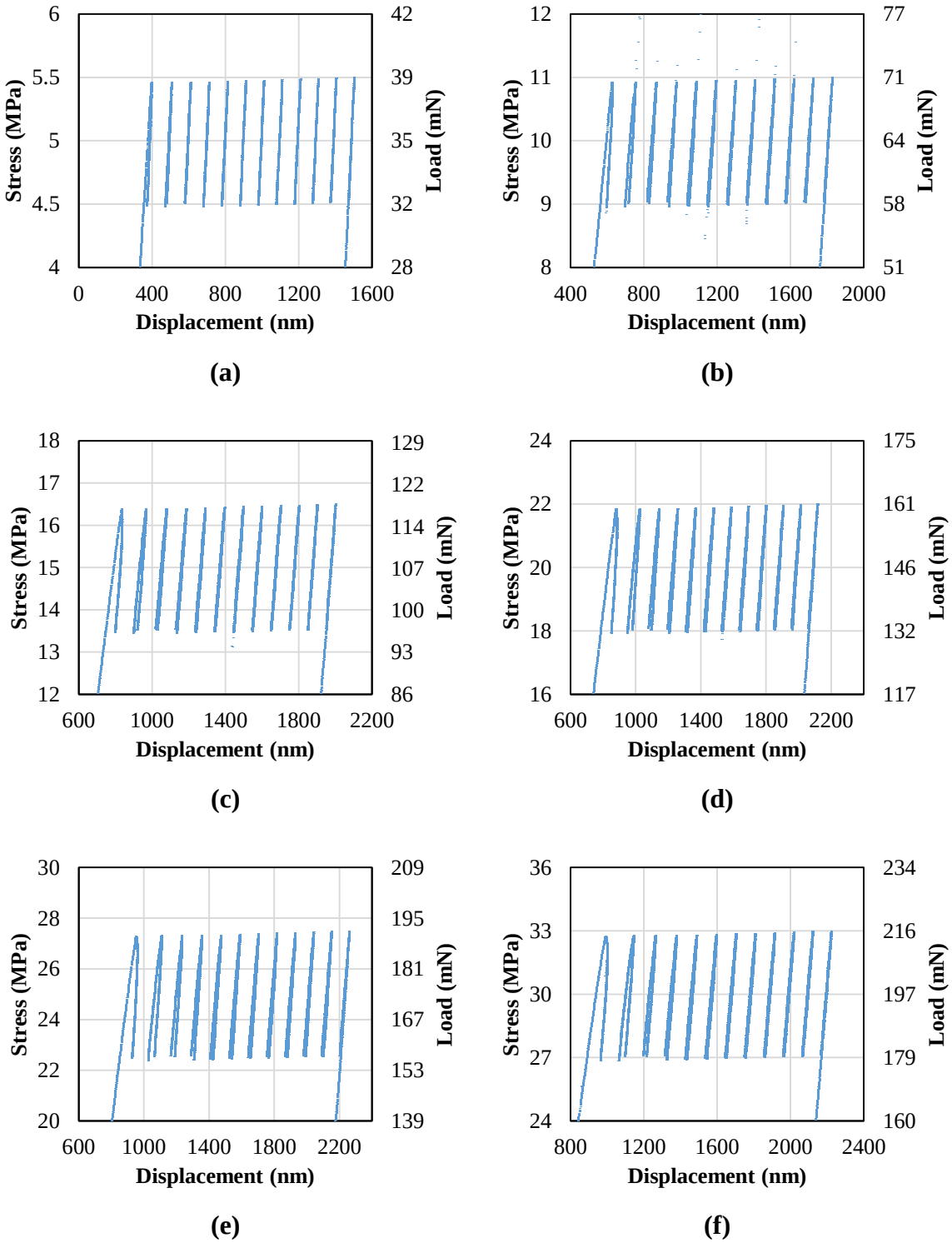

Figure A.16 (cont.)

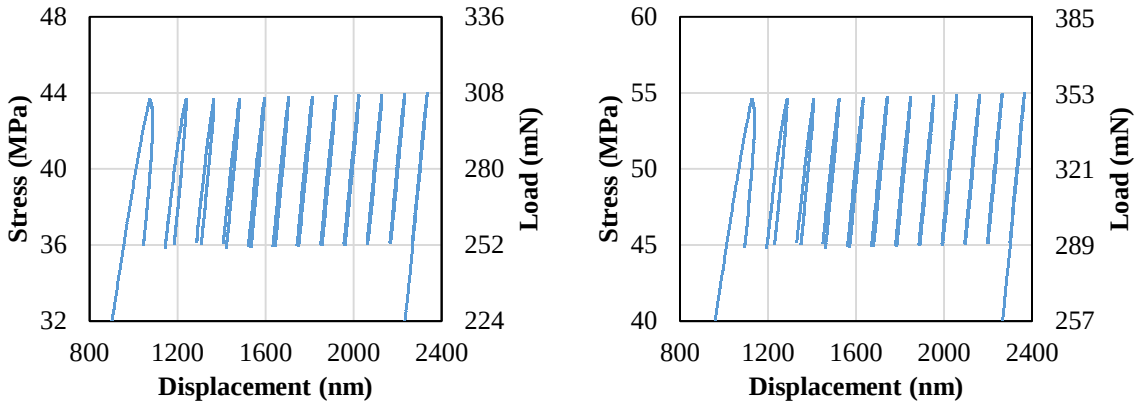

(g) **(h)**

Figure A.16 Detail of cyclic compression of Cu spring films with 2400 nm seed spacing subjected to **(a)** 5 MPa, **(b)** 10 MPa, **(c)** 15 MPa, **(d)** 20 MPa, **(e)** 25 MPa, **(f)** 30 MPa, **(g)** 40 MPa, **(h)** 50 MPa mean stress with an amplitude of 10% of the mean.

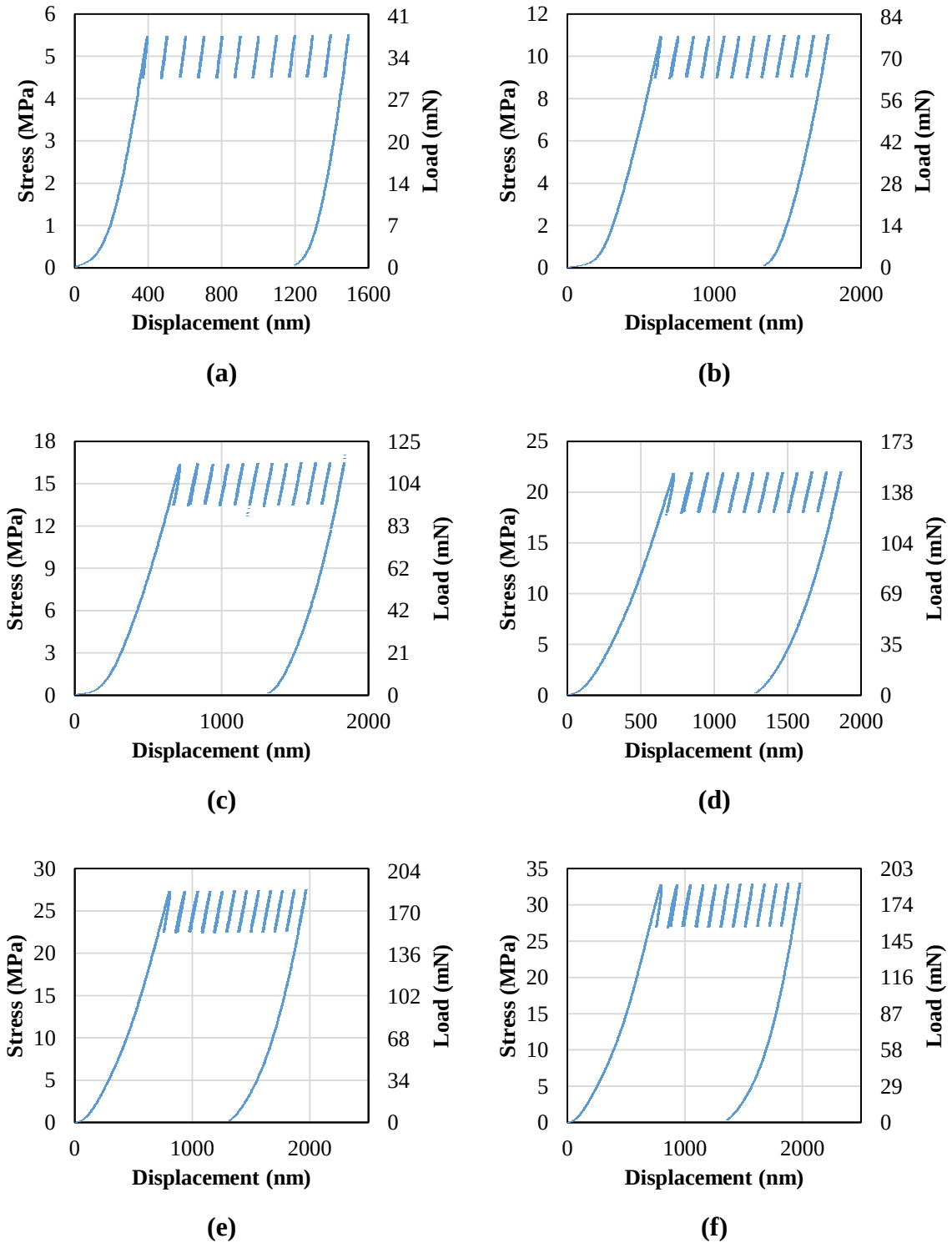

Figure A.17 (cont.)

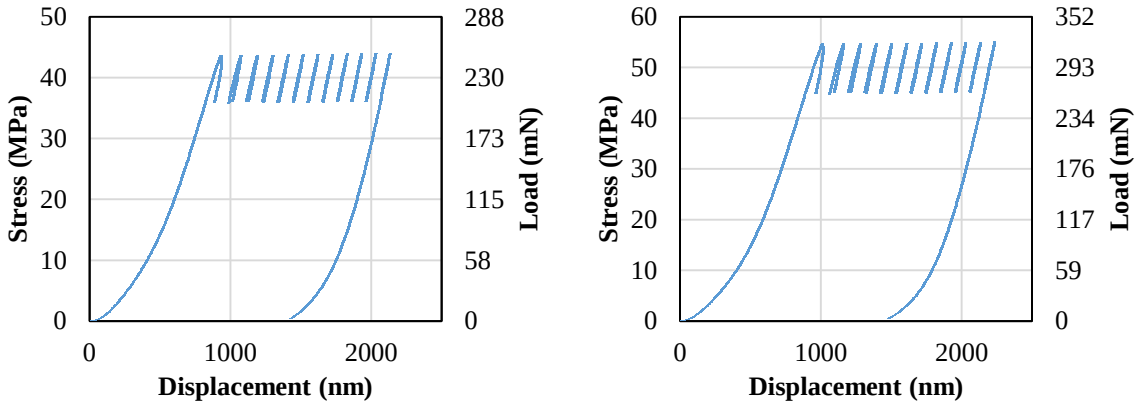

(g) **(h)**

Figure A.17 Cyclic compression of Cu spring films with 2800 nm seed spacing subjected to **(a)** 5 MPa, **(b)** 10 MPa, **(c)** 15 MPa, **(d)** 20 MPa, **(e)** 25 MPa, **(f)** 30 MPa, **(g)** 40 MPa, **(h)** 50 MPa mean stress.

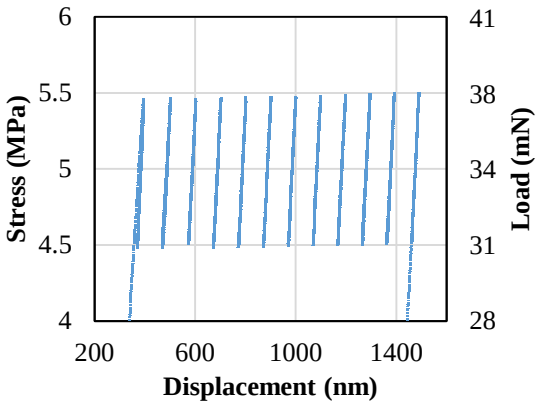

(a)

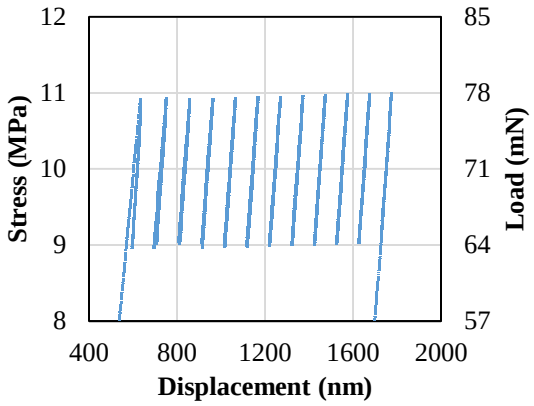

(b)

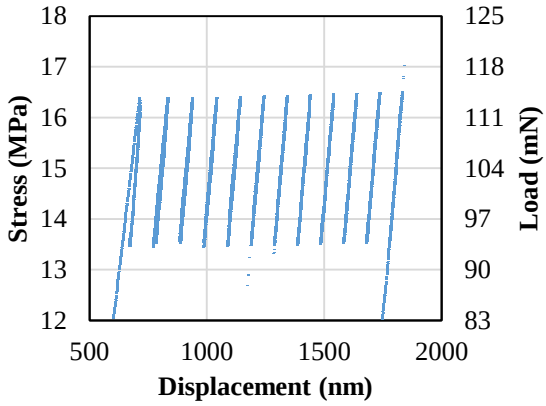

(c)

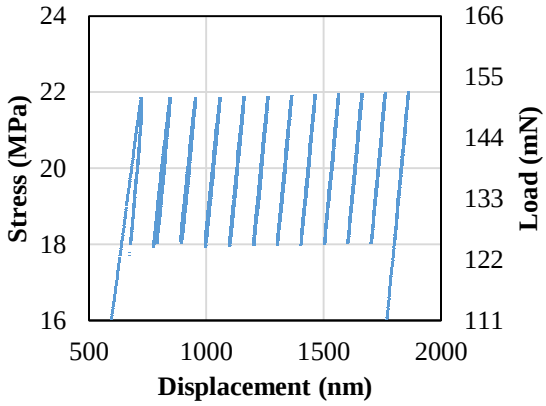

(d)

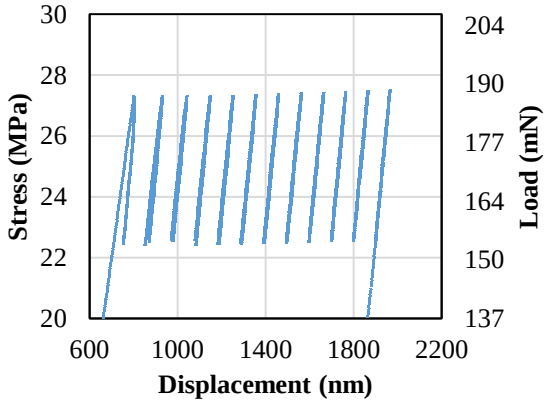

(e)

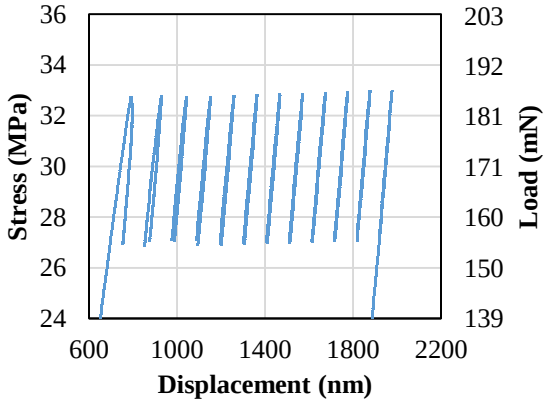

(f)

Figure A.18 (cont.)

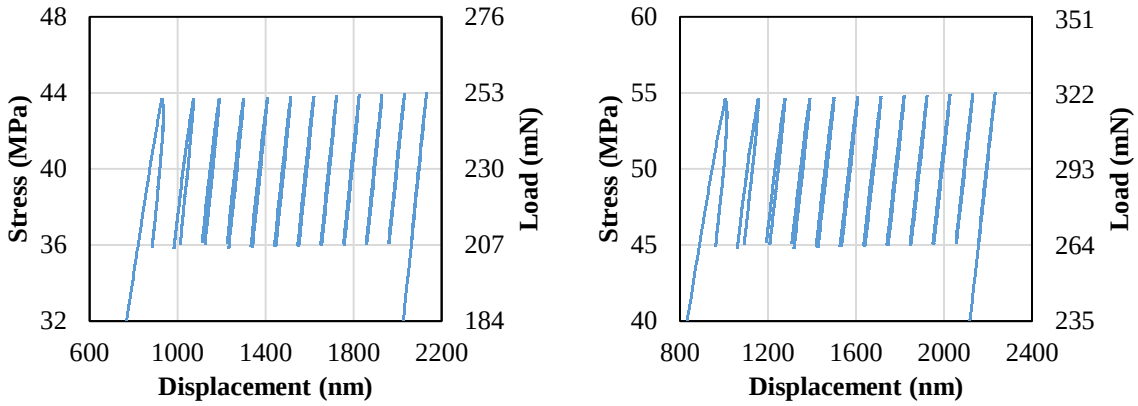

Figure A.18 Detail of cyclic compression of Cu spring films with 2800 nm seed spacing subjected to **(a)** 5 MPa, **(b)** 10 MPa, **(c)** 15 MPa, **(d)** 20 MPa, **(e)** 25 MPa, **(f)** 30 MPa, **(g)** 40 MPa, **(h)** 50 MPa mean stress with an amplitude of 10% of the mean.

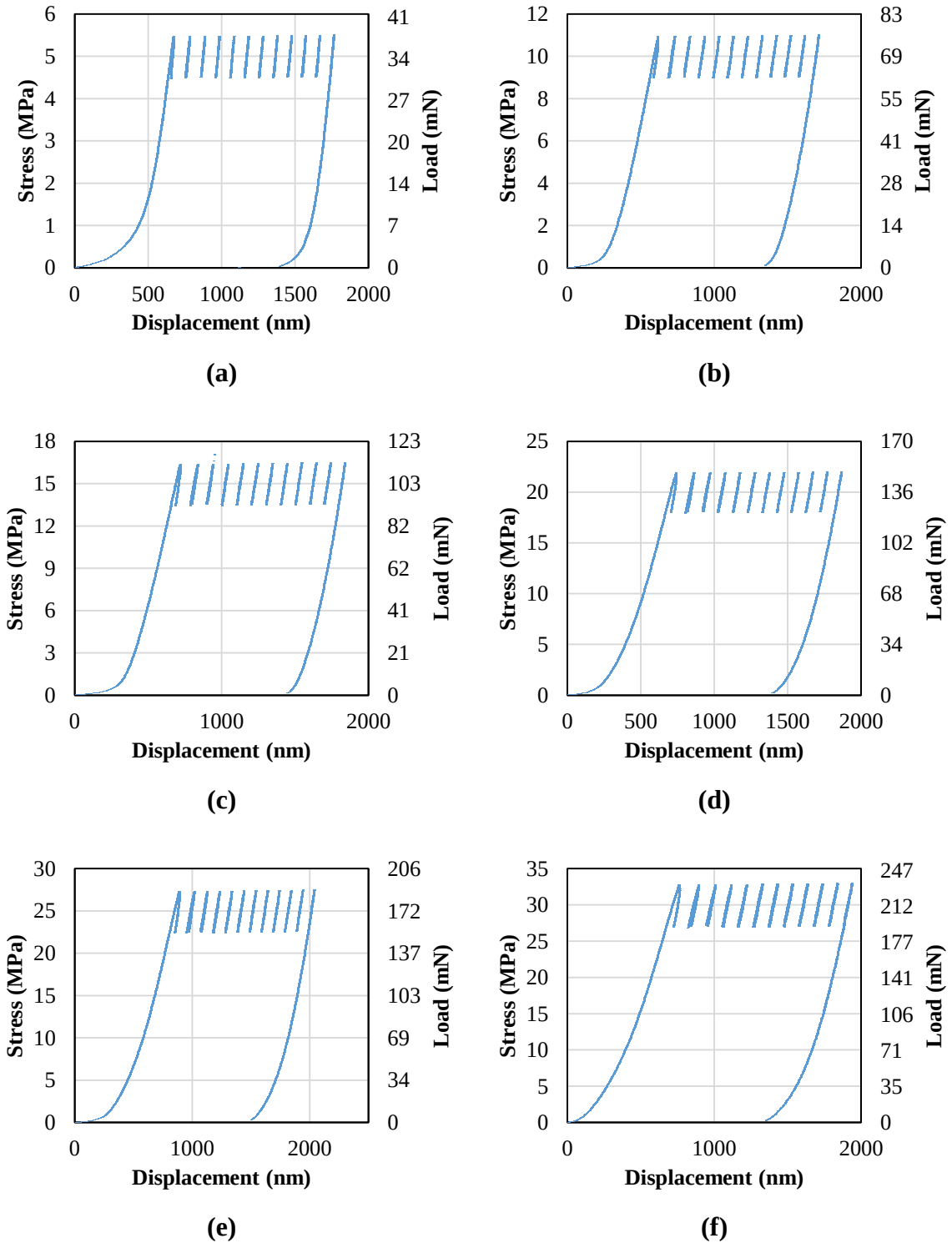

Figure A.19 (cont.)

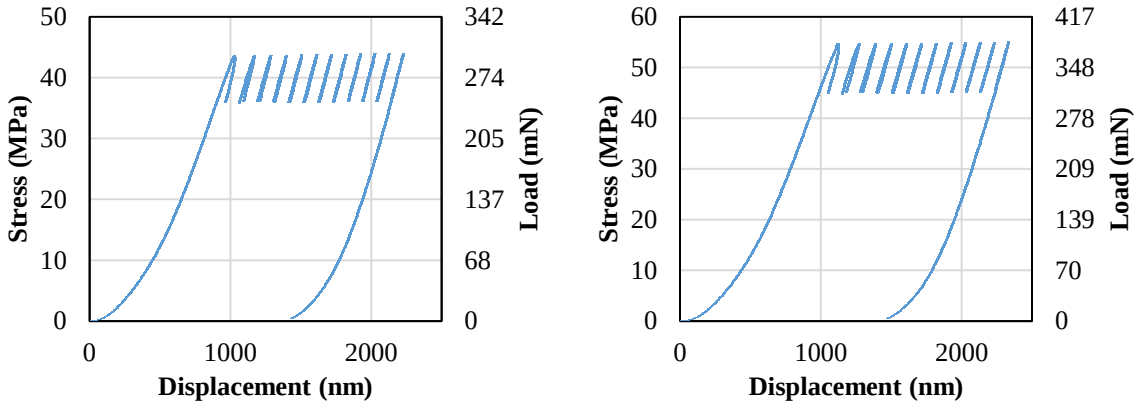

Figure A.19 Cyclic compression of Cu spring films with 3200 nm seed spacing subjected to **(a)** 5 MPa, **(b)** 10 MPa, **(c)** 15 MPa, **(d)** 20 MPa, **(e)** 25 MPa, **(f)** 30 MPa, **(g)** 40 MPa, **(h)** 50 MPa mean stress.

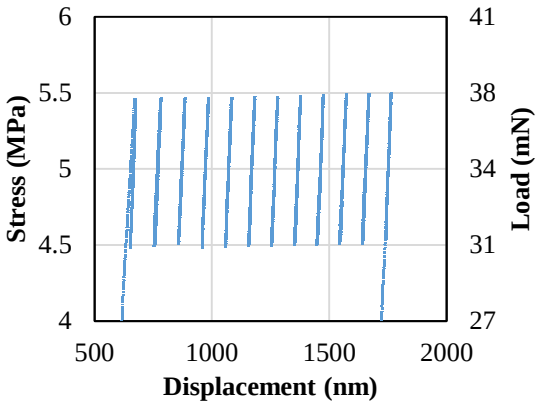

(a)

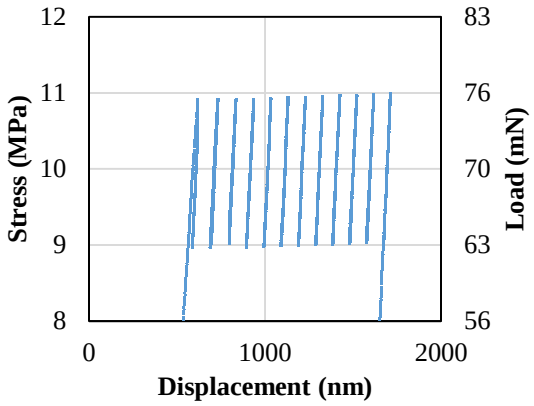

(b)

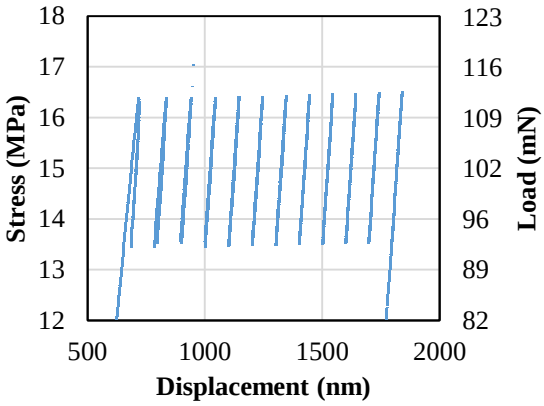

(c)

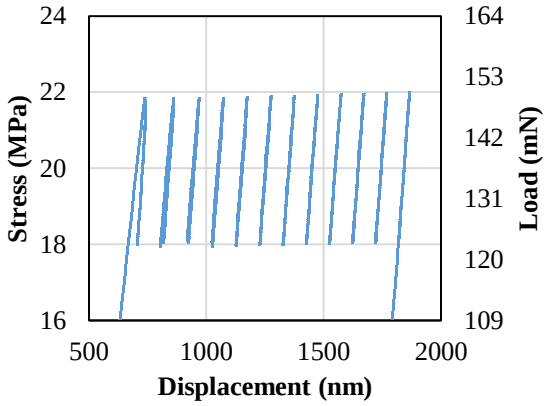

(d)

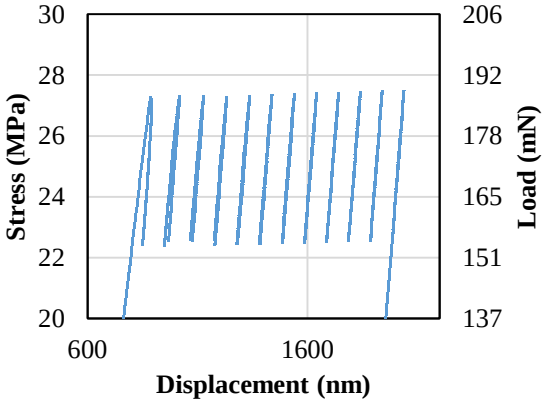

(e)

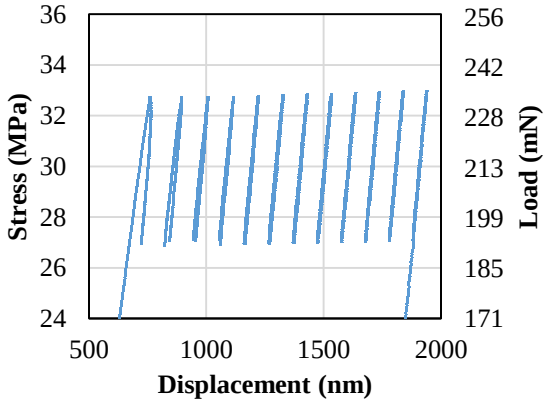

(f)

Figure A.20 (cont.)

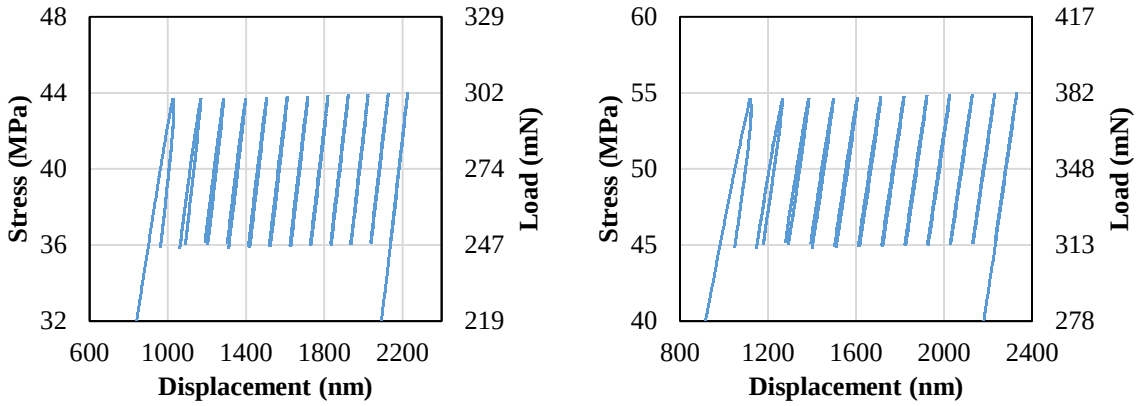

(g) **(h)**

Figure A.20 Detail of cyclic compression of Cu spring films with 3200 nm seed spacing subjected to **(a)** 5 MPa, **(b)** 10 MPa, **(c)** 15 MPa, **(d)** 20 MPa, **(e)** 25 MPa, **(f)** 30 MPa, **(g)** 40 MPa, **(h)** 50 MPa mean stress with an amplitude of 10% of the mean.

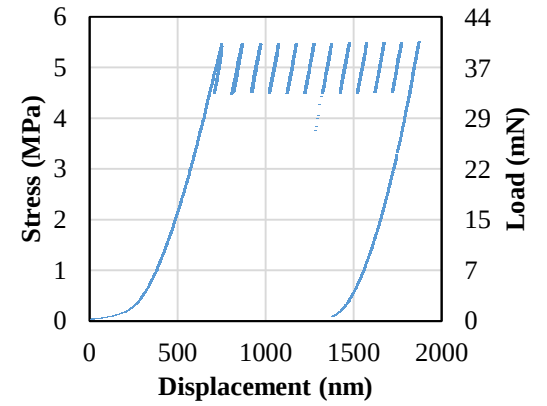

(a)

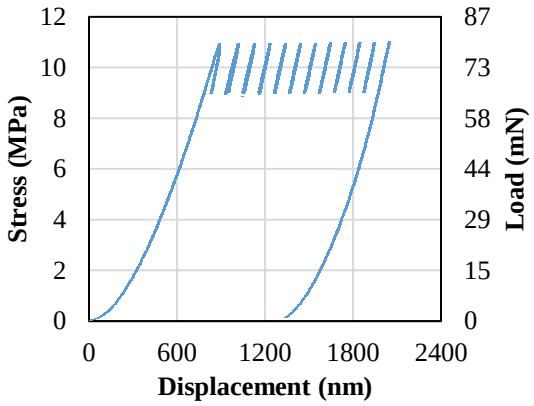

(b)

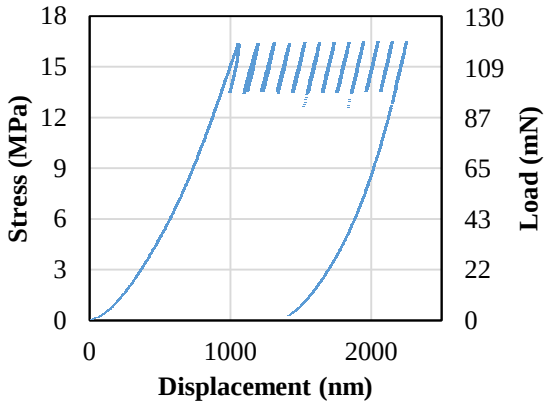

(c)

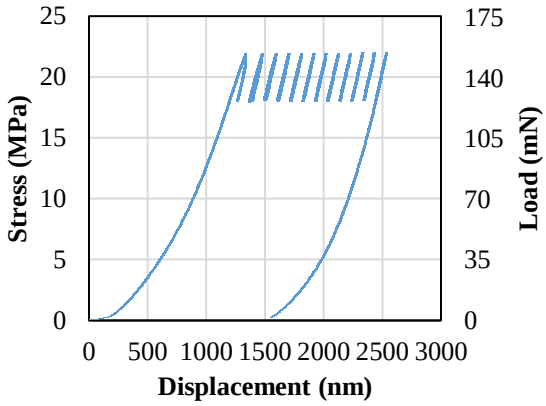

(d)

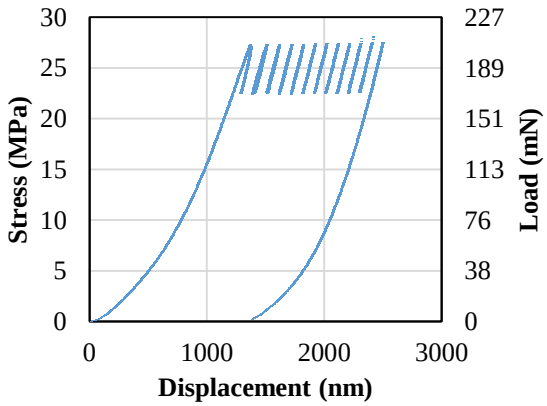

(e)

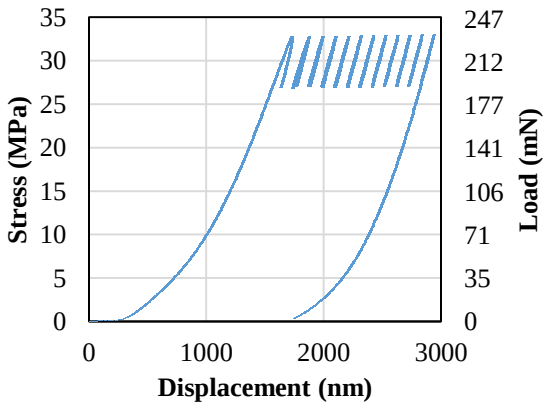

(f)

Figure A.21 (cont.)

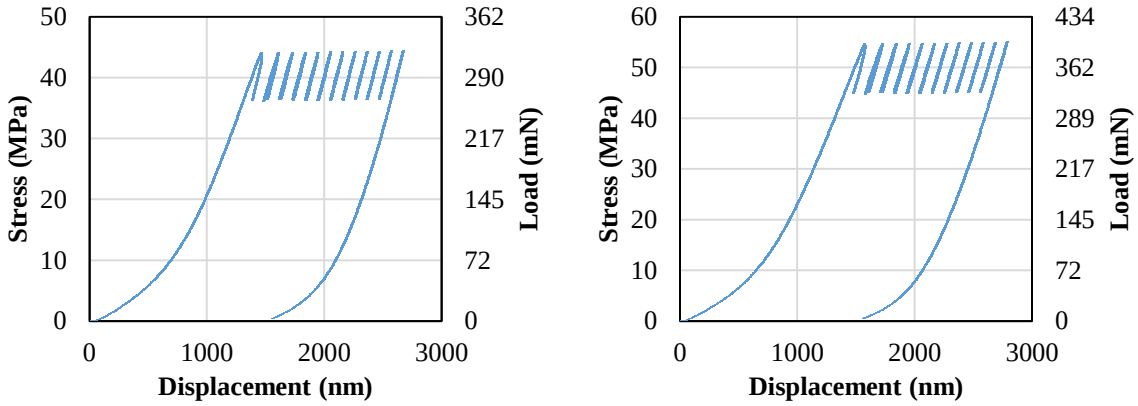

(g) **(h)**

Figure A.21 Cyclic compression of Cu spring films on unseeded substrate subjected to **(a)** 5 MPa, **(b)** 10 MPa, **(c)** 15 MPa, **(d)** 20 MPa, **(e)** 25 MPa, **(f)** 30 MPa, **(g)** 40 MPa, **(h)** 50 MPa mean stress.

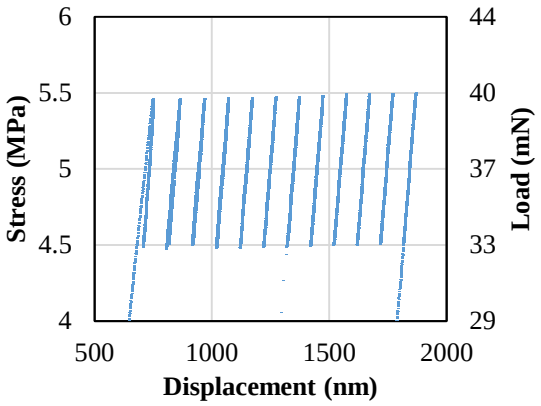

(a)

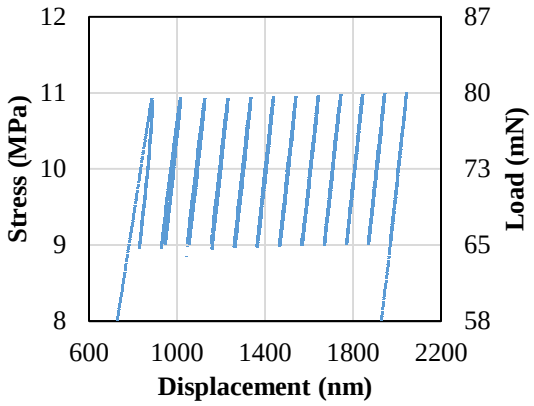

(b)

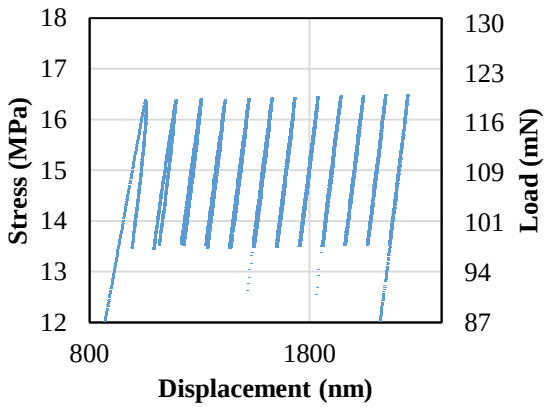

(c)

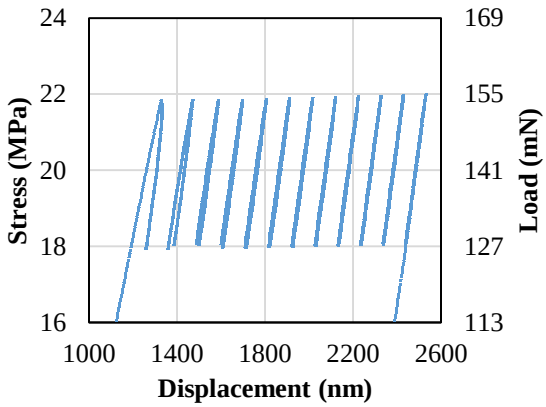

(d)

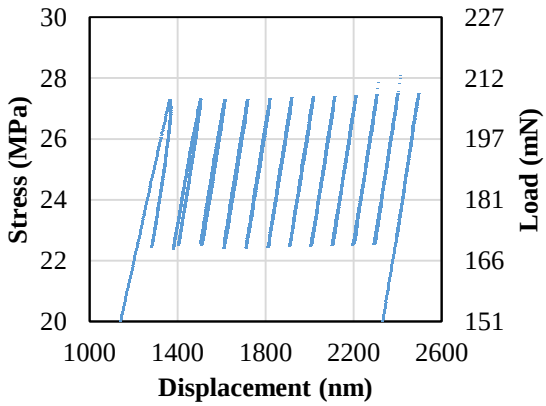

(e)

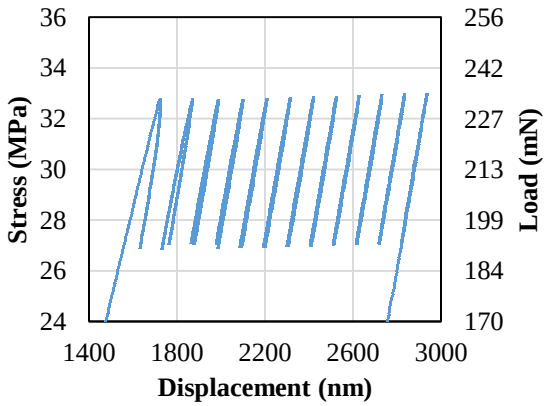

(f)

Figure A.22 (cont.)

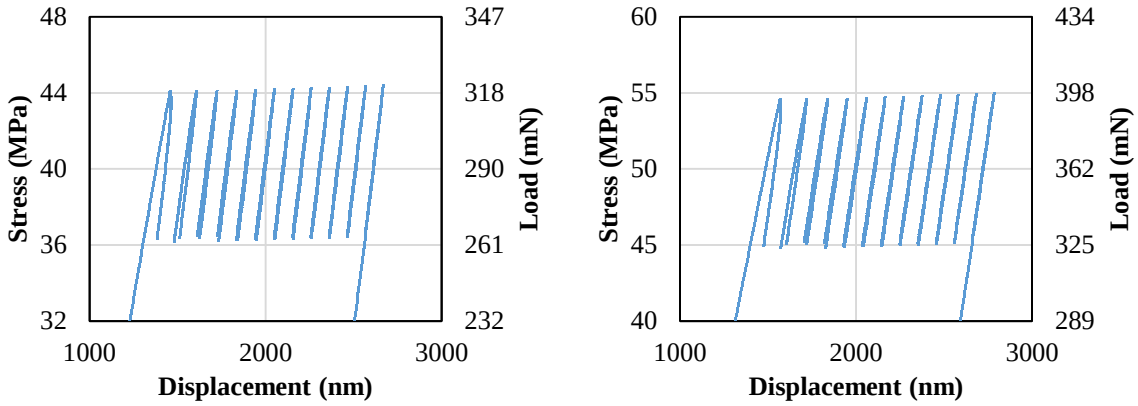

(g) **(h)**

Figure A.22 Detail of cyclic compression of Cu spring films on unseeded substrate subjected to **(a)** 5 MPa, **(b)** 10 MPa, **(c)** 15 MPa, **(d)** 20 MPa, **(e)** 25 MPa, **(f)** 30 MPa, **(g)** 40 MPa, **(h)** 50 MPa mean stress with an amplitude of 10% of the mean.

Appendix B

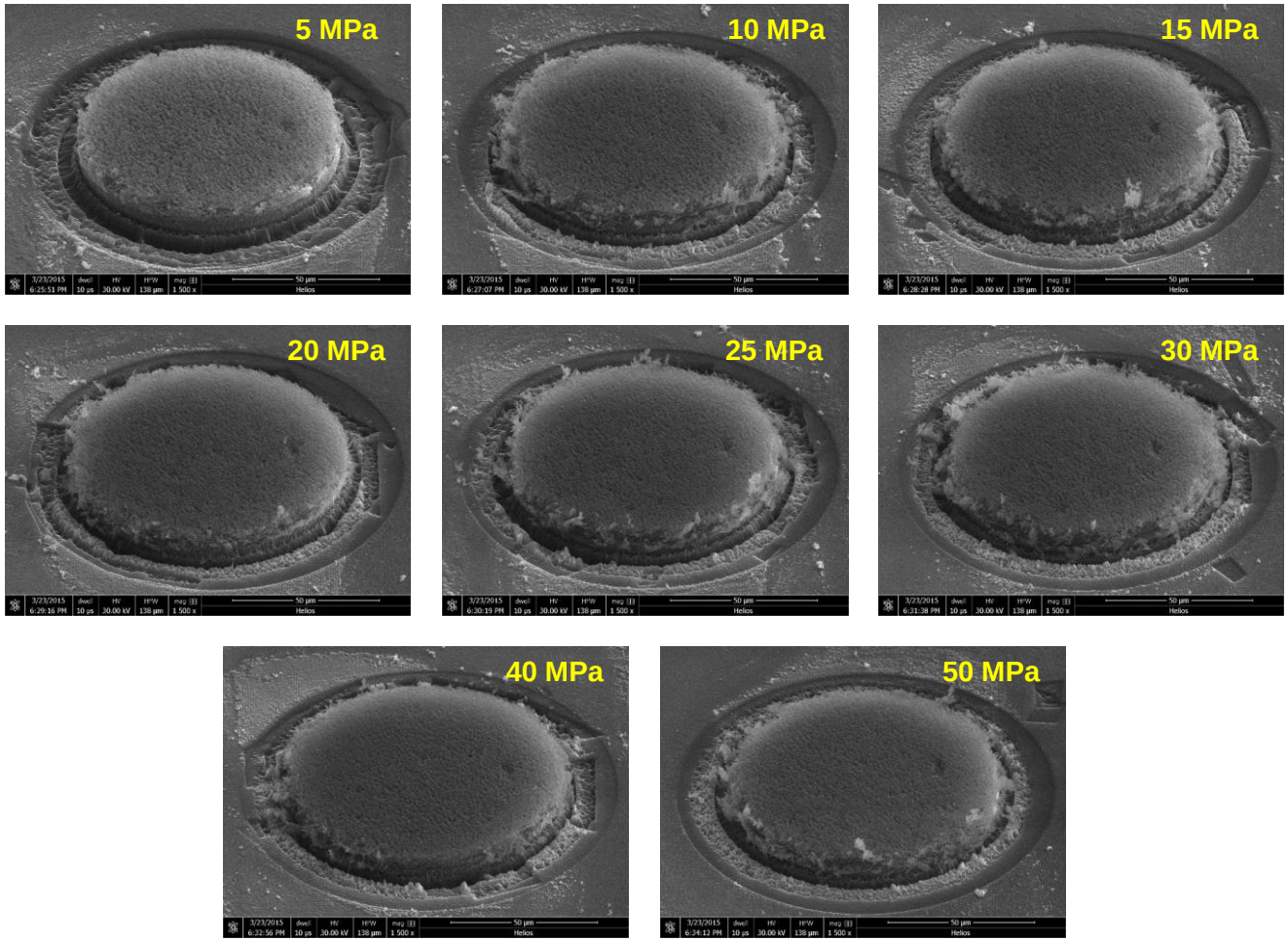

Figure B.1 Top view SEM images of 4-turn Si spring films with 900 nm seed spacing before and after testing.

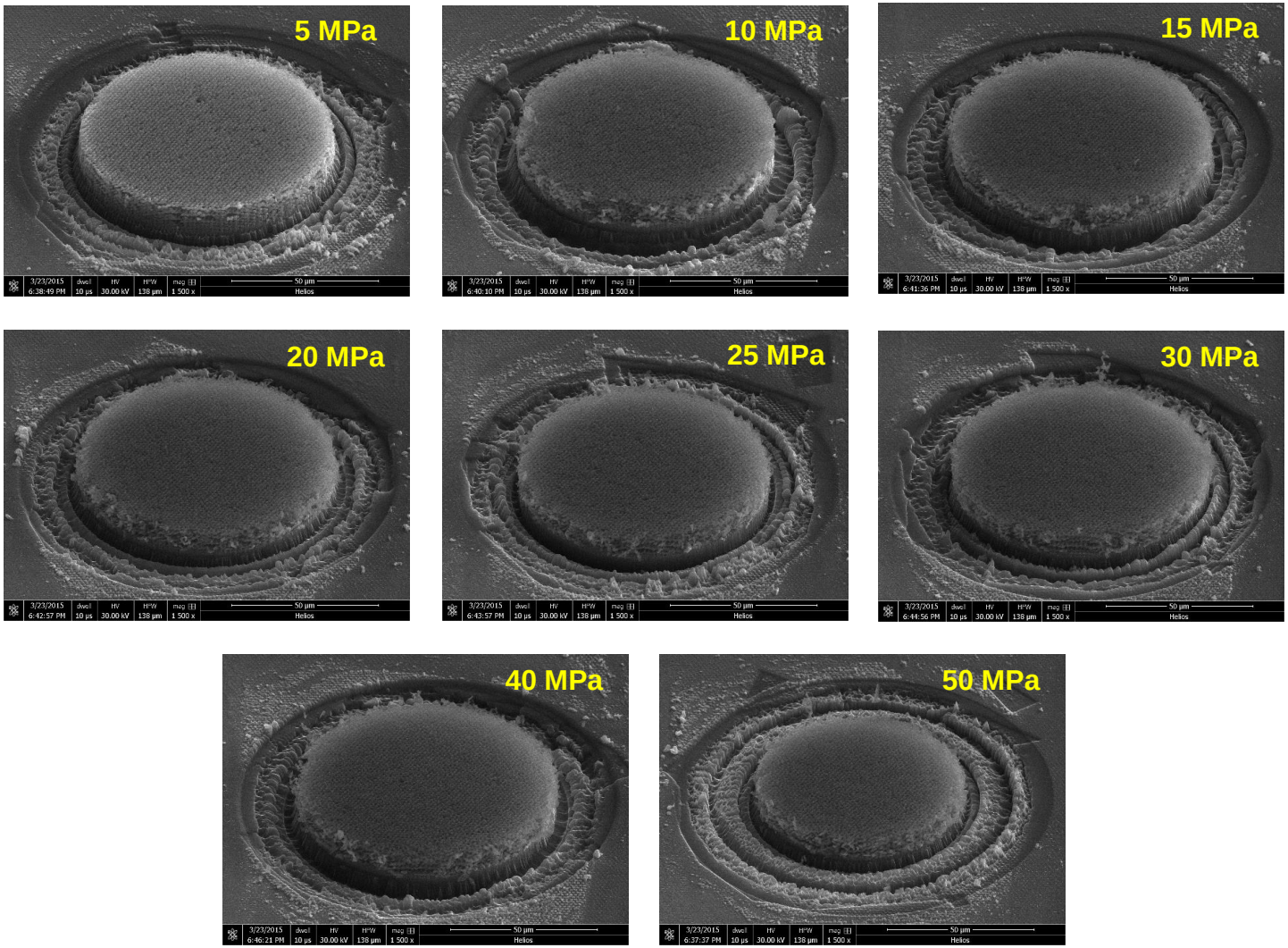

Figure B.2 Top view SEM images of 4-turn Si spring films with 1500 nm seed spacing before and after testing.

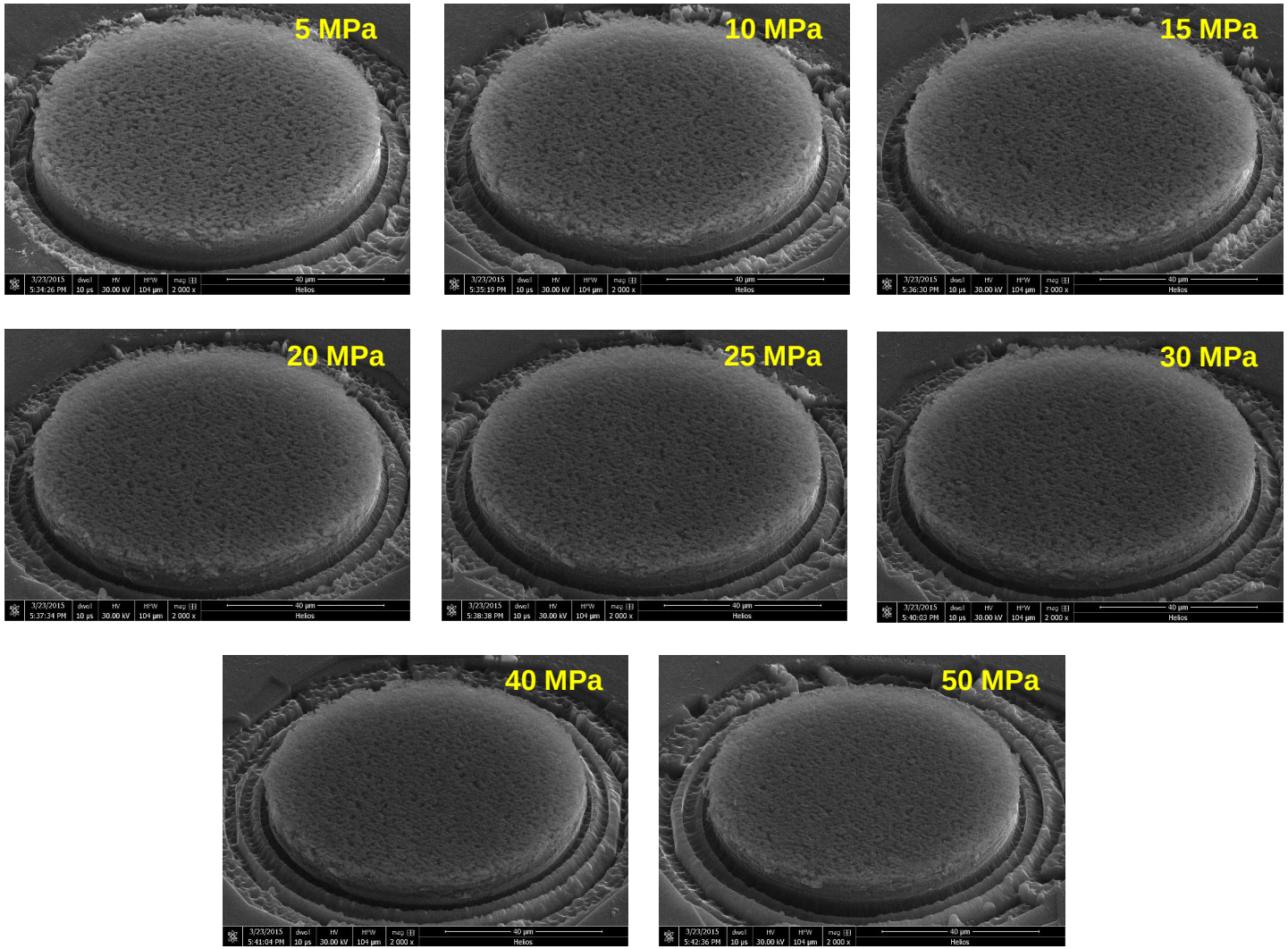

Figure B.3 Top view SEM images of 4-turn Si spring films on unseeded substrate before and after testing.

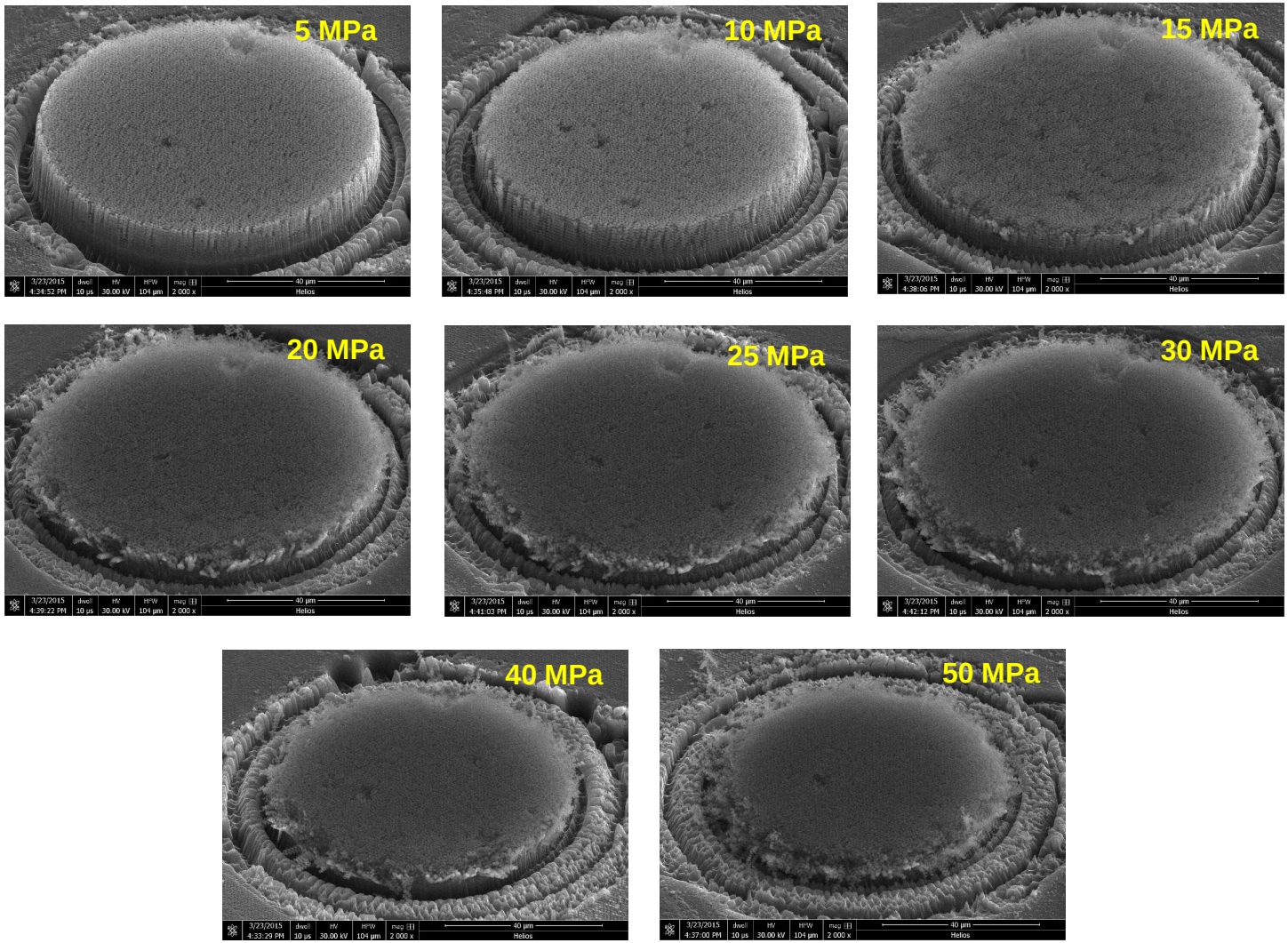

Figure B.4 Top view SEM images of 10-turn Si spring films with 900 nm seed spacing before and after testing.

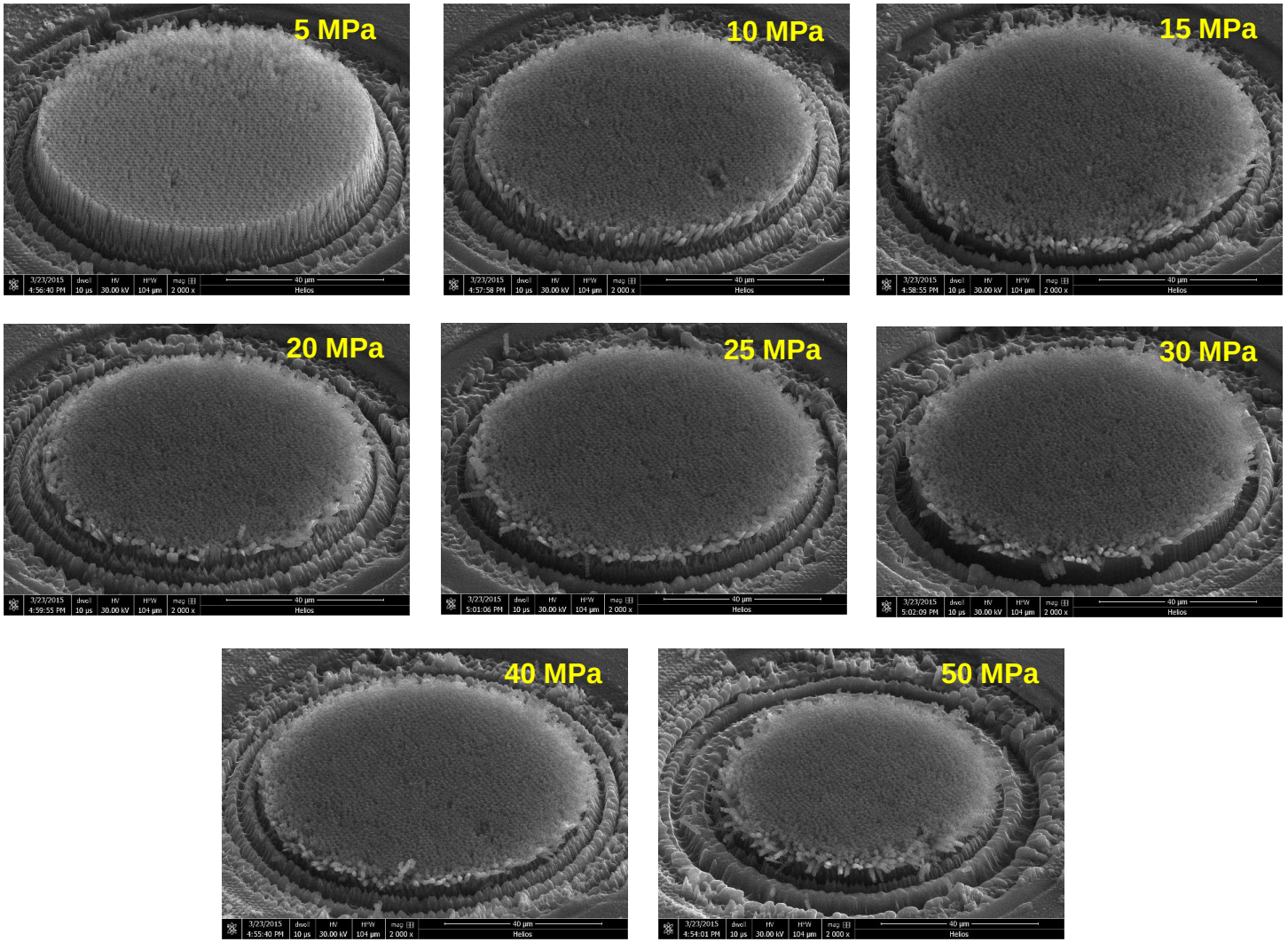

Figure B.5 Top view SEM images of 10-turn Si spring films with 1500 nm seed spacing before and after testing.

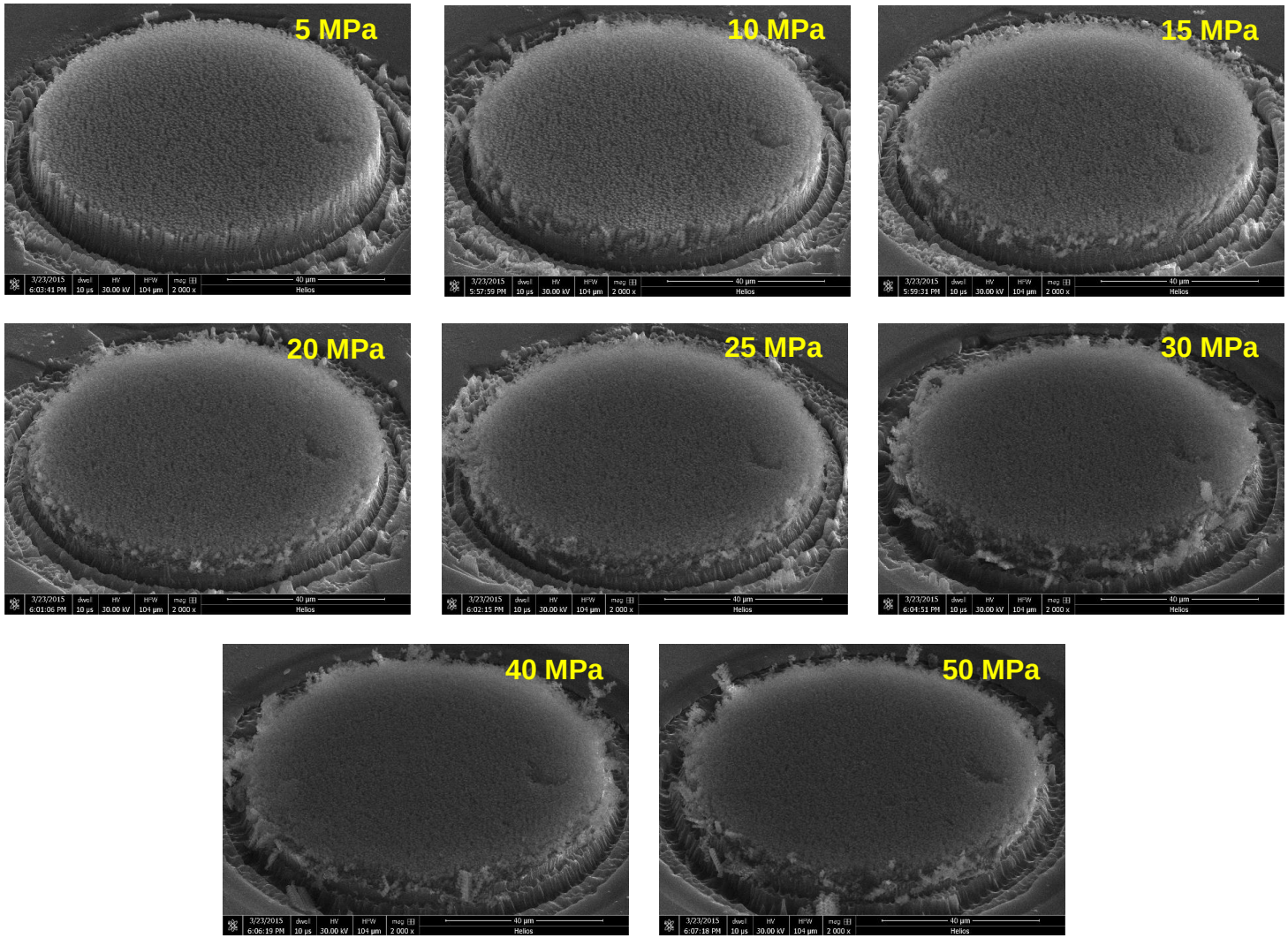

Figure B.6 Top view SEM images of 10-turn Si spring films on unseeded substrate before and after testing.

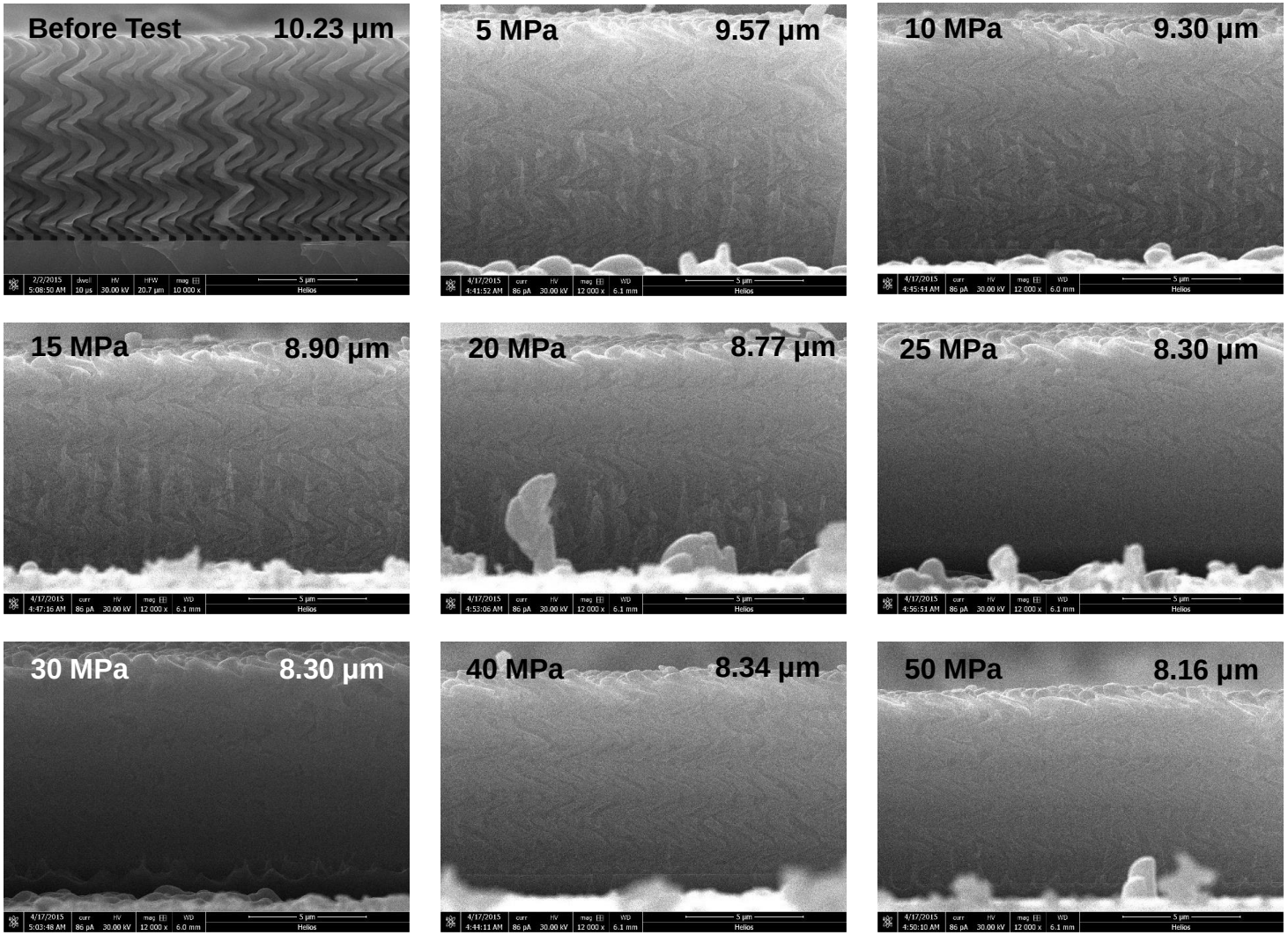

Figure B.7 4-turn Si spring films with 900 nm seed spacing before and after testing showing the spring heights.

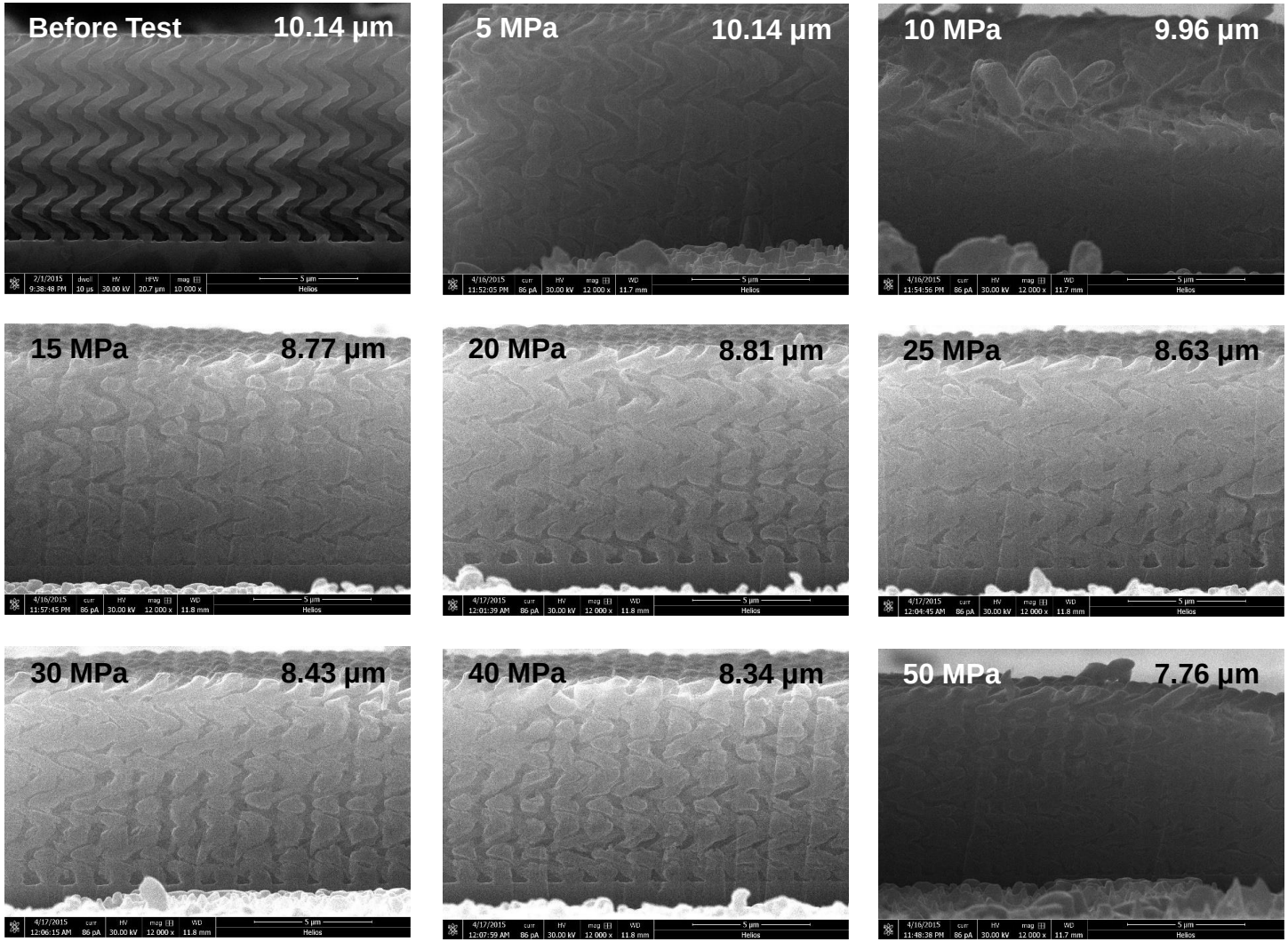

Figure B.8 4-turn Si spring films with 1500 nm seed spacing before and after testing showing the spring heights.

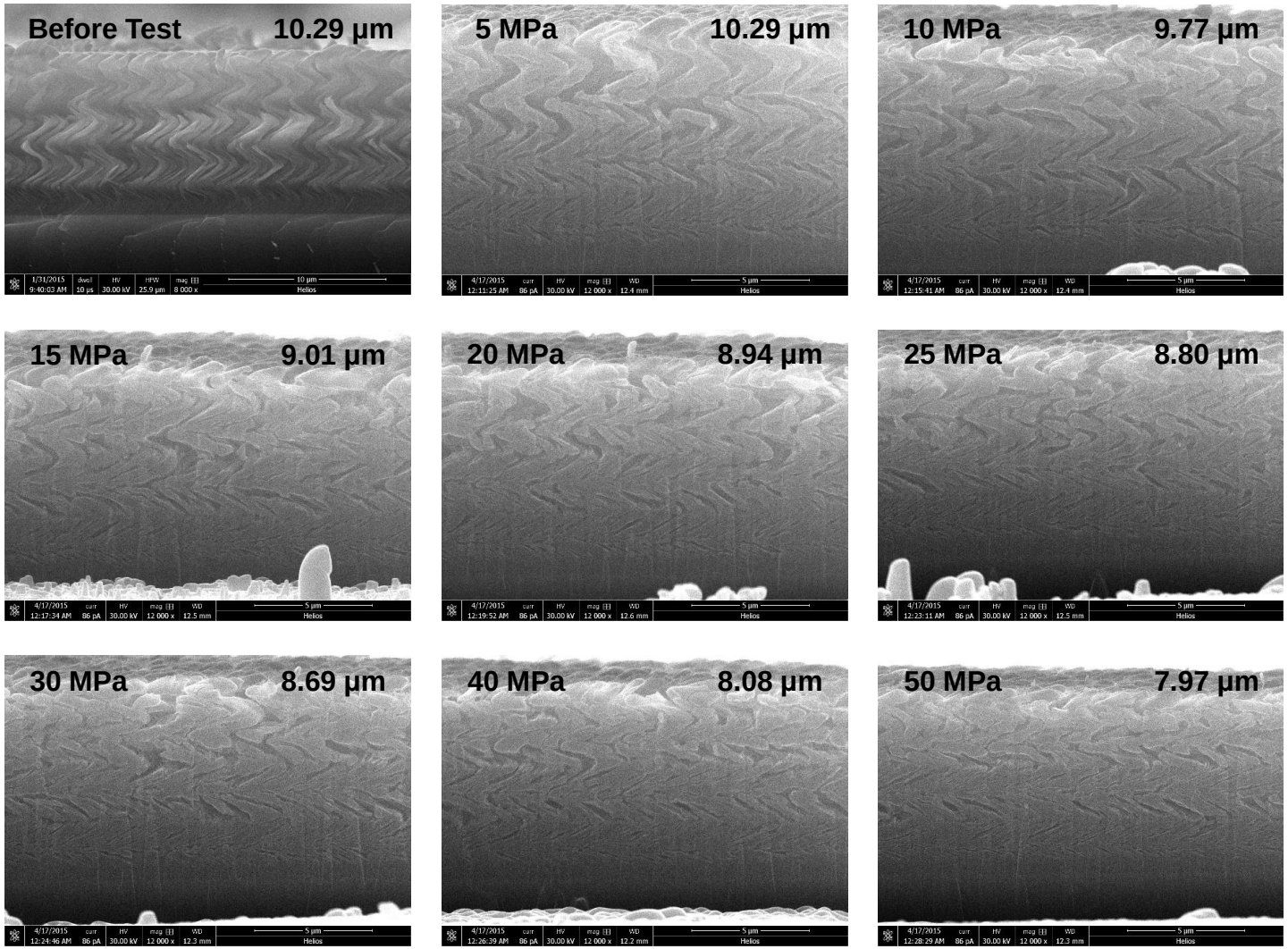

Figure B.9 4-turn Si spring films on unseeded substrate before and after testing showing the spring heights.

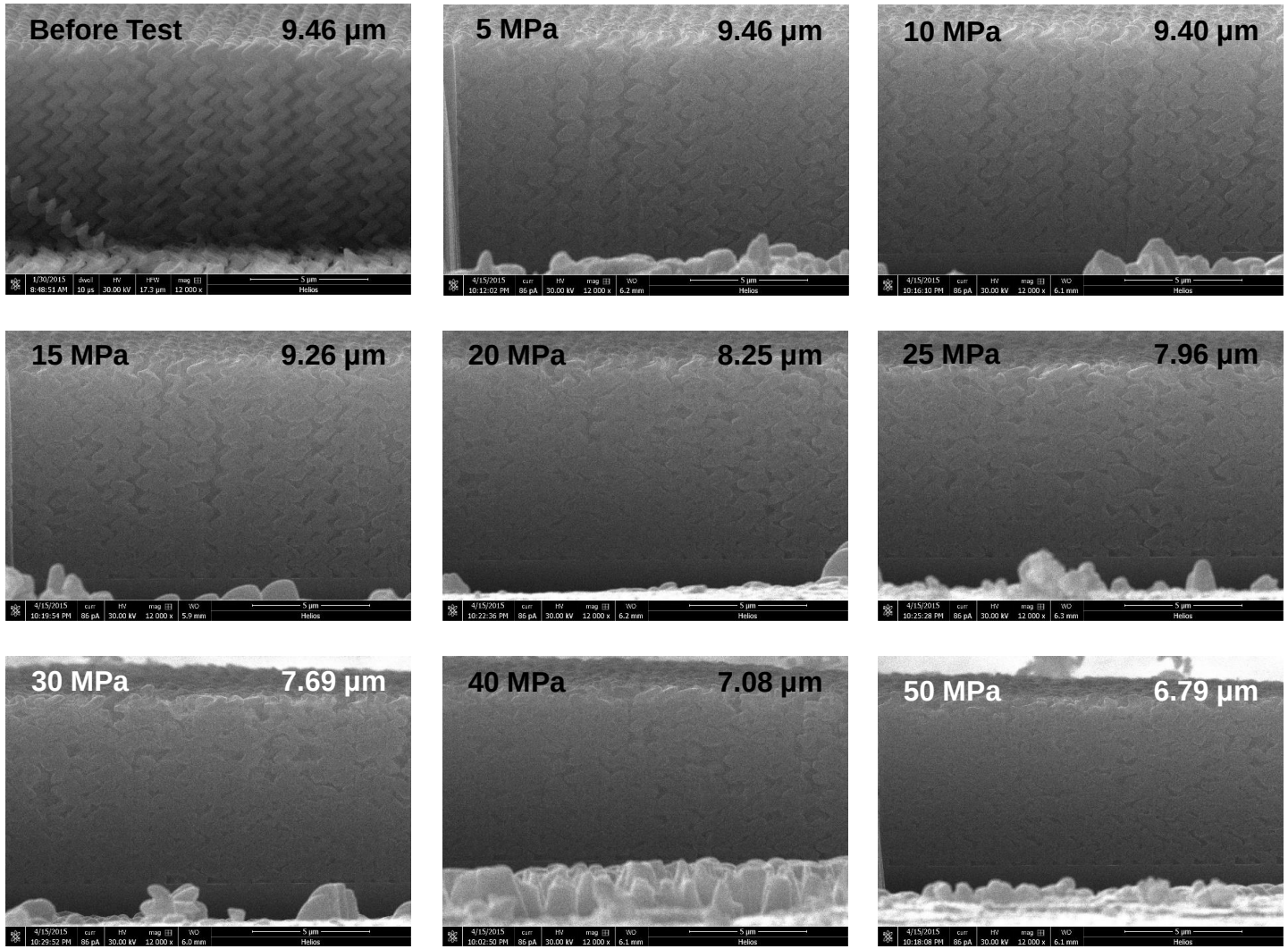

Figure B.10 10-turn Si spring films with 900 nm seed spacing before and after testing showing the spring heights.

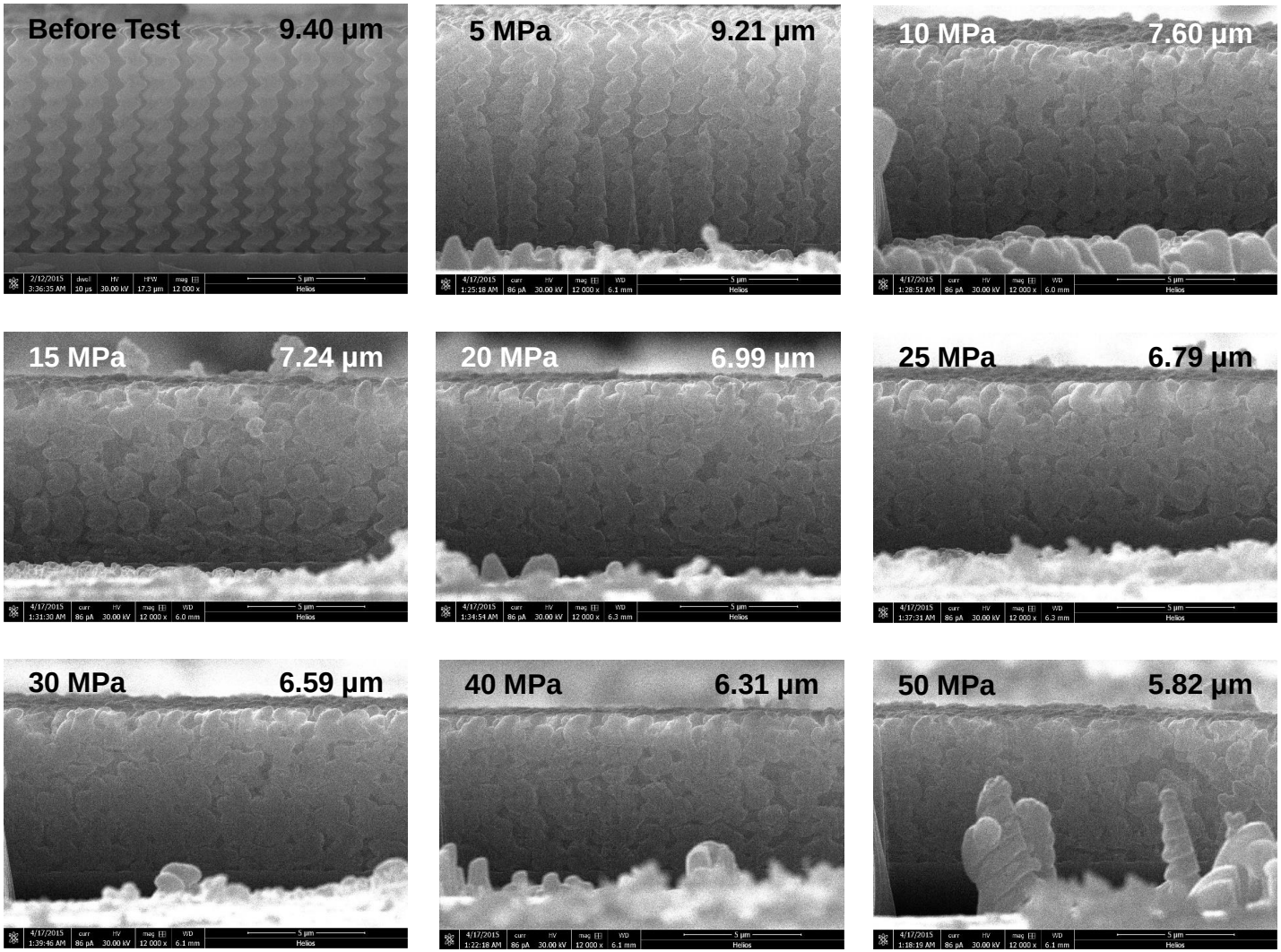

Figure B.11 10-turn Si spring films with 1500 nm seed spacing before and after testing showing the spring heights.

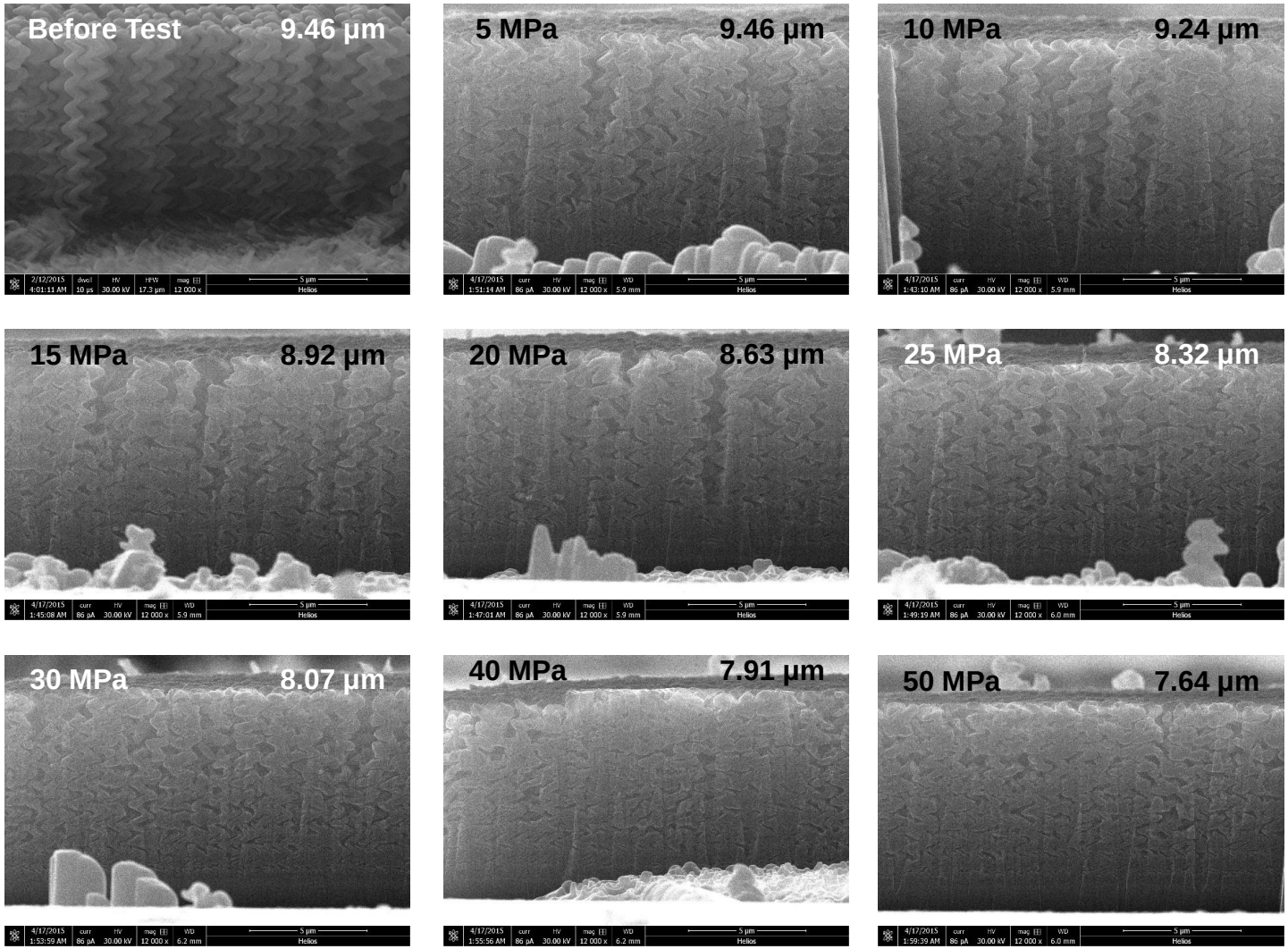

Figure B.12 10-turn Si spring films on unseeded substrate before and after testing showing the spring heights.

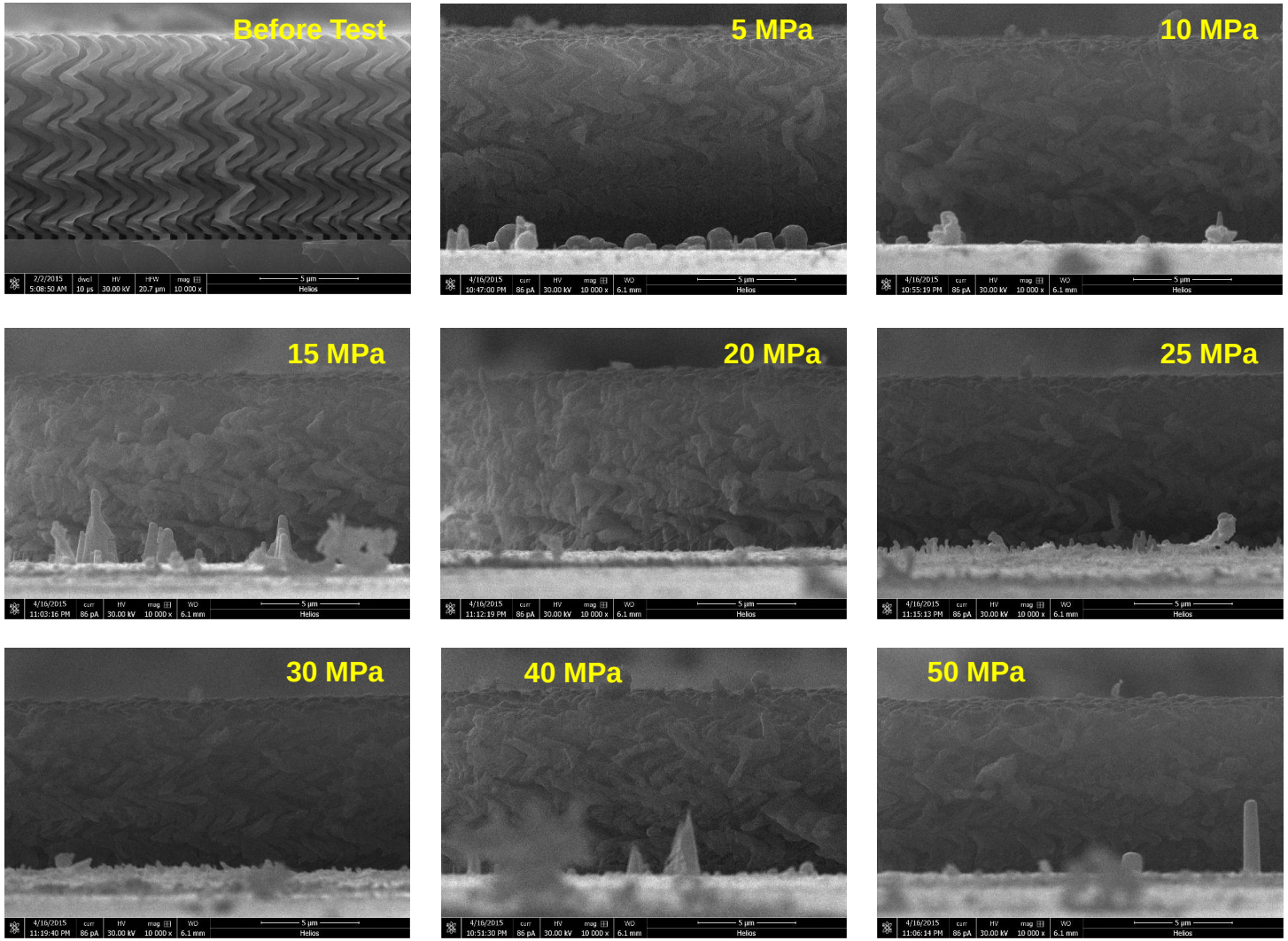

Figure B.13 Edge images of 4-turn Si spring films with 900 nm seed spacing before and after testing.

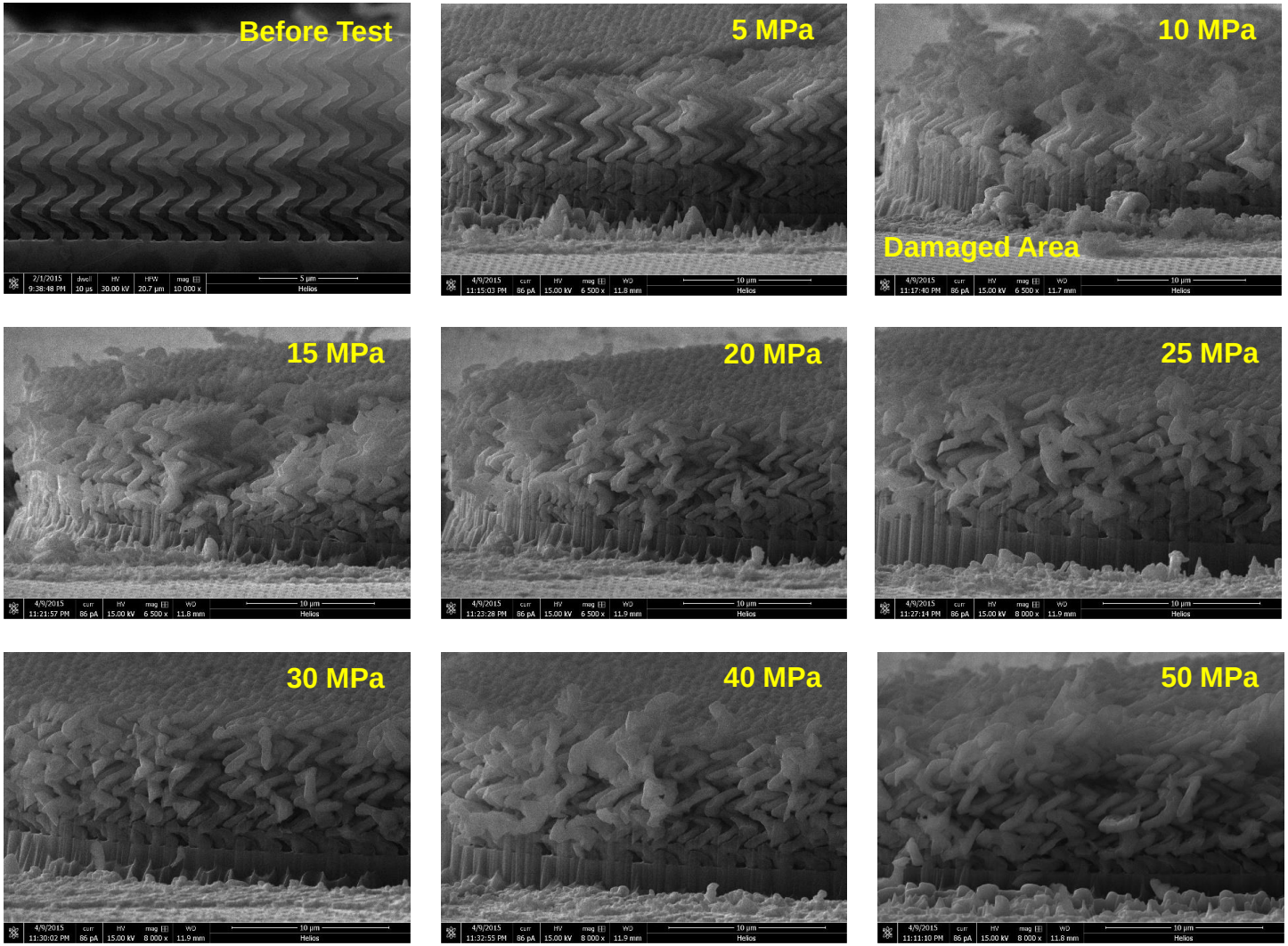

Figure B.14 Edge images of 4-turn Si spring films with 1500 nm seed spacing before and after testing.

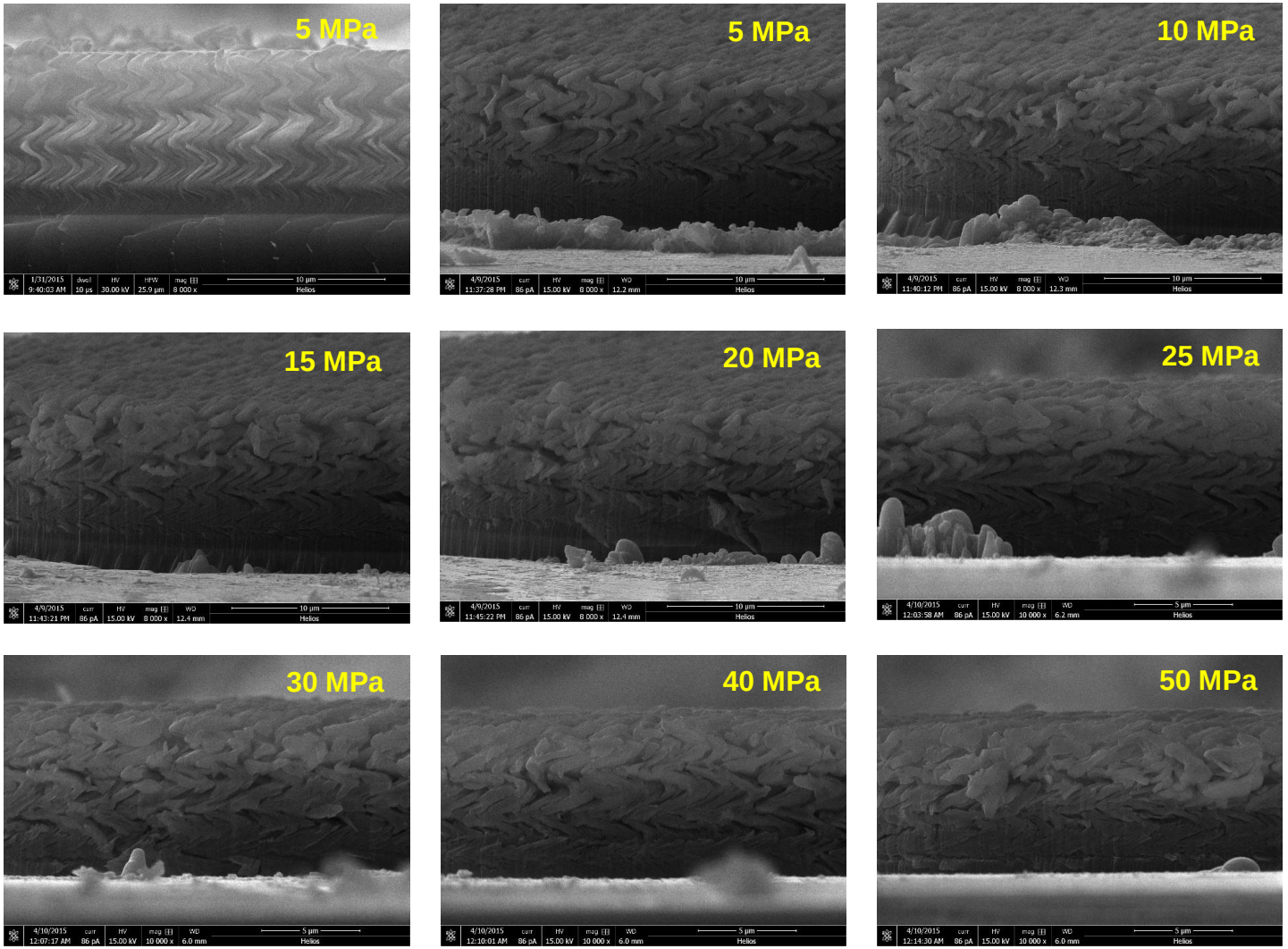

Figure B.15 Edge images of 4-turn Si spring films on unseeded substrate before and after testing.

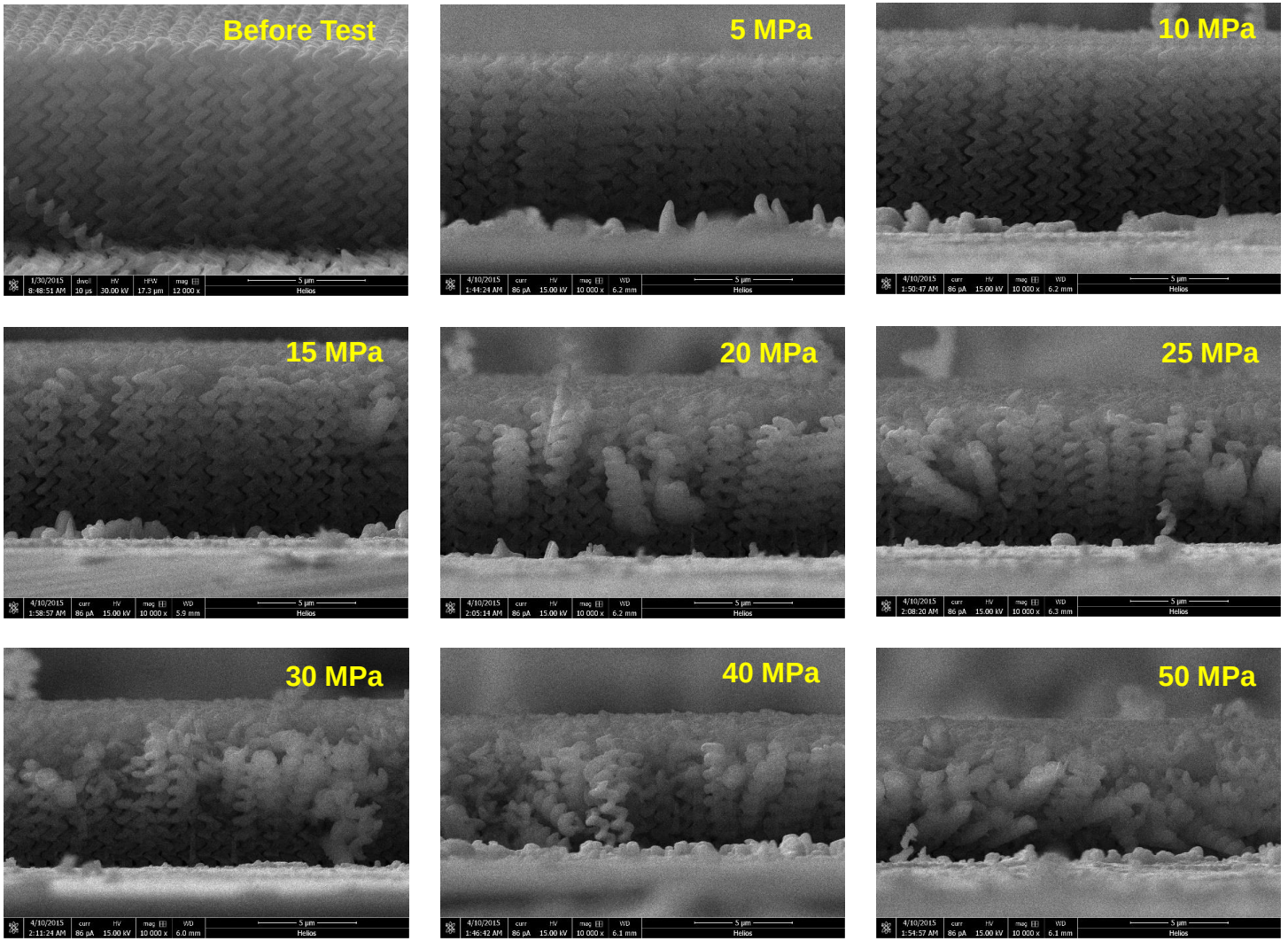

Figure B.16 Edge images of 10-turn Si spring films with 900 nm seed spacing before and after testing.

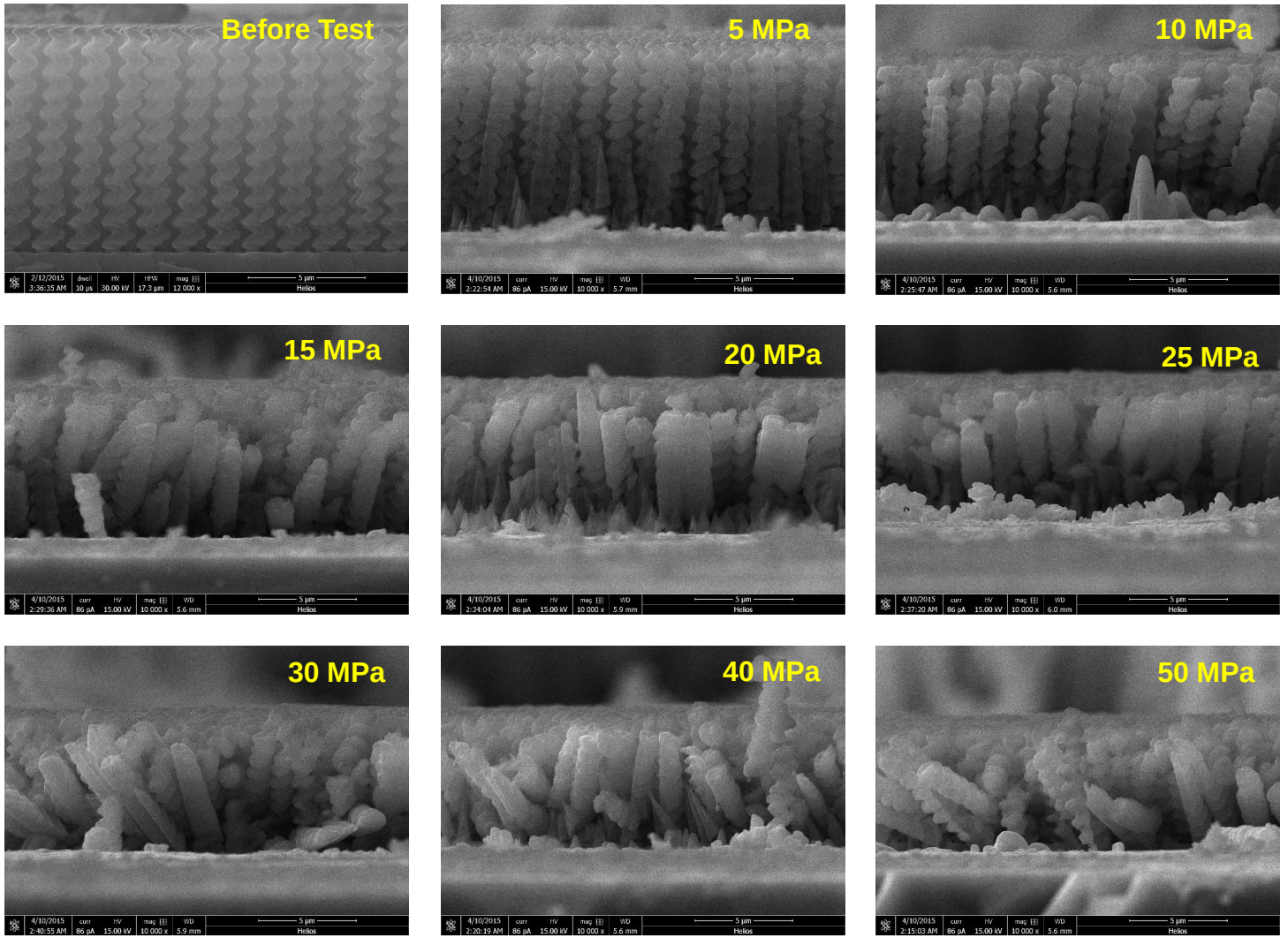

Figure B.17 Edge images of 10-turn Si spring films with 1500 nm seed spacing before and after testing.

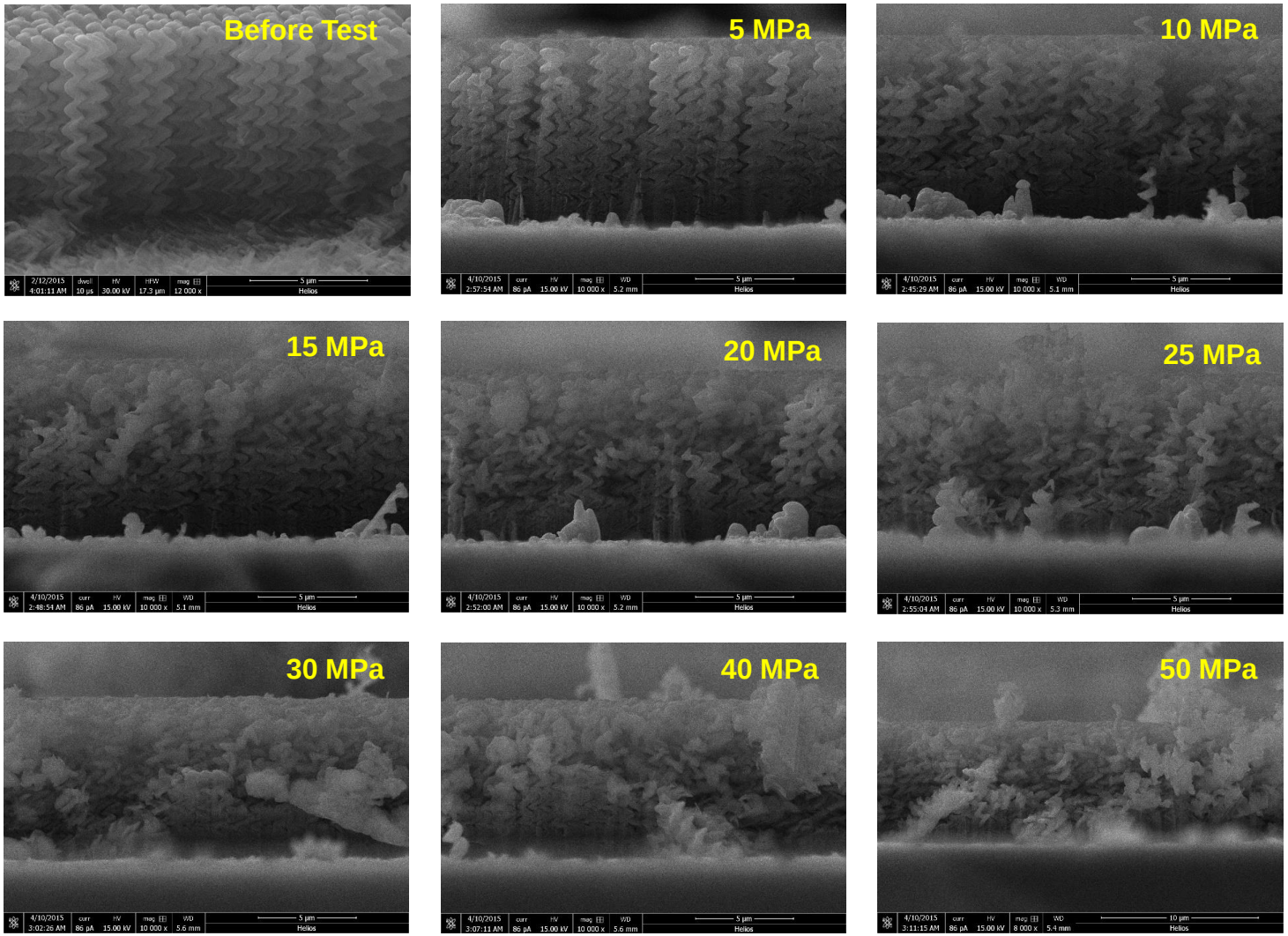

Figure B.18 Edge images of 10-turn Si spring films on unseeded substrate before and after testing.

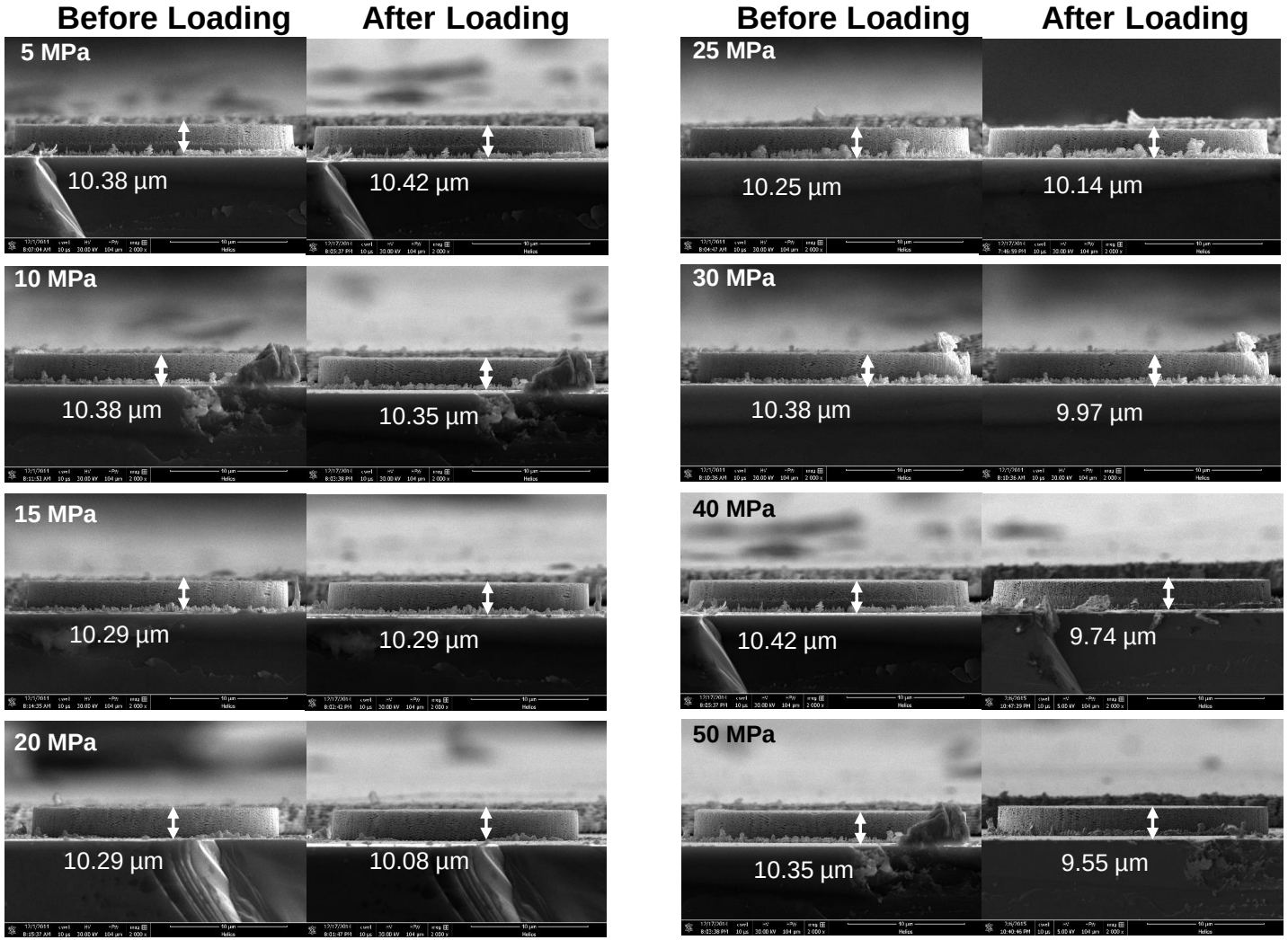

Figure B.19 10-turn Cu spring films with 2000 nm seed spacing before and after testing showing the spring heights.

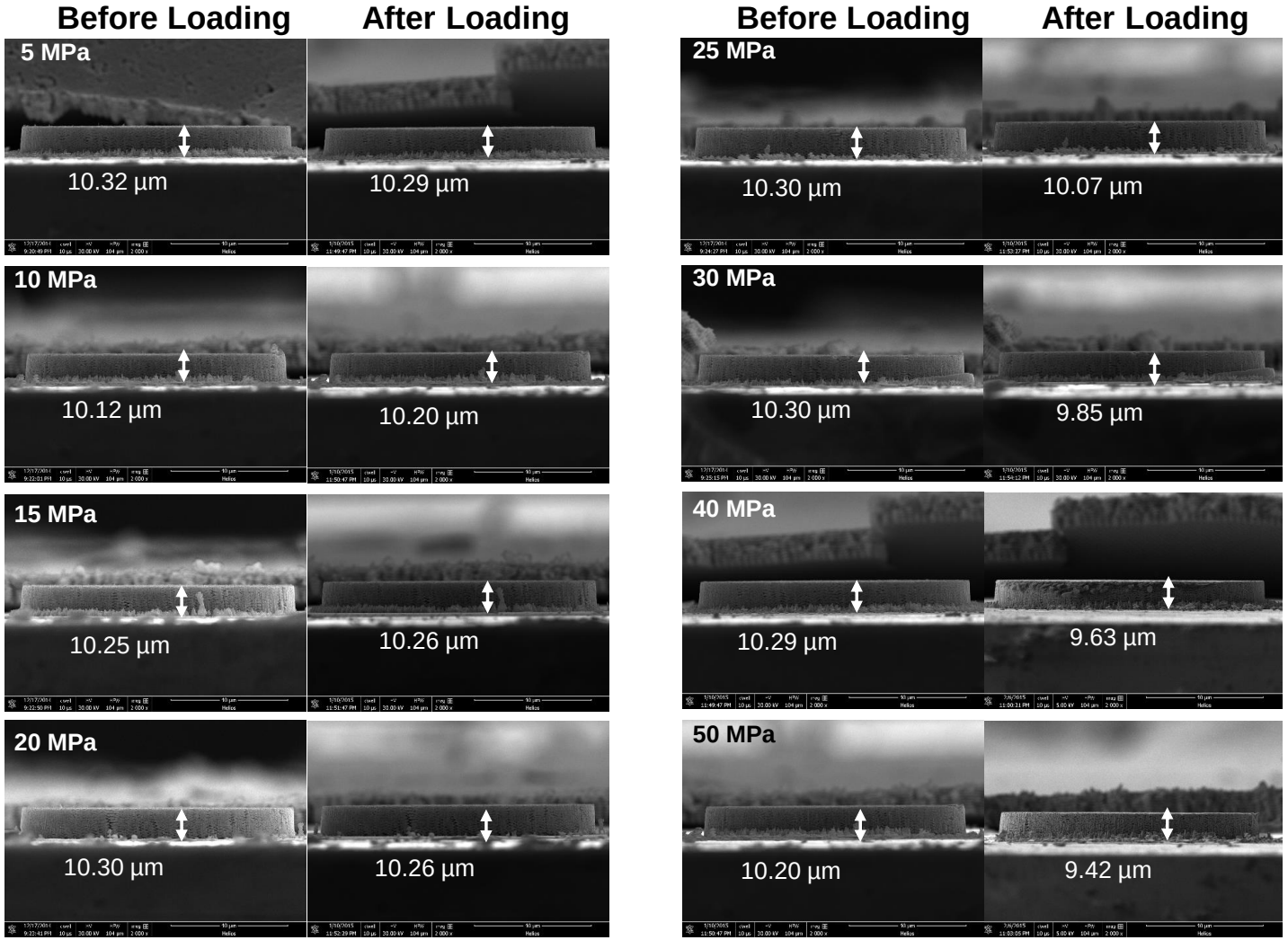

Figure B.20 10-turn Cu spring films with 2400 nm seed spacing before and after testing showing the spring heights.

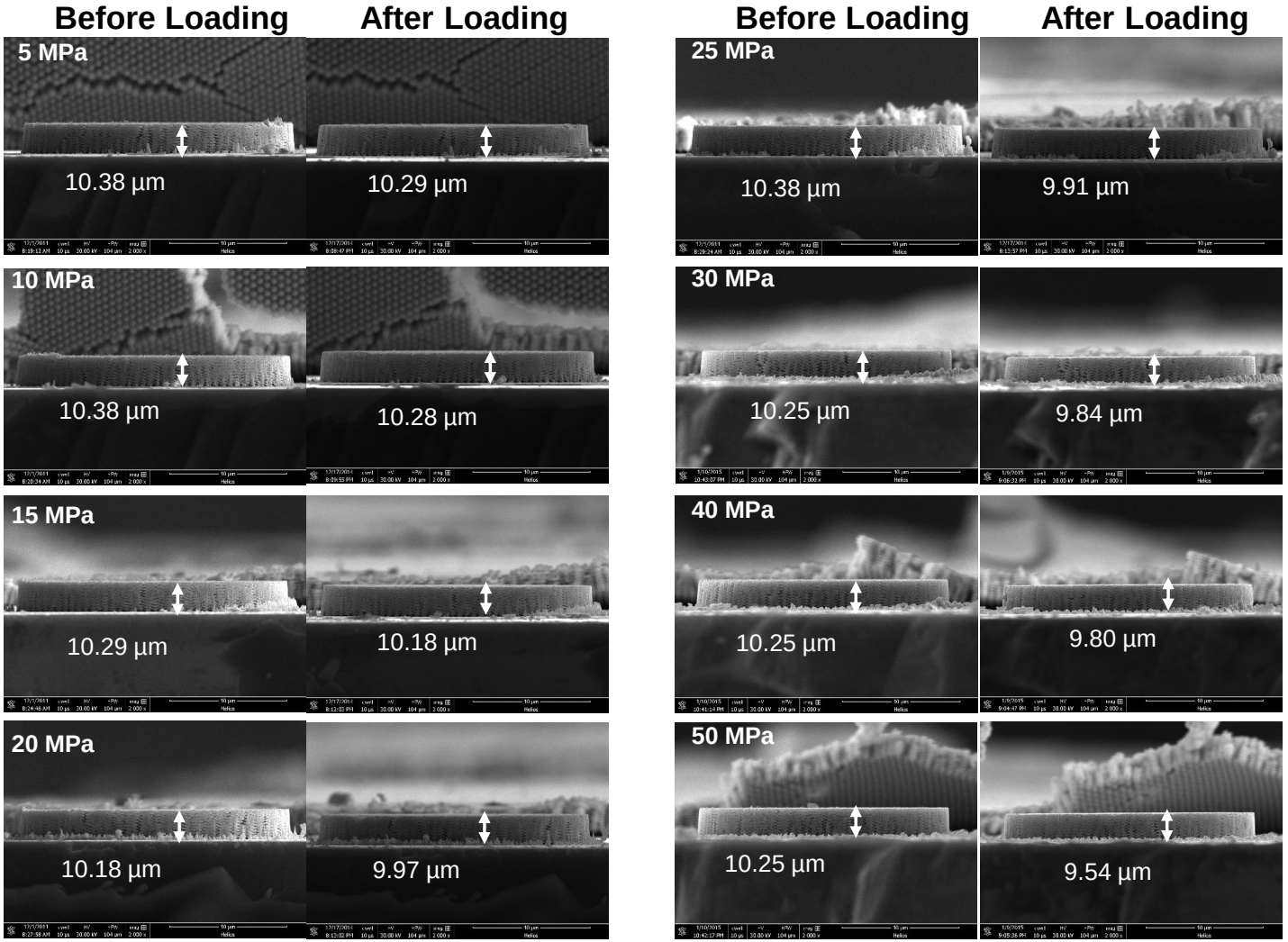

Figure B.21 10-turn Cu spring films with 2800 nm seed spacing before and after testing showing the spring heights.

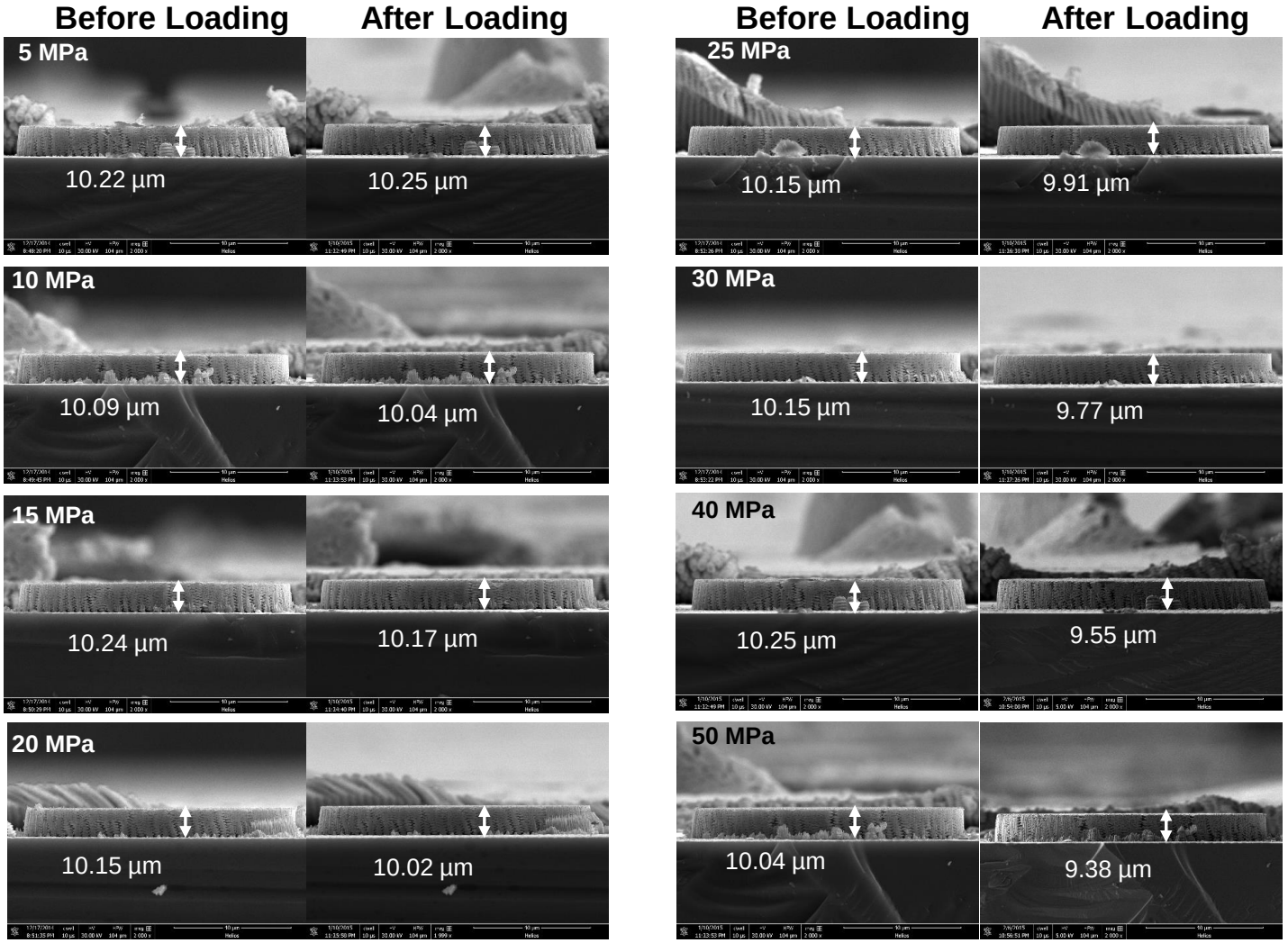

Figure B.22 10-turn Cu spring films with 3200 nm seed spacing before and after testing showing the spring heights.

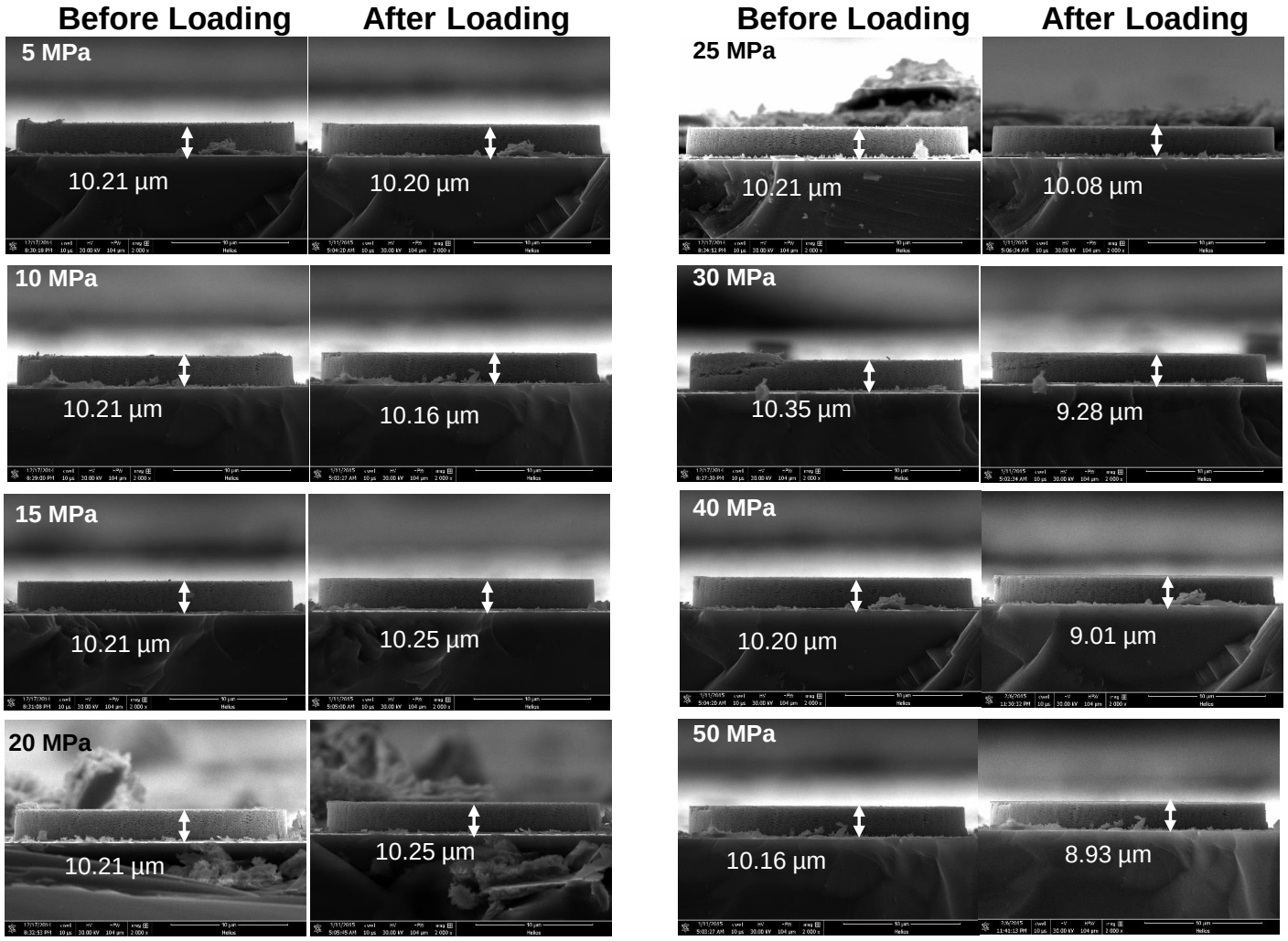

Figure B.23 10-turn Cu spring films on unseeded substrate before and after testing showing the spring heights.

Appendix C

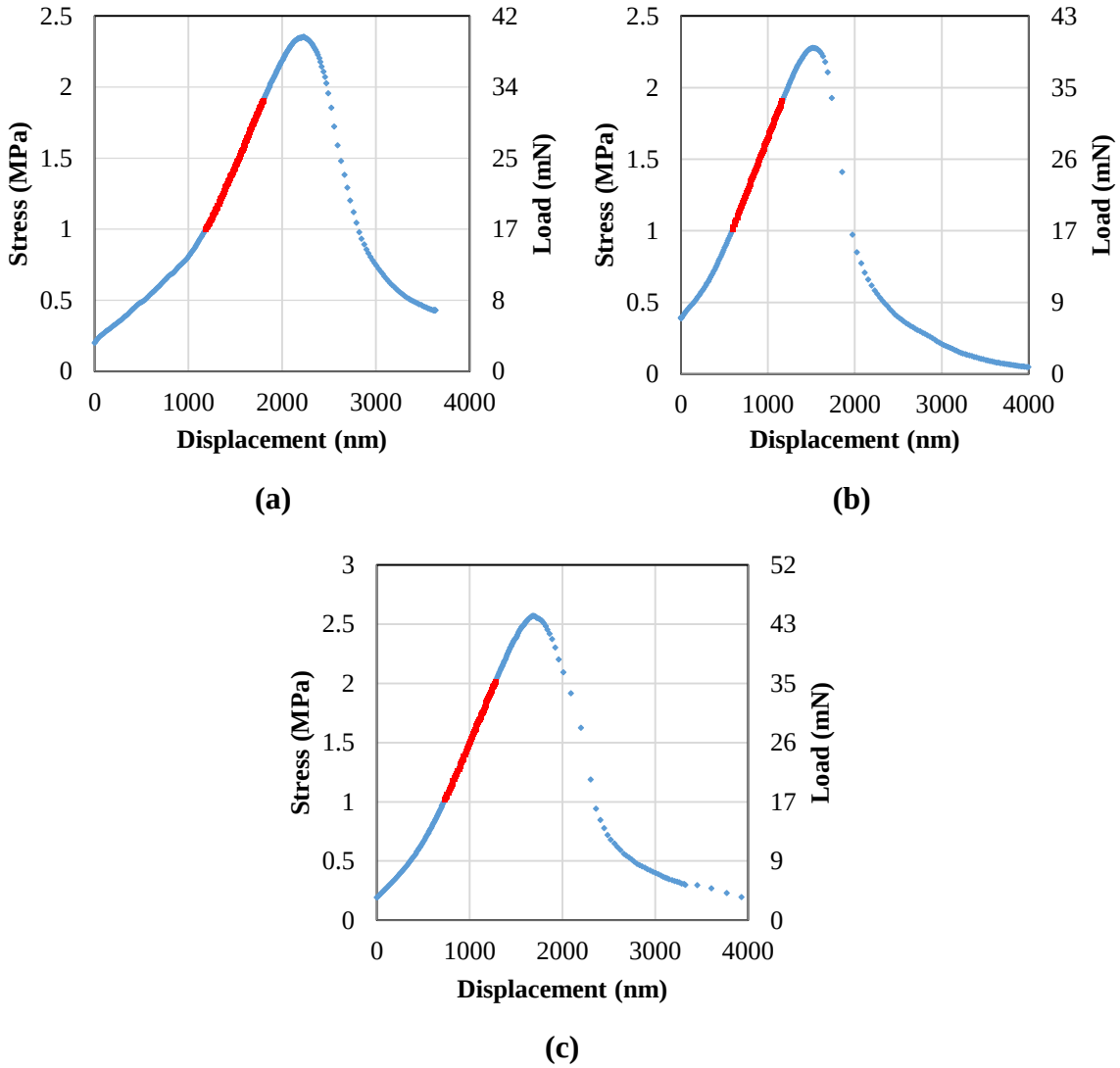

Figure C.1 Shear behavior of 4-turn Si spring films with 900 nm seed spacing. The red data points were used to compute the shear stiffness.

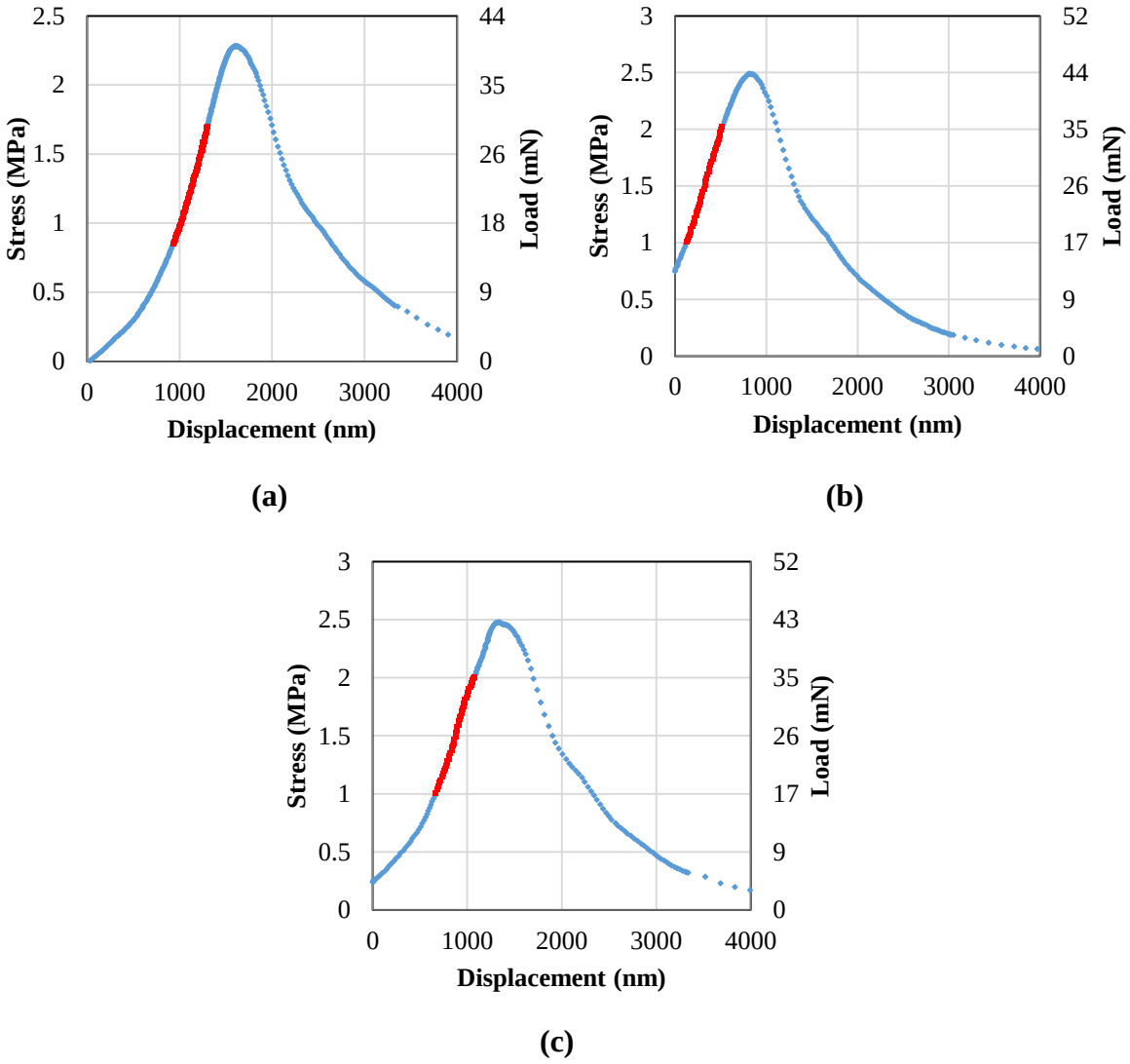

Figure C.2 Shear behavior of 4-turn Si spring films with 1500 nm seed spacing. The red data points were used to compute the shear stiffness.

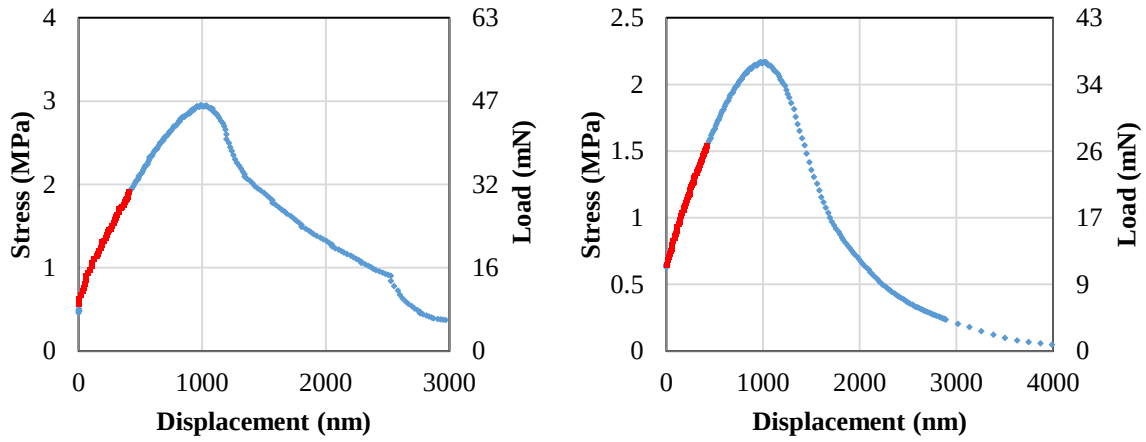

(a) **(b)**

Figure C.3 Shear behavior of 4-turn Si spring films with no seeding. The red data points were used to compute the shear stiffness.

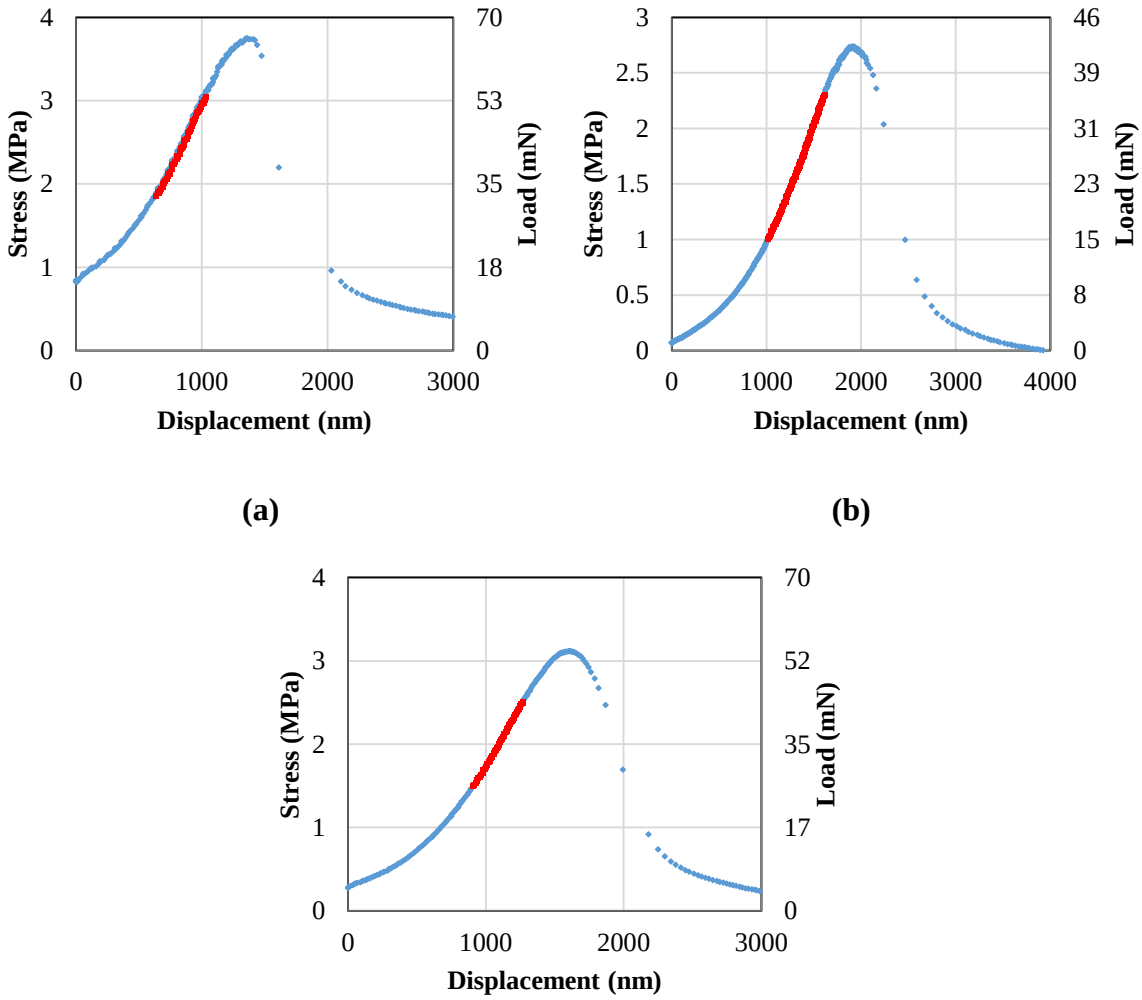

Figure C.4 Shear behavior of 10-turn Si spring films with 900 nm seed spacing. The red data points were used to compute the shear stiffness.

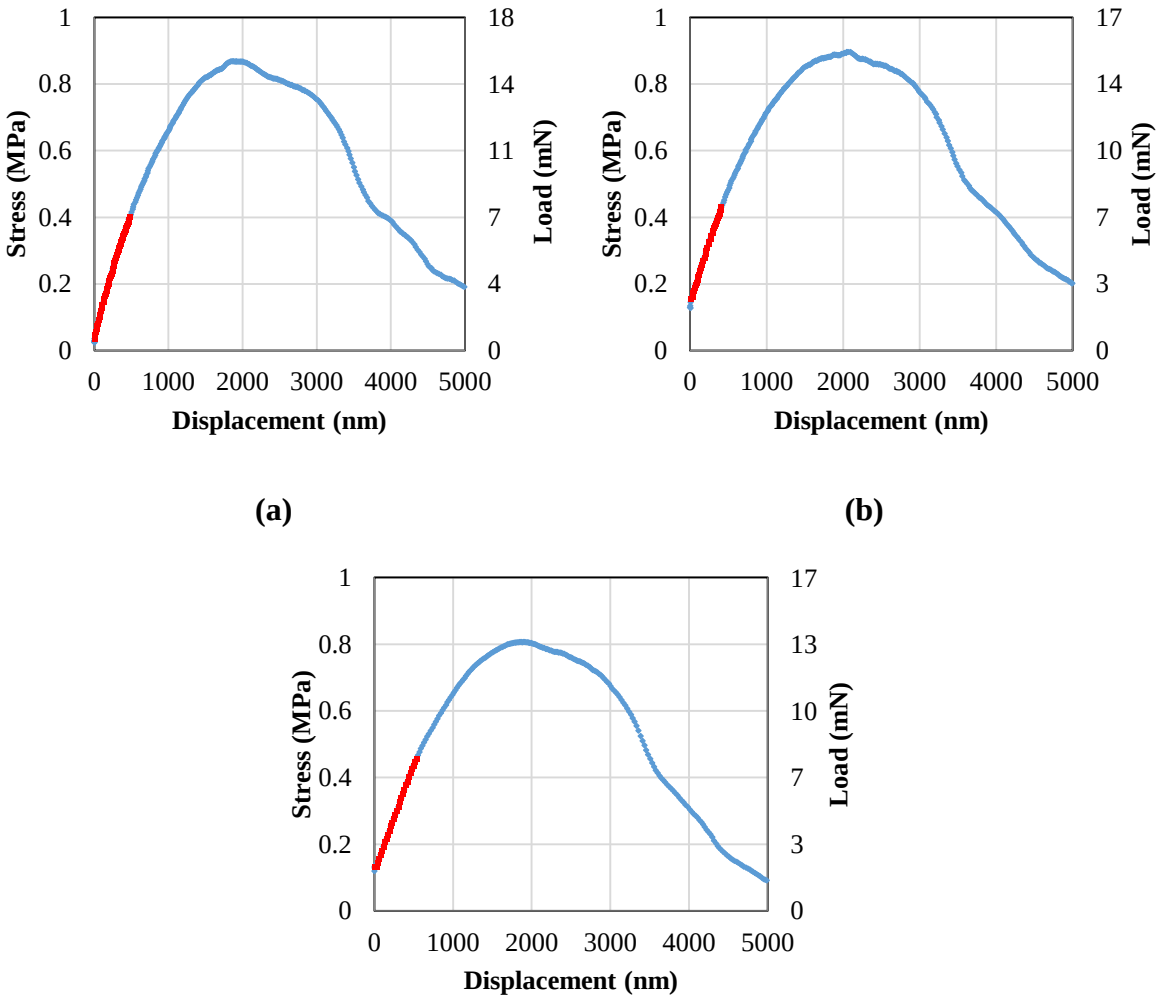

Figure C.5 Shear behavior of 10-turn Si spring films with 1500 nm seed spacing. The red data points were used to compute the shear stiffness.

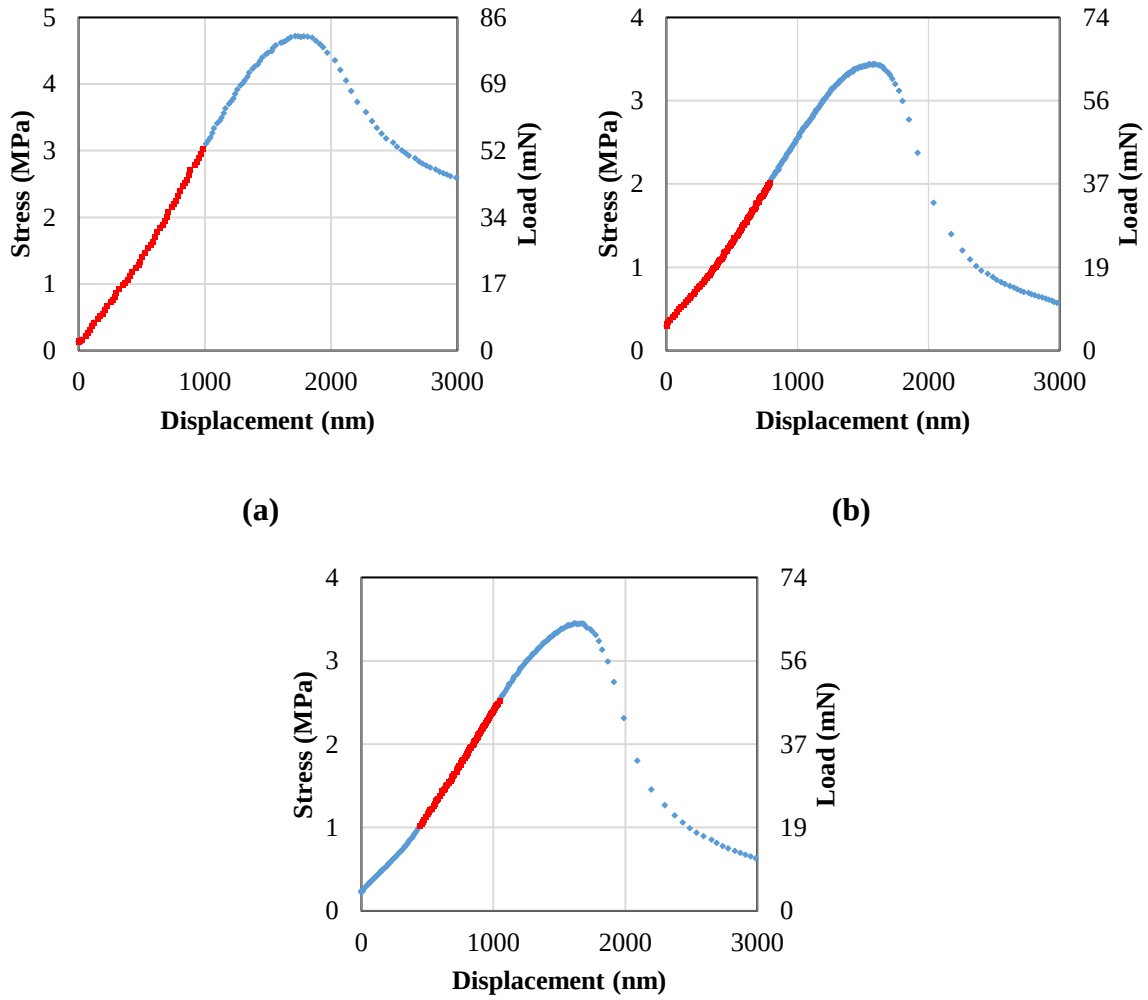

Figure C.6 Shear behavior of 10-turn Si spring films on unseeded substrate. The red data points were used to compute the shear stiffness.

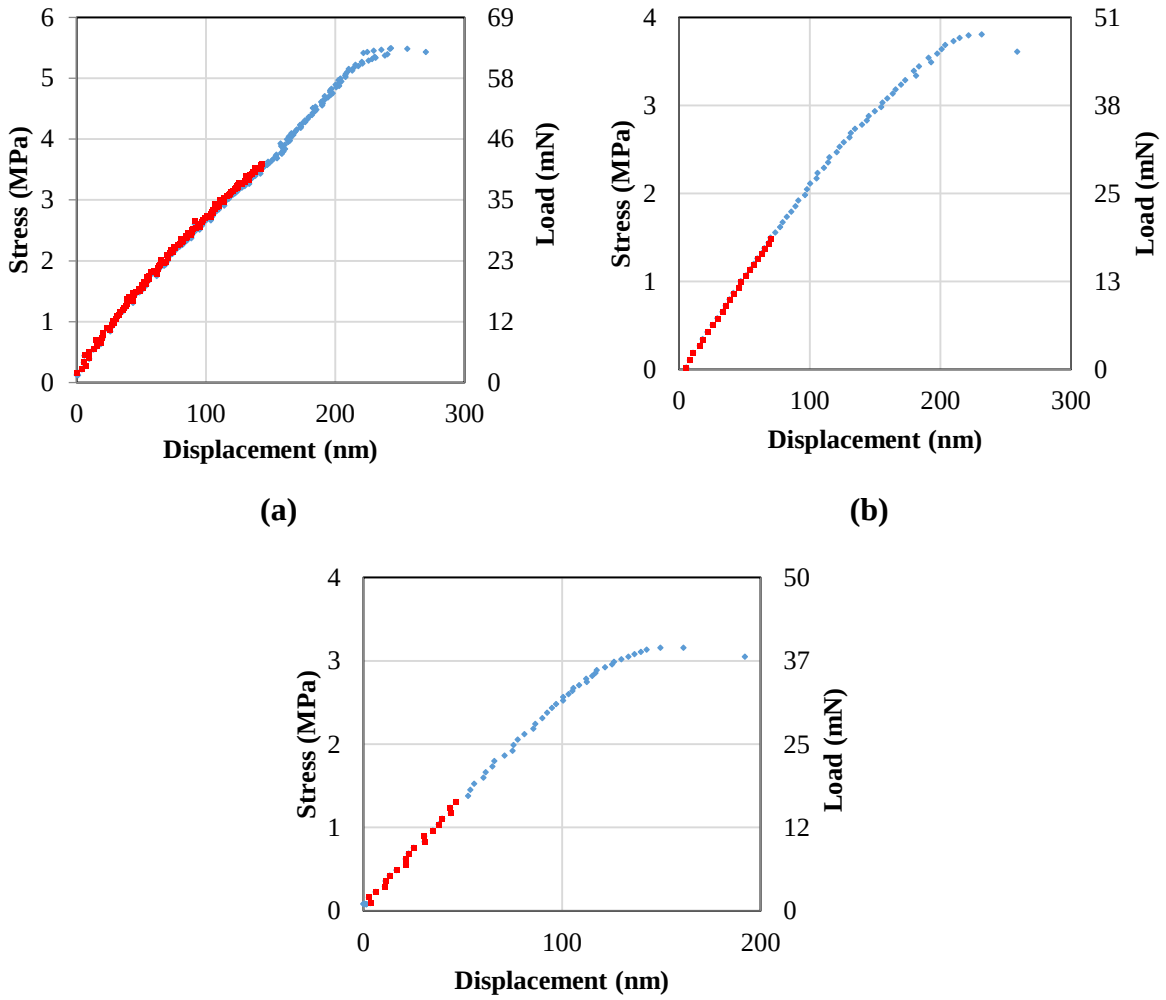

Figure C.7 Shear behavior of 10-turn Cu spring films with 2000 nm seed spacing. The red data points were used to compute the shear stiffness.

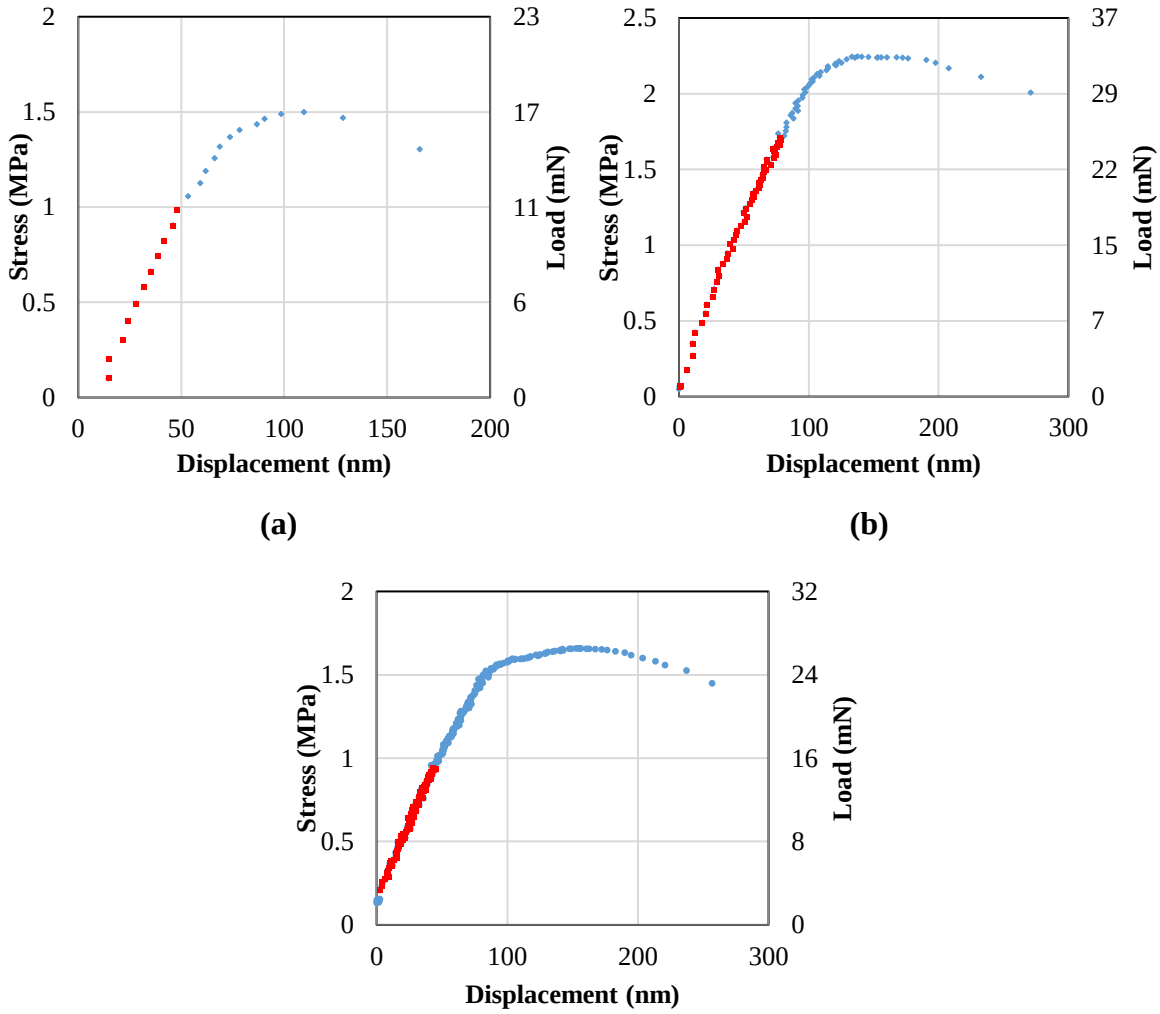

Figure C.8 Shear behavior of 10-turn Cu spring films with 2400 nm seed spacing. The red data points were used to compute the shear stiffness.

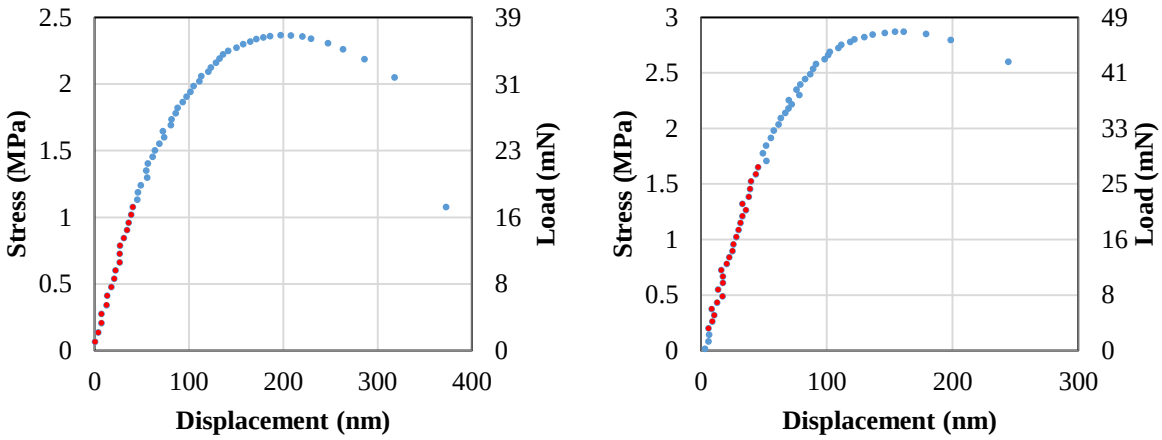

(a) **(b)**

Figure C.9 Shear behavior of 10-turn Cu spring films with 2800 nm seed spacing. The red data points were used to compute the shear stiffness.

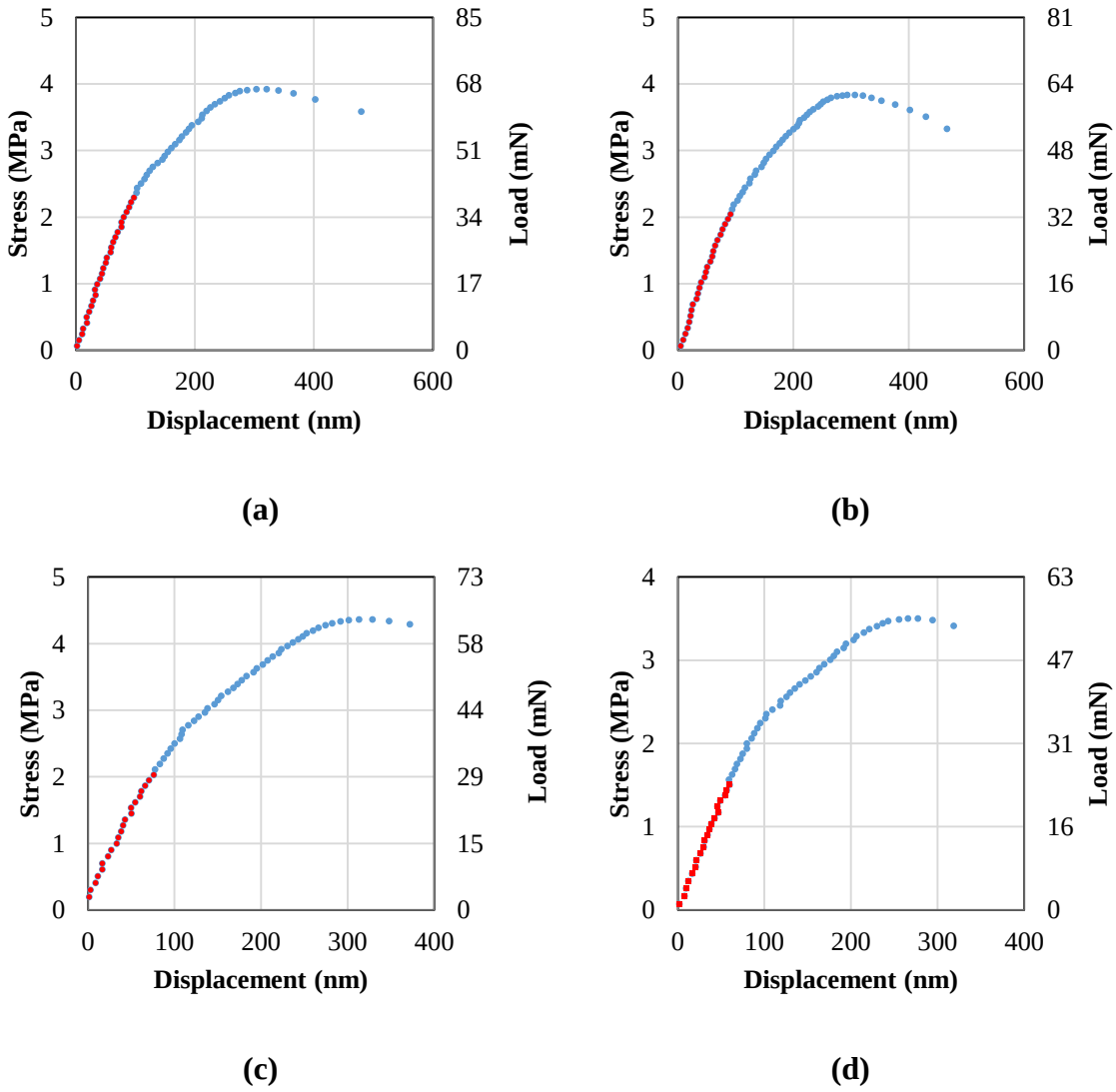

Figure C.10 Shear behavior of 10-turn Cu spring films with 3200 nm seed spacing. The red data points were used to compute the shear stiffness.

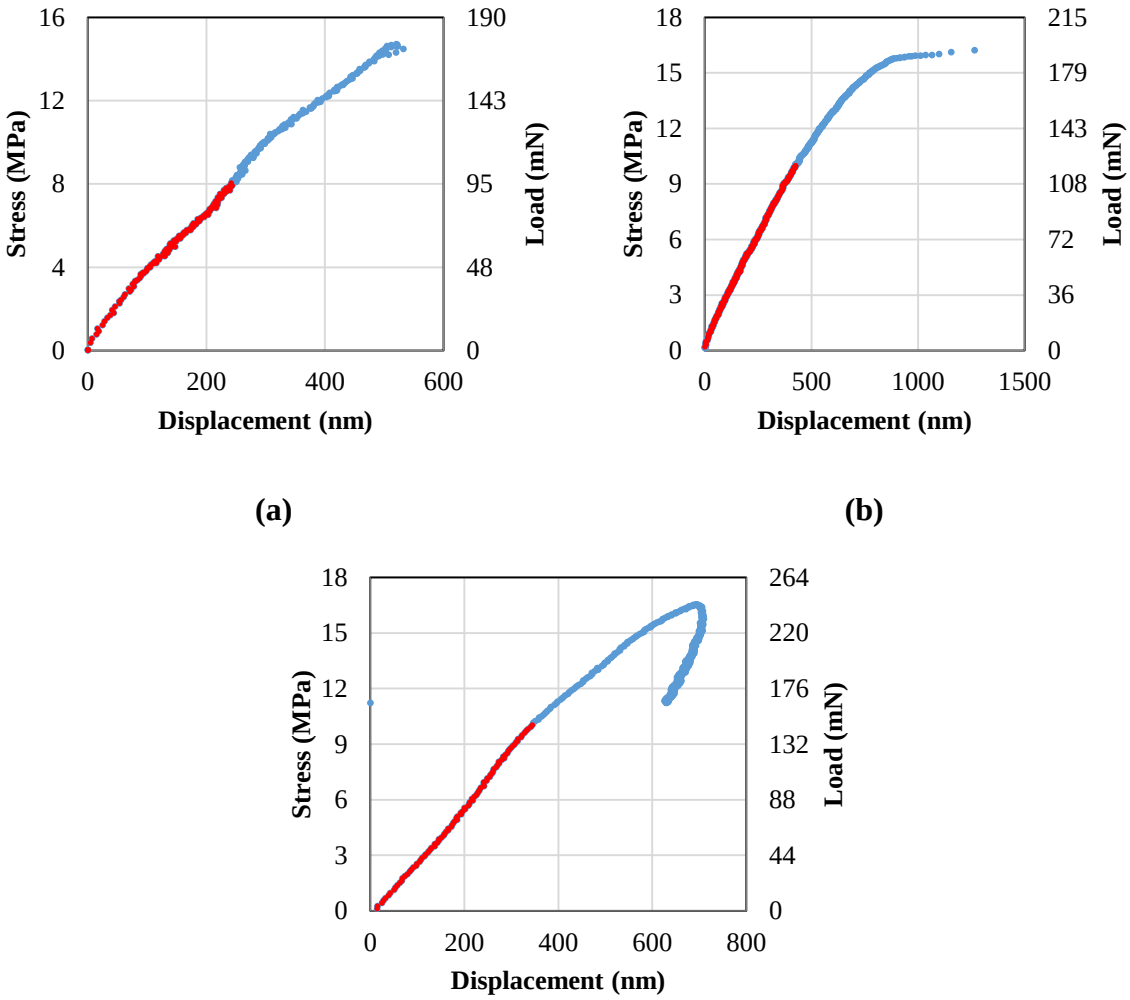

Figure C.11 Shear behavior of 10-turn Cu spring films with 3200 nm seed spacing. The red data points were used to compute the shear stiffness.

Appendix D

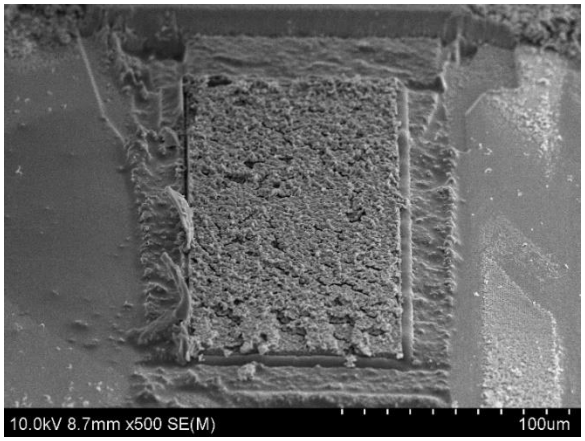

(a)

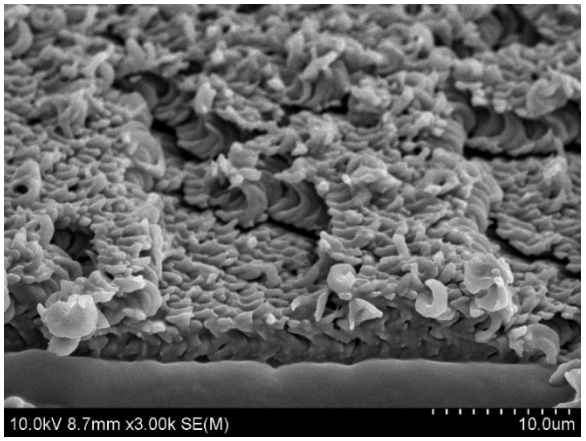

(b)

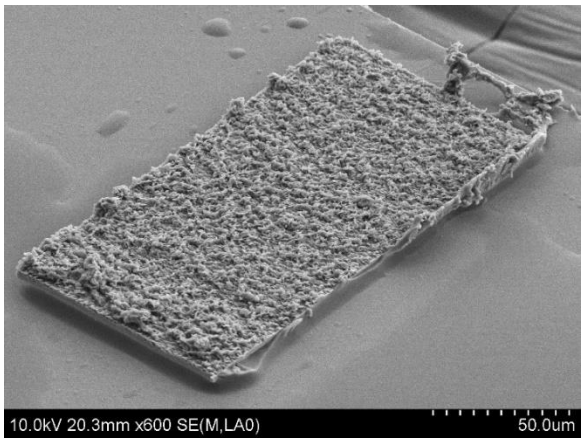

(c)

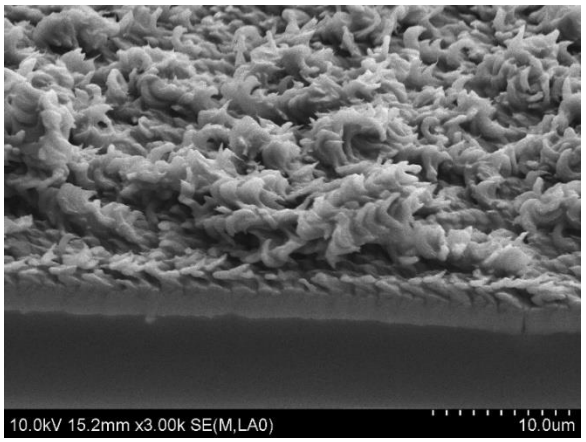

(d)

Figure D.1 Shear failure surfaces of a Si film with 4 turns and 900 nm seed spacing: **(a,b)** substrate, **(c,d)** cap.

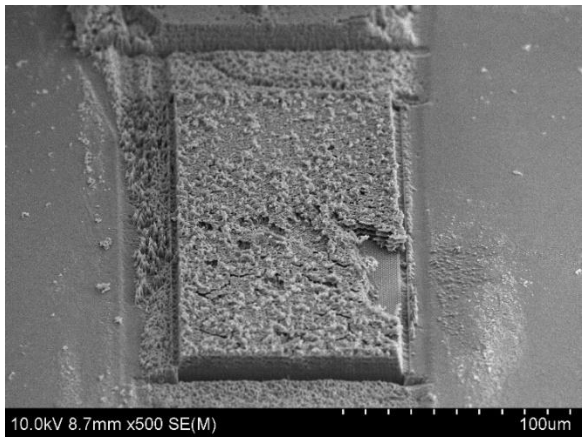

(a)

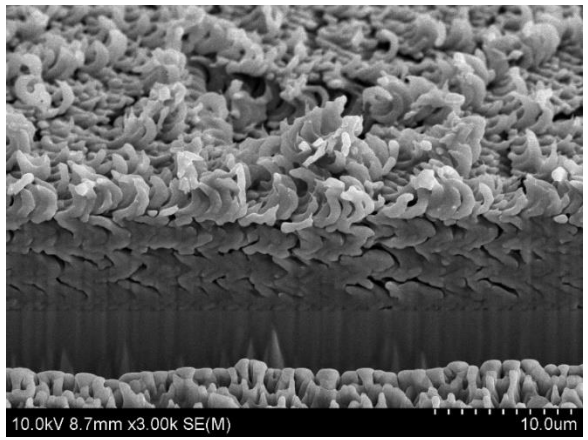

(b)

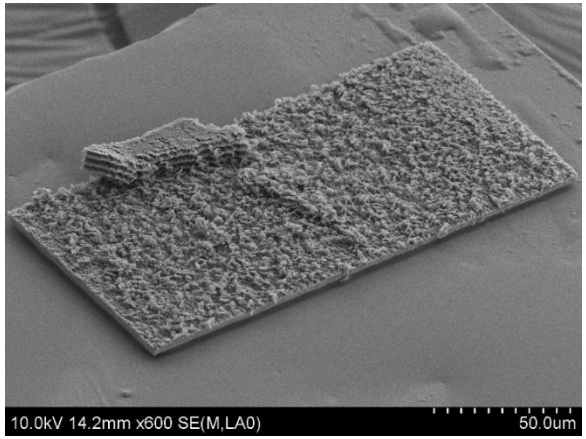

(c)

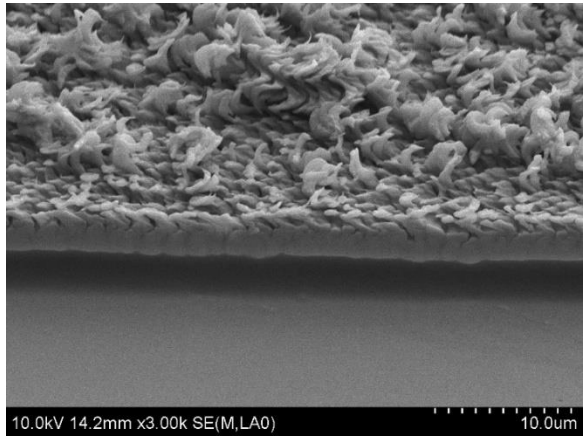

(d)

Figure D.2 Shear failure surfaces of a Si film with 4 turns and 900 nm seed spacing: **(a,b)** substrate, **(c,d)** cap.

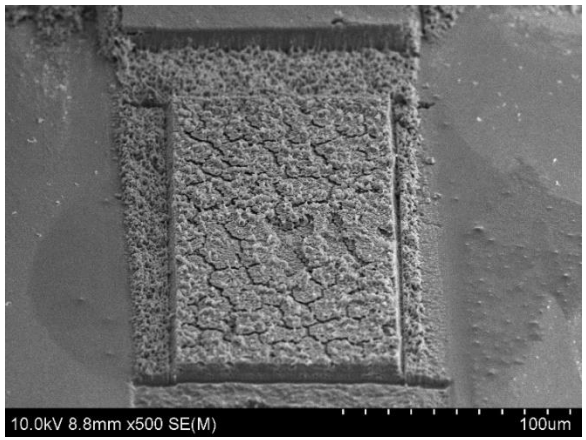

(a)

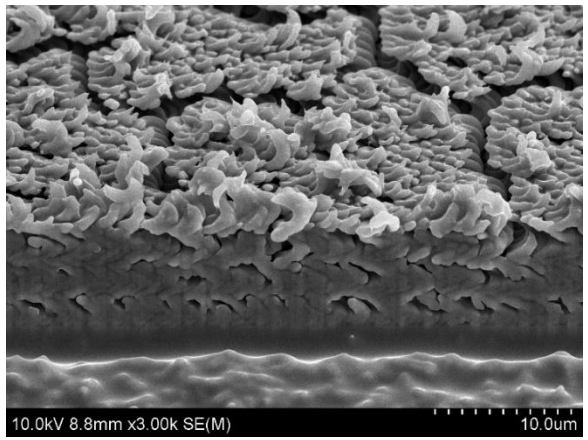

(b)

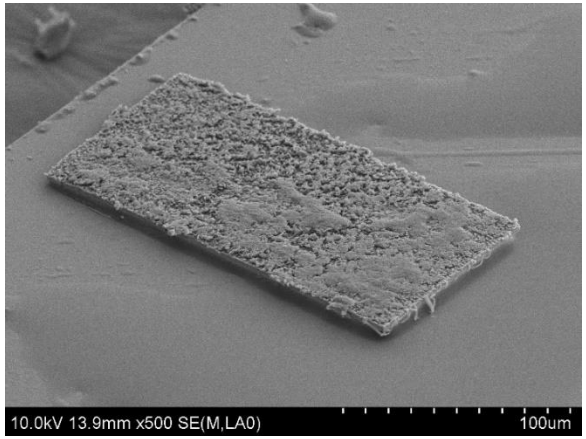

(c)

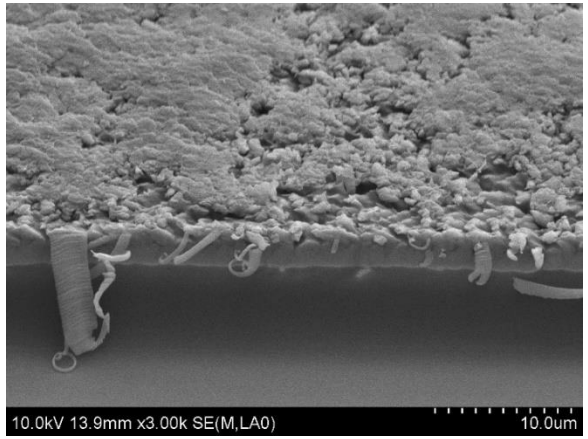

(d)

Figure D.3 Shear failure surfaces of a Si film with 4 turns and 900 nm seed spacing: **(a,b)** substrate, **(c,d)** cap.

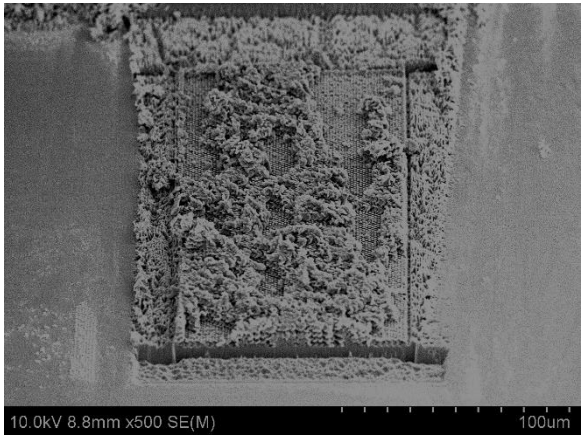

(a)

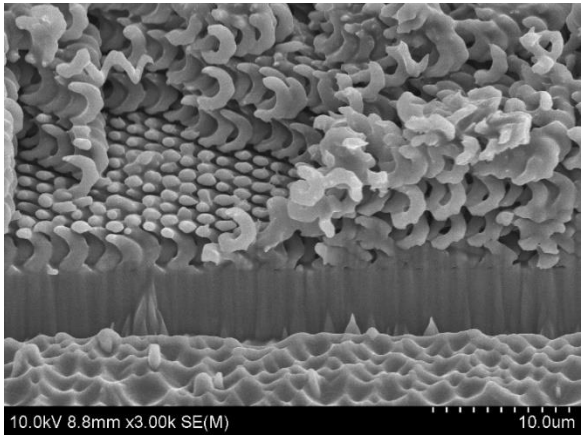

(b)

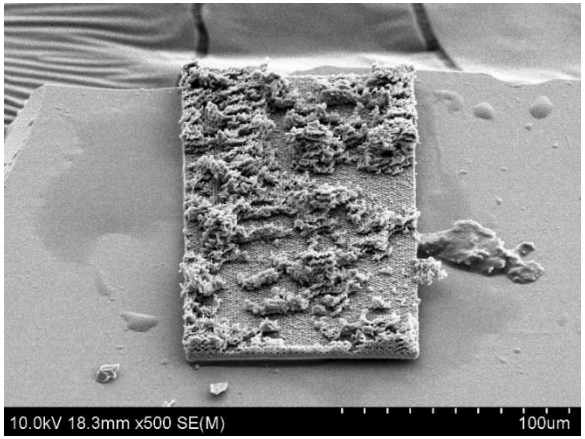

(c)

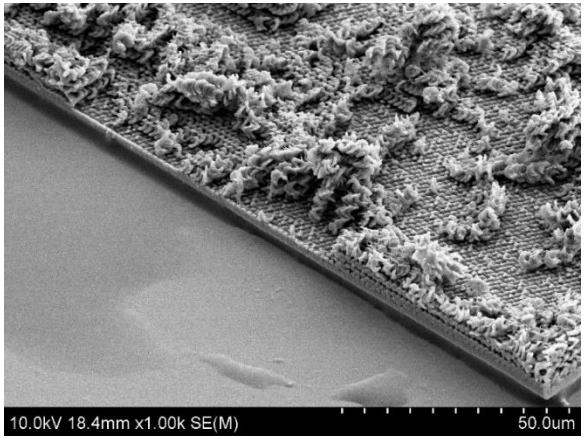

(d)

Figure D.4 Shear failure surfaces of a Si film with 4 turns and 1500 nm seed spacing: **(a,b)** substrate, **(c,d)** cap.

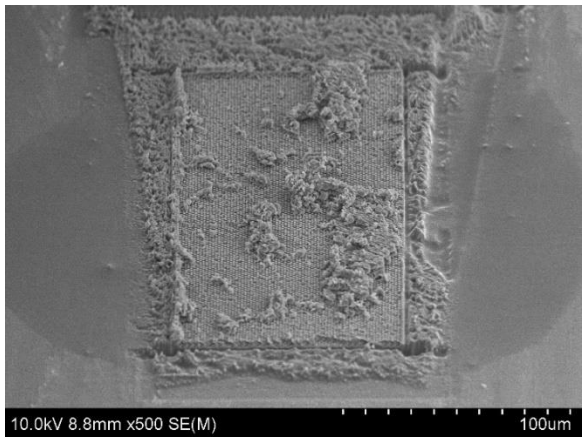

(a)

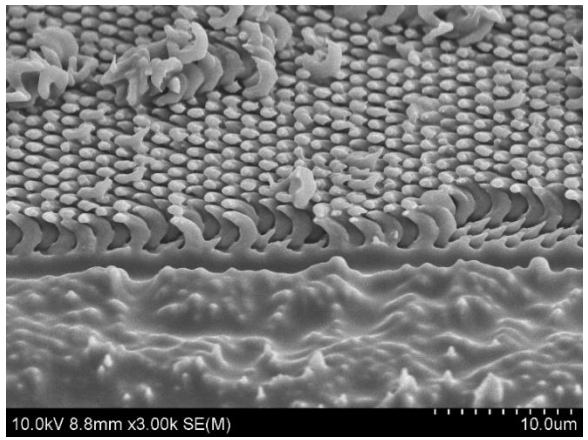

(b)

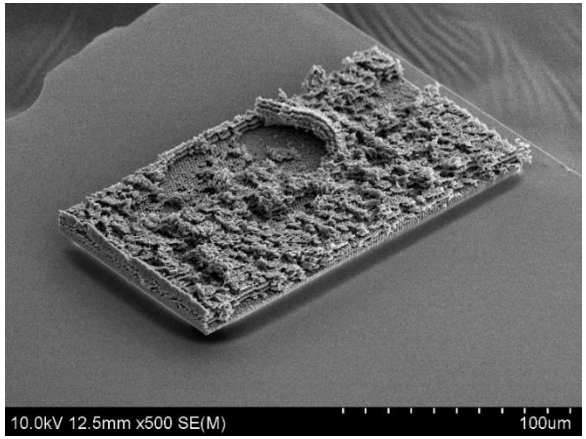

(c)

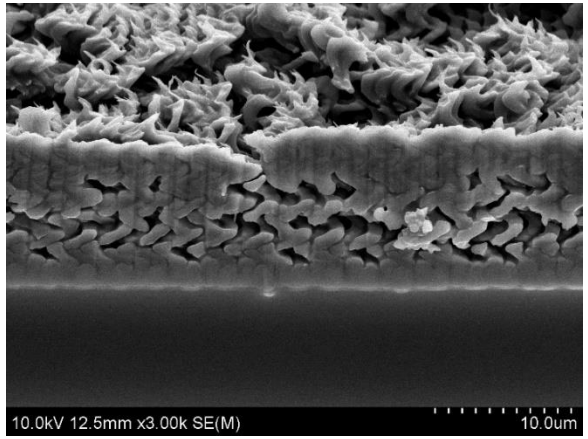

(d)

Figure D.5 Shear failure surfaces of a Si film with 4 turns and 1500 nm seed spacing: **(a,b)** substrate, **(c,d)** cap.

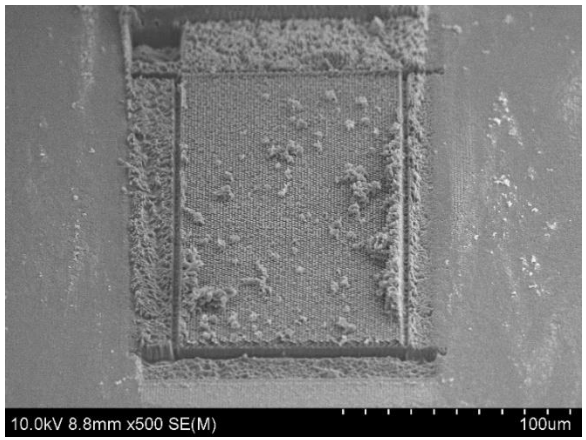

(a)

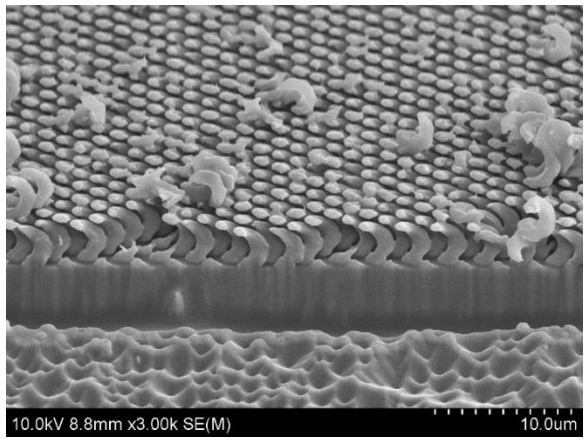

(b)

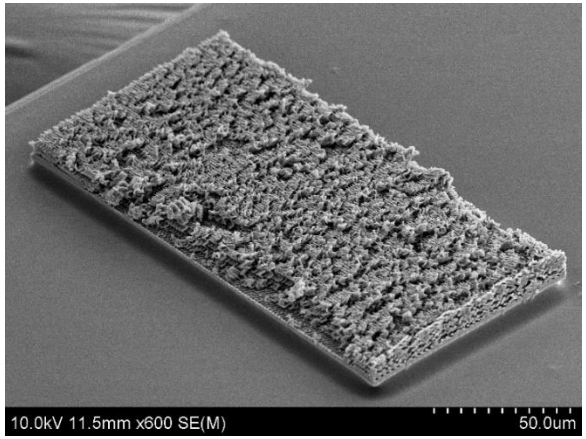

(c)

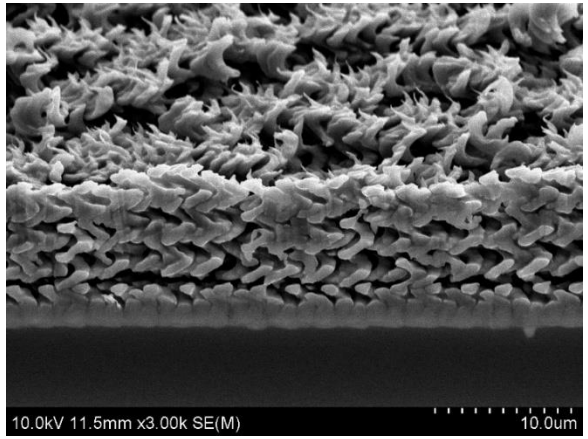

(d)

Figure D.6 Shear failure surfaces of a Si film with 4 turns and 1500 nm seed spacing: **(a,b)** substrate, **(c,d)** cap.

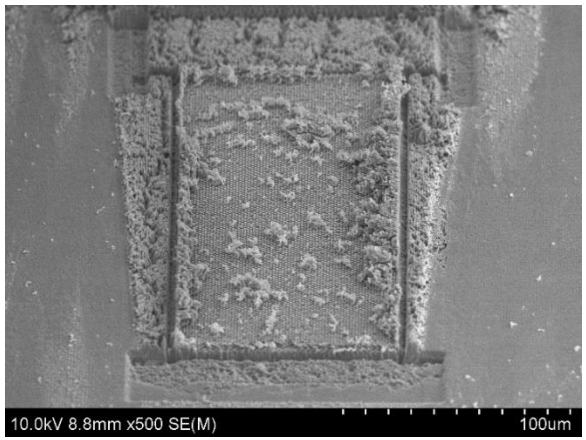

(a)

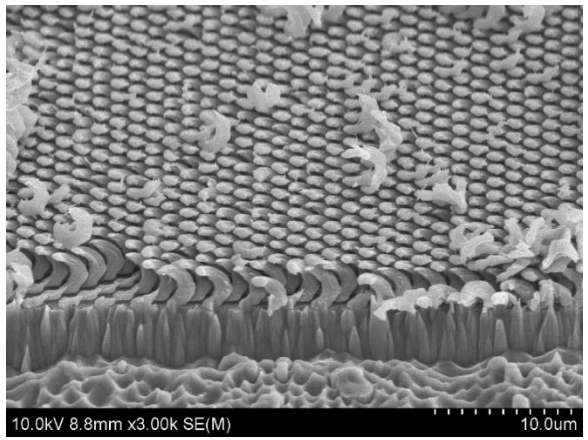

(b)

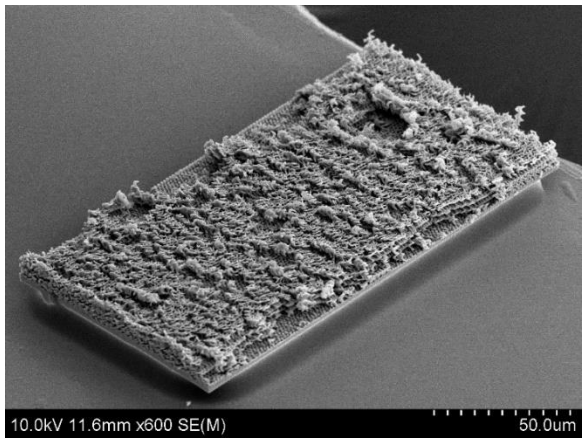

(c)

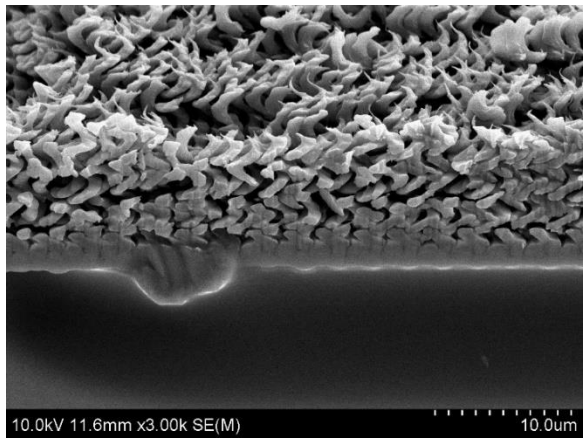

(d)

Figure D.7 Shear failure surfaces of a Si film with 4 turns and 1500 nm seed spacing: **(a,b)** substrate, **(c,d)** cap.

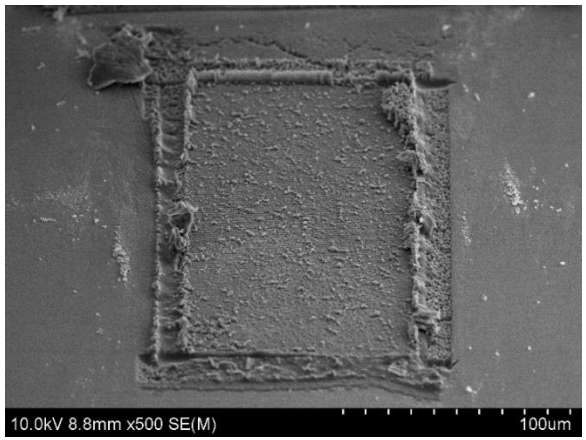

(a)

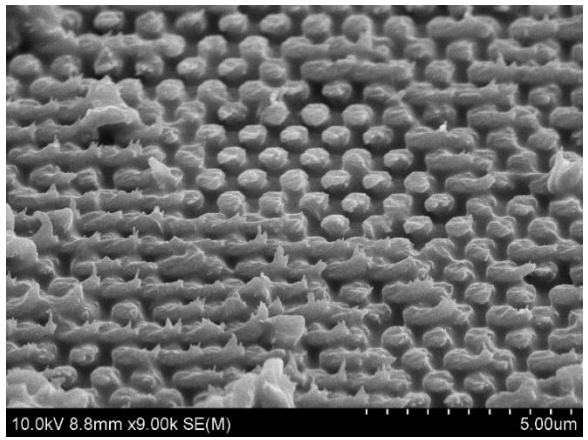

(b)

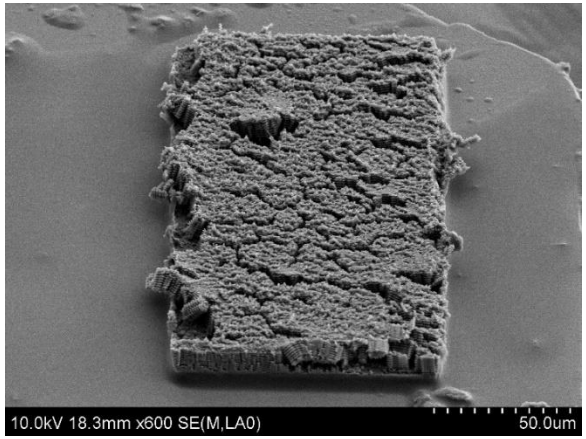

(c)

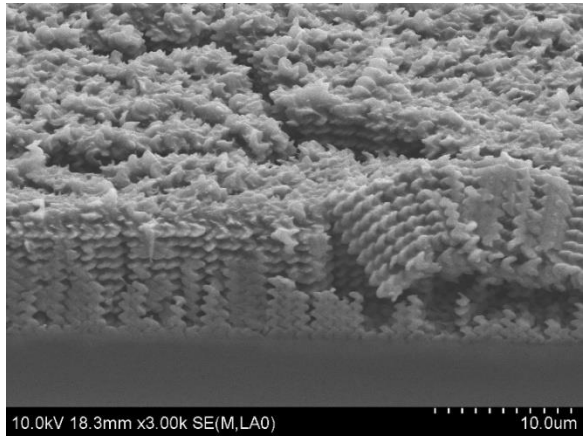

(d)

Figure D.8 Shear failure surfaces of a Si film with 10 turns and 900 nm seed spacing: **(a,b)** substrate, **(c,d)** cap.

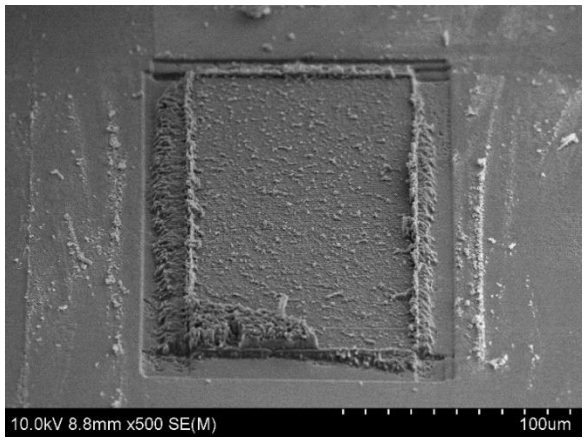

(a)

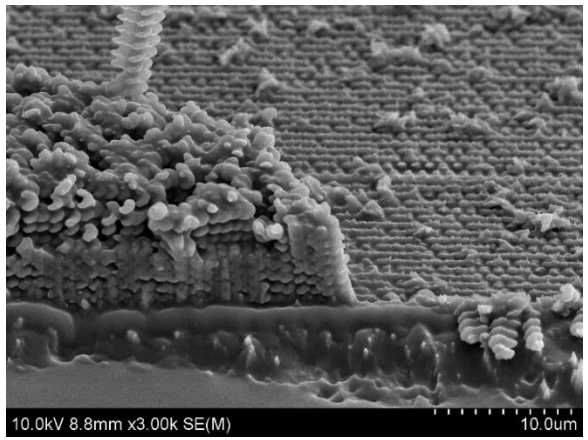

(b)

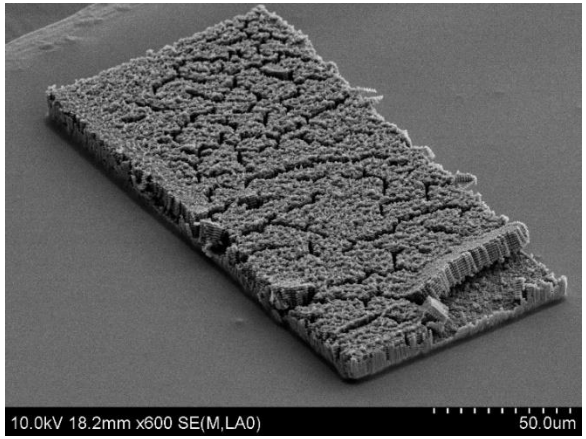

(c)

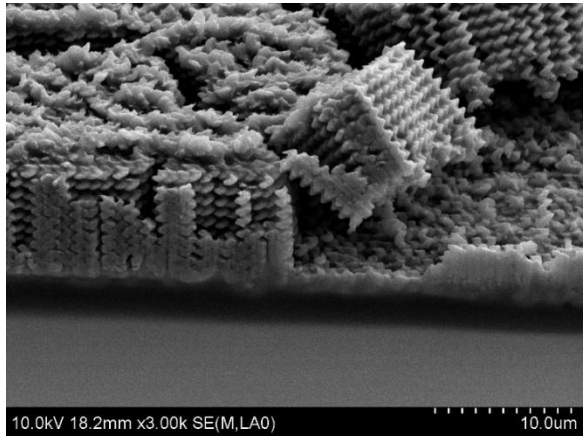

(d)

Figure D.9 Shear failure surfaces of a Si film with 10 turns and 900 nm seed spacing: **(a,b)** substrate, **(c,d)** cap.

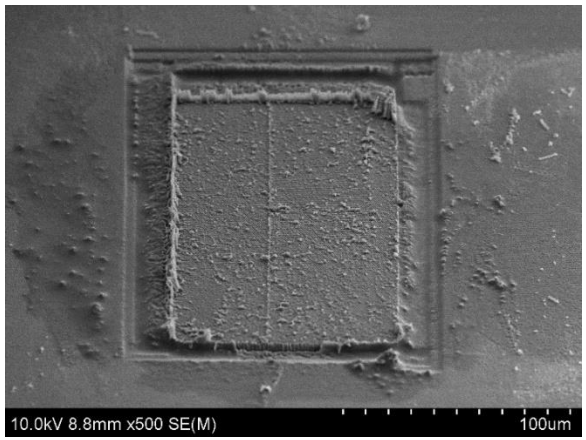

(a)

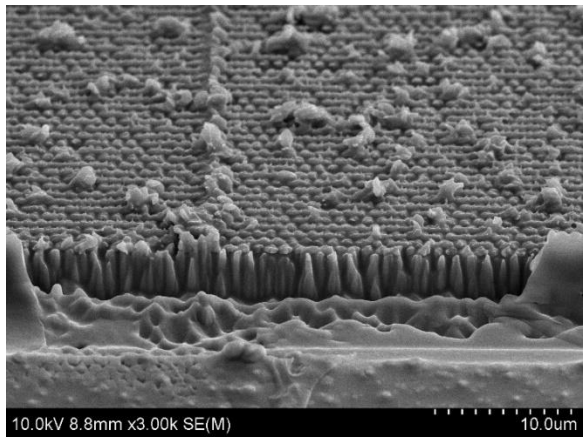

(b)

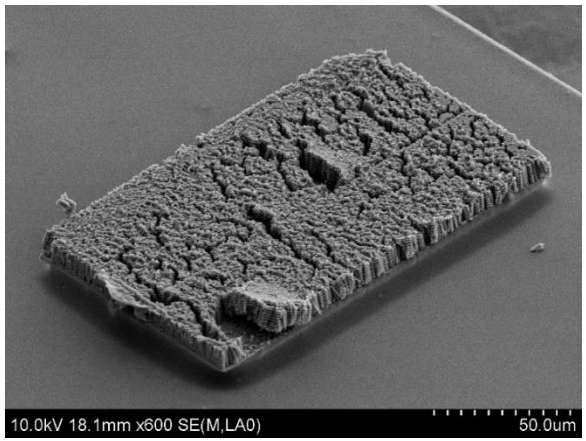

(c)

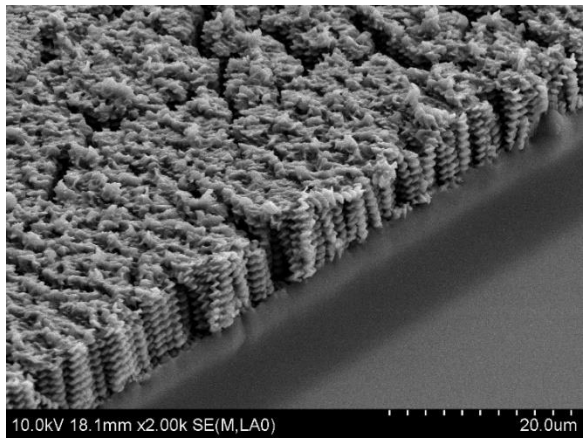

(d)

Figure D.10 Shear failure surfaces of a Si film with 10 turns and 900 nm seed spacing: **(a,b)** substrate, **(c,d)** cap.

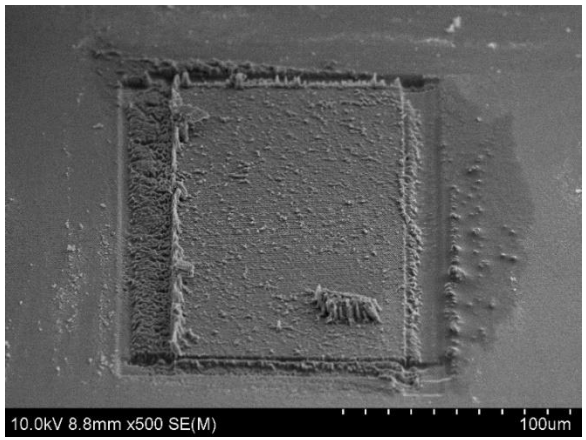

(a)

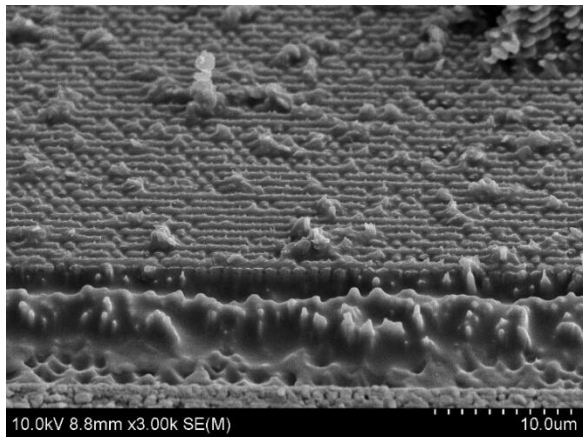

(b)

Figure D.11 Shear failure at the substrate side of a Si film with 10 turns and 900 nm seed spacing.

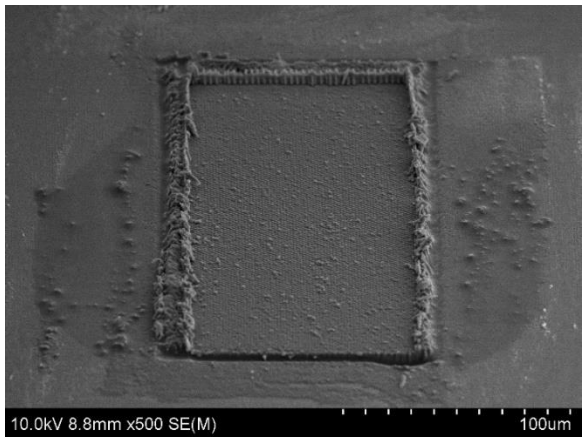

(a)

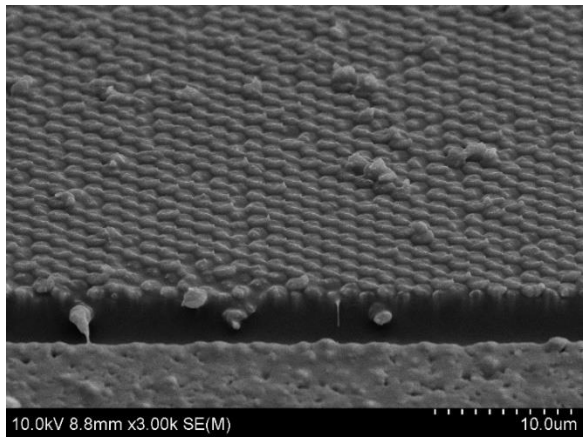

(b)

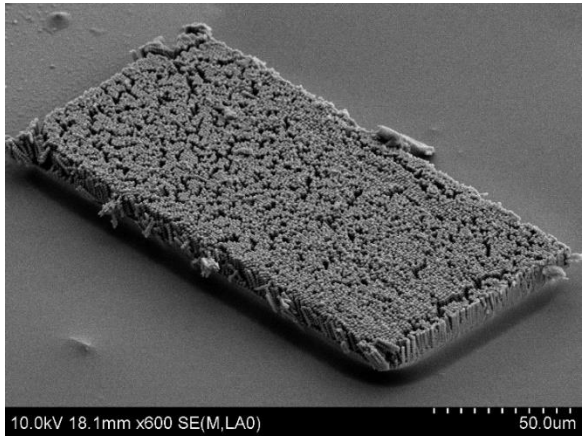

(c)

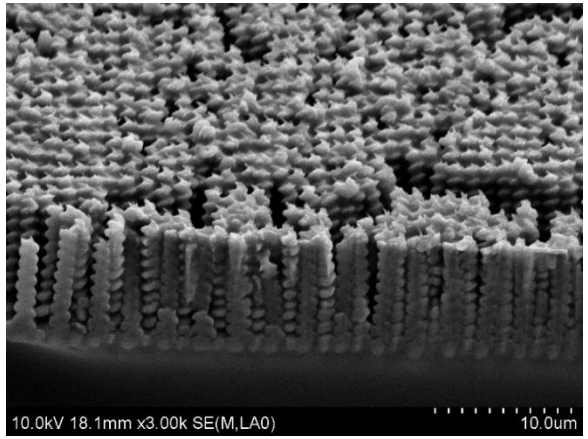

(d)

Figure D.12 Shear failure surfaces of a Si film with 10 turns and 1500 nm seed spacing: **(a,b)** substrate, **(c,d)** cap.

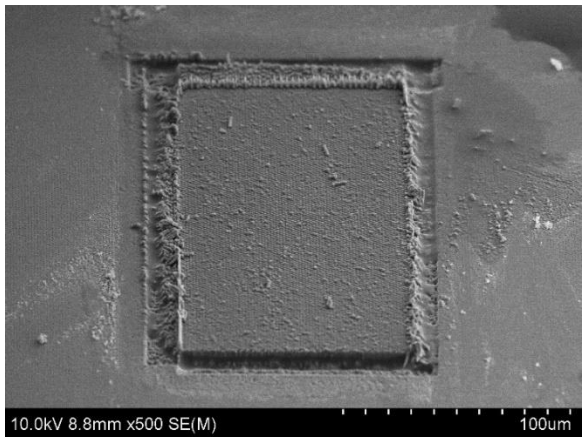

(a)

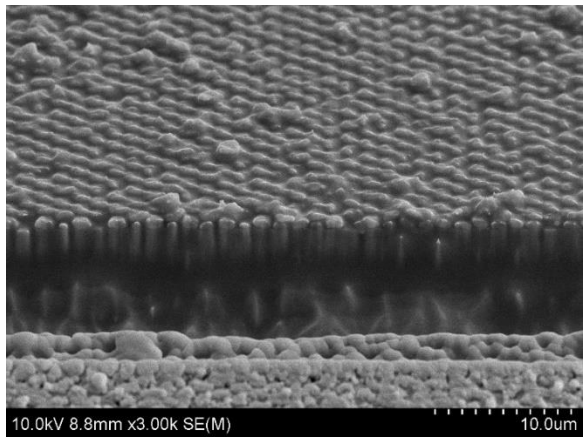

(b)

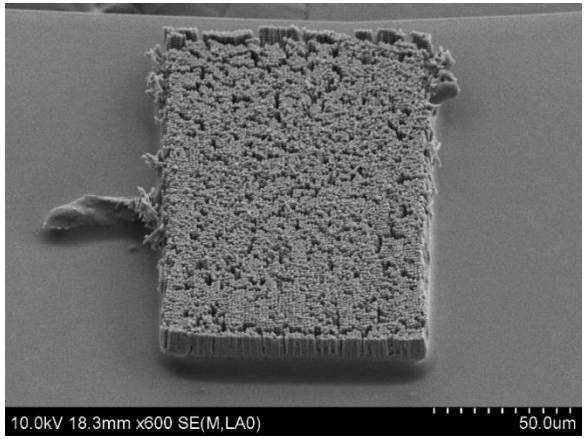

(c)

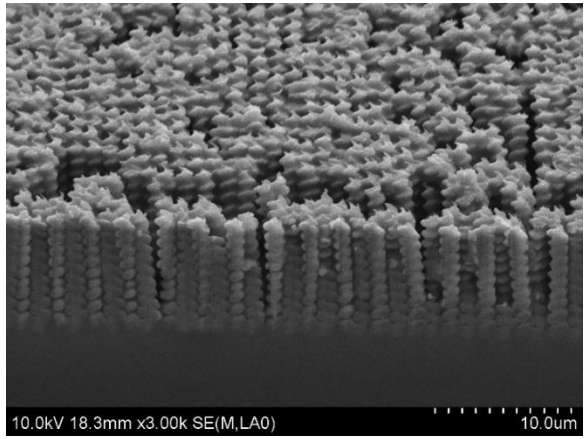

(d)

Figure D.13 Shear failure surfaces of a Si film with 10 turns and 1500 nm seed spacing: **(a,b)** substrate, **(c,d)** cap.

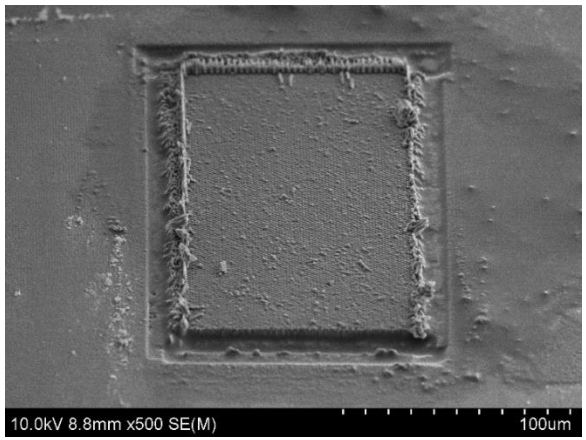

(a)

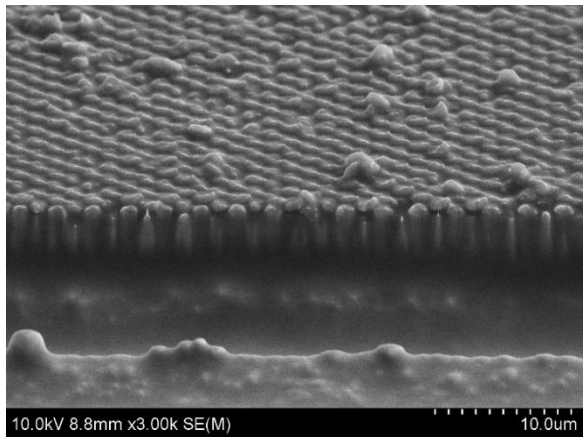

(b)

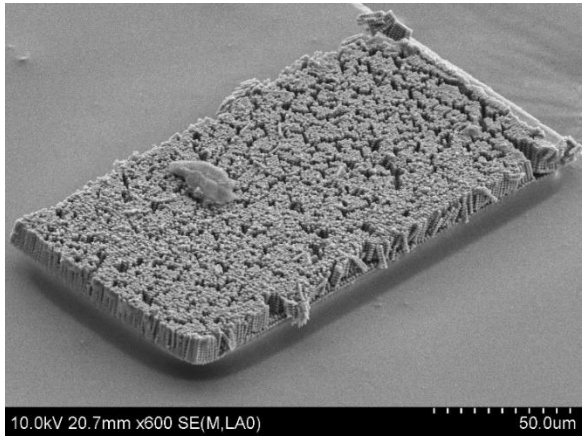

(c)

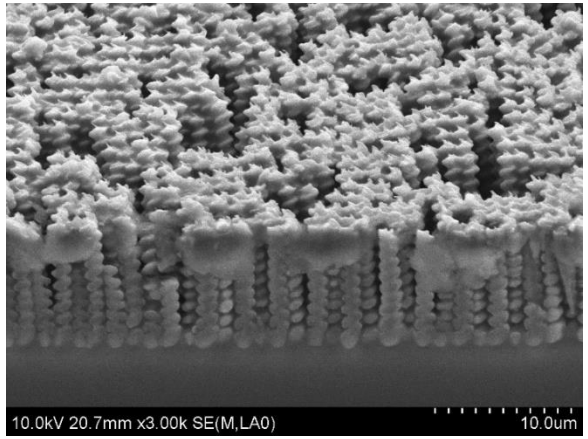

(d)

Figure D.14 Shear failure surfaces of a Si film with 10 turns and 1500 nm seed spacing: **(a,b)** substrate, **(c,d)** cap.

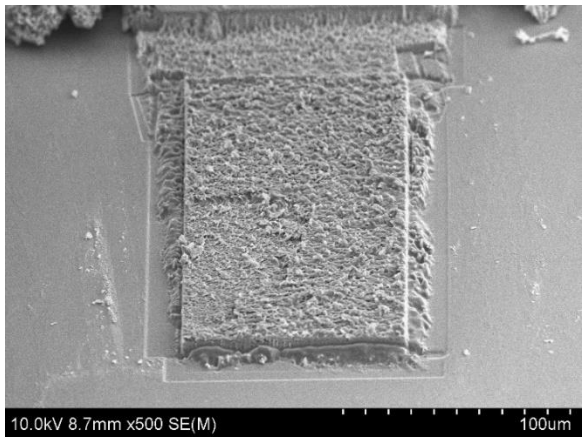

(a)

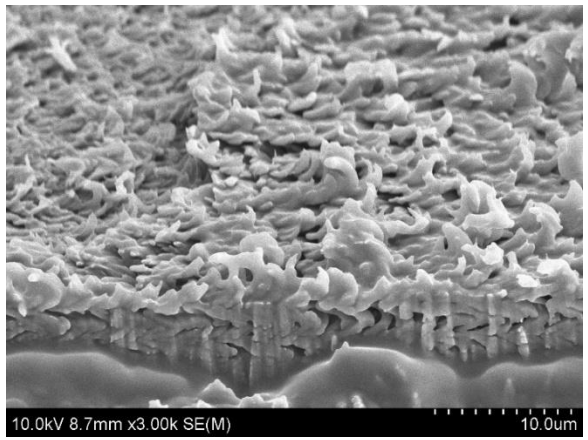

(b)

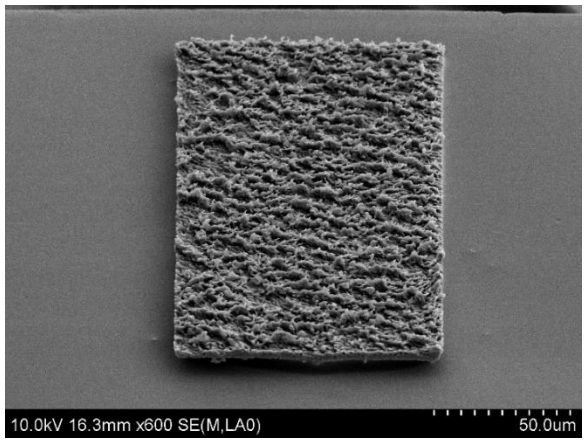

(c)

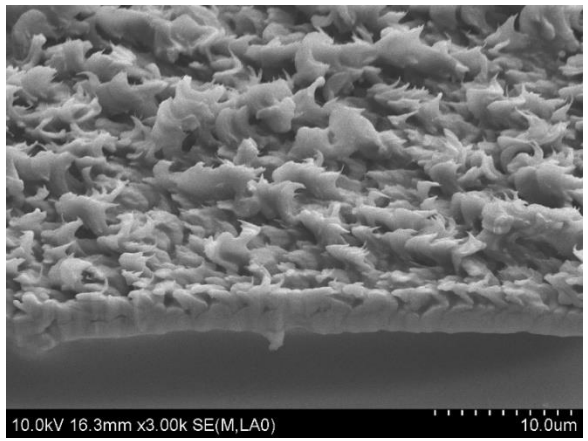

(d)

Figure D.15 Shear failure surfaces of a Si film with 4 turns and unseeded substrate: **(a,b)** substrate, **(c,d)** cap.

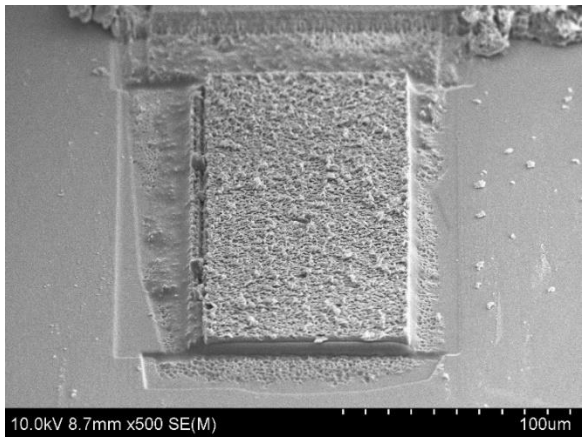

(a)

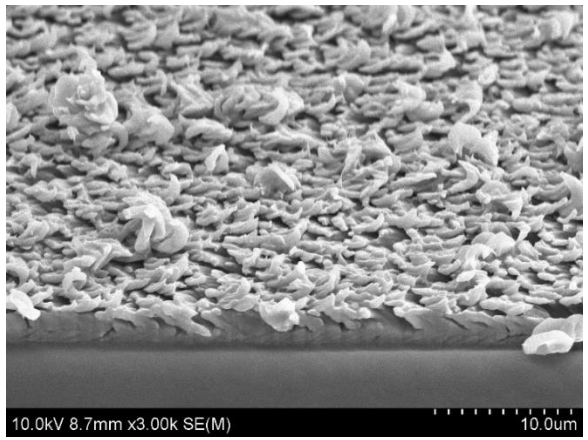

(b)

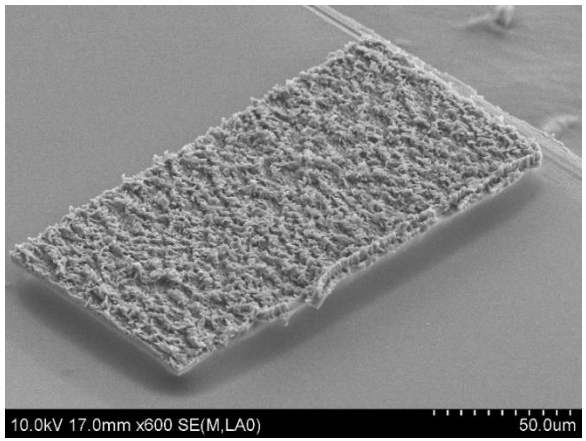

(c)

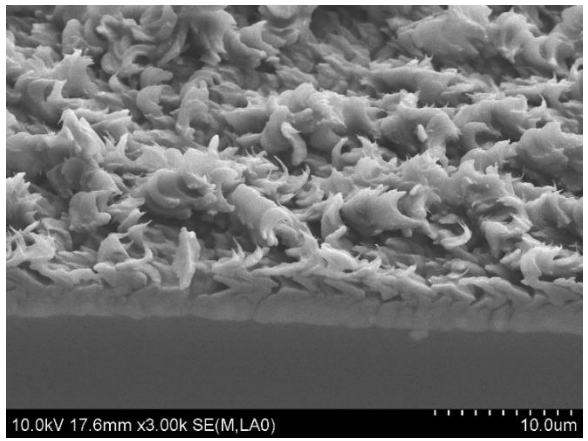

(d)

Figure D.16 Shear failure surfaces of a Si film with 4 turns and unseeded substrate: **(a,b)** substrate, **(c,d)** cap.

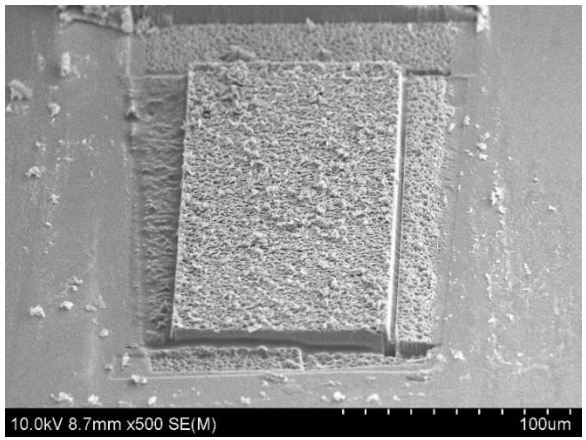

(a)

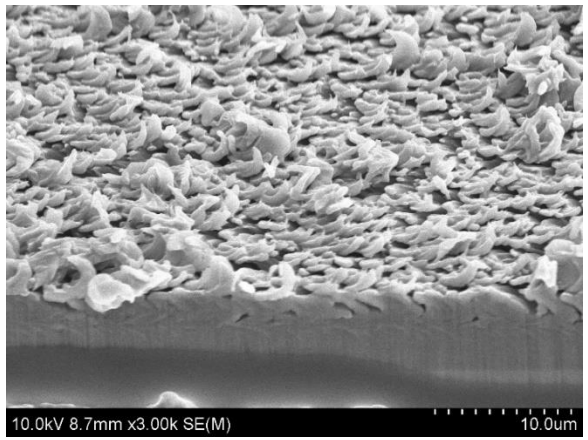

(b)

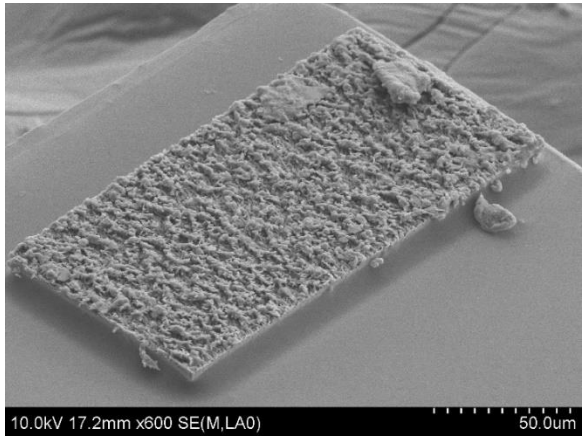

(c)

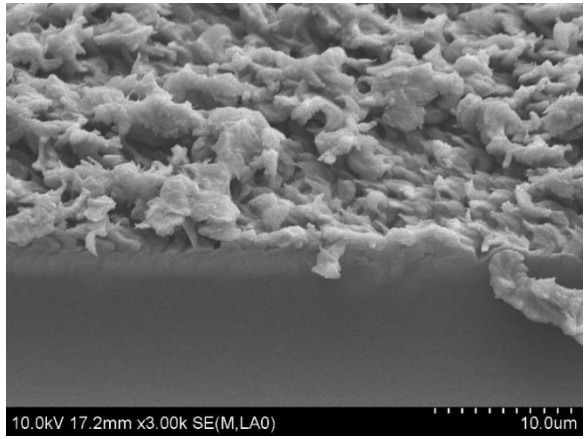

(d)

Figure D.17 Shear failure surfaces of a Si film with 4 turns and unseeded substrate: **(a,b)** substrate, **(c,d)** cap.

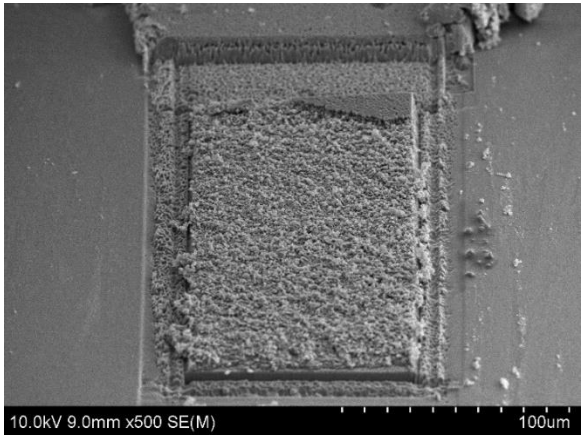

(a)

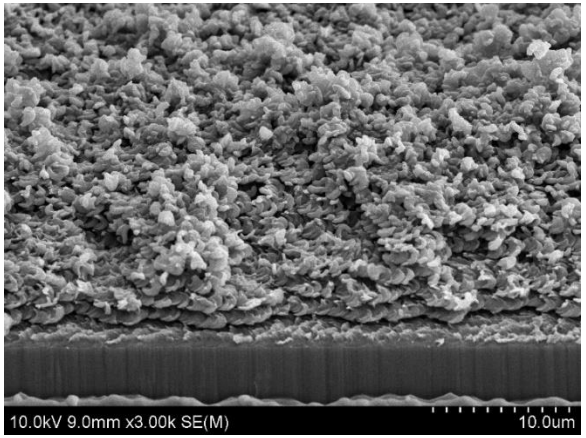

(b)

Figure D.18 Shear failure at the substrate side of a Si film with 10 turns and unseeded substrate.

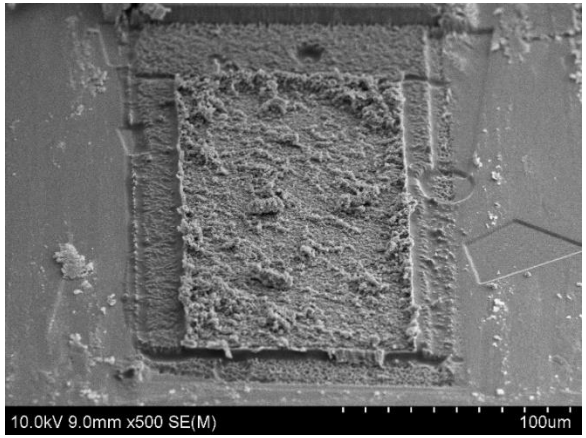

(a)

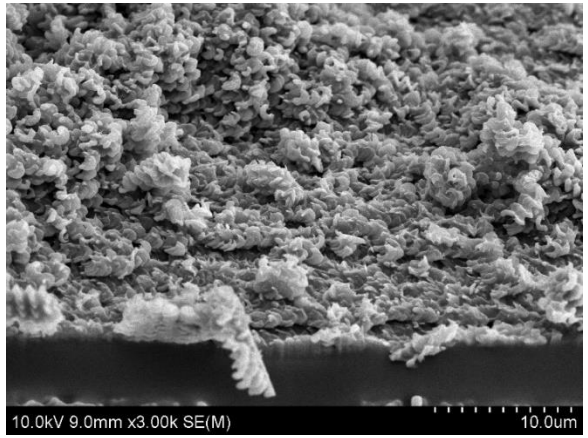

(b)

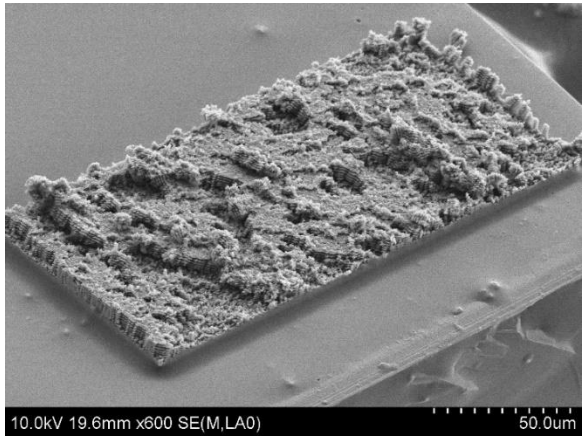

(c)

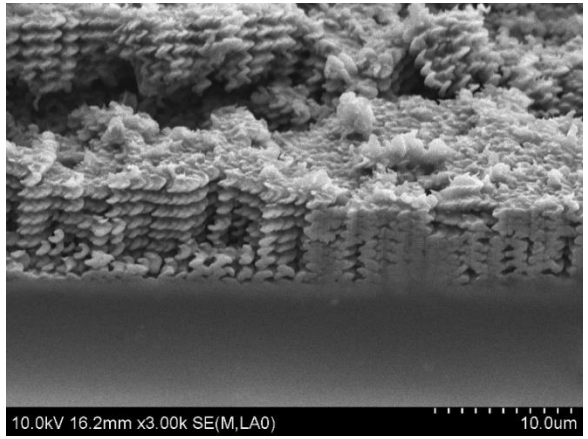

(d)

Figure D.19 Shear failure surfaces of a Si film with 10 turns and unseeded substrate: **(a,b)** substrate, **(c,d)** cap.

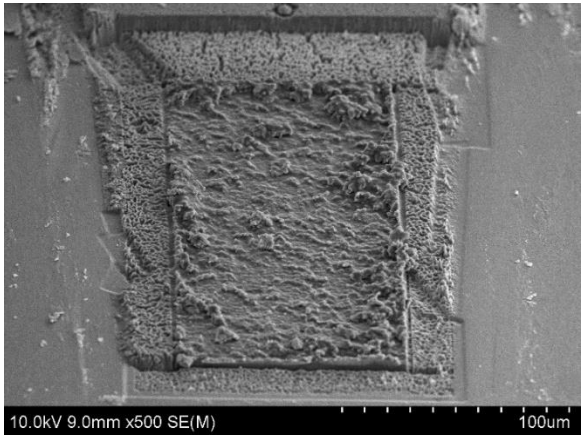

(a)

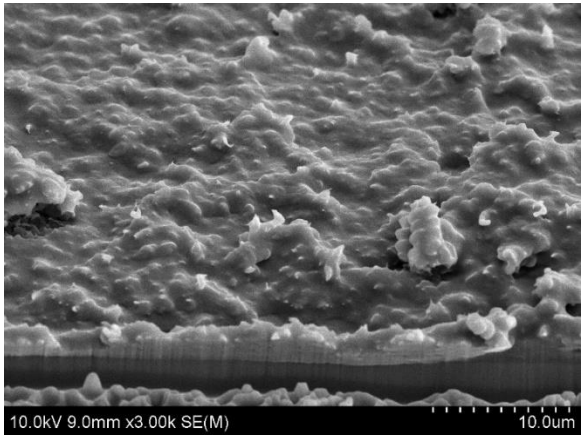

(b)

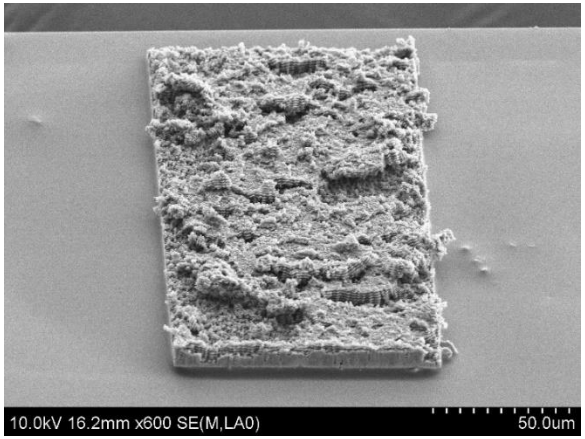

(c)

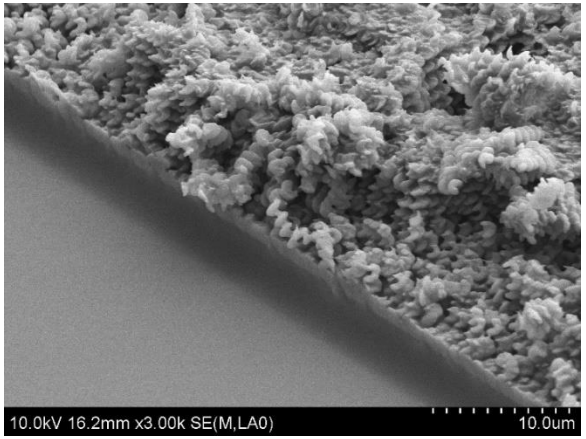

(d)

Figure D.20 Shear failure surfaces of a Si film with 10 turns and unseeded substrate: **(a,b)** substrate, **(c,d)** cap.

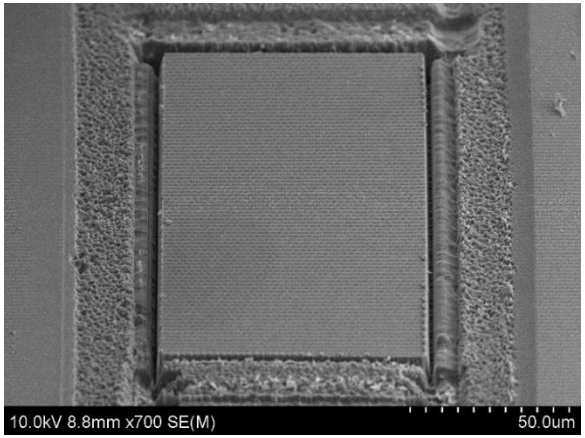

(a)

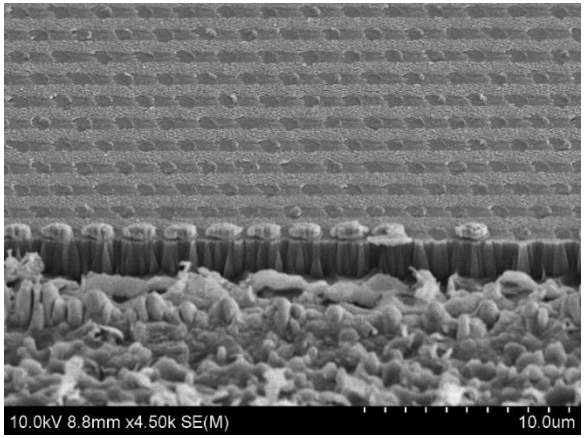

(b)

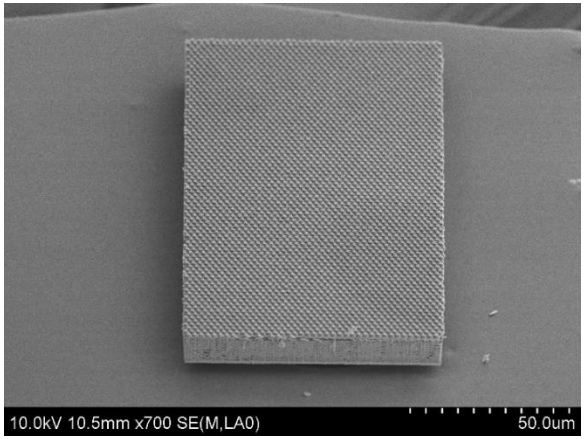

(c)

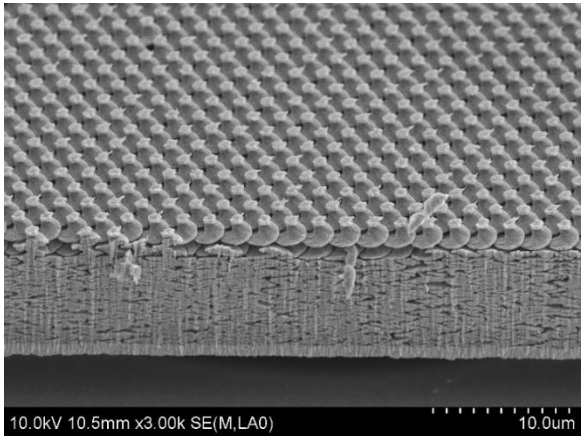

(d)

Figure D.21 Shear failure surfaces of a Cu film with 10 turns and 2000 nm seed seeding: **(a,b)** substrate, **(c,d)** cap.

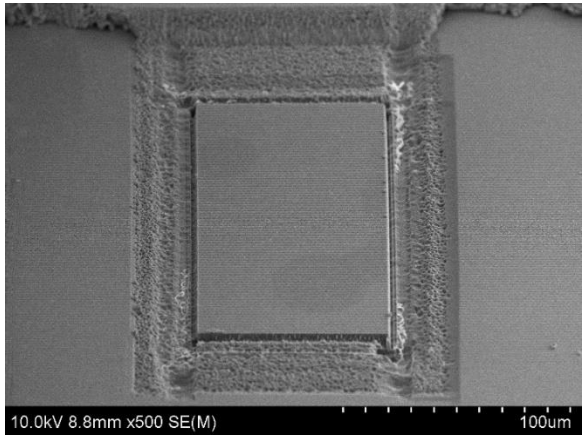

(a)

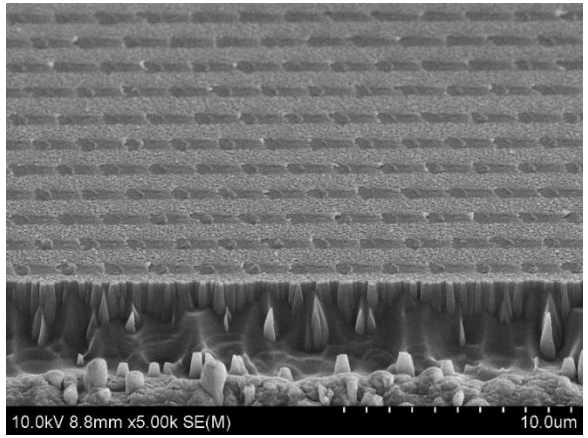

(b)

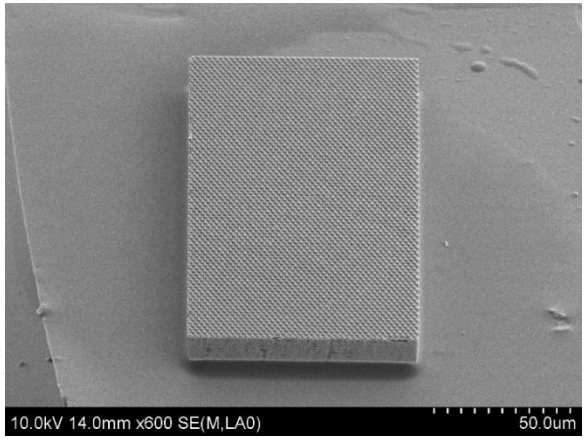

(c)

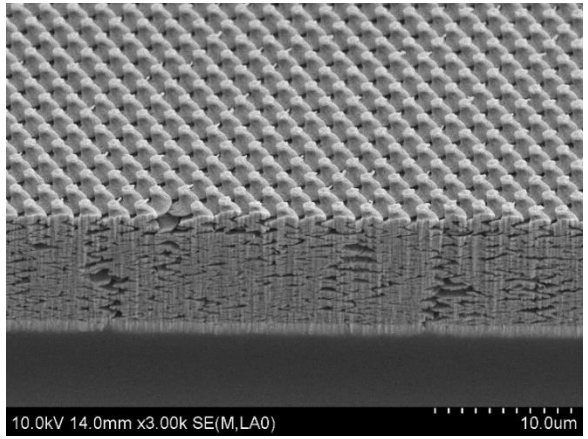

(d)

Figure D.22 Shear failure surfaces of a Cu film with 10 turns and 2000 nm seed seeding: **(a,b)** substrate, **(c,d)** cap.

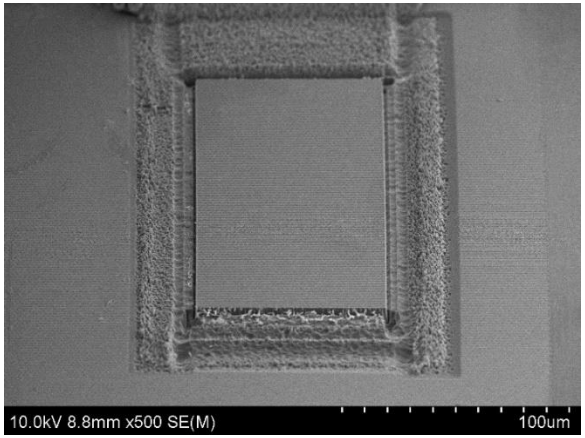

(a)

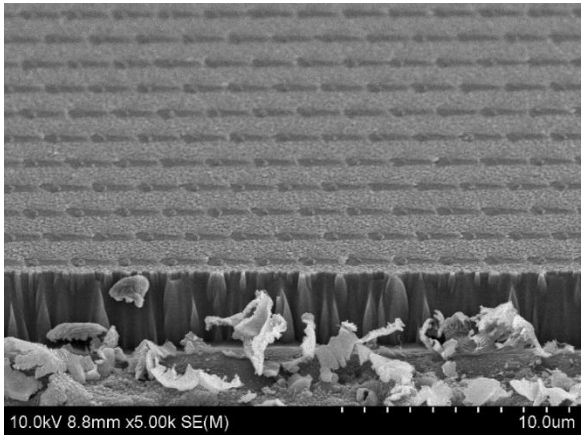

(b)

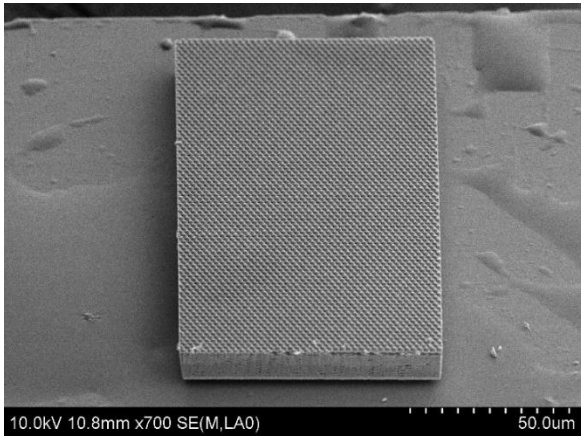

(c)

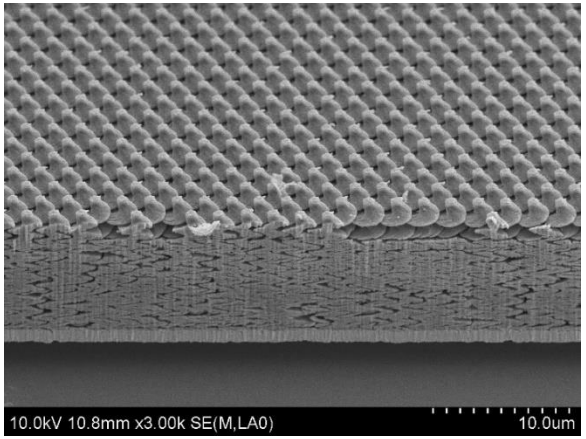

(d)

Figure D.23 Shear failure surfaces of a Cu film with 10 turns and 2000 nm seed seeding: **(a,b)** substrate, **(c,d)** cap.

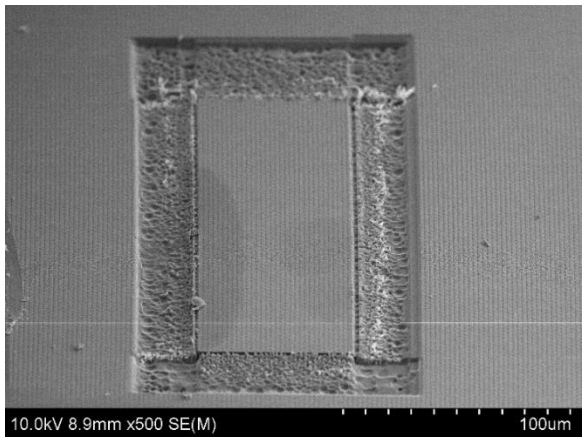

(a)

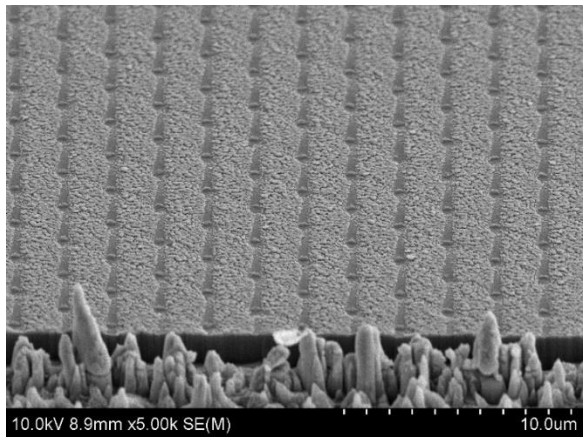

(b)

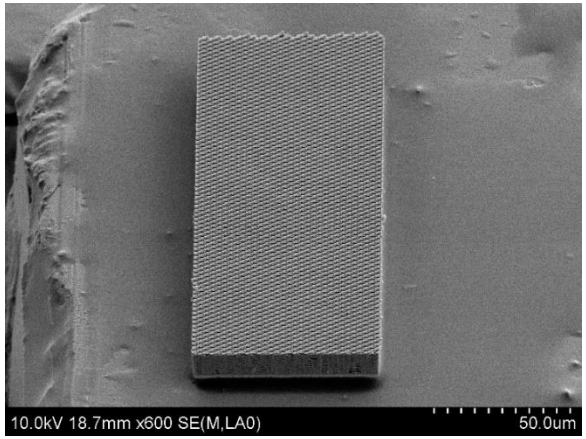

(c)

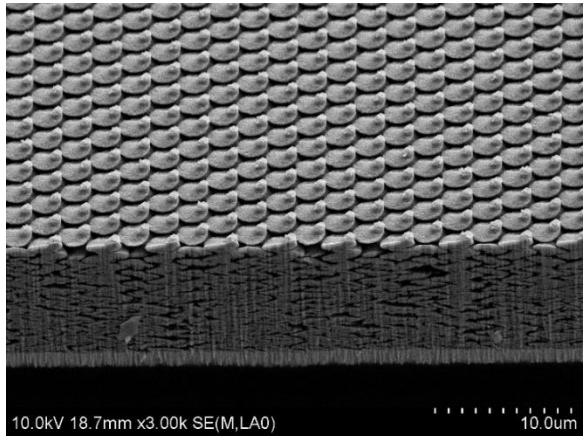

(d)

Figure D.24 Shear failure surfaces of a Cu film with 10 turns and 2400 nm seed seeding: **(a,b)** substrate, **(c,d)** cap.

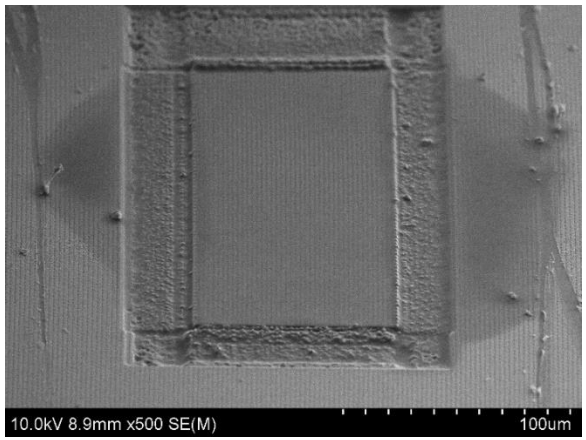

(a)

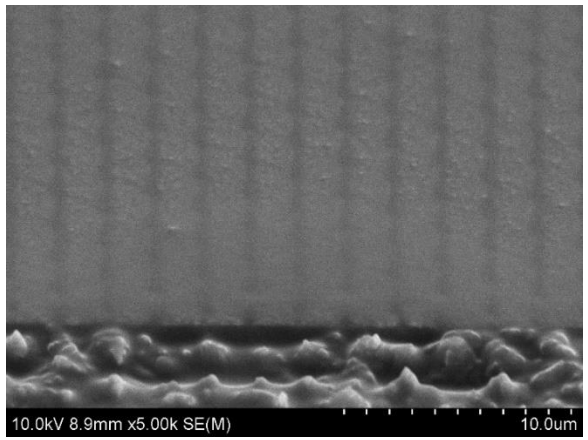

(b)

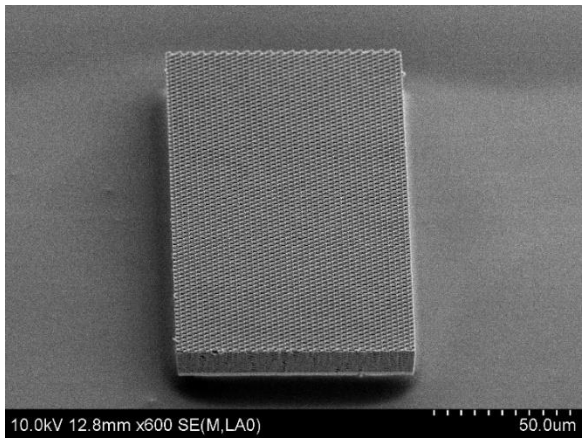

(c)

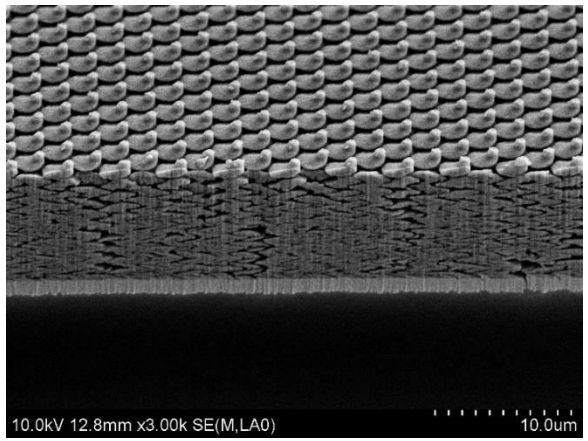

(d)

Figure D.25 Shear failure surfaces of a Cu film with 10 turns and 2400 nm seed seeding: **(a,b)** substrate, **(c,d)** cap.

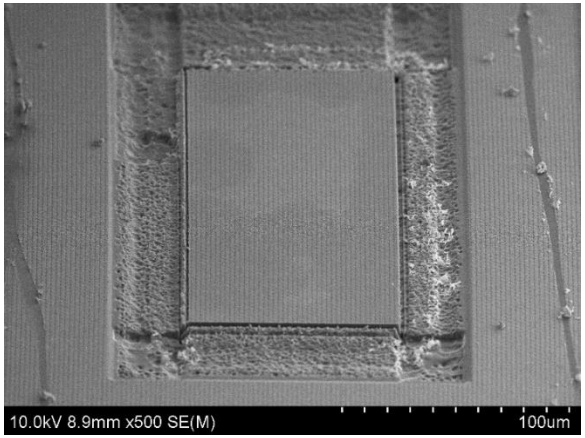

(a)

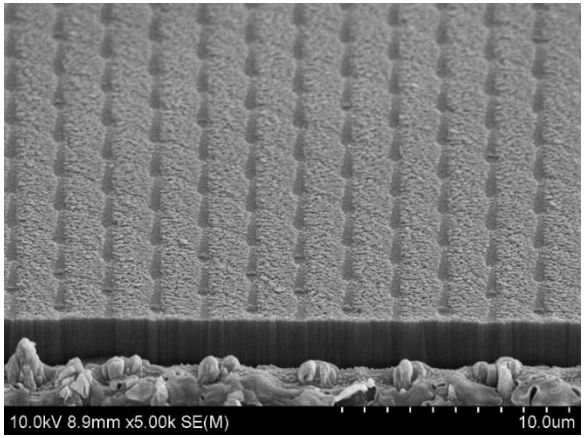

(b)

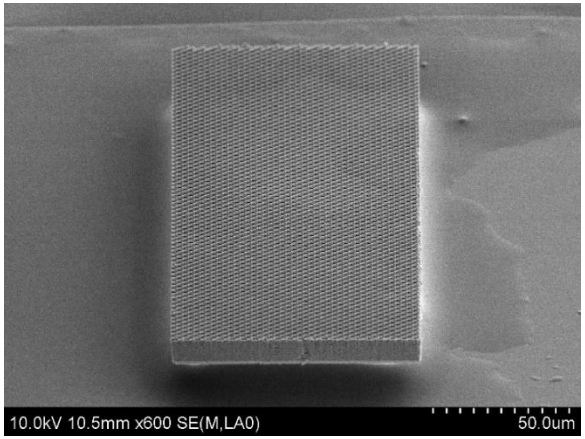

(c)

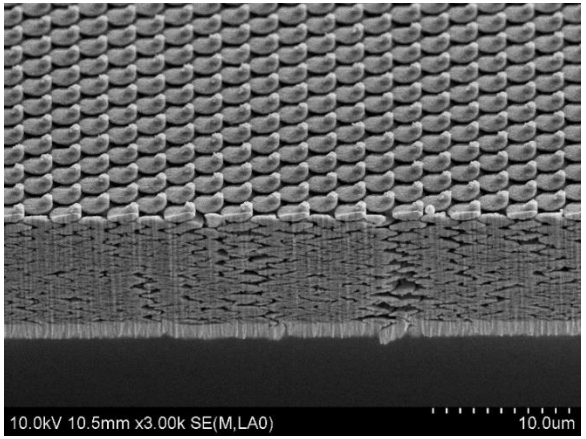

(d)

Figure D.26 Shear failure surfaces of a Cu film with 10 turns and 2400 nm seed seeding: **(a,b)** substrate, **(c,d)** cap.

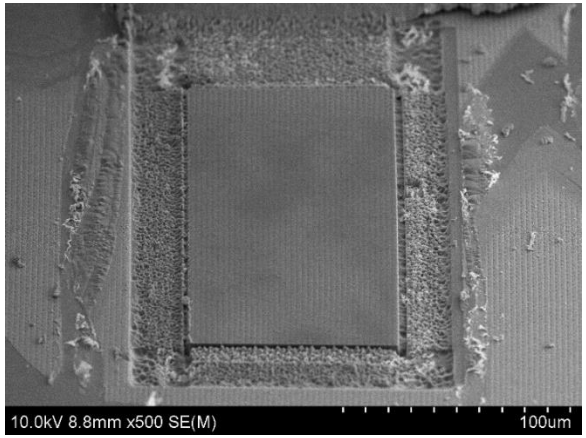

(a)

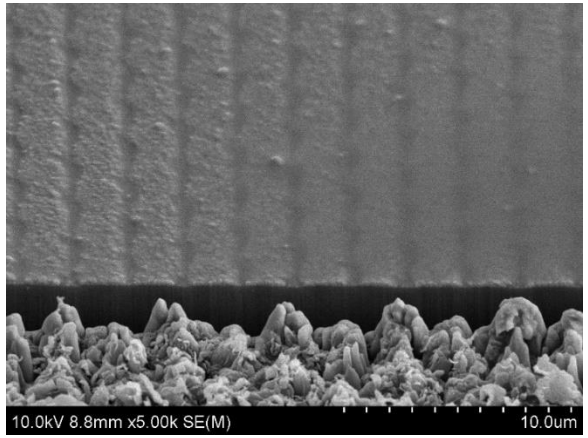

(b)

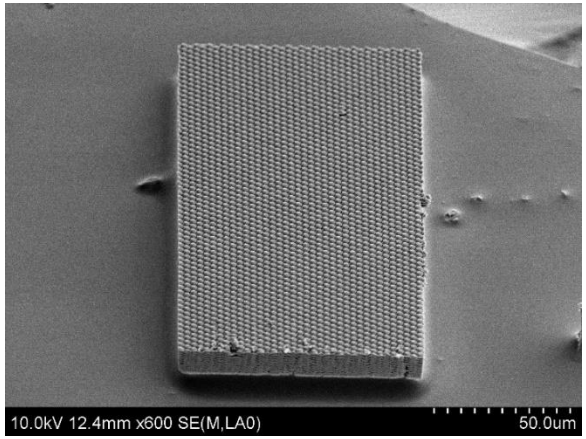

(c)

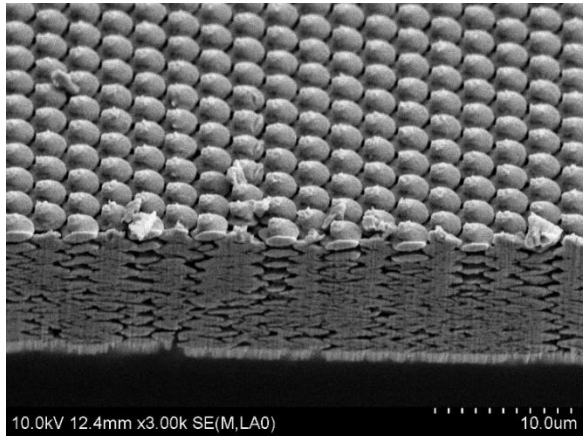

(d)

Figure D.27 Shear failure surfaces of a Cu film with 10 turns and 2800 nm seed seeding: **(a,b)** substrate, **(c,d)** cap.

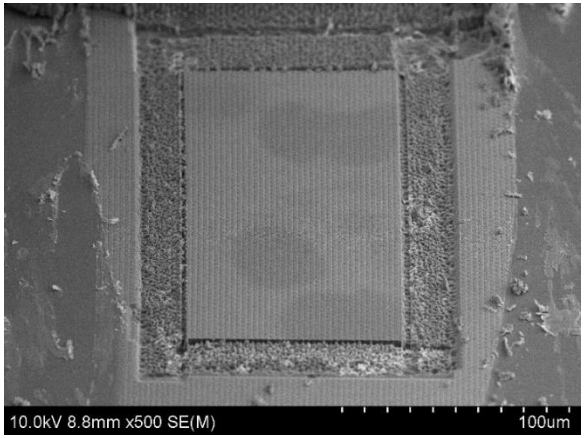

(a)

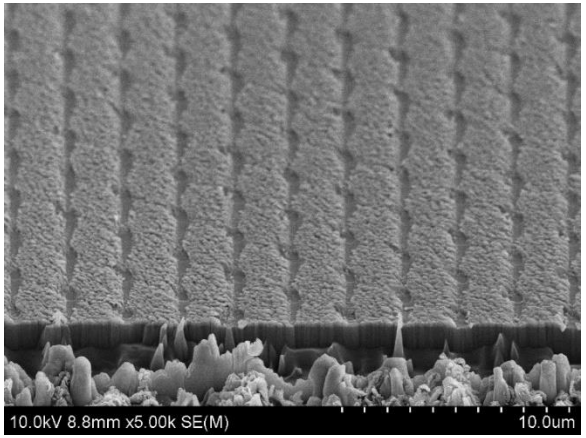

(b)

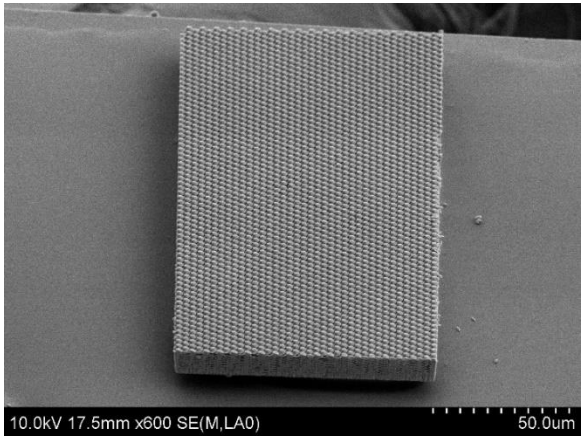

(c)

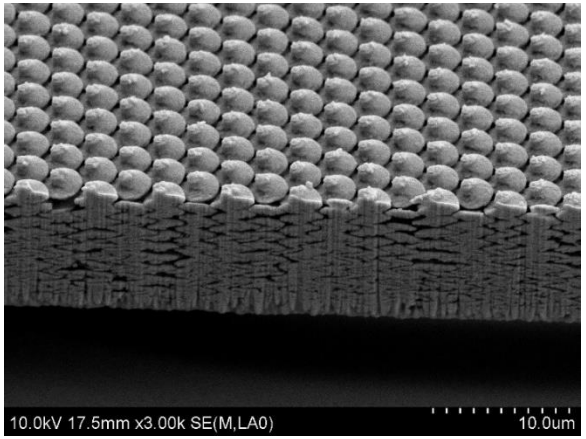

(d)

Figure D.28 Shear failure surfaces of a Cu film with 10 turns and 2800 nm seed seeding: **(a,b)** substrate, **(c,d)** cap.

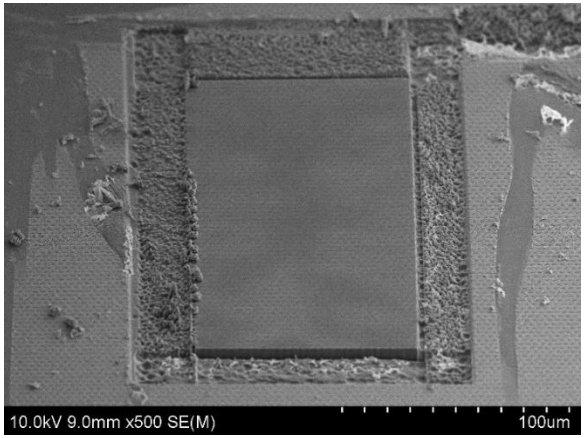

(a)

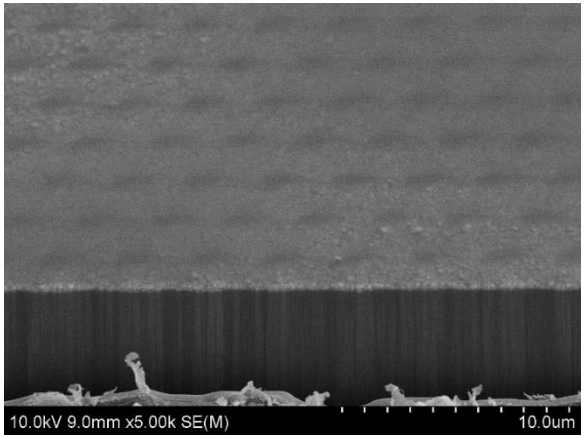

(b)

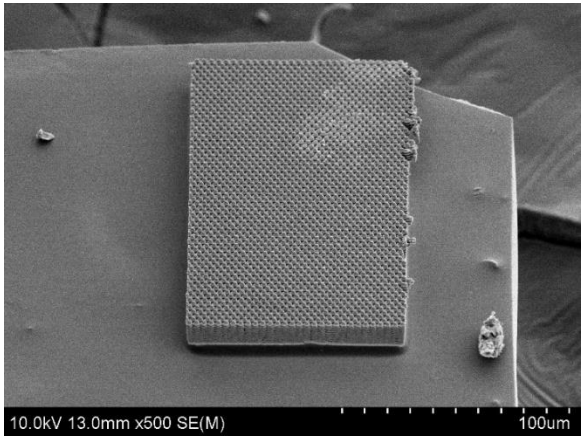

(c)

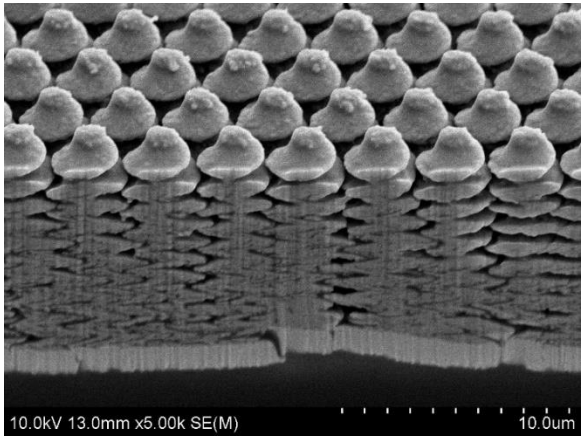

(d)

Figure D.29 Shear failure surfaces of a Cu film with 10 turns and 3200 nm seed seeding: **(a,b)** substrate, **(c,d)** cap.

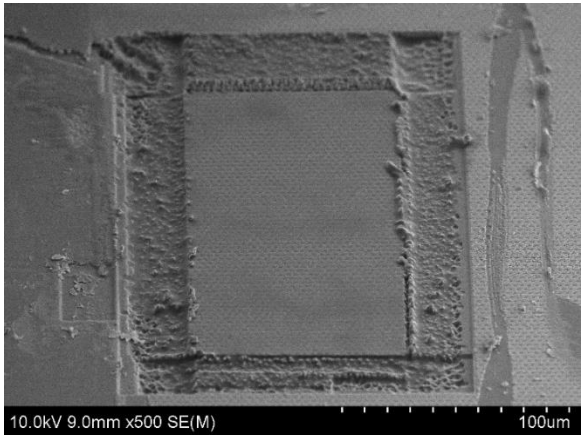

(a)

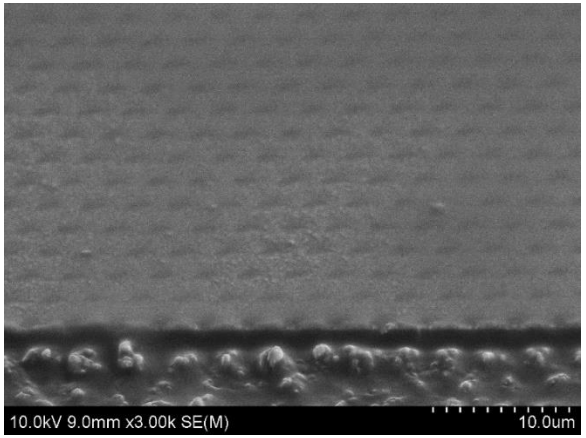

(b)

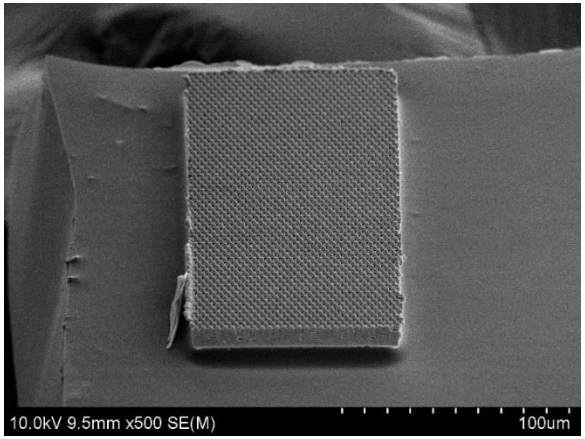

(c)

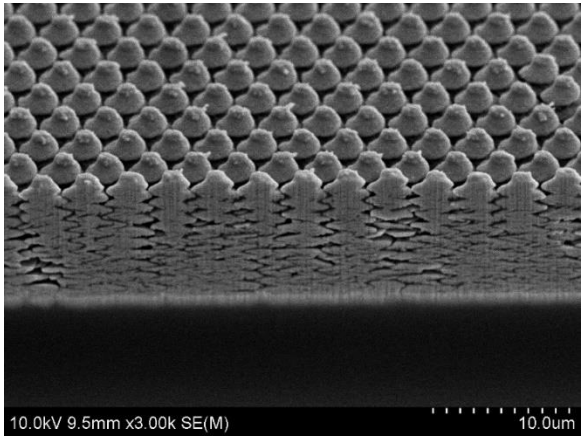

(d)

Figure D.30 Shear failure surfaces of a Cu film with 10 turns and 3200 nm seed seeding: **(a,b)** substrate, **(c,d)** cap.

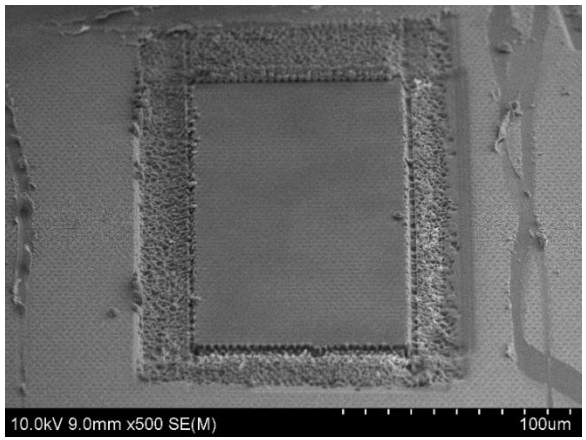

(a)

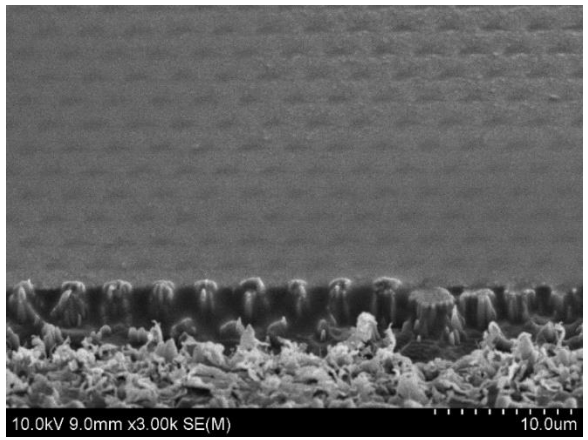

(b)

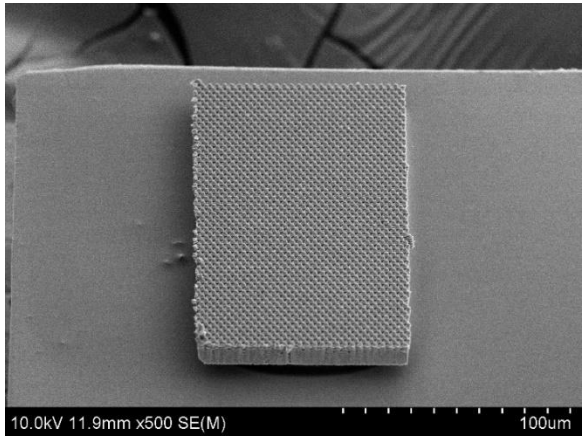

(c)

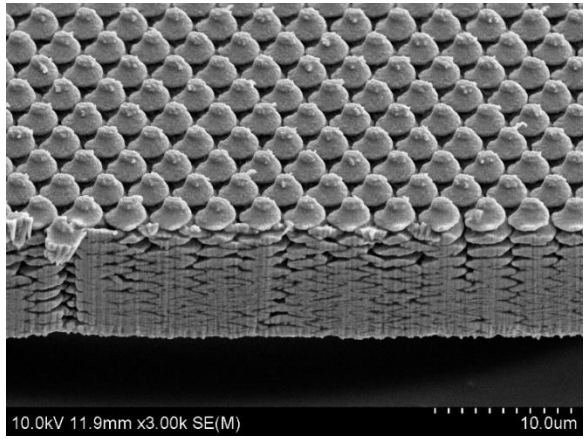

(d)

Figure D.31 Shear failure surfaces of a Cu film with 10 turns and 3200 nm seed seeding: **(a,b)** substrate, **(c,d)** cap.

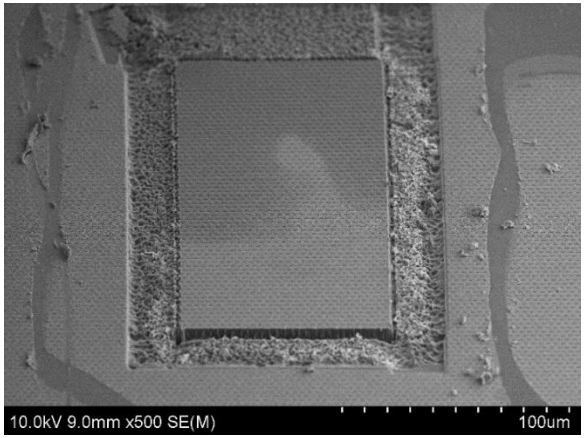

(a)

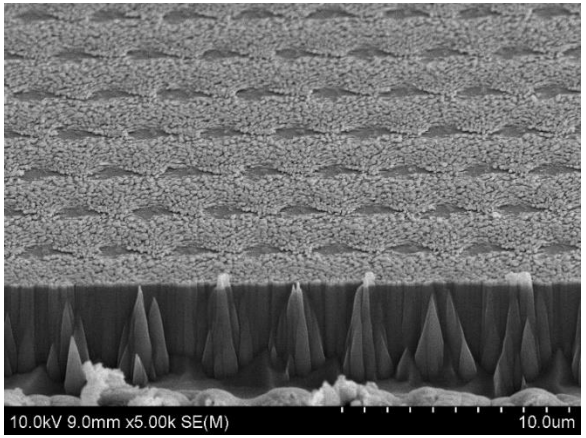

(b)

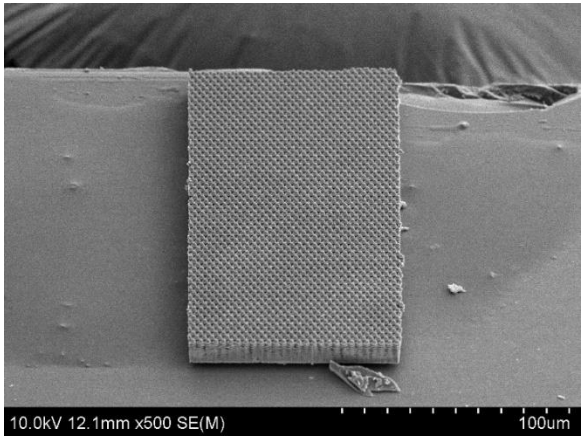

(c)

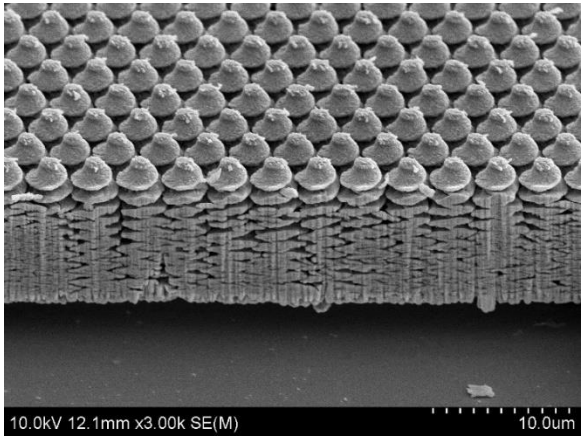

(d)

Figure D.32 Shear failure surfaces of a Cu film with 10 turns and 3200 nm seed seeding: **(a,b)** substrate, **(c,d)** cap.

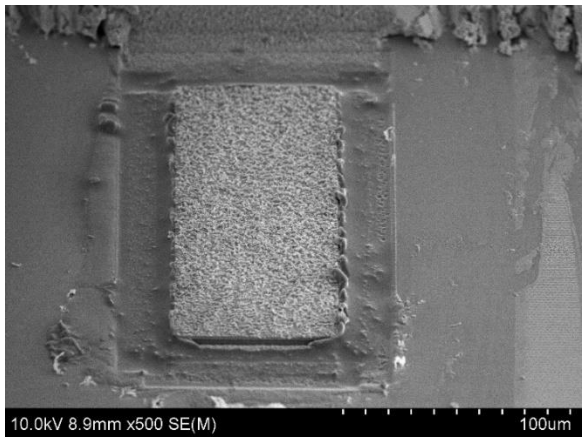

(a)

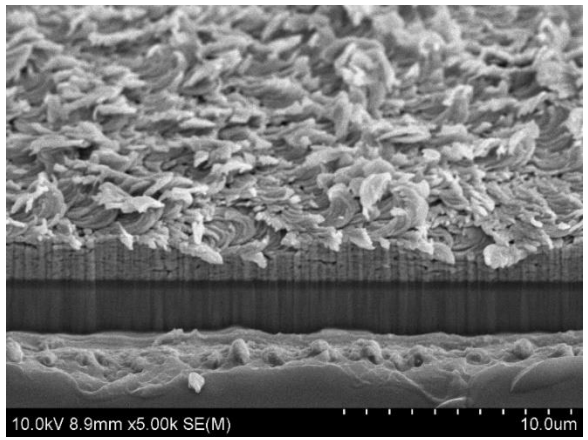

(b)

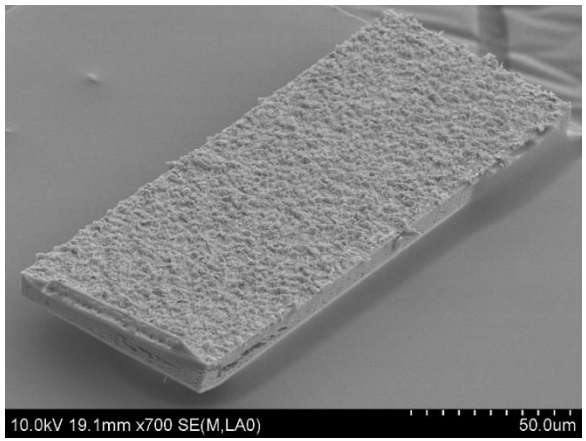

(c)

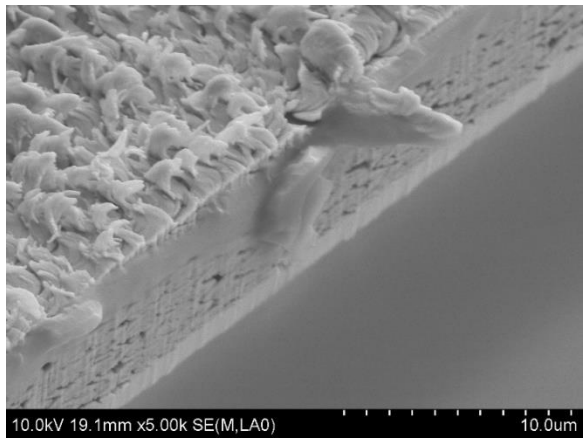

(d)

Figure D.33 Shear failure surfaces of a Cu film with 10 turns and unseeded substrate: **(a,b)** substrate, **(c,d)** cap.

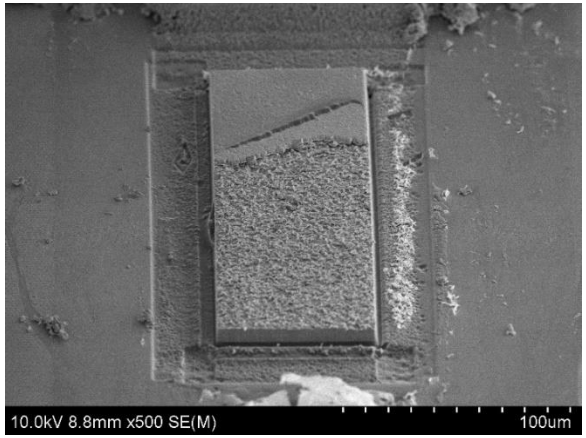

(a)

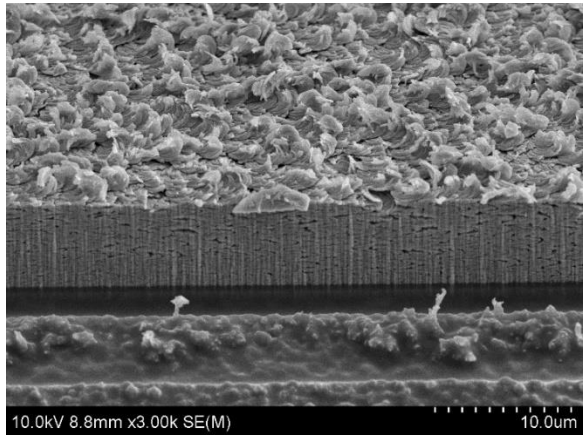

(b)

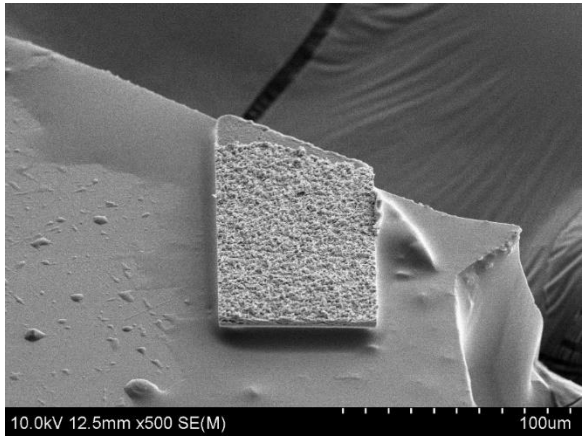

(c)

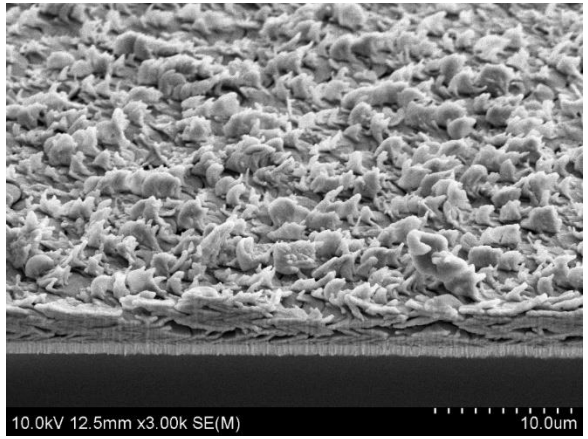

(d)

Figure D.34 Shear failure surfaces of a Cu film with 10 turns and unseeded substrate: **(a,b)** substrate, **(c,d)** cap.

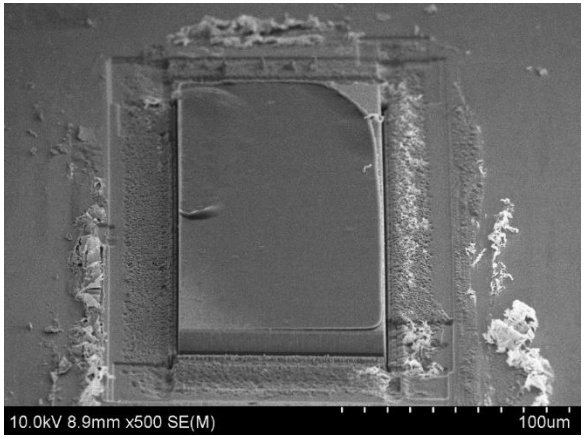

(a)

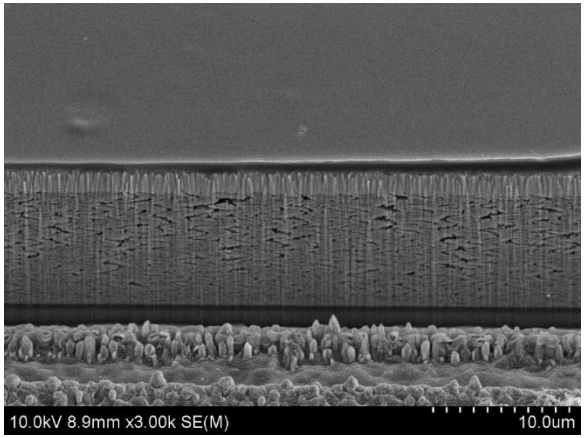

(b)

Figure D.35 Shear failure at the substrate side of a Cu film with 10 turns and unseeded substrate.